Imperial College London
Department of Aeronautics

Multiscale energy transfers in the near wake of a model wind turbine

Neelakash Biswas

Submitted in part fulfillment of the requirements for the degree of
Doctor of Philosophy in Aeronautics of Imperial College London,
October 2024

Abstract

This thesis examines the multiscale nature of coherent dynamics in a wind turbine wake using a series of particle image velocimetry (PIV) experiments. The near wake dynamics is studied at different tip speed ratios (λ) and for different levels of freestream turbulence (FST). The near wake is found to be dominated by multiple coherent structures, including the tip vortices, distinct vortex sheddings from the nacelle and tower, and wake meandering. A convective length scale (L_c) related to the pitch of the tip vortices is defined that is shown to be a better length scale than turbine diameter (D) to demarcate the near wake from the far wake. With negligible FST, the near wake length is found to be $\approx 3L_c$ for a range of λs tested. With elevated FST, wake meandering is seen to become more energetic, while the tip vortices broke down earlier, leading to a shorter near wake ($< 3L_c$). With negligible FST, a decreasing trend of wake meandering frequency with λ is observed, similar to vortex shedding from a porous plate at varying porosity, upholding the notion of wake meandering being a global instability of the turbine. The energy exchanges to and from the different frequencies are studied using the multiscale triple decomposed coherent kinetic energy budget equations developed by Baj & Buxton (Phys. Rev. Fluids, vol. 2, 2017, 114607). Various modes such as the primary (energised by the mean flow), secondary (energised by triadic interactions) and mixed (having multiple energy sources) modes are identified in the wind turbine wake, especially in the tip vortex system, where a complex network of nonlinear triadic energy transfers is observed. Contrastingly, the modes associated with the sheddings from the nacelle or tower and wake meandering are always found to be primarily energised by the mean flow.

Acknowledgements

First and foremost, I would like to express my heartfelt gratitude for my supervisor Prof. Oliver Buxton without whose support this thesis truly would not have been possible. I not only found in him an excellent supervisor who helped me set the direction of the project with crucial technical inputs, but also he was a huge source of motivation and a parent for me away from home. Be it setting up an impromptu meeting for a quick discussion or correcting a draft of a paper, his responses have always been extremely quick. Honestly, I could not have wished for a more understanding and motivating supervisor.

I am grateful to the College and the Department for providing me the PhD funding through the President's PhD Scholarship scheme without which I could not have taken up this wonderful PhD project.

I must thank Dr. Andrew Wynn from the Department of Aeronautics at Imperial with whom we had several insightful discussions on implementing Optimal mode decomposition and mode clustering. These discussions were crucial for me to better understand my data and resolve some issues I was having with the technique initially.

During the initial part of my experiments, several people helped me set up my experiments. I am thankful to Oliver's past PhD student Dr. Krishna Kankanwadi who first taught me how to operate the hydrodynamics flume, lasers and the cameras. At the same time, I thank Oliver's postdoc Dr. Jiangang Chen for patiently entertaining all my queries related to the camera and laser synchronization. Additionally, I must thank all the technical stuff at Imperial, especially Mr. Roland Hutchins and Mr. Franco Gimmaria for helping me in designing and manufacturing the wind turbine model.

There is a long list of people who helped me resolve several non-academic issues during my PhD without which this thesis certainly would not have been of the current standard.

I probably had one of the most turbulent starts to my PhD as it started when Covid19 peaked in the UK. Upon exiting quarantine in London, I was immediately faced with a national lockdown. This isolation, in both my personal life and work life (we did not have access to the labs or office desks) led to a rapid decline in my mental health. I suffered from an inability to sleep and anxiety. After discussions with Oliver, we both decided that the best course of action for me was to return to India for a short period of time to recuperate. This occurred at a timely

point in my PhD since I was still in the process of finalizing designs for my experiments. These designs subsequently required raw materials to be ordered and eventually for the models to be manufactured. While this was taking time, I traveled back to India and started working on a data set from one of Oliver's previous PhD students to develop the tools for modal decomposition and energy budget analysis that could be directly applied to my own data set when available. At this time the UK was still in a full lockdown whilst the situation in India was far more satisfactory.

Suddenly, the situation in India deteriorated rapidly and my entire family contracted Covid19. Whilst I was ill with the disease myself, my father had a much more serious case. He was moved to intensive care and the doctors were not too hopeful about his recovery. Paying for private medical care exacted a very large financial toll on me and all our savings were exhausted in no time. In this extremely challenging situation, one of my Juniors from IIT Kharagpur, Akash Bhunia (now a PhD student at the Texas A&M University) took the initiative to raise crowd funding. Despite being a junior, he had important life experiences to share with me which helped me identify the roots of my mental health issues and helped me face my fears. With his kind help, the crowd funding was timely set up and we could continue my father's treatment thanks to the generous donations from my friends, family and even my professors from IIT. After spending 5 weeks in intensive care he slowly started recovering and I got a much needed boost to my mental strength. I started preparing for a return to the UK.

However, I kept getting tested positive for Covid19 for nearly 2 months although I did not have any symptoms. I had to cancel/reschedule my flights at least 6 times trying to enter UK but all in vein. To make things worse, soon after, UK government moved India to a red list (travel ban) completely eliminating my remaining chances to return to the UK soon. In total, I was stuck in India for nearly six months. I can't thank Oliver enough for supporting me and believing in me in this difficult period of my life. He was extremely understanding throughout this period and even offered my financial help. We kept working remotely, in fact we got some interesting results analyzing the data set he had provided me. Finally, we ended up publishing the results in the Journal of Fluid Mechanics soon after I returned to the UK.

In the UK, I made many good friends who made my stay here enjoyable. I shared many fond memories with friends from the Indian society and the cricket society at Imperial and also with my flatmates, especially from the Victoria League Student house. Here I must talk about Sallar Ali Qazi (also doing PhD in Aeronautics at Imperial) who was probably among the first few

persons I met in the UK. He was not only someone I could share everything with, he was also like a saviour to me. From letting me stay at his place when I was briefly homeless (due to some tenancy issues) to lending me money whenever I was broke (quite often), he has always had my back. I feel sorry to admit that I have occasionally used him as a bank that gives away interest-free loans. I was indeed lucky to have got such friends away from home who would care for me as a family member.

I must thank my past supervisors from India, Dr. Sandeep Saha from IIT Kharagpur, and Prof. Debopam Das from IIT Kanpur who first introduced me to the beautiful world of fluid dynamics and motivated me to have a research career.

Finally, I would like to thank my parents. They have been a constant source of strength for me. I could not have completed my PhD without their ceaseless love, encouragement and support.

Dedication

This thesis is dedicated to my parents Sri Parthapratim Biswas and Srimati Aparajita Biswas.

Declaration

I hereby declare that this thesis, and the research to which it refers, are entirely my own work and has not been submitted for any other award. Where other sources of information have been used they have been acknowledged and fully referenced.

The copyright of this thesis rests with the author. Unless otherwise indicated, its contents are licensed under a Creative Commons Attribution-Non Commercial 4.0 International License (CC BY-NC). Under this license, you may copy and redistribute the material in any medium or format. You may also create and distribute modified versions of the work. This is on the condition that: you credit the author and do not use it, or any derivative works, for a commercial purpose. When reusing or sharing this work, ensure you make the license terms clear to others by naming the license and linking to the license text. Where a work has been adapted, you should indicate that the work has been changed and describe those changes. Please seek permission from the copyright holder for uses of this work that are not included in this license or permitted under UK Copyright Law.

Neelakash Biswas
London
October, 2024

To see the rainbow you must go through the rain.

Contents

Abstract i

Acknowledgements ii

1 Introduction 1

1.1 Multiscale generated turbulence 1

1.2 Wind turbine wakes 6

1.3 Thesis outline and objectives 13

1.4 Publications 14

2 Experimental methods 15

2.1 Experimental facility 15

2.1.1 Illumination system 15

2.1.2 Particles 17

2.2 Design of the wind turbine model 17

2.3 PIV experiments without freestream turbulence 20

2.4 Grid characterisation and experiments with freestream turbulence 25

3 The multiscale nature of the dynamics in a wind turbine wake 30

3.1 Introduction . . . 30

3.2 Instantaneous vorticity field . . . 30

3.3 Mean velocity field . . . 35

3.4 Important frequencies . . . 37

3.4.1 Frequency maps . . . 44

3.4.2 Strength of frequencies . . . 47

3.5 The definition of near wake . . . 50

3.6 The nature and origin of wake meandering . . . 53

3.7 Conclusion . . . 59

4 Effect of freestream turbulence on the near wake coherent dynamics 62

4.1 Introduction . . . 62

4.1.1 Test cases . . . 62

4.2 Vorticity field . . . 63

4.3 Effect of freestream turbulence on the important frequencies . . . 65

4.4 Extent of the near wake . . . 73

4.5 Conclusions . . . 76

5 Multiscale triple decomposition and energy budget analysis: a simple flow 77

5.1 Introduction . . . 77

5.2 The simple multiscale flow . . . 77

5.2.1 Mean flow properties . . . 79

5.2.2 Dominant frequencies in the flow field . . . 81

5.3 Multiscale triple decomposition: extraction of coherent structures 86
5.3.1 Extraction of primary coherent structures 88
5.3.2 Secondary modes and phase averaging 91
5.4 Energy budget analysis 93
5.4.1 Mean energy budget 96
5.4.2 Energy budgets of primary shedding modes 100
5.4.3 On the origin of the secondary coherent structures 106
5.4.4 Energy exchanges for the harmonics 110
5.4.5 Summarising the energy cascade 112
5.5 Conclusion 114

6 Coherent energy budgets in wind turbine wake 117

6.1 Introduction 117
6.2 Coherent modes in the wake 118
6.2.1 Tip vortices 119
6.2.2 Low-frequency modes 121
6.3 Energy exchanges 124
6.3.1 Triadic interactions 130
6.4 Summary of the energy exchanges for the tip vortices 133
6.5 The near wake and wake recovery 136
6.6 On the choice of the modal decomposition technique 140
6.7 Conclusion 143

7 Effect of freestream turbulence on the energy exchanges in wind turbine wake 145

7.1 Introduction . . . 145

7.2 Mode clustering . . . 146

7.2.1 The nature of the wake meandering mode in the presence of FST . . . 150

7.2.2 The modes related to the tip vortices . . . 152

7.3 Effect of FST on the kinetic energy budgets . . . 153

7.4 Triadic interactions . . . 159

7.5 Conclusions . . . 160

8 Conclusions 161

8.1 Summary of Thesis Achievements . . . 161

8.2 Future Work . . . 163

Bibliography 165

A Additional notes on PIV resolution and convergence of the OMD modes 179

A.1 Spatial resolution of the PIV data used in chapter 5 . . . 179

A.2 Convergence and selection of the OMD modes in the wind turbine wake presented in chapter 6 . . . 180

List of Tables

2.1 Parameters associated with different experiments without freestream turbulence. Here δx represents the spatial resolution of the experiments. f_{aq}, δt, and T are the acquisition frequency, time between successive laser pulses and total time of data acquisition respectively. The freestream velocity was set to 0.2 m/s for all the experiments except experiments 1E and 1F for which it was increased to 0.3 m/s and 0.4 m/s respectively. 22

2.2 Parameters associated with different experiments in experimental campaign 5. . 29

List of Figures

1.1 (a) Square and (b) I type fractal grids used by Hurst and Vassilicos (2007) 2

1.2 An illustration of the space scale unfolding (SSU) mechanism (image reproduced from (Baj, 2018)) 3

1.3 An illustration of coherent motions in the wake of a wind turbine (image reproduced from (Porté-Agel et al., 2020)) 5

1.4 Dye visualization images of tip vortex evolution at different tip speed ratios λ (image reproduced from (Okulov et al., 2014)) 7

1.5 Flow visualization of the tip vortices when one blade is axially displaced by $+0.013D$ (top) and when one blade is azimuthally displaced by 5.7^o (bottom) (image reproduced from (Abraham and Leweke, 2023)) 7

1.6 Clouds formed behind wind turbines tracing the wake of the turbines at the Horns Rev ofshore wind farm near Denmark. The photograph is taken by Christian Steiness (see Hasager et al. (2013) for more details about the photograph.) 8

1.7 Instantaneous streamwise velocity field behind a turbine (image reproduced from (Gupta and Wan, 2019)). 12

2.1 Photographs of the experimental setup. In (b), the laser sheet is purposefully aligned with the nacelle surface, at an offset from the tower. 16

2.2 (a) A side view of the wind turbine model assembly, (b) a front view of the model. (c) shows an individual blade and the blade section at the root. 18

2.3 Variation of power (C_P) and thrust (C_T) coefficient of the turbine with tip speed ratio (λ) obtained from blade element momentum theory. 19

2.4 Snapshots showing the 3 blades of the turbine passing through the same point at $\lambda = 6$. 20

2.5 Mean streamwise velocity and turbulence intensity profiles at the rotor location. 21

2.6 A schematic of the wind turbine model and the fields of view used in the different experiments. The streamwise distance x is measured from the rotor plane and transverse distances z and y are measured from the nacelle centreline. Experiment 1 and 4 focused on the plane aligned with the tower's axis and streamwise direction, *i.e.* xy plane (sub figure 2.6(a)), while experiments 2 and 3 focused on xz planes at different y offsets (sub figure 2.6(c)). The planes of different experiments are also shown as the dashed lines in subfigure 2.6(b). 23

2.7 Regular grids (a) SRG38 and (b) SRG111 and fractal grids (c) SFG5 and (d) SFG7 used in this study (image reproduced from Kankanwadi (2022)). 24

2.8 (a) Mean velocity field and (b) turbulence intensity (T_i) field behind the regular grid SRG38. 26

2.9 Variation of mean streamwise velocity along the centreline ($y = 0$, $z = 0$) behind the grids (a) SRG38, (b) SRG111, (c) SFG7 and (d) SFG5. The shaded region shows the variation of mean streamwise velocity within the field of view considered. 26

2.10 Variation of turbulence intensity (T_i) at hub height with distance from the grids (a) SRG38, (b) SRG111, (c) SFG7 and (d) SFG5. The dashed vertical lines show the position of the rotor plane in different experiments. The shaded region shows the variation of T_i within the field of view considered. 27

2.11 Streamwise autocorrelation function of transverse velocity fluctuation (a) $2D$ and (b) $5D$ downstream of the grid SRG38 at the geometric centreline ($y = 0, z = 0$). In (b), the black curve shows the fitted bi-Gaussian curve. The strongest secondary autocorrelation peak is shown by the red '+' sign. The red dashed line shows the cutoff, the data below which was discarded during fitting. 28

2.12 Variation of integral length scale (L_v) at hub height with distance from the grids (a) SRG38, (b) SRG111, (c) SFG7 and (d) SFG5. The dashed vertical lines show the position of the rotor plane in different experiments. The shaded region shows the variation of L_v within the field of view considered. 28

3.1 Instantaneous vorticity fields of a wind turbine wake for (a) $\lambda = 4.5$ and (b) $\lambda = 6$ in the xy plane. Fields of view from experiment 1A and experiment 1B (at different time instants) are stitched together for a visual representation of the entire wake. 31

3.2 Instantaneous vorticity fields of a wind turbine wake in $xz(y = 0)$ plane (experiment 2A) for (a) $\lambda = 4.5$ and (b) $\lambda = 6$. Subfigures (c) and (d) show the vorticity fields at an offset ($y = -0.35D$) plane (experiment 2B) for $\lambda = 4.5$ and 6 respectively. 32

3.3 Instantaneous vorticity fields in the $xy(z = 0)$ plane for $\lambda = 6$ for (a) $U_\infty = 0.3$ m/s and (b) $U_\infty = 0.4$ m/s. The fields are noisy around $x/D \approx 2.1$ since a part of the laser beam leaked while forming the sheet using a cylindrical lens. The data is useful elsewhere in the field. 34

3.4 Mean velocity deficit at (a) $x/D = 0.5$, (b) $x/D = 1.0$, (c) $x/D = 1.5$, (d) $x/D = 2.0$, (e) $x/D = 2.5$, and (f) $x/D = 3.0$ for $\lambda = 4.5$ and 6. The black dashed lines represent a Gaussian fit to the mean velocity deficit profiles corresponding to $\lambda = 6$. 36

3.5 Transverse velocity spectra obtained at $x/L_c = 1$ for (a) $\lambda = 4.5$ and (e) $\lambda = 6$. Subfigures (b) and (f) show the same at $x/L_c = 1$, $y/D = 0.55$ for the two tip speed ratios. Similarly, subfigures (c) and (g) show the spectra at $x/L_c = 4$ for $\lambda = 4.5$ and $\lambda = 6$ respectively. The corresponding spectra at $x/L_c = 4$, $y/D = 0.55$ are shown in (d) and (h). Strouhal numbers St_C and St_D are defined based on L_c and D as the length scales, respectively, and U_∞ as the velocity scale. 38

3.6 Transverse velocity spectra obtained at (a) $x/D = 0.5$, $z/D = 0$ and (b) $x/D = 1.5$, $z/D = 0$ in the plane $y = 0$ (experiment 2A). The same is shown at an offset plane (experiment 2B) at (c) $x/D = 0.5$, $z/D = 0$, and (d) $x/D = 1.5$, $z/D = 0$. All the spectra are shown for $\lambda = 6$ only. 41

3.7 (a) Transverse velocity fluctuations just behind the tower and (b) corresponding spectra for $\lambda = 6$. The gray line in (a) is the unfiltered signal and the red line is the filtered signal. The spectra are obtained based on the unfiltered signal. (c) and (d) show the same for $\lambda = 4.5$. 43

3.8 Zones of dominant frequencies for $\lambda = 4.5$ 43

3.9 Zones of dominant frequencies for $\lambda = 6$. 46

3.10 Zones of dominant frequencies for $\lambda = 4.5$ in the plane (a) $y = 0$ and (b) $y = -0.35D$. Subfigures (c) and (d) show the same for $\lambda = 6$. 47

3.11 Zones of dominant frequencies for $\lambda = 6$ in the plane $z = 0$ for (a) $U_\infty = 0.3$ m/s and (b) $U_\infty = 0.4$ m/s. 48

3.12 The evolution of the 'strength' of different frequencies with streamwise distance for (a) $\lambda = 4.5$ (a) and (b) $\lambda = 6$. The strength is calculated as the magnitude of the largest peak in the spectra of transverse velocity at a particular streamwise location. 49

3.13 Strength of different frequencies in the $xz(y = 0)$ plane for (a) $\lambda = 4.5$ and (c) $\lambda = 6$ respectively. Sub figures (b) and (d) show the same in an offset plane $y = -0.35D$. 50

3.14 Variation of relative strength of $3f_r$ and f_{wm} with streamwise distance scaled by (a) turbine diameter D and (b) convective length scale L_c for different tip speed ratios. 52

3.15 Streamwise variation of the amplitudes of the modes at frequencies $3f_r$ and f_{wm} for $\lambda = 6$ when (a, c) $U_\infty = 0.3$ m/s and (b, d) $U_\infty = 0.4$ m/s. In (a) and (b) the strength is obtained using an FFT of the transverse velocity fluctuation, whilst (c) and (d) are based on Welch's PSD estimation. 53

3.16 Transverse velocity components of the phase-averaged wake meandering modes for (a) $\lambda = 4.5$ and (b) $\lambda = 6$. 54

3.17 (a) Axial induction factor obtained from the blade element momentum method for $\lambda = 6$. (b) Variation of rotor porosity with λ. 55

3.18 Transverse velocity spectra obtained at $x/D = 2$ and $z/D = 0$ for $\lambda = 5.2$ using (a) FFT and (b) Welch's PSD estimation. 56

3.19 Variation of wake meandering Strouhal number with λ at (a) $x/D = 2$, (b) $x/D = 3$, and (c) $x/D = 5$. '- -' shows the linear best fit lines. 58

3.20 Power spectra obtained using the Welch's PSD estimation at $x/D = 4$ and $y/D = 0$ from experiment 4 for $\lambda = 6$. (a) is obtained using the entire time series *i.e.* with the data sampled at 100 Hz. In (b-d) the data is down sampled at (b) 50 Hz, (c) 20 Hz and (d) 10 Hz. The length of the windows used in the PSD estimation was fixed to $N/2$ for all the cases, where N is the time series length in the corresponding case. 58

4.1 (a) Parameter space of turbulence intensity (T_i) and integral length scale (L_v) produced by different turbulence generating grids. (b) shows the effective tip speed ratios (λ_{eff}) for $\lambda_\infty = 6$ 63

4.2 Vorticity field for the cases (a) 1, (b) 2a, (c) 3, and (d) 4b. 64

4.3 Spectra at $x/D = 0.5$ and $y/D = 0.55$ for the cases (a) 1, (b) 2a, (c) 3, and (d) 4b. 65

4.4 Spectra at $x/D = 4$ and $y/D = 0$ for the cases (a) 1, (b) 2a, (c) 3, and (d) 4b. The transverse velocity spectra stacked in column (i) are obtained using FFT. The power spectra in columns (ii) - (v) are obtained using the Pwelch PSD estimator having window lengths (ii) 4000, (iii) 3000, (iv) 2000 and (v) 1000. The total length of the data was 5455 snapshots. The windows had 50% overlap in each case. 67

4.5 Dominant frequency maps for the cases (a) 1, (b) 2a, (c) 3, and (d) 4b obtained from the power spectra. The power spectra are obtained using Pwelch's PSD estimation with a window length of 3000. 68

4.6 Power spectra in the freestream (without the turbine) and in the wake, $0.5D$ downstream of the turbine for (a) no grid case, (b) case 2a, (c) case 3 and (d) case 4b obtained using Pwelch's PSD estimation with a window length of 3000. 70

4.7 Spectra for case 2a at $x/D = 0.5$ and (a) $y/D = 0.55$ and (b) $y/D = 0.53$. Subfigures (c) and (d) show the same for the case 2b. 71

4.8 Transverse variation of PSD amplitude averaged over WMFB for different FST cases at (a) $x/D = 1$, (b) $x/D = 3$ and (c) $x/D = 5$. Here N_f denotes the number frequencies in the WMFB. 72

4.9 PSD amplitudes averaged over WMFB and transverse distance y for different FST cases. 72

4.10 Variation of the strength of frequencies for the cases (a) 1, (b) 2a, (c) 3 and (d) 4b. 74

4.11 Variation of the near wake length with (a) T_i and (b) L_v. The near wake is scaled by L_c. For each case L_c is calculated based on λ_{eff}. 75

4.12 Phase averaged vorticity field for $3f_r$ for the no grid case. The fitted circle shows the average size of the tip vortices. 76

5.1 A schematic of the main cylinder and control rod assembly. 78

5.2 Flow states adopted from Cicolin et al. (2021) for the flow past a circular cylinder and a control rod in the range $\theta = 90° - 180°$ and for a fixed radial position $R/D = 0.7$. State I occurs for $90° \leq \theta \leq 115°$, State II for $120° \leq \theta \leq 125°$, and State III for $135° \leq \theta \leq 180°$ at this particular Re. At $\theta = 130°$ the flow develops a bistability between states II and III. 79

5.3 Mean streamwise velocity field for (a) $\theta = 90^o$ (b) $\theta = 110^o$ (c) $\theta = 115^o$. The dashed lines depict the extent of the recirculation region for the main cylinder wake in the presence of a control rod, whilst the solid line represents the same for a bare cylinder. 80

5.4 Normalised v_{rms} field for (a) $\theta = 90°$ (b) $\theta = 110°$ (c) $\theta = 115°$ 81

5.5 Frequency spectra of the transverse velocity fluctuation at $x/D = 1$ (a,c,e,g) and $x/D = 2$ (b,d,f,h) for the bare cylinder (a,b), $\theta = 90°$ (c,d), $\theta = 110°$ (e,f) and $\theta = 115°$ (g,h). Here S_t is the Strouhal number calculated based on the main cylinder's diameter (D) and the freestream velocity (U_∞). 82

5.6 (a) transverse velocity time series and (b) corresponding transverse velocity spectra at $x/D = 1, y/D = -0.7$ showing the primary and secondary modes for $\theta = 90°$. (c) transverse velocity time series and (d) corresponding fft spectra at $x/D = 3.5, y/D = 0.35$ showing the main cylinder's shedding mode and the harmonics at the same θ. 85

5.7 Streamwise evolution of the maximum normalised spectral peak of the transverse velocity associated with different modes for (a) $\theta = 90°$ and (b) $\theta = 110°$. 86

5.8 OMD spectra for $\theta = 90^o$ and $\theta = 110^o$ 88

5.9 Modes associated with (a) the control rod shedding frequency and (b) the cylinder shedding frequency at $\theta = 90°$. (c) and (d) shows the second and third harmonics of the main cylinder shedding mode respectively. The filled contour shows the energy of the modes while the contour lines represent iso-phase lines of transverse velocity fluctuation of the modes. The contour lines are shown from $-\pi$ to π at step size (a) $\pi/2$ (b) $\pi/15$ (c) $\pi/10$ and (d) $\pi/7$. The '+' sign shows the location where the kinetic energies of the modes attain a maximum. 89

5.10 Modes associated with (a) control rod shedding frequency and (b) cylinder shedding frequency at $\theta = 110°$. (c) and (d) shows the second and third harmonics of the main cylinder's shedding mode respectively. The filled contour shows the energy of the modes while the contour lines represent iso-phase lines of transverse velocity fluctuation of the modes. The contour lines are shown from $-\pi$ to π at step size (a) $\pi/2$ (b) $\pi/15$ (c) $\pi/10$ and (d) $\pi/7$. The '+' sign shows the location where the kinetic energies of the modes attain a maximum. 90

5.11 Energy and iso-phase lines associated with (a) low-frequency $(f_c - f_m)$ and (b) high-frequency $(f_c + f_m)$ secondary modes for $\theta = 90°$. The corresponding modes for $\theta = 110°$ are shown in fig (c) and (d). The contour lines are shown between $-\pi$ to π at a step size of $\pi/2$ for all the modes. The '+' sign shows the location where kinetic energy is maximum. 92

5.12 Terms of the mean kinetic energy budget for $\theta = 90°$ at (a) $x/D = 1$, (b) $x/D = 2$ and (c) $x/D = 3$. The energy budget terms (denoted by E in the figure) are non-dimensionalised by U_∞^3/D. 96

5.13 Streamwise evolution of the integrated kinetic energy budget terms for (a) bare cylinder and (b) $\theta = 90°$. The horizontal $(- \cdot -)$ line shows the 0 level for a reference. (c) Net contribution of different sink terms. The energy budget terms are denoted by the generic E letter. 99

5.14 Coherent energy budget terms of the main cylinder's shedding mode at (a) the location where the peak in the spectrum of transverse velocity component of the mode attains a maximum, *i.e.* $x/D \approx 1.51$ (b) wake intersection point ($x/D \approx 0.97$) for $\theta = 90°$. The same plots for $\theta = 110°$ are shown in fig. (c) at $x/D \approx 1.48$ and (d) at $x/D \approx 0.76$ respectively. The corresponding budget terms for the control rod's fundamental shedding mode for $\theta = 90°$ are shown in fig. (e) for $x/D \approx 0.1$ and in (f) for $x/D \approx 0.97$. The same plots for $\theta = 110°$ are shown in fig. (g) at $x/D \approx 0.3$ and (h) at $x/D \approx 0.76$ respectively. 100

5.15 Streamwise evolution of the kinetic energy budget terms for (a) the main cylinder's and (b) the control rod's fundamental shedding modes at $\theta = 90°$. Plots (c) and (d) show the same $\theta = 110°$. The horizontal $(- \cdot -)$ line shows the 0 level for a reference. 102

5.16 Net energy transfers through coherent energy production and non-linear triadic energy transfer terms for (a) the main cylinder's fundamental shedding mode, and (b) the control rod's fundamental shedding mode for $\theta = 90°$. Black bars show a gain of energy and red bars show a loss of energy for the respective mode. 104

5.17 Kinetic energy budget terms for (a) low- and (b) high-frequency secondary coherent modes for $\theta = 90°$ at the wake intersection point. Figure (c-d) shows the same for $\theta = 110°$ at the corresponding wake intersection point. 105

5.18 Streamwise evolution of the integrated kinetic energy budget terms for (a) low- and (b) high-frequency secondary modes for $\theta = 90°$. Figure (c-d) shows the same for $\theta = 110°$. 107

5.19 Streamwise evolution of certain triadic energy transfer terms for (a) low- and (b) high-frequency secondary modes at $\theta = 90°$. 108

5.20 Net energy transfer through coherent energy production and non-linear triadic energy transfer terms for (a) low- and (b) high-frequency secondary modes at $\theta = 90°$. The colours of the bars bear the same meaning as in figure 5.16. 109

5.21 Streamwise evolution of the kinetic energy budget terms for (a) the second harmonic ($2f_m$) and (b) the third harmonic ($3f_m$) of the main cylinder shedding mode for $\theta = 90°$. The region highlighted in yellow color is excluded in further analysis to avoid spatially incoherent region of the modes. 110

5.22 Net contribution from the production and triadic interaction terms for (a) the second harmonic ($2f_m$) and (b) the third harmonic ($3f_m$) of the main cylinder. The colours of the bars bear the same meaning as in figure 5.16. 112

5.23 Effect of changing the domain of integration on the coherent energy production and triadic interaction terms of the (a) second and (b) third harmonics of the main cylinder's shedding frequency for $\theta = 90°$. 113

5.24 Combined schematic energy transfer diagram for the different modes identified within the flow. The modes are arranged such that characteristic frequency of the modes increases from bottom to top. The thick full headed arrows show the net energy transfer between the various modes and the mean flow. The single headed arrows show the non-linear triadic energy transfer between two modes. A solid line shows non-linear energy transfer from low-frequency to high-frequency, whilst the dashed lines show energy transfers from high-frequency to low-frequency - an inverse cascade. 114

6.1 OMD spectra obtained for (a) $\lambda = 6$ and (b) $\lambda = 5$ from experiment 1G. The modes shown by a + sign are selected for a lower order representation of the flow. The high frequency modes with $St_D > 1$ are related to the tip vortices. The low frequency modes ($St_D < 1$) are associated with wake meandering, and the sheddings from the nacelle and the tower. 118

6.2 Transverse velocity component of the OMD modes associated with f_r - $6f_r$ for $\lambda = 6$ (a - f) and $\lambda = 5$ (g - l). The + sign shows the location where the kinetic energy associated with the individual modes is maximum. 120

6.3 Transverse velocity component of the low frequency modes (labeled as 1-6 in figure 6.1) for $\lambda = 6$ (a - f) and $\lambda = 5$ (g - l). 122

6.4 Transverse velocity components of the OMD modes associated with frequencies (a) f_n and (b) f_{wm} for $\lambda = 5.5$ obtained from experiment 1D. 123

6.5 Transverse velocity components of the OMD modes associated with frequencies (a) f_r, (b) $2f_r$, (c) $3f_r$, (d) f_n obtained in the xz ($y = 0$) plane. Sub figure (e) shows the tower's vortex shedding mode at an offset plane $y = -0.35D$. The modes are shown for $\lambda = 6$ only. 124

6.6 Energy budget terms of equation 5.5 summed over the domain of investigation for different modes for (a) $\lambda = 6$ and (b) $\lambda = 5$. 125

6.7 Streamwise evolution of the spanwise (along y) averaged energy budget terms of equation 5.5 for (a) f_r, (b) $2f_r$ and (c) $3f_r$ for $\lambda = 6$. Sub figures (d)-(f) show the same for $\lambda = 5$. 127

6.8 Streamwise evolution of the energy budget terms of equation 5.5 averaged along the z direction for (a) f_r, (b) $2f_r$ and (c) $3f_r$ for $\lambda = 6$. 128

6.9 Streamwise evolution of the spanwise (along y) averaged energy budget terms of equation 5.5 for (a) f_{wm} in the xy plane. Streamwise evolution of the energy budget terms averaged along z direction for (b) f_n in the $y = 0$ plane, (c) f_T in the $y = -0.35D$ plane. 128

6.10 Triadic energy exchanges for (a) $\lambda = 6$ and (b) $\lambda = 5$ from experiment 1G. 129

6.11 Net traidic transfers for (a) $\lambda = 5$, (b) $\lambda = 5.3$, (c) $\lambda = 5.5$, (d) $\lambda = 6$, (e) $\lambda = 6.6$, (f) $\lambda = 6.9$. 131

6.12 Energy transfers from different frequencies in different triads to (a) f_r, (b) $2f_r$, (c) $3f_r$, (d) $4f_r$, (e) $5f_r$ and (f) $6f_r$. The possible traids are shown on the right. . 132

6.13 Triadic energy transfer pathways among the modes $f_r - 4f_r$ for (a) $\lambda = 6$ and (c) $\lambda = 5$. The line types and the colour of the arrows showing inter frequency energy transfers are consistent with those used to represent triads in figure 6.12. The solid black arrow show the positive contribution from the $\tilde{P}_l$ term in equation 5.5. The thickness of the arrows varies according to the magnitude of the energy transfers as indicated. (b) shows the magnitudes of the energy transfers from $3f_r$ to $2f_r$ in triad 1 and from $4f_r$ to $3f_r$ in triad 2 for different λs. 134

6.14 Filled contours showing relative kinetic energy of the wake meandering mode with respect to the mode associated with f_r (denoted by $\tilde{k}_{f_{wm}} - \tilde{k}_{f_r}$) for (a) $\lambda = 6$ and (b) $\lambda = 5$. The solid and dashed black lines correspond to $\tilde{k}_{f_{wm}} - \tilde{k}_{f_r} = 0$ and $\tilde{k}_{f_{wm}} - \tilde{k}_{3f_r} = 0$ respectively. The $+$ sign shows the location where the kinetic energy corresponding to f_r is maximum. The dash-dotted vertical line shows the streamwise location corresponding to 3 convective length scales or $3L_c$ defined in chapter 3. 139

6.15 (a) Streamwise variation of spanwise averaged mean flow production term for the tip vortex system (shown by the solid lines) and f_r (shown by the dashed line) for diffrerent λs. (b) The variation of the location where wake recovery initiates or x_{wr} with λ (–●–). The solid black line shows the streamwise location $x/D = 3L_c$. 139

6.16 (a) Mean flow production term ($\tilde{P}_l$) of f_r for $\lambda = 6$, (b) shows the leading term of $\tilde{P}_l$. The '+' sign marks the location of the sign change. 141

6.17 Transverse velocity components of the sPOD modes associated with frequencies (a) f_r, (b) $2f_r$, (c) $3f_r$, (d) $4f_r$, (e) $5f_r$ and $6f_r$ for $\lambda = 6$. 141

6.18 Transverse velocity components of the dominant sPOD modes associated with wake meandering. 142

6.19 (a) sPOD spectra. The circles show the modes selected to construct the reduced order representation of the flow. (b) Energy budget terms of the sPOD modes summed over the entire domain. 142

7.1 1st, 2nd and 5th iterations of the mode clustering algorithm for the case 2a. The chosen parameters were as follows: $r = 175$, $\zeta_{spat} = 0.94$, and $\zeta_{spec} = 0.3$. 146

7.2 Variation of the number of converged modes (N_c) with ζ_{spat} for different ζ_{spec} for the cases (a) 2a, (b) 3 and (c) 4b. 148

7.3 Variation of the number of converged modes (N_c) with ζ_{spat} for (a) case 1, (b) case 2b, (c) case 2c, (d) case 4a, (e) case 4c and (f) case 4d. 148

7.4 1st, 2nd and final iterations of the mode clustering algorithm for the no grid case (a-c), case 3 (d-f) and case 4b (g-i). 149

7.5 Two dominant wake meandering modes for the cases (a,b) without FST, (c,d) case 2a, (e,f) case 3, (g,h) case 4b. 151

7.6 Example low frequency modes for the (a) no grid case and (b) case 4b that are not considered to be a part of the coherent component of the flow. 152

7.7 Modes associated with $3f_r$ (a,c,e,g) and f_r (b,d,f,h) for no grid case (a,b), case 2a (c,d), case 3 (e,f) and case 4b (g,h). 152

7.8 Modes associated with $3f_r - f_{wm}$ (a,c) and $3f_r + f_{wm}$ (b,d) case 2a (a,b) and case 2b (c,d). 153

7.9 Summed budget terms for (a) no grid case, (b) case 2a, (c) case 3 and (d) case 4b. 154

7.10 Summed $\tilde{P}_l$ term for the frequencies in the WMFB for different FST cases. The x axis on the top shows the turbulence intensity of each case. 155

7.11 Summed components of the $\tilde{P}_l$ term for (a) case 1 and (b) case 2a. 156

7.12 Mean streamwise velocity profiles for selected FST cases at (a) $x/D = 1$, (b) $x/D = 3$ and (c) $x/D = 5$. 157

7.13 Transverse gradient of mean streamwise velocity for selected FST cases at (a) $x/D = 1$, (b) $x/D = 3$ and (c) $x/D = 5$. 157

7.14 Summed correlation $\overline{\tilde{u}^m \tilde{v}^l}$ for (a) case 1 and (b) case 2a. 158

7.15 Inter frequency triadic energy transfers for (a) no grid case, (b) case 2a and (c) case 3. 160

8.1 Vorticity field in the wake of a turbine with an aerodynamic nacelle for $\lambda = 6$. . 163

A.1 (a) Mean turbulent kinetic energy and (b) Kinetic energy of the control rod's shedding mode obtained from two data sets at $x/D = 0.65$. 180

A.2 (a) OMD spectra for different ranks r. (b) and (c) show the streamwise evolution of the spanwise-averaged $\tilde{P}_l$ term for f_r and f_{wm} respectively for different r. . . 181

A.3 (a) OMD spectrum for $\lambda = 6$ from experiment 1E. The '$\circ$' symbols show the additional low-frequency modes ($St_D < 1$) retained. (b) shows the energy budget terms of equation 5.5 summed over the domain of investigation for all the modes including the additional low frequency modes. 182

A.4 (a) OMD spectrum for $\lambda = 6$ from experiment 1E. The '$\circ$' symbols show the additional modes retained in the range $1 \lesssim St_D \lesssim 3$. (b) shows the streamwise evolution of the spanwise-averaged net triadic energy production term for $f_r - 3f_r$ with (circles) and without (solid lines) the inclusion of the additional modes. . . 183

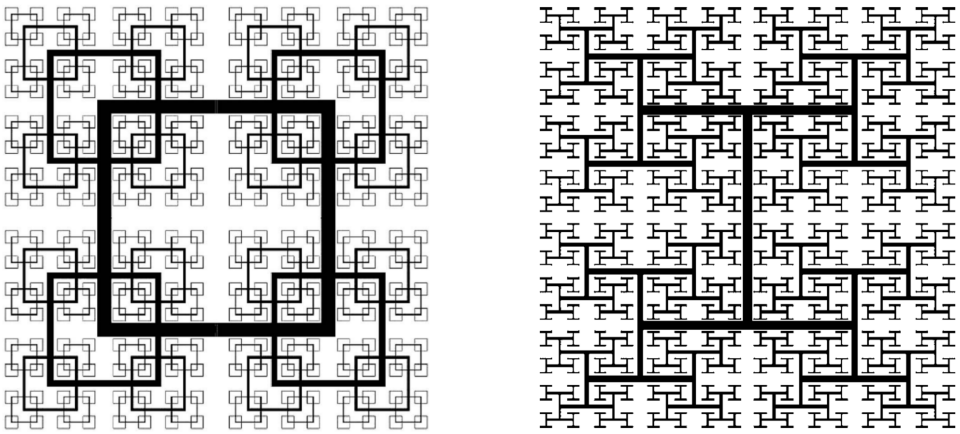
Chapter 1

Introduction

1.1 Multiscale generated turbulence

Multiscale flows are encountered everywhere, for instance the air flow through a city with buildings of multiple sizes or a flow through a forest could be a good example of a multiscale flow. In a multiscale flow, forcings are introduced at different length and time scales simultaneously, which can lead to interesting properties such as enhanced mixing (Laizet and Vassilicos, 2015) and the generation of new coherent structures (Baj and Buxton, 2017, 2019). To better understand the physics of multiscale generated turbulence, space-filling fractal grid (SFG) generated turbulence has been used as a canonical example (Hurst and Vassilicos, 2007; Mazellier and Vassilicos, 2010; Laizet and Vassilicos, 2015). A typical SFG used in these studies is shown in figure 1.1. In these SFGs, the bars having different thicknesses, produce individual wakes of different sizes. The interaction of these wakes yields the multiscale flow. Through numerical simulations, Laizet and Vassilicos (2012) showed enhanced scalar transfer and turbulent diffusion in the turbulence generated downstream of fractal grids. In order to physically explain the enhanced mixing in fractal grids, the authors proposed the space scale unfolding (SSU) mechanism. The central concept of the SSU mechanism and the resultant enhanced mixing (compared to that in a single scale flow) relies on the fact that behind a multiscale fractal grid, the wakes of the individual grid elements (which are of different sizes) intersect at different downstream locations, or in other words, a spatial 'unfolding' occurs. Such a scenario is shown through a

simplified schematic in figure 1.2 which shows three wake-generating bodies of different sizes. Note that the individual wakes intersect at different downstream locations. As a result of this spatial unfolding, a fluid parcel initially trapped in the wake of the small element can be easily entrained into the bigger wakes as they intersect. This mechanism is absent in regular grids where all the wakes of the individual elements intersect at the same location causing a large burst of turbulence intensity at a short distance from the grid (Laizet and Vassilicos, 2012). Baj and Buxton (2019) performed experiments to mimic the SSU scenario by considering the flow through a two-dimensional multiscale array of bars similar to that depicted in figure 1.2. They released a high Schimdt number scalar into the wake of the smallest bar and observed stable transverse bursts of the scalar in the vicinity of the wake intersection points, similar to the SSU mechanism.



(a) (b)

Figure 1.1: (a) Square and (b) I type fractal grids used by Hurst and Vassilicos (2007)

Another interesting facet of multiscale flows is the generation of new coherent structures and non-linear energy exchanges. Baj and Buxton (2017) first categorically studied the physics of generation of these new coherent structures in a two-dimensional multiscale array of bars. The authors not only observed the frequencies associated with the vortex sheddings from the bars, but also new frequencies were observed that exactly corresponded to the sum/difference between the two (distinct) vortex-shedding frequencies associated with the wakes of the two differently-sized bars intersecting. A triple decomposition method proposed by Baj et al. (2015) was applied to extract the spatio-temporal structures of the coherent modes associated with each of the frequencies. Here, the instantaneous velocity field $\boldsymbol{u}(\boldsymbol{x}, t)$ (where $\boldsymbol{x}$ and t denote

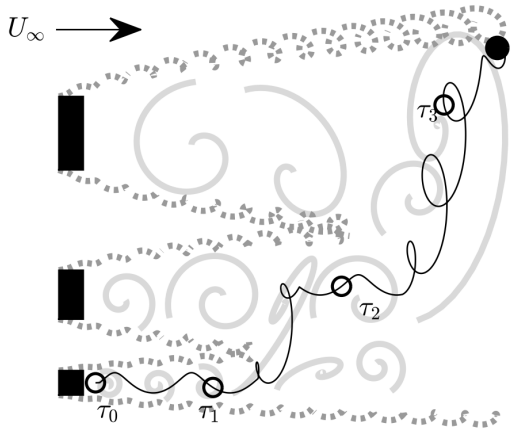


Figure 1.2: An illustration of the space scale unfolding (SSU) mechanism (image reproduced from (Baj, 2018))

space and time respectively) is decomposed in the following form

$$\boldsymbol{u}(\boldsymbol{x},t) = \bar{\boldsymbol{u}}(\boldsymbol{x}) + \sum_{l} \tilde{\boldsymbol{u}}_l(\boldsymbol{x},t) + \boldsymbol{u}''(\boldsymbol{x},t) \tag{1.1}$$

Here $\bar{\boldsymbol{u}}(\boldsymbol{x})$ is the mean component, $\boldsymbol{u}''(\boldsymbol{x},t)$ is the stochastic component and $\sum_l \tilde{\boldsymbol{u}}_l(\boldsymbol{x},t)$ represents the sum of velocity modes corresponding to individual coherent structures in the flow. This differs from the triple decomposition proposed by Hussain and Reynolds (1970), where the flow field was decomposed into mean, a single periodic (*i.e.* only one characteristic frequency) and fluctuating components, and hence the simultaneous existence of multiple coherent motions was not addressed. In previous works, a data-driven approach to extracting the coherent modes in equation 1.1 has been taken, typically using a modal decomposition technique (Taira et al., 2017). Among them, one of the most commonly used one is Proper Orthogonal Decomposition (POD), where the flow field is decomposed into a series of orthogonal modes that are ranked according to their energy content (Lumley, 1967; Sirovich, 1987). Despite some limitations, POD has been widely used to identify coherent structures and for reconstruction and modelling of a large variety of flows (Taira et al., 2017). One major limitation of POD is that it only yields spatial modes and the temporal coefficients of the modes are often not mono-chromatic *i.e.* they contain multiple frequencies (Taira et al., 2017; Towne et al., 2018). To circumvent this issue, Towne et al. (2018) combined Fourier transform with POD and named it spectral POD or sPOD. sPOD was shown to be capable of providing time-harmonic modes at discrete frequencies from time resolved

data (Schmidt et al., 2018; Nekkanti and Schmidt, 2021). Another commonly used method is Dynamic Mode Decomposition (DMD), first proposed by Schmid (2010), which assumes that the time evolution of the flow can be governed by a time invariant, best-fit linear operator $\mathbf{A}$ and the eigen-decomposition of the operator gives the so-called DMD modes. Several variants of the original DMD algorithm have since been proposed with added advantages (Schmid, 2022). One amongst them is Optimal Mode Decomposition or OMD proposed by Wynn et al. (2013). The original DMD algorithm obtained the time dynamics by projecting the flow data onto a POD subspace. Contrastingly, Wynn et al. (2013) took a more generalised approach solving a two-way optimisation problem for the flow's dynamics and a low order subspace of $\mathbf{A}$. There are also other analysis techniques such as the global stability analysis and the resolvent analysis that use the Navier-Stokes equation linearsied about a base flow (Huerre and Monkewitz, 1990; Theofilis, 2011; McKeon and Sharma, 2010; Sharma and McKeon, 2013). In global stability analysis the linearised system is solved as a generalised eigenvalue problem yielding the most amplified linear modes. In contrast, resolvent analysis uses the nonlinear convection term in the Navier-Stokes equation as a forcing term and sets up an input-output problem, the inputs being the forcings and outputs being the response modes.

Once the coherent modes are identified using a modal decomposition tool of choice, assessing the energy budgets of the individual modes can reveal deeper insights. Baj and Buxton (2017) derived a multiscale triple decomposed coherent kinetic energy (CKE) budget equation to understand the kinetic exchanges to/from an individual coherent mode. The modes were obtained using OMD. The CKE budget ($\tilde{k}_l$) equation can be represented in symbolic form as

$$\frac{\partial \tilde{k}_l}{\partial t} = -\tilde{C}_l + \tilde{P}_l - \hat{P}_l + \left(\tilde{T}_l^+ - \tilde{T}_l^-\right) - \tilde{\epsilon}_l + \tilde{D}_l \tag{1.2}$$

In equation 1.2, the term on the left hand side indicates the rate of change of kinetic energy in coherent mode l. The source/sink terms are placed on the right hand side. These include convection ($\tilde{C}_l$), production from the mean flow ($\tilde{P}_l$), production of stochastic turbulent kinetic energy directly from coherent mode l ($\hat{P}_l$), triadic energy production ($\tilde{T}_l^+ - \tilde{T}_l^-$), direct dissipation from coherent mode l ($\tilde{\epsilon}_l$) and diffusion ($\tilde{D}_l$). The full composition of each of these terms is available in Baj and Buxton (2017). Baj and Buxton (2017) showed that the triadic energy

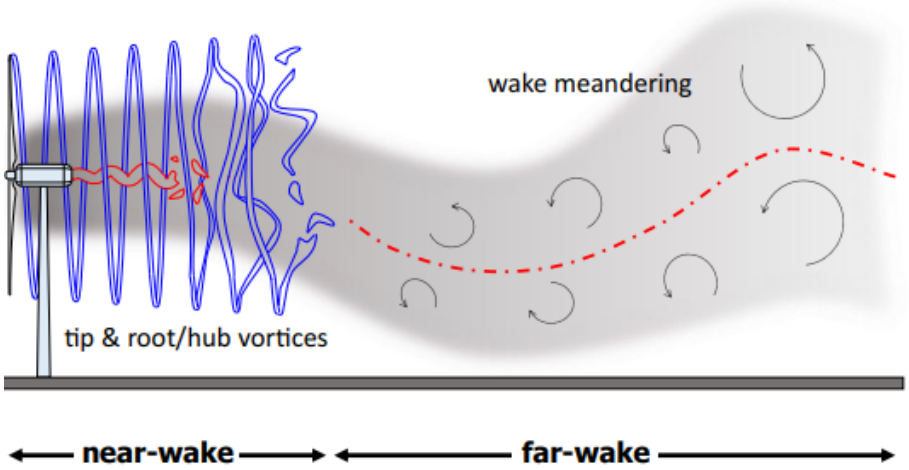


Figure 1.3: An illustration of coherent motions in the wake of a wind turbine (image reproduced from (Porté-Agel et al., 2020))

production term can become significant only when there exists three frequencies that linearly combine to zero or in other words, there is a triad in the form

$$f_l \pm f_m \pm f_n = 0 \tag{1.3}$$

Note that each of the new frequencies observed by Baj and Buxton (2017) being a linear combination of two vortex shedding frequencies, a triad was formed by each of the new frequencies. By assessing the CKE budget terms for each of the modes, the authors reported that the vortex shedding modes were energised primarily by the mean flow, hence identifying them as the 'primary' modes. Contrastingly, the new frequencies were found to be energised solely by the non-linear triadic energy exchange term. Therefore, the new frequencies were denoted as the 'secondary' modes. The primary goal of this thesis is to explore these interesting properties of multiscale flows in a wind turbine wake which is a more complex example of a multiscale flow. In particular, the generation and evolution of various coherent motions present in a wind turbine wake is studied in detail using the CKE budget analysis discussed above.

1.2 Wind turbine wakes

The near wake (coarsely defined as the region within 2-4 rotor diameters (D) downstream of the rotor plane) of a wind turbine is multiscale in nature as the flow is forced simultaneously at multiple length scales, for example by the tower, nacelle, blade tip/root vortices etc., thereby introducing coherence into the overall wake at multiple time/length scales simultaneously (Porté-Agel et al., 2020; Crespo et al., 1999; Abraham et al., 2019). The schematic in figure 1.3 shows the tip and root/hub vortices in the near wake and wake meandering in the far wake which is associated with large-scale transverse displacement of the entire wake (Chamorro et al., 2013; Okulov et al., 2014; Porté-Agel et al., 2020). The most pronounced structures in the near wake are the tip vortices, which follow a helical path in the wake. The dynamics of the tip vortices have been studied extensively through numerous experimental (Sherry et al., 2013a; Okulov et al., 2014; Lignarolo et al., 2014, 2015) and numerical studies (Ivanell et al., 2010; Lu and Porté-Agel, 2011; Sarmast et al., 2014; Hodgkin et al., 2022) as well as through stability analysis and a dynamical system's framework (Widnall, 1972; Gupta and Loewy, 1974; Delbende et al., 2021). The stability analysis of Widnall (1972) showed the presence of three different instability modes of a single helical vortex filament, a short-wave mode, a long-wave mode and the mutual inductance mode. Gupta and Loewy (1974) further extended the work for a multi bladed rotor. A pictorial demonstration of each of the instability types can be found in figure 6 of Widnall (1972). Among these modes the dominant mode is the mutual inductance mode where the neighbouring filaments attempt to roll up around one another (Widnall, 1972; Felli et al., 2011; Sherry et al., 2013a; Brown et al., 2022). The growth of this mode and ultimately the break up process of the helical vortices depends on several factors such as the pitch of the vortex system, the strength of the vortex filaments as well as the nature of disturbances introduced (Sherry et al., 2013a; Okulov et al., 2014; Quaranta et al., 2015, 2019). For a given blade design, the pitch and strength of the vortex system depend on the tip speed ratio λ, defined as $\lambda = \omega R/U_\infty$, where R is the turbine radius, ω is the rotational speed, and U_∞ is the freestream velocity. Several works have studied the effect of λ on the tip vortex instability and break up process (Sherry et al., 2013a; Okulov et al., 2014). As can be seen from figure 1.4 reproduced from Okulov et al. (2014), increasing λ reduces the pitch of the tip vortices and results in an earlier and stronger interaction.

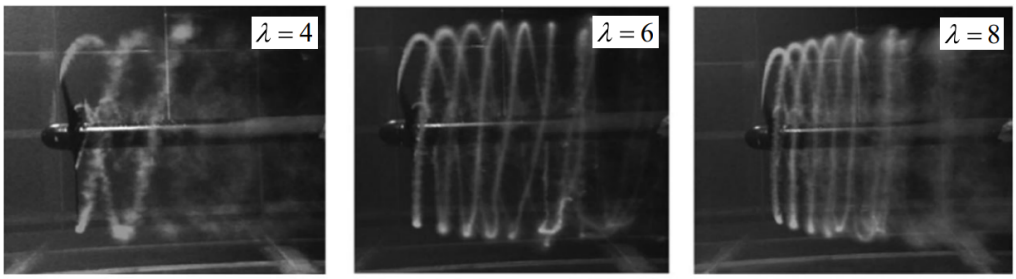


Figure 1.4: Dye visualization images of tip vortex evolution at different tip speed ratios λ (image reproduced from (Okulov et al., 2014))

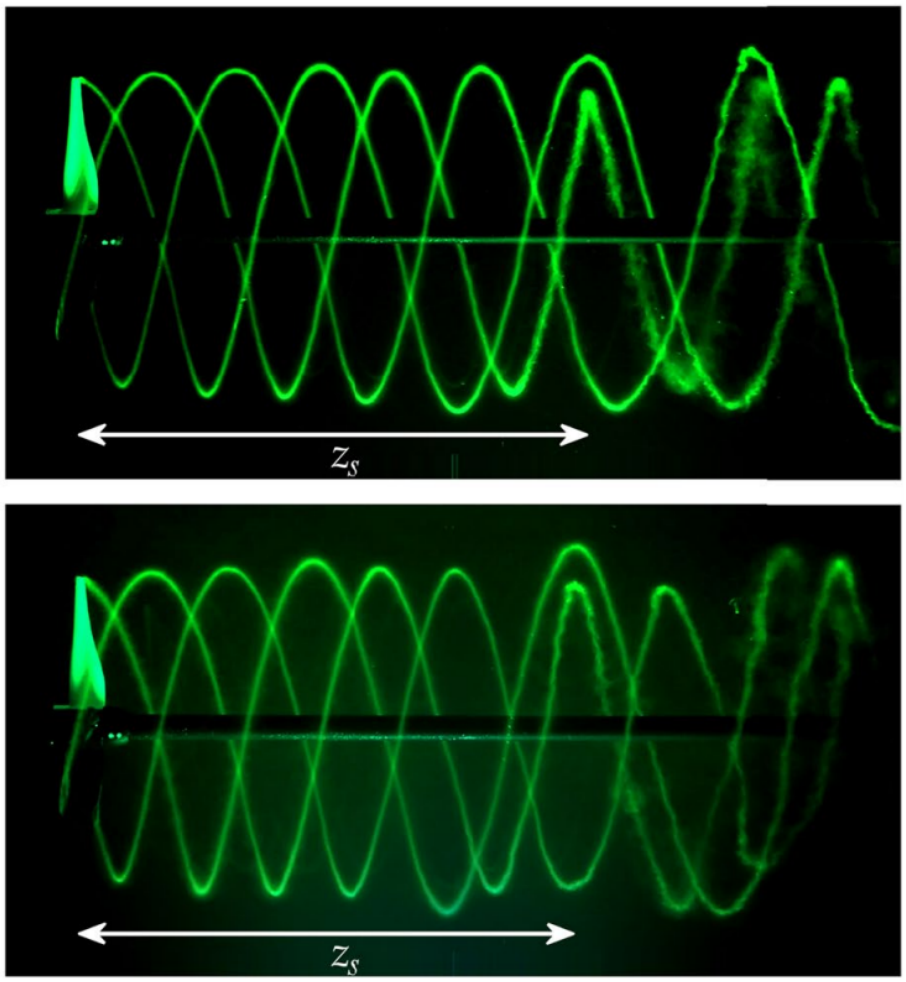


Figure 1.5: Flow visualization of the tip vortices when one blade is axially displaced by $+0.013D$ (top) and when one blade is azimuthally displaced by 5.7^o (bottom) (image reproduced from (Abraham and Leweke, 2023))

At the same tip speed ratio, the tip vortex instability and break up process also depend on the type of disturbances introduced. Disturbances to the vortices can be introduced through blade imperfections, due to wind turbine geometry such as the tower and due to freestream turbulence.

Blade imperfections have been introduced into the system by dynamically changing the frequency or the pitch of the blades (Quaranta et al., 2015; Brown et al., 2022) or passively by introducing a small radial or axial/azimuthal displacement to the blade tips (Ramos-García et al., 2023; Abraham and Leweke, 2023). Abraham and Leweke (2023) studied the propagation of the tip vortices for different types of blade imperfections using volumetric flow visualization. Two such cases are shown here in figure 1.5. The top figure corresponds to an axial displacement of $0.013D$ in one of the blades (case D in Abraham and Leweke (2023)) and the bottom case corresponds to an azimuthal displacement of 5.7^o in one of the blades. They used the leapfrogging distance (defined as the distance from the rotor where adjacent helical vortex loops swap positions) shown by z_s in figure 1.5 to quantify the effect of blade asymmetry. It was reported that for the top case the leapfrogging distance reduced by 17% compared to that for the baseline case (without any asymmetry in the blades) for $\lambda = 3$. Further, as can be seen from figure 1.5, z_s was comparable for the two cases highlighting an equivalence between axial and azimuthal disturbances.



Figure 1.6: Clouds formed behind wind turbines tracing the wake of the turbines at the Horns Rev ofshore wind farm near Denmark. The photograph is taken by Christian Steiness (see Hasager et al. (2013) for more details about the photograph.)

Depending on the blade configuration, distinct root vortices can also form near the root region of the blade (Sherry et al., 2013a). However, they are much less persistent in comparison to the tip vortices, whose dynamics and breakdown is particularly important to initiate the recovery

of the turbine wake. Medici (2005) noted that the tip vortex system in the near field acts as a shield, restricting the exchange of mass and momentum with the outer, background fluid. Lignarolo et al. (2015) showed that there was a net kinetic energy entrainment into the wake only after the tip vortices broke down. Hence, breakdown of the tip vortices is a necessary process to re-energise the wake in the far field, hence reducing the velocity deficit. In wind farms, where multiple turbines are placed in close proximity, the wake of upstream turbines can adversely impact the downstream turbines, contributing to significant amount of power losses and fatigue damage (Vermeer et al., 2003; Stevens and Meneveau, 2017; Porté-Agel et al., 2020). The photograph in figure 1.6 shows the wake of real wind turbines (traced by clouds formed behind them) interacting with downstream turbines at the Horns Rev ofshore wind farm near Denmark. An earlier breakdown of the tip vortices and an accelerated wake recovery can therefore have a large impact in improving farm level performance.

Different modal decomposition techniques such as POD and DMD have been applied to wind turbine wakes to understand the development and evolution of coherent structures and to develop reduced order models (Sarmast et al., 2014; Debnath et al., 2017; De Cillis et al., 2021). Sarmast et al. (2014) applied DMD to a LES data set of a wind-turbine wake and found that the dominant modes in the initial phase of tip-vortex evolution agreed well with the predictions of linear stability analysis. Debnath et al. (2017) performed POD and DMD on a LES data set of a wind-turbine wake with and without a nacelle and tower. For both cases, the dominant mode they reported had a frequency 3 times the rotor's evolution frequency, *i.e.* $3f_r$ (where f_r is denoted as the turbine's rotational frequency). Clearly this mode was associated with the tip vortices of the three-bladed turbine. A similar work by De Cillis et al. (2021) performed POD on a LES data set of the wake of a wind turbine with/without a nacelle and a tower. In the presence of the nacelle and tower, the POD modes in the near field ($x < 3.5D$) highlighted the tip vortices (with characteristic frequency $3f_r$), its first super-harmonic (characteristic frequency $6f_r$) and modes associated with vortex shedding from the tower (characteristic frequency f_T). Kinjangi and Foti (2023) applied DMD to a LES data set of a wind-turbine wake that involved a nacelle but no tower. They found modes associated with the turbine's rotational frequency (f_r), blade passing frequency ($3f_r$) or the tip vortices, their harmonics and the nacelle's shedding frequency.

Frequencies forming a triad have been known to exist in wind turbine wakes (particularly in the form of frequencies related to the tip vortices) without an explicit focus on triadic interactions (Felli et al., 2011). Therefore, the role of the triadic energy transfers in the tip vortex merging process and the overall wake evolution is yet to be quantified. Kinjangi and Foti (2023) recently performed an interesting study on a LES data set of a wind-turbine wake using a scale specific CKE equation similar to that derived by Baj and Buxton (2017). The authors identified the dominant resonant triads in the wake and quantified the scale-specific kinetic energy of different modes interacting triadically. However, the direction of energy exchanges to and from the modes, as well as the role of the energy exchanges on the evolution of the wake was not thoroughly discussed. This will be an important aspect of the present work.

To make the wake dynamics further complicated, real scale turbines are almost always exposed to freestream turbulence, which could be produced due to the presence of the atmospheric boundary layer or turbulence produced by upstream wind turbines. The level of freestream turbulence is often measured using the turbulence intensity (T_i), defined as $T_i = \sqrt{(\overline{u'^2})}/U_\infty$ (where U_∞ is the freestream velocity and $\sqrt{(\overline{u'^2})}$ is the standard deviation of velocity time history). In onshore sites wind turbines are exposed to higher turbulence intensity ($T_i < 15\%$) for most of their operating life (Elliott and Cadogan, 1990; Gambuzza and Ganapathisubramani, 2023), while for offshore sites freestream turbulence intensity is generally milder: $6\% < T_i < 8\%$ (Barthelmie et al., 2005; Türk and Emeis, 2010). In the presence of freestream turbulence the tip vortices were found to break down earlier (in comparison to a non-turbulent background), leading to faster wake recovery (Chamorro and Porté-Agel, 2009; Wu and Porté-Agel, 2012). A linear relationship between T_i and the wake recovery rate (estimated from the wake expansion rate) was reported (Niayifar and Porté-Agel, 2016; Carbajo Fuertes et al., 2018; Gambuzza and Ganapathisubramani, 2023). In engineering wake models, the wake recovery rate is often assumed to be a function of T_i alone. However, the spectral characteristic of the incoming flow has been recently shown to also influence the evolution of the wake significantly (Gambuzza and Ganapathisubramani, 2023; Hodgson et al., 2023). Gambuzza and Ganapathisubramani (2023) performed PIV experiments on a rotor model and reported that the wake generated by the turbine evolved more rapidly in the presence of low integral time scales in the freestream turbulence. Similarly, the numerical simulations of Hodgson et al. (2023) reported that the tip

vortices broke down earlier in the presence of shorter time scales in the inflow. To summarise, the above works conclude that a high turbulence intensity inflow with short time scales can result in a quicker wake recovery in the near wake.

In the near wake, freestream turbulence breaks down the dominant coherent structures *i.e.* the tip vortices. In contrast, freestream turbulence likely plays a different role on the dominant far wake structures, which have long been associated with wake meandering. Here wake meandering is defined as the large transverse displacements of the wake centreline (which can be roughly defined as the location of maximum velocity deficit) in the far wake region. Chamorro et al. (2013) studied the performance of a hydrokinetic turbine in a *turbulent* open channel flow and found a dominant frequency in the far wake ($x/D > 4$). The corresponding Strouhal number based on D and U_∞ was ≈ 0.28. The authors associated this frequency with wake meandering. Similarly in a flow containing negligible freestream turbulence, Okulov et al. (2014) found a single dominant Strouhal number ≈ 0.23 in the far wake (which they defined as the streamwise distance, $x > 2.5D$). They also reported that the Strouhal number was nearly independent of operating conditions. A similar Strouhal number in the range (0.15 - 0.4) has been noted in several other works (Chamorro et al., 2013; Foti et al., 2018; Medici and Alfredsson, 2008; Heisel et al., 2018) and has been associated with wake meandering. Although, the dominance of wake meandering in the far wake has been known for many years, the scientific community still holds varied opinions about the genesis of the meandering motion in the far wake. For instance, wake meandering has been seen as a passive advection of the turbine wake due to large scale atmospheric structures (Larsen et al., 2008; Espana et al., 2011). In contrast, Okulov et al. (2014) observed wake meandering when the free stream turbulence level was negligible. The authors proposed that wake meandering could be related to the instability of the shed vortices and connected it to the slow precession motion of the helicoidal vortex system. On a similar note, the importance of the nacelle in the generation of wake meandering was reported through experiments (Howard et al., 2015), linear stability analysis (Iungo et al., 2013) and numerical simulations (Kang et al., 2014; Foti et al., 2016, 2018). The large eddy simulations of Foti et al. (2018) showed that wake meandering is related to the slow precession motion of the helical hub vortex formed behind the nacelle. The authors suggested that the hub vortex grows radially and interacts with the outer wake which can potentially augment wake meandering.

The distance from the rotor plane, where a wake meandering frequency has been observed, has varied in different studies. For instance, Chamorro et al. (2013) found wake meandering only after 3 rotor diameters whereas, Okulov et al. (2014) reported the presence of a wake meandering frequency as close as $1.5D$ from the rotor (see figure 6 of Okulov et al. (2014)) where they found small variation in the frequency for different operating conditions. Medici and Alfredsson (2008) reported a similar observation at 1 diameter downstream of the rotor and concluded that the wake meandering frequency varied with both tip speed ratio and the thrust coefficient of the rotor.

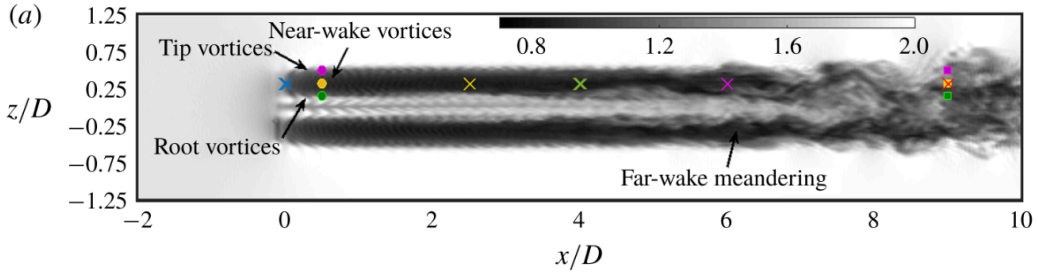


Figure 1.7: Instantaneous streamwise velocity field behind a turbine (image reproduced from (Gupta and Wan, 2019)).

Alongside the notion that wake meandering is related to the instability of vortices shed from the turbine, recent works suggest that it could also be triggered by freestream turbulence. There is a newly established consensus that wind turbines do not simply advect the structures present in the freestream as was originally assumed by the dynamic wake meandering model (Larsen et al., 2008). Instead, a turbine has a dynamic response *i.e.* certain frequencies in the freestream can be amplified in the wake (Mao and Sørensen, 2018; Heisel et al., 2018; Gupta and Wan, 2019; Hodgson et al., 2023). Mao and Sørensen (2018) identified nonlinear optimal perturbations to a wind turbine wake modeled as an actuator disk. They reported that as the inflow perturbation amplitude increased, the optimal perturbation frequency reduced from $St \approx 0.63$ to $St = 0.25$ for $Re_D = 1000$. As Re_D was increased to 3000, the optimal perturbation frequency further reduced to $St = 0.16$. These low frequencies fall well within the accepted range of wake meandering frequencies (Medici and Alfredsson, 2008; Chamorro et al., 2013; Okulov et al., 2014). Beyond $Re = 3000$, Mao and Sørensen (2018) noted that the optimal frequency did not change, indicating a possible Re invariance. Similarly, through field experiments, Heisel et al. (2018) reported that the wind turbine amplifies a range of frequencies in the inflow yielding

spectral peaks in the range $St = 0.3 - 0.4$ in the far wake. These observations align well with the argument of Howard et al. (2015) that that wake meandering is a rotor scale instability which depends on the velocity deficit and hence turbine's operating condition, the initial perturbation to which can come either from the rotor itself, for example from the nacelle, or from freestream turbulence. There is therefore a significant evidence that wake meandering in a utility-scale turbine can be influenced by several factors including the turbine's operating condition, turbine geometry as well as inflow turbulence (Heisel et al., 2018; Mao and Sørensen, 2018; Gupta and Wan, 2019). Nevertheless, a thorough understanding of the cause of wake meandering still remains elusive which is perhaps indicated by the ineludible scatter of Strouhal numbers associated with wake meandering observed in different studies (Medici and Alfredsson, 2008). For instance, Gupta and Wan (2019) argues that wake meandering is purely a convective type instability. However, the effect of the nacelle was not properly captured in their study as can be seen from the instantaneous velocity field in figure 1.7. An unphysical jet is formed in the central region of the wake similar to that indicated by Foti et al. (2018) that can potentially alter the stability properties of the wake. A part of the experiments reported in this thesis were particularly designed to better understand the nature of wake meandering.

1.3 Thesis outline and objectives

The aim of the thesis is to better understand the coherent dynamics and the multi-scale energy exchanges taking place in a wind turbine wake. A modular wind turbine model is designed and a series of particle image velocimetry (PIV) experiments are performed. The details of the wind turbine and the PIV experiments are discussed in chapter 2. In chapter 3, the important frequencies in the wake of the turbine are characterized and it is studied how they depend on the tip speed ratio in the absence of any freestream turbulence. Further, the nature and origin of wake meandering is studied without any freestream turbulence and any possible variation of its strength and frequency on the turbine's operating condition is investigated. Chapter 4 reports how freestream turbulence affects the important frequencies present in the wake that were identified earlier in chapter 3. Having identified the important frequencies with/without freestream turbulence, the aim was to identify the coherent modes associated with the frequencies

and then to quantify the energy budgets of each of the modes. For this purpose the coherent kinetic energy budget equation derived by Baj and Buxton (2017) in conjunction with the triple decomposition method proposed by Baj et al. (2015) is used. However, before applying the analysis on a wind turbine wake, the analysis is first performed on a simplified two dimensional multiscale flow consisting of a large cylinder (so called main cylinder) and a small cylinder (termed as the control rod) by using PIV data from Cicolin et al. (2021). This is discussed in chapter 5 where a deeper understanding of the energy exchange processes in a multiscale flow is developed. In chapter 6 the multiscale energy budget analysis is extended to a wind turbine wake and the following questions are addressed: (a) does a wind turbine wake consist of modes showing energy exchanges similar to that observed in simple two dimensional multiscale flows? (b) what is the role of nonlinear triadic interaction in the tip vortex merging process? how does it depend on the tip speed ratio? and (c) how can we connect the modal energy exchange processes to wake recovery?. Finally, chapter 7 explores how freestream turbulence can affect the multiscale energy exchanges in a wind turbine wake.

1.4 Publications

As a part of the thesis the following journal articles were published or are currently under preparation:

- **Biswas N.**, and Buxton O. R. H - Effect of freestream turbulence on the coherent dynamics of a rotor wake, *Under preparation.*
- **Biswas N.**, and Buxton O. R. H (2024) Energy exchanges between coherent modes in the near wake of a wind turbine model at different tip speed ratios, *J. Fluid Mech.*, **996**, A8.
- **Biswas N.**, and Buxton O. R. H (2024) Effect of tip speed ratio on coherent dynamics in the near wake of a model wind turbine, *J. Fluid Mech.*, **979**, A34.
- **Biswas N.**, Cicolin M. M., and Buxton O. R. H (2022) Energy exchanges in the flow past a cylinder with a leeward control rod, *J. Fluid Mech.*, **941**, A36:1-34.

Chapter 2

Experimental methods

2.1 Experimental facility

All the experimental campaigns were conducted in the closed-loop hydrodynamics flume at the department of Aeronautics at Imperial College London. The flume has a cross sectional area of 60cm $\times$ 60cm at the operating depth of water and a length of 8.2m. The freestream velocity U_∞ was kept constant at 0.2 m/s for most of the experiments. The wind turbine model was vertically hung into the flume in an inverted fashion (as shown in figure 2.2(a)) such that the nacelle centreline was positioned at the centre of the flume *i.e.* 30 cm away from either the water surface or the bottom surface of the flume. The streamwise distance x was measured from the rotor plane. The y co-ordinate measured the height from the nacelle centreline as shown in figure 2.2(a). The z co-ordinate was along the width of the flume, again measured from the nacelle centreline. Figure 2.1 here shows some photographs taken during setting up an experiment.

2.1.1 Illumination system

A dual cavity, high speed Litron LDY304 Nd:YLF laser was used as the illumination source for the particle image velocimetry (PIV) experiments. Most of the PIV experiments were performed at an acquisition frequency of 100Hz. The laser, however, had an operational frequency range of 200Hz - 20000Hz. The laser was therefore often operated at a frequency much higher than the

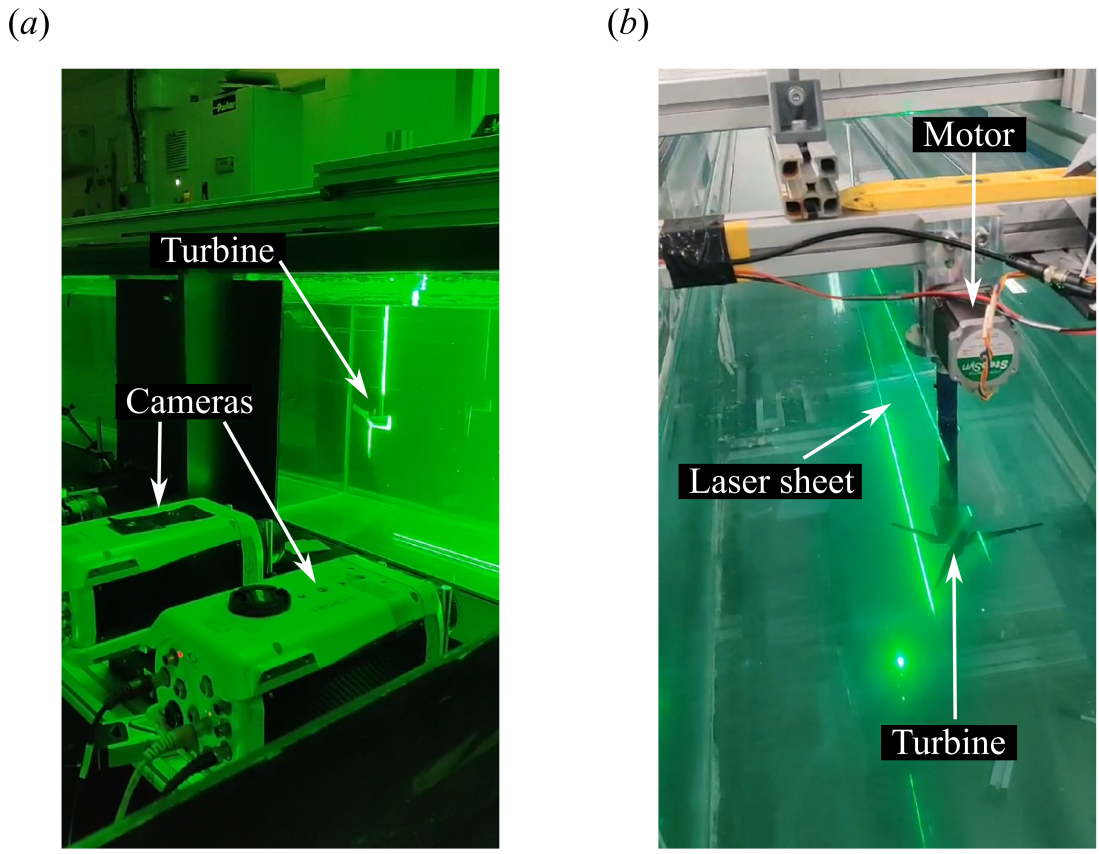


Figure 2.1: Photographs of the experimental setup. In (b), the laser sheet is purposefully aligned with the nacelle surface, at an offset from the tower.

data acquisition frequency, usually at 1000Hz. Most of the laser pulses were therefore unused. The laser was synchronised with the cameras through a digital pulse generator Stanford DG645. On average, the laser provided 30mJ of energy per pulse at 1000Hz. The wavelength of the emitted light was 527nm. The beam diameter was $\approx$ 5mm. The beam was steered externally using a combination of mirrors and finally the beam was focused onto a thin laser sheet (see figure 2.1(b)) by passing it through a convex lens and a plano-concave lens. For some experiments that needed a large field of view (FOV), two plano concave lenses were combined in series to produce a reduced focal length and hence a wider sheet. In addition, sometimes a non-polarising 50-50 beam splitter was used to split the beam. The two beams were separately expanded into individual sheets. The two sheets were then carefully stitched together to yield a larger FOV. All the optical equipment used were manufactured by ThorLabs.

2.1.2 Particles

The flow was seeded with hollow glass spheres of diameter $d_p \approx 10\mu$m. The density of the particles (ρ_p) was $\approx 1.1\times$ density of water (ρ_w). The particle response time based on a Stoke's flow approximation $\left(\tau_p = \frac{\rho_p}{\rho_w}\frac{{d_p}^2}{18\nu_w}\right)$ was estimated to be $\approx 6.1\mu s$. Based on previous studies in the same facility, the Komgorov time scale (τ_η) was estimated to be $\approx$ 10ms (Baj, 2018). This resulted in a Stokes number $\tau_p/\tau_\eta \approx 6.1 \times 10^{-4} \ll 1$, hence, the particles were expected to follow the flow faithfully.

2.2 Design of the wind turbine model

A modular wind turbine was designed for operation in the hydrodynamics flume. The diameter (D) of the model was restricted to 20 cm to keep the blockage low (8.7% based on turbine diameter which is comparable to blockages encountered in previous experimental studies (Sherry et al., 2013a; Miller et al., 2019)). A moderate freestream velocity (U_∞) was chosen in order to avoid unwanted deflections at the tips of the blades. The Reynolds number based on the turbine diameter ($Re_D = U_\infty D/\nu$) was $\approx$ 40000 for $U_\infty = 0.2$ m/s. Note that standard wind turbines operate at a high chord based Reynolds number $Re_c \approx 10^6$ (See figure 1 of (Lissaman, 1983)) and at such Re, standard airfoils operate at high maximum lift to drag ratio $O(100)$ (See table 1 of (Sunada et al., 1997)) which is impossible to achieve in a small scale model (for which the chord based Re_c is barely $\approx$ 9000 here) unless a pressurised facility is used to tailor the density of the incoming flow (Miller et al., 2019). Accordingly, there is inherently a Reynolds number mismatch of $O(100)$. At $Re_c \approx 10^4$, thin flat plate airfoils perform better than standard thicker smooth airfoils (McMasters and Henderson, 1980; Winslow et al., 2018; Sunada et al., 1997; Hancock and Pascheke, 2014). Thus, a flat plate airfoil with thickness ratio 5% and camber ratio 5% was initially chosen for the blade which gives the best performance at low Reynolds number ($Re \sim 4 \times 10^3$) (Sunada et al., 1997). However the blades were found to be incapable of sustaining the structural loads under the present experimental conditions and hence the thickness ratio was increased to 10% for more structural rigidity. The operating angle of attack was selected to be 5^o. The chord and twist distribution of the blades were similar to that used by Hancock and Pascheke (2014). Near the root section, the blade was linearly

interpolated to a circular section which was fixed to the hub. Experiments were conducted at tip speed ratios in the range $4.5 \leq \lambda \leq 6.9$.

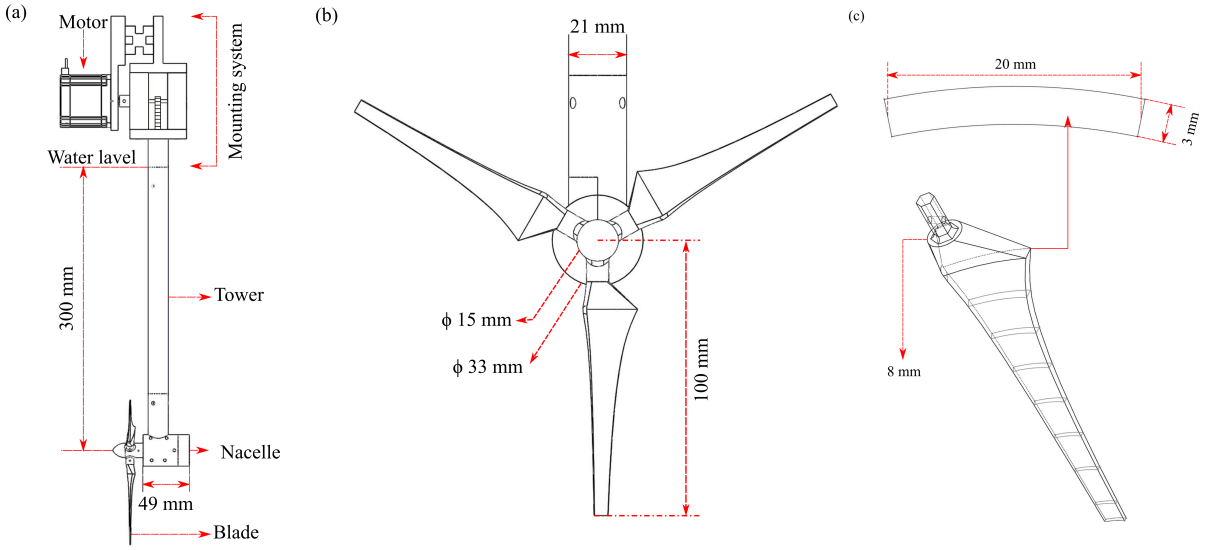


Figure 2.2: (a) A side view of the wind turbine model assembly, (b) a front view of the model. (c) shows an individual blade and the blade section at the root.

The nacelle was represented as a cylindrical body of diameter 3.3 cm and length 4.9 cm. A hollow cylindrical tower of outer diameter 2.1 cm was attached to the nacelle. The tower was attached at the top to a mounting frame and the wind turbine model was hung in an inverted fashion in the flume. A side view of the wind turbine model assembly is shown in figure 2.2(a). Similarly, figure 2.2(b) shows a representative front view. A stepper motor RS 829-3512 was used along with a drive and signal generator to rotate the turbine at a prescribed RPM. Note that, the blades were connected in a way that the turbine produced a wake acting similarly to a real wind turbine, despite being operated by a motor. The motor, along with the speed controlling electronics, were located outside the flume as shown in figure 2.2(a). The torque from the motor was transmitted to the turbine shaft via a belt and pulley mechanism. The pulley and the shaft were placed inside the nacelle and the belt ran through the hollow tower which restricted any further reduction in the diameter of the nacelle or tower. Note that in multi-megawatt turbines, the nacelle diameter is often $< 5\%$ of the rotor diameter and the tower diameter is $\approx 3\%$ of the rotor diameter (Desmond et al., 2016). The design constraints in the present experimental model, however, resulted in a nacelle diameter to rotor diameter ratio of 16.5% and tower diameter to rotor diameter ratio of 10.5%. In small-scale models used

in laboratory experiments it is not often possible to have a nacelle and tower with shape and size exactly similar to full-scale turbines. For instance Howard et al. (2015) and Chamorro et al. (2013) had a nacelle to turbine diameter ratio of $\approx 9\%$, Pierella and Sætran (2017) and Barlas et al. (2016) had a nacelle $\approx 13 - 14\%$ of the rotor diameter. On the other hand, some studies had a nacelle much longer than usual (Okulov et al., 2014; Pierella and Sætran, 2017). Pierella and Sætran (2017) had a tower diameter of 11.7% of the turbine diameter. Akin to these studies, although the effect of the nacelle and tower could be overestimated with respect to a utility-scale turbine in the present experiments, important inferences can be drawn that can aid the understanding of the wake physics of wind turbines, and rotors more generally.

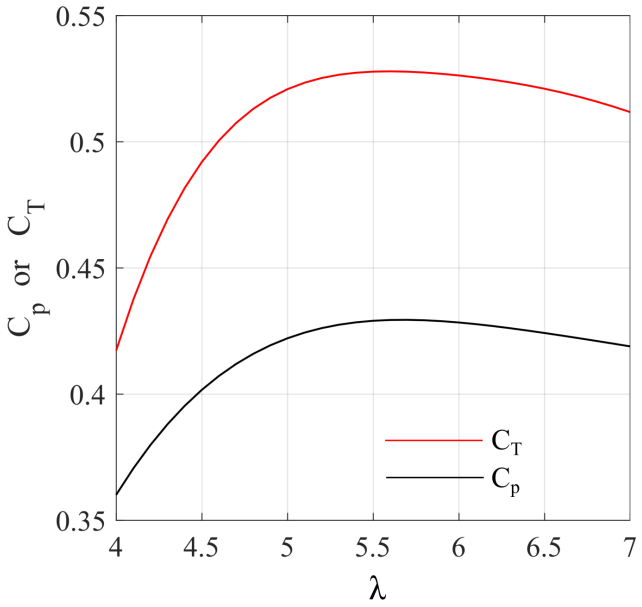


Figure 2.3: Variation of power (C_P) and thrust (C_T) coefficient of the turbine with tip speed ratio (λ) obtained from blade element momentum theory.

A characteristic of the wind turbine model was that the individual components such as the nacelle, the tower and the blades could be disconnected individually and easily replaced. Figure 2.2(c) shows the type of blades used in this work. For this blade, the conventional blade element momentum method (see Burton et al. (2011)) was used to estimate the power (C_P) and thrust (C_T) coefficients of the turbine at different tip speed ratios. The $C_l - \alpha$ curve of the blade sections required for the calculation at comparable Reynolds number was obtained from Sunada et al. (1997). The drag on the blade elements was ignored. The calculations were performed only based on the part of the blades from the root (maximum chord) to tip. The results are

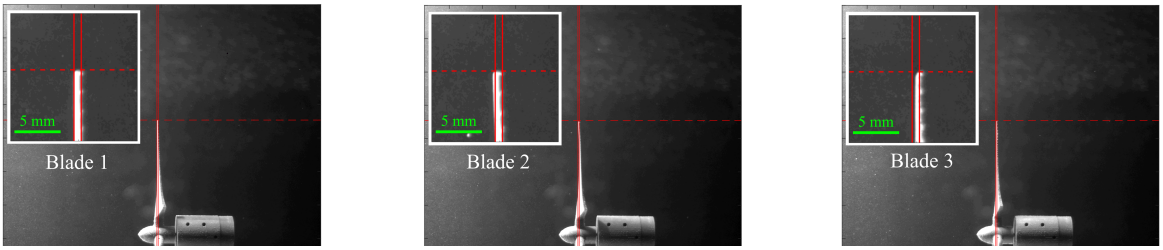


Figure 2.4: Snapshots showing the 3 blades of the turbine passing through the same point at $\lambda = 6$.

shown in figure 2.3 here.

As discussed in chapter 1, blade asymmetry can have a significant impact on the instability and breakdown of the tip vortices. In any experimental set up, some degree of asymmetry in the blades is inevitable. It is therefore important to document any such asymmetry in order for the results from the current experiments to be comparable to experiments on other facilities. The turbine's rotation was recorded when operating at a tip speed ratio of 6 ($U_\infty = 0.2$ m/s). Figure 2.4 here shows some snapshots when the 3 blades pass through the same vertical position. The tips are zoomed in in the insets. There is negligible difference in the radial location (shown by the dashed line) of the tip. The solid vertical lines show the position of blade 1 and are used to compare the positions of blades 2/3. It can be seen that there is a small difference in the axial location of the tip which is less than $0.5mm$. As mentioned earlier, the chord of the blades used are quite small to make it look more like conventional wind turbines. This resulted in a tip chord of $5mm$ and tip thickness of just $0.5mm$. Therefore, slight differences in the blade orientation were possible at the tip.

2.3 PIV experiments without freestream turbulence

A series of PIV experiments were performed on the wind turbine model under different experimental campaigns as shown in table 2.1. At a freestream velocity of 0.2 m/s, the boundary layer thickness at the bottom wall at the test section was measured to be $\approx$ 6.5cm (Baj, 2018). The field of view (FOV) of all the experiments were positioned well outside the boundary layer on the bottom surface (see table 2.1). To assess the freestream condition, a separate PIV experiment was conducted without the wind turbine. Figure 2.5 shows the turbulence intensity (T_i) and

mean velocity (U_∞) profiles measured at the position of the turbine disk, while the turbine was removed. The freestream velocity profile is uniform across the rotor, showing no effect of the boundary layer developing at the bottom wall of the flume in the vicinity of the rotor. The turbulence intensity is $\approx 1\%$. No extra freestream turbulence was added.

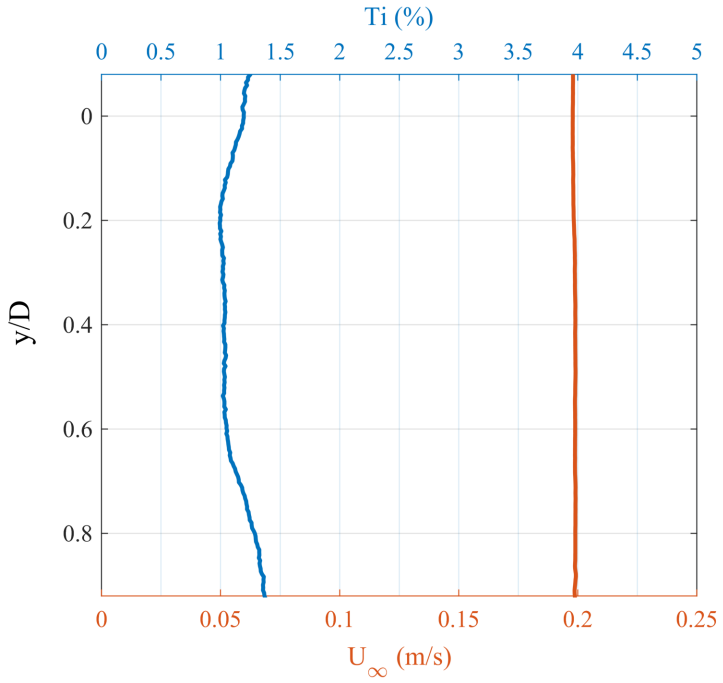


Figure 2.5: Mean streamwise velocity and turbulence intensity profiles at the rotor location.

Four different experimental campaigns, named campaigns 1 - 4, were first conducted to capture different regions and properties of the flow. The details of the experiments can be found in table 2.1 and figure 2.6. In campaign 1, seven different experiments were conducted in the plane of symmetry aligned with the tower axis ($z = 0$). The first experiment in campaign 1 (henceforth referred to as 1A) focused on the region $0 \leq y/D \leq 0.85$, measured from the symmetry line. Three Phantom v641 cameras were used to obtain a stitched field of view spanning $0.25 \leq x/D \leq 3.45$ in the streamwise direction. Similarly experiment 1B focused on the region $-0.85 \leq y/D \leq 0$ which contains the wake region of the tower. The third experiment (1C) covered the central region, $-0.42 \leq y/D \leq 0.43$. Experiments 1A-C were conducted only for the two main tip speed ratios $\lambda = 4.5$ and $\lambda = 6$. Experiments 1D, E and F had a field of view similar to experiment 1A. Experiment 1D was run for 5 tip speed ratios different from the

Exp	λ	FOV	Plane	δx(mm)	f_{aq}(Hz)	δt(s)	T(s)
1A	4.5, 6	$0.25D < x < 3.45D$, $0 < y < 0.85D$	$z = 0$	1.76	100	0.01	54.75
1B	4.5, 6	$0.25D < x < 3.45D$, $-0.85D < y < 0$	$z = 0$	1.76	100	0.01	54.75
1C	4.5, 6	$0.25D < x < 3.45D$, $-0.42D < y < 0.43D$	$z = 0$	1.76	100	0.01	54.55
1D	5.3, 5.5, 6.4, 6.6, 6.9	$0.2D < x < 3.17D$, $0 < y < 0.93D$	$z = 0$	2.07	100	0.01	54.55
1E	6 ($U_\infty = 0.3$ m/s)	$0.2D < x < 3.17D$, $0 < y < 0.93D$	$z = 0$	2.07	100	0.01	54.55
1F	6 ($U_\infty = 0.4$ m/s)	$0.2D < x < 3.17D$, $0 < y < 0.93D$	$z = 0$	2.07	200	0.005	27.27
1G	4.5, 5, 5.5, 6	$0.5D < x < 5D$, $-0.35D < y < 0.75D$	$z = 0$	2.35	100	0.01	54.55
2A	4.5, 6	$0.29D < x < 1.95D$, $-0.73D < z < 0.69D$	$y = 0$	1.84	100	0.01	54.55
2B	4.5, 6	$0.29D < x < 1.95D$, $-0.73D < z < 0.69D$	$y = -0.35D$	1.84	100	0.01	54.55
3A	4.5-6	$x \in (2D \pm 0.062D)$, $-0.6D < z < 0.6D)$	$y = 0$	1.64	10	0.01	900
3B	4.5-6	$x \in (3D \pm 0.062D)$, $-0.6D < z < 0.6D)$	$y = 0$	1.64	10	0.01	900
3C	4.5-6	$x \in (5D \pm 0.062D)$, $-0.6D < z < 0.6D)$	$y = 0$	1.64	10	0.01	900
4	4.5, 5, 5.5, 6	$1.75D < x < 4.7D)$, $y \in (\pm 0.12D)$	$z = 0$	2.11	100	0.01	219

Table 2.1: Parameters associated with different experiments without freestream turbulence. Here δx represents the spatial resolution of the experiments. f_{aq}, δt, and T are the acquisition frequency, time between successive laser pulses and total time of data acquisition respectively. The freestream velocity was set to 0.2 m/s for all the experiments except experiments 1E and 1F for which it was increased to 0.3 m/s and 0.4 m/s respectively.

two main tip speed ratios (see table 2.1 for details). Experiments 1E and F were run for a single $\lambda = 6$, but for different freestream velocities, $U_\infty = 0.3$ m/s and $U_\infty = 0.4$ m/s respectively. Finally, experiment 1G had the largest spatial extent (up to x/D =5) obtained by stitching the fields of view from 3 Phantom v641 cameras. Four λs from 4.5-6 were tested in experiment 1G.

In experimental campaign 2, two Phantom v641 cameras were used simultaneously to capture the near wake ($0.29 \leq x/D \leq 1.95$) in the xz plane. Experiment 2A focused on the symmetry plane ($y = 0$), while experiment 2B focused on an offset plane ($y = -0.35D$) such that a

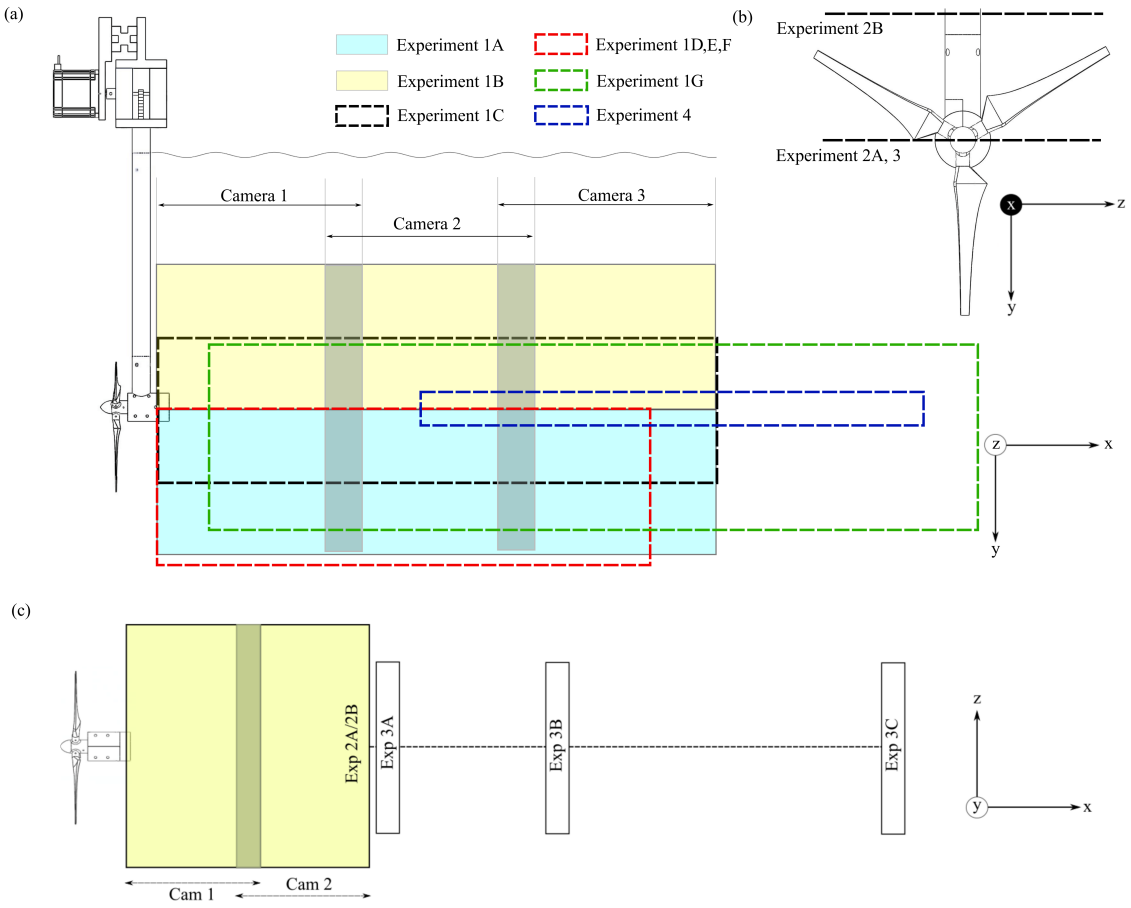


Figure 2.6: A schematic of the wind turbine model and the fields of view used in the different experiments. The streamwise distance x is measured from the rotor plane and transverse distances z and y are measured from the nacelle centreline. Experiment 1 and 4 focused on the plane aligned with the tower's axis and streamwise direction, *i.e.* xy plane (sub figure 2.6(a)), while experiments 2 and 3 focused on xz planes at different y offsets (sub figure 2.6(c)). The planes of different experiments are also shown as the dashed lines in subfigure 2.6(b).

stronger influence from the tower-wake is captured. All the parameters associated with the different experiments are tabulated in table 2.1. For experiments 1 A-D, G and 2, each camera captured images (of dimension 2560px $\times$1600px) in double frame single exposure mode at an acquisition frequency (f_{aq}) of 100 Hz which was found to be adequate to resolve all scales of dynamic importance for the present study. Data was obtained for a total time (T) of more than 54s (corresponding to $\approx$ 77 turbine rotations for the lowest $\lambda = 4.5$ and $U_\infty = 0.2$ m/s). For experiments 1E and 1F, data was obtained for a time period corresponding to $\approx$ 153 and $\approx$ 102 rotor revolutions.

The objective of campaigns 3 and 4 was to obtain the wake meandering frequency accurately.

Only one camera was used for each experiment in campaign 3 and the field of view was shrunk into a thin strip of dimension 2560 px ×256 px (see figure 2.6(c)) which facilitated obtaining a large time series of data (900 s, which is close to 180 wake meandering cycles) within the memory constraints of the camera. The tip speed ratio was slowly varied from 4.5 to 6 in increments of 0.1. The acquisition frequency was reduced to 10Hz and the time between successive laser pulses (δt) was kept fixed at 0.01s for all experiments. The fields of view of the experiments were centred at $x = 2D$, $3D$ and $5D$ as shown in figure 2.6. Experiment 4 used a longer strip obtained using 2 cameras. The acquisition frequency was 100 Hz and $\delta = 0.01$s. The images acquired were processed in PIVlab (Thielicke and Stamhuis, 2014). The adaptive cross correlation algorithm in PIVlab used a multi-pass, fast Fourier transform to determine the average particle displacement. An initial interrogation area (IA) of 64×64 pixels was reduced in 3 passes with a final IA size of 16×16 pixels with 50% overlap in the x and y directions. The spatial resolution (δx) of the experiments were close and were around $1.64 - 2.35$mm (see table 2.1). The smallest scales of dynamic importance in the near field, *i.e.* the tip vortex cores were found to span $\approx 6\delta x$. Since the interrogation windows had a 50% overlap, meaning that adjacent vectors in the velocity fields were spaced $\delta x/2$ apart, the tip vortex cores spanned ≈ 12 PIV vectors. Accordingly, all scales of dynamic importance are believed to be resolved adequately. All the results from these experiments are discussed in chapters 3 and 6.

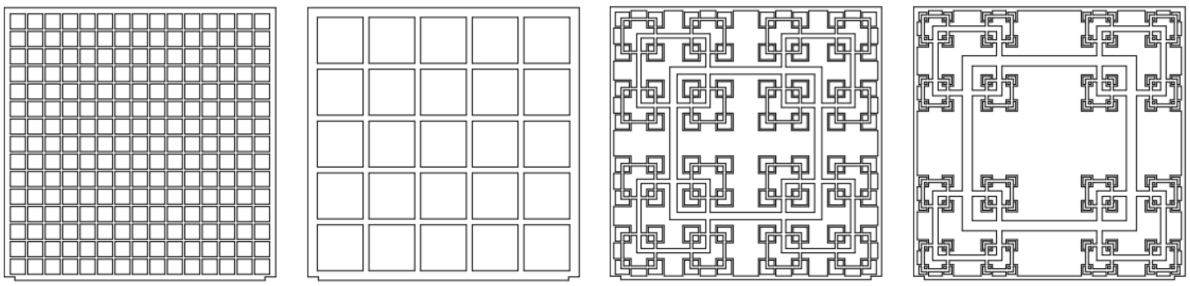


Figure 2.7: Regular grids (a) SRG38 and (b) SRG111 and fractal grids (c) SFG5 and (d) SFG7 used in this study (image reproduced from Kankanwadi (2022)).

2.4 Grid characterisation and experiments with freestream turbulence

The experimental campaigns discussed in section 2.3 had negligible freestream turbulence ($T_i \approx 1\%$). A separate experimental campaign was conducted to study the effect of freestream turbulence on the wind turbine wake. To generate freestream turbulence, 4 different passive turbulence generating grids were used. These are shown in figure 2.7. Among these two were regular grids and two were fractal grids. The flow fields behind these grids were first characterised using PIV experiments. 2 Phantom v641 cameras were used simultaneously to give a stitched field of view length $\approx 2.45D$ (49cm). The FOV was $\approx$ 18cm ($0.9D$) wide and the centre of the FOV coincided with the centre of the flume (*i.e.* 30cm from the bottom wall). The grid was moved upstream keeping the optical setup intact and a number of non-synchronous experiments were conducted for a particular grid to obtain time averaged statistics over a certain streamwise distance as required. As an example the mean velocity field and the turbulence intensity field behind the grid SRG38 is shown in figure 2.8. Note that just behind the grid, there is a significant amount of acceleration. The pressure drop across the grid reduces the water depth slightly, hence continuity yields the acceleration. Although the acceleration reduces with downstream distance, the local mean velocity is slightly greater than U_∞ even at the farthest location measured. This increment in the freestream velocity needs to be taken into account as it can result into slight changes in the tip speed ratio of the turbine. The turbulence intensity is the highest ($\approx 15\%$) near the grid and monotonically reduces to $\approx 3.5\%$ further downstream.

The variation of the mean streamwise velocity behind all the grids are shown in figure 2.9. The solid black line shows the variation of the mean centreline velocity (along $y = 0, z = 0$). The jumps in the variation (especially for SFG7) are due to the fact that mean data from multiple non-synchronous PIV experiments were stitched together. The streamwise mean velocity also varies along the y direction. Therefore, the transverse variation of the mean velocity is indicated by the shaded region. The grid is located at $x/D = 0$. The dashed vertical lines show the position of the wind turbine in different experiments. Similarly, the variation of turbulence intensity (T_i) behind the grids is shown in figure 2.10.

Another important quantity to characterise the nature of freestream turbulence is the integral

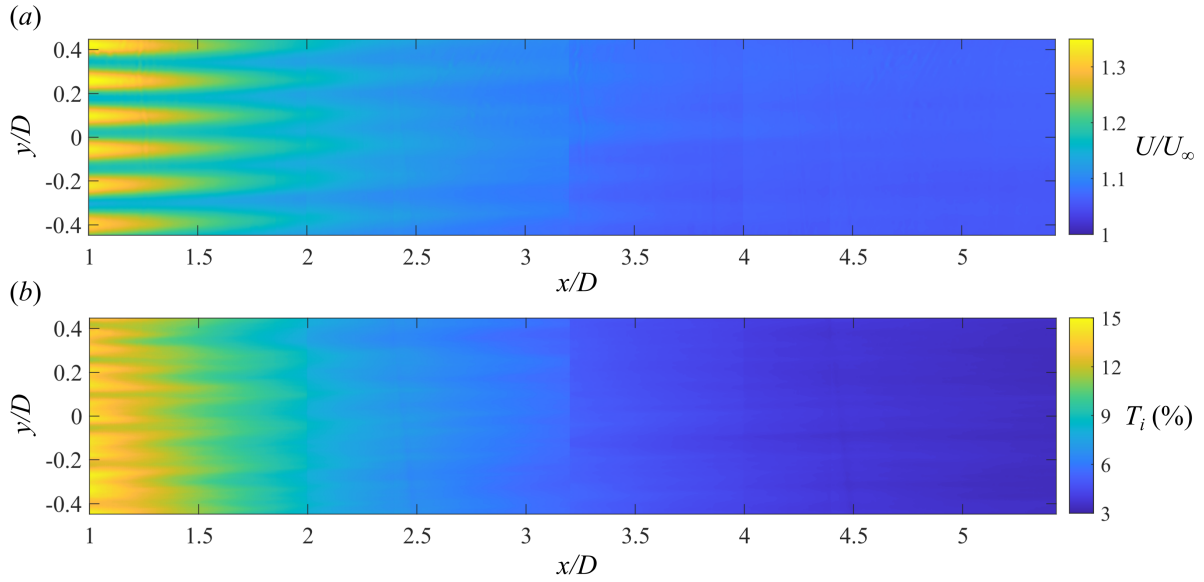


Figure 2.8: (a) Mean velocity field and (b) turbulence intensity (T_i) field behind the regular grid SRG38.

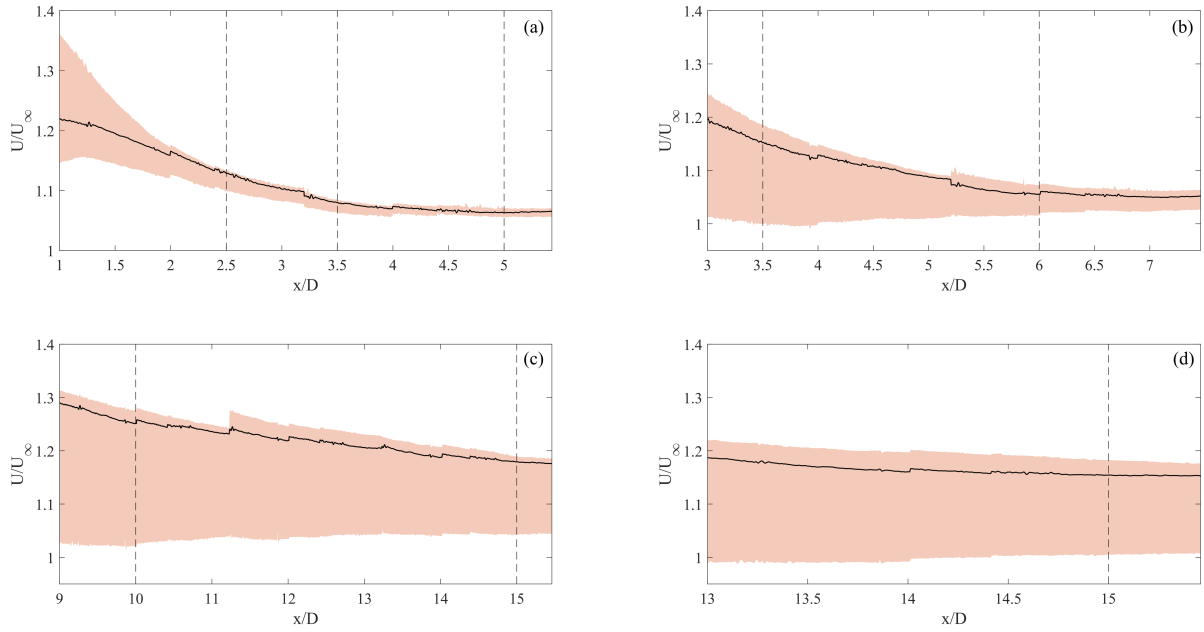


Figure 2.9: Variation of mean streamwise velocity along the centreline ($y = 0$, $z = 0$) behind the grids (a) SRG38, (b) SRG111, (c) SFG7 and (d) SFG5. The shaded region shows the variation of mean streamwise velocity within the field of view considered.

length scale (L_v). L_v is estimated using equations 2.1.

$$R'_{21}(\mathbf{x}, r) = \frac{\overline{u'_2(\mathbf{x})u'_2(\mathbf{x}+r\mathbf{e}_1)}}{\sqrt{\overline{u'_2(\mathbf{x})^2}}\sqrt{\overline{u'_2(\mathbf{x}+r\mathbf{e}_1)^2}}} \qquad L_v = \int_0^{\hat{r}} R'_{21}dr \tag{2.1}$$

Here R'_{21} represents the streamwise autocorrelation function of transverse velocity fluctuation (u'_2). $r\mathbf{e}_1$ represents some displacement r along the $\mathbf{e}_1$ direction ($\mathbf{e}_1$ is the unit vector along the streamwise direction). Finally L_v is calculated by integrating R'_{21} up to a certain distance $\hat{r}$ where R'_{21} becomes zero. Measuring $\hat{r}$ is not trivial since the nature of R'_{21} changes with streamwise distance. Figure 2.11 shows the variation of R'_{21} along the the centreline ($y = 0$, $z = 0$), and $2D$ and $5D$ away from the grid SRG38. Closer to the grid, R'_{21} clearly falls off to zero, while further downstream it does not. Therefore, a fitting function needs to be used. Note that the background correlation shows multiple secondary peaks, the strongest one is shown by the '+' sign in figure 2.11(b). A cutoff twice the peak value was used (as shown by the red dashed line) and the data above the cutoff was used for fitting. A bi-Gaussian function was used for fitting (two separate Gaussian curves were fitted on both side of the peak). As an example, the fitted curve is shown in figure figure 2.11(b) by the black line. Following equation 2.1, L_v was calculated on both the sides and an average of the two was taken. Towards the end of the FOV where fitting could not be performed on both sides, L_v was estimated simply based on data from one side.

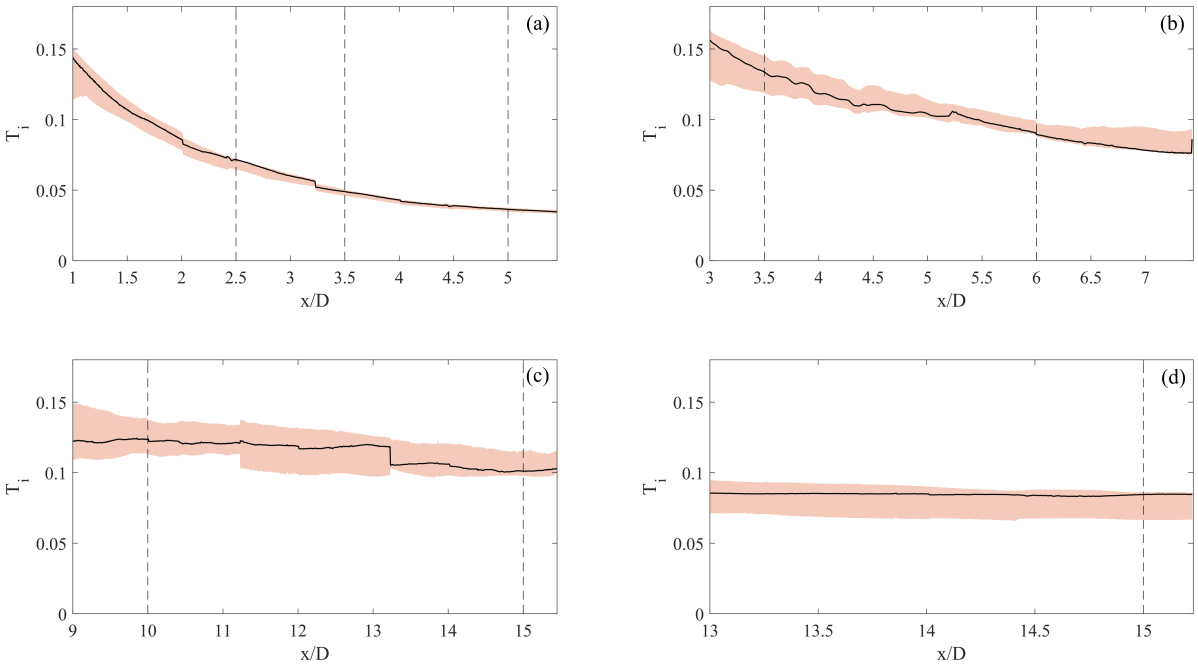


Figure 2.10: Variation of turbulence intensity (T_i) at hub height with distance from the grids (a) SRG38, (b) SRG111, (c) SFG7 and (d) SFG5. The dashed vertical lines show the position of the rotor plane in different experiments. The shaded region shows the variation of T_i within the field of view considered.

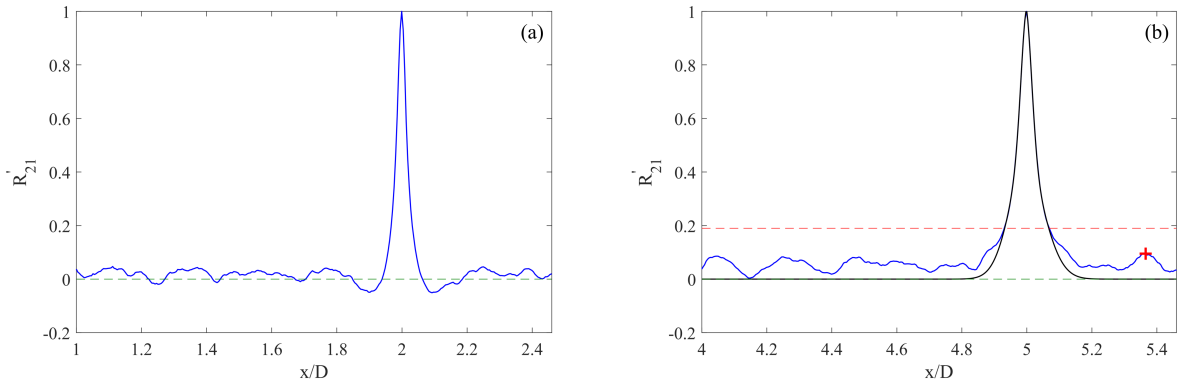


Figure 2.11: Streamwise autocorrelation function of transverse velocity fluctuation (a) $2D$ and (b) $5D$ downstream of the grid SRG38 at the geometric centreline ($y = 0, z = 0$). In (b), the black curve shows the fitted bi-Gaussian curve. The strongest secondary autocorrelation peak is shown by the red '+' sign. The red dashed line shows the cutoff, the data below which was discarded during fitting.

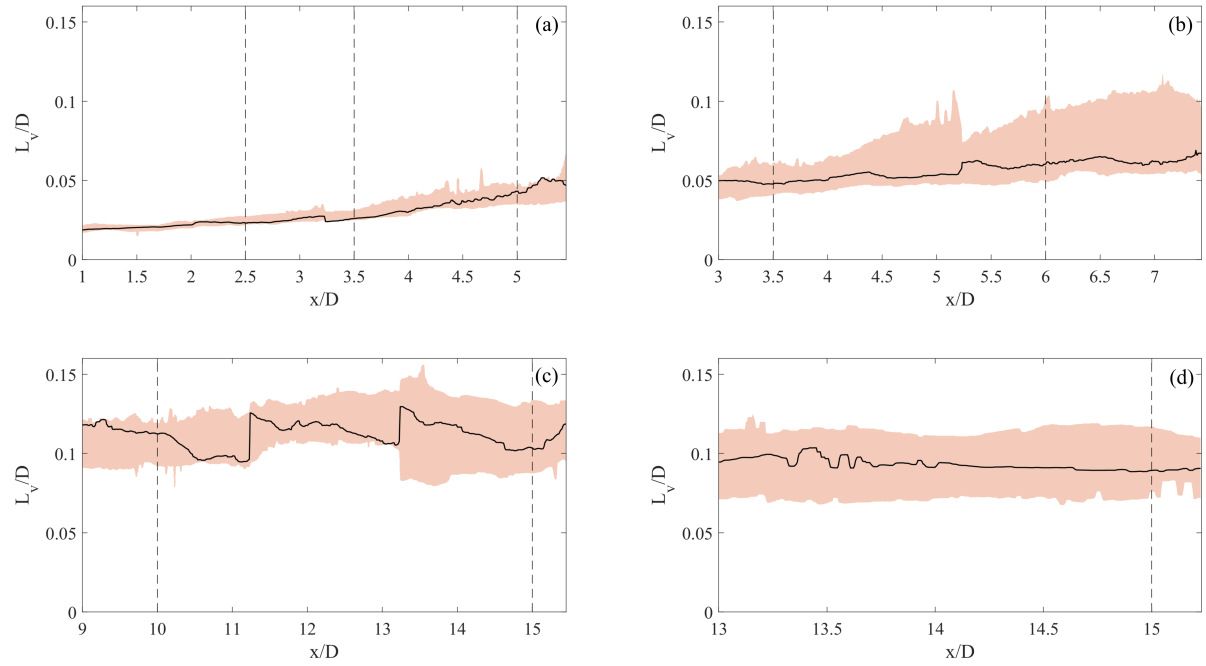


Figure 2.12: Variation of integral length scale (L_v) at hub height with distance from the grids (a) SRG38, (b) SRG111, (c) SFG7 and (d) SFG5. The dashed vertical lines show the position of the rotor plane in different experiments. The shaded region shows the variation of L_v within the field of view considered.

Figure 2.12 shows the variation of integral length scale (L_v) along the geometrical centreline. Similar to figure 2.9, the filled contour shows transverse variation of L_v. The dashed vertical lines show the positions of the turbine in different experiments.

The experiments with added freestream turbulence (FST), denoted as experiment 5, had the

Exp	Grid	Distance from the turbine	T_i %	L_v (D)	U/U_∞	λ_{eff}
5A	SRG38	$2.5D$	7.1	0.024	1.13	5.3
5B	SRG38	$3.5D$	4.9	0.026	1.08	5.6
5C	SRG38	$5D$	3.6	0.043	1.06	5.7
5D	SRG111	$3.5D$	13.1	0.048	1.15	5.2
5E	SRG111	$6D$	9	0.061	1.06	5.7
5F	SFG7	$10D$	12.4	0.111	1.25	4.8
5G	SFG7	$15D$	11.1	0.107	1.21	5
5H	SFG5	$15D$	8.5	0.084	1.15	5.2

Table 2.2: Parameters associated with different experiments in experimental campaign 5.

same field of view as that in experiment 1G discussed earlier in section 2.3. All the parameters such as δx, f_{aq}, δt and T were kept the same. 8 FST cases were studied by changing the grid type and the distance between the grid and the turbine. The important parameters associated with these experiments are tabulated in table 2.2. The turbine was operated at a tip speed ratio (λ) of 6. However, since the grids induce an acceleration to the flow, the effective tip speed ratio $\lambda_{eff} = \lambda \times U_\infty/U$ reduced for all the cases. The results of these experiments are discussed in chapters 4 and 7.

Chapter 3

The multiscale nature of the dynamics in a wind turbine wake

3.1 Introduction

The multiscale nature of wind turbine wakes was introduced in chapter 1. In this chapter a detailed analysis is performed to identify the frequencies present in the near wake of a wind turbine at different tip speed ratios (λ). For this purpose, the data from the experiments 1-4 (as tabulated in table 2.1) were utilised which did not have any additional source of freestream turbulence. The freestream turbulence intensity (T_i) was approximately 1%. The results presented in this chapter were published in Biswas and Buxton (2024a).

3.2 Instantaneous vorticity field

Figure 3.1(a-b) show instantaneous vorticity fields at $\lambda = 4.5$ and $\lambda = 6$ ($U_\infty = 0.2$ m/s) in the xy ($z = 0$) plane. Note that the fields of view from experiments 1A and 1B are stitched together for a visual representation of the dynamics within the entirety of the interrogated wake domain but they were not acquired concurrently. The flow fields in figure 3.1 are inherently complex and contain several length/time scales. In the top plane (experiment 1A), the array of the tip vortices can be seen which acts as a boundary between the wind turbine wake and the

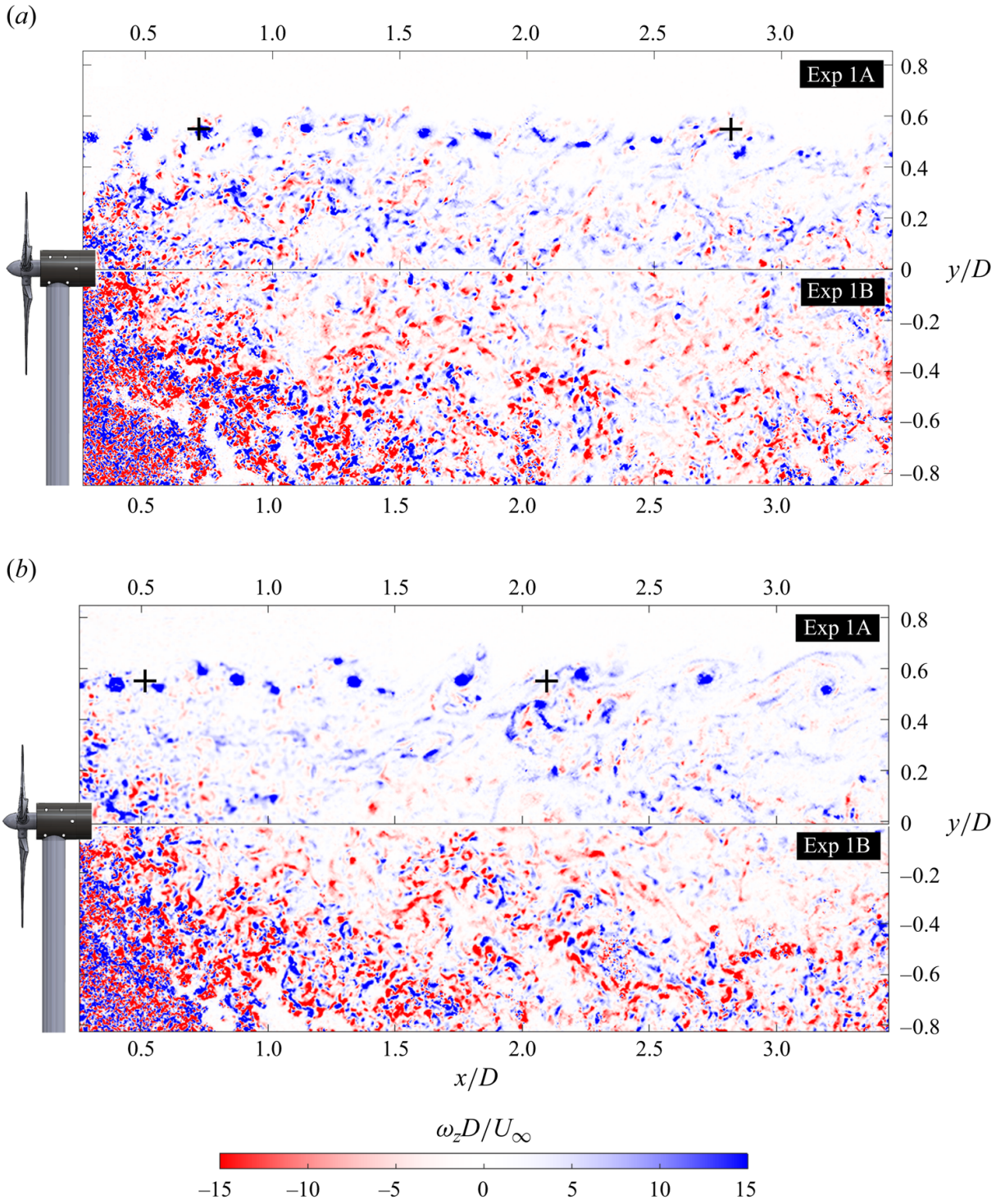


Figure 3.1: Instantaneous vorticity fields of a wind turbine wake for (a) $\lambda = 4.5$ and (b) $\lambda = 6$ in the xy plane. Fields of view from experiment 1A and experiment 1B (at different time instants) are stitched together for a visual representation of the entire wake.

freestream. Trailing sheet-like vortices can also be seen being shed along the span of the blade (Abraham et al., 2019). For $\lambda = 4.5$, the tip vortices shed from the 3 blades start interacting

after a streamwise distance of $x/D \approx 2$ and initiate the merging process. Until $x/D \approx 2$, the wake boundary remains nearly horizontal or in other words, in the presence of the tip vortices, the wake does not expand in the very near field. This supports the observation of Medici (2005); Lignarolo et al. (2015) who noted that the tip vortices in the near field act as a shield to prevent mixing with the outer fluid. From figure 3.1 here, it can be seen that beyond $x/D \approx 2$ the interaction and merging of the tip vortices aid wake expansion and wake recovery. For $\lambda = 6$, the turbine operates at a higher thrust coefficient (see chapter 2) leading to stronger tip vortices that are more closely spaced (due to higher rotational speed). This results in an earlier interaction and merging of the tip vortices (Felli et al., 2011; Sherry et al., 2013a).

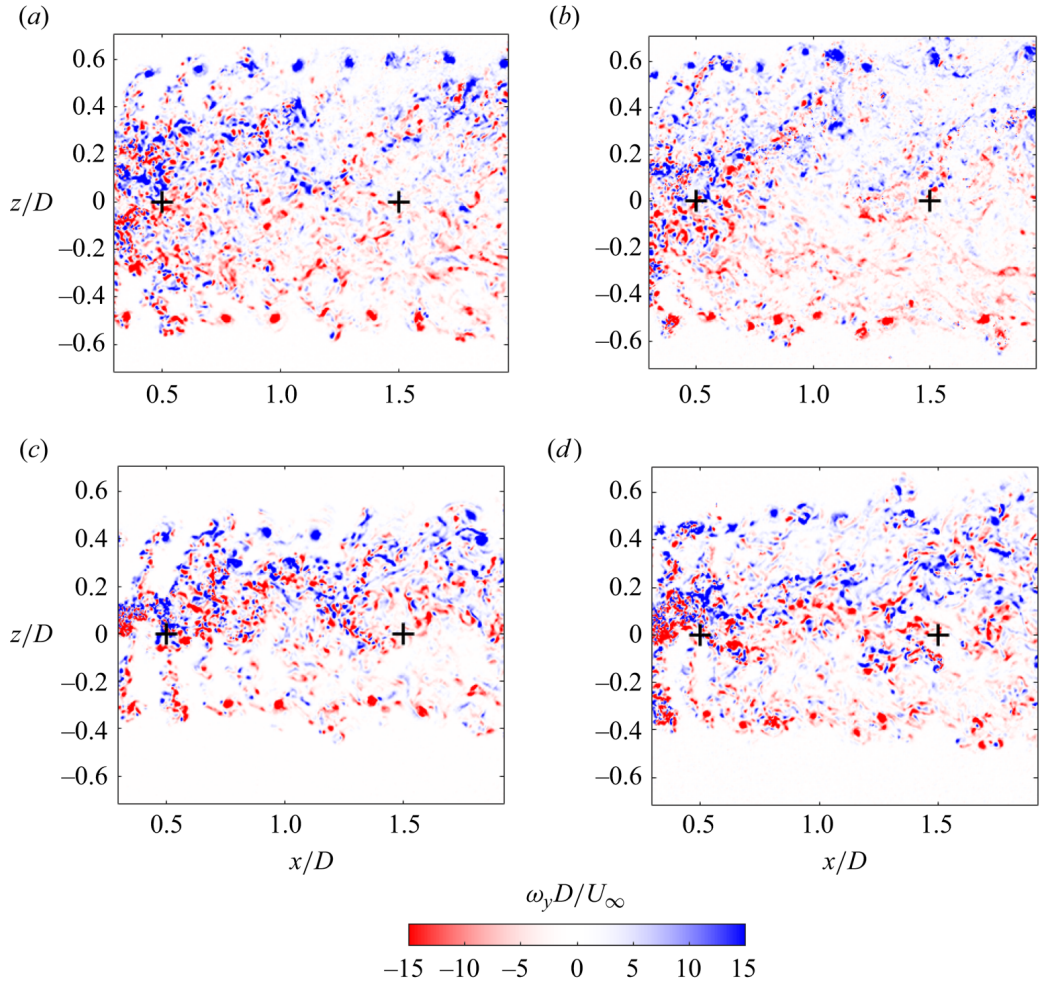


Figure 3.2: Instantaneous vorticity fields of a wind turbine wake in $xz(y = 0)$ plane (experiment 2A) for (a) $\lambda = 4.5$ and (b) $\lambda = 6$. Subfigures (c) and (d) show the vorticity fields at an offset $(y = -0.35D)$ plane (experiment 2B) for $\lambda = 4.5$ and 6 respectively.

In the lower plane (experiment 1B), the vorticity field looks drastically different from the top plane. The tip vortices in the lower plane interact with the tower's vortex shedding which

significantly increases the vorticity levels. Note that vortices are shed from the tower in an oblique fashion. Such an oblique nature of vortex shedding from the tower was also reported by De Cillis et al. (2021) through numerical simulations. Several factors can lead to oblique vortex shedding from the tower such as the strongly sheared inflow condition (Silvestrini and Lamballais, 2004) caused by the rotor and finite-span effects of the tower near the nacelle (Williamson, 1996). It has been shown that the presence of shear or end effects can lead to oblique vortex shedding which can promote three-dimensionality in the wake (Silvestrini and Lamballais, 2004; Williamson, 1996). Such oblique three-dimensional vortex shedding from the tower can be clearly observed in supplementary videos 1 and 2 (shown by a blue arrow)[†]. Interestingly, upward bursts of turbulent fluid are observed from around the wake centre line at several instances. These are shown by white arrows in supplementary videos 1 and 2. The origin of these bursts are not clearly understood yet. They are most likely related to the complex three-dimensional vortex shedding from the tower and its interaction with the nacelle's vortex shedding. It should, however, be kept in mind that the effect of the tower/nacelle could be more pronounced in the present experiments than for utility-scale turbines due to the relatively large size of the tower and nacelle as was discussed in chapter 2. Nevertheless, the flow field shown in figure 3.1 is qualitatively similar to that observed in an actual turbine (see figure 7 of Abraham et al. (2019)). Abraham et al. (2019) utilised natural snowfall to visualise the wake of a utility-scale turbine in the symmetry plane (xy plane according to the present nomenclature) and showed that the flow structures in the lower plane were significantly more chaotic and distorted due to the presence of the tower. Hence, the present experiments are believed to replicate the wake of an actual turbine well in spite of the geometric dissimilarities and inherent Reynolds number difference.

Figure 3.2 shows the instantaneous vorticity fields in the xz plane at different y offsets for $\lambda = 4.5$ and 6 (experiment 2). At the symmetry plane (figures 3.2(a, b)) the evolution of the tip vortices and trailing sheet vortices looks similar to that obtained from experiment 1A (see supplementary videos 3 and 4). Figures 3.2(c, d) show the vorticity field at an offset (experiment 2B) from the nacelle. The central region of the wake shows an oscillatory behaviour (see supplementary videos 5 and 6) which was not pronounced in the symmetry plane in experiment 2A. It is evident that

[†]Please find the supplementary videos here.

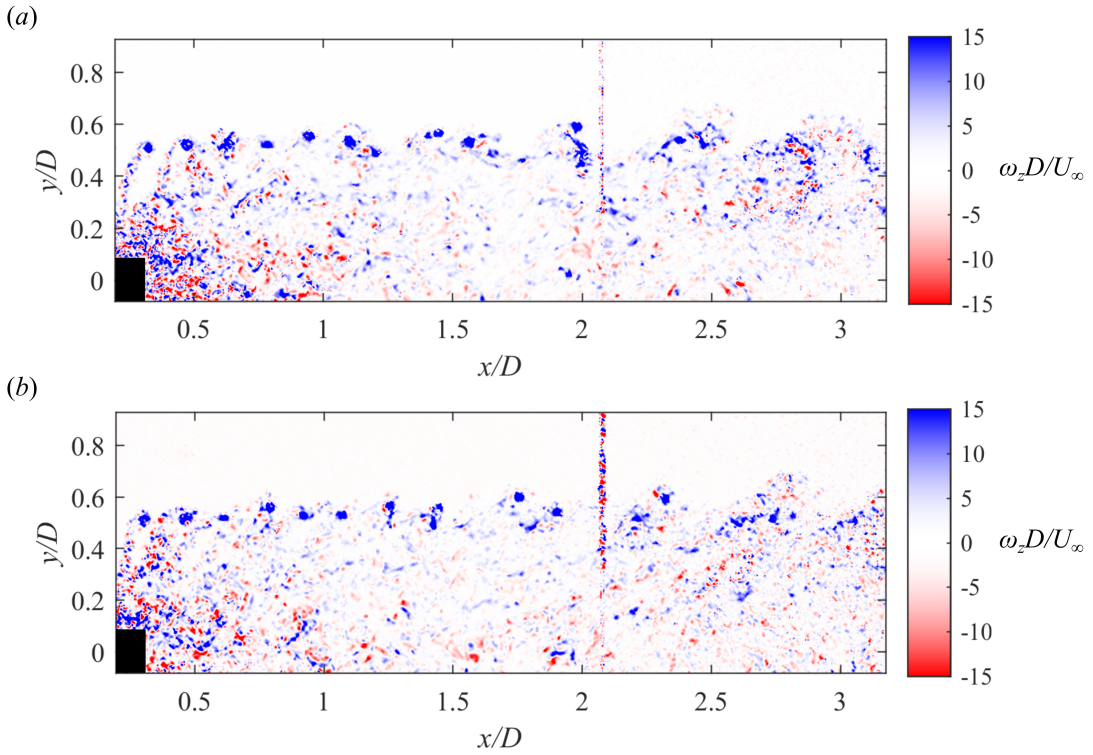


Figure 3.3: Instantaneous vorticity fields in the $xy(z = 0)$ plane for $\lambda = 6$ for (a) $U_\infty = 0.3$ m/s and (b) $U_\infty = 0.4$ m/s. The fields are noisy around $x/D \approx 2.1$ since a part of the laser beam leaked while forming the sheet using a cylindrical lens. The data is useful elsewhere in the field.

this oscillation results from the vortex shedding of the tower which interacts with the vortices shed from the blades. From supplementary videos 5 and 6 it can be seen that the vortex shedding pattern from the tower is not perfectly regular as it interacts with the regular passage of trailing sheet vortices. It is also interesting to observe that the wakes in figure 3.2 appear to be slightly deflected towards the side $z > 0$. Such asymmetric expansion of the wake was also observed by Howard et al. (2015). Due to the rotation of the turbine, the wake rotates in the opposite sense (Medici and Alfredsson, 2006). The turbine of Howard et al. (2015) rotated in a anti-clockwise sense when viewed from the upwind side. They found the wake to be slightly deflected in a negative z direction (following our nomenclature). Our turbine rotated in a clockwise sense and we observe a deflection in the opposite, positive z direction. The vortex shedding from the tower likely has a role in the lateral deflection of the wake. Note from figures 3.2(c,d) that the shed vortices from the tower is also deflected towards the $+z$ side therefore pushing the wake boundary in one side. This laterally deflected vortex shedding from the tower is likely due to the fact the resultant velocity vector ahead of the tower is inclined at an angle to the freestream direction. As

seen from the upwind side, the flow induced by the turbine rotates in the anticlockwise direction which inclines the resultant incoming velocity vector towards $+z$ side ahead of the tower. This can be better visualized by looking at figure 2.6(a) in chapter 2. Nevertheless, there could also be a non-negligible contribution from slight experimental misalignment of the rotor plane with the freestream direction.

Finally, experiments 1E and 1F considered higher free stream velocities ($U_\infty = 0.3$ m/s and $U_\infty = 0.4$ m/s respectively), hence a higher Re_D at a single $\lambda = 6$. Typical vorticity fields are shown in figure 3.3. Some noise in the data can be observed around $x/D \approx 2.1$. This was due to a leakage of the laser beam from the side of the cylindrical lens that forms the laser sheet. Nevertheless, the data was valid elsewhere in the FOV and useful inferences could still be drawn. Comparing with figure 3.1, it can be seen that the tip vortices break down earlier owing to the higher Re.

3.3 Mean velocity field

The mean velocity deficit ($\Delta U/U_\infty$, where $\Delta U = U_\infty - U$) profiles at different streamwise distances for the two main tip speed ratios are shown in figure 3.4. The plots are only shown in the xy plane (experiment 1A & B). A Gaussian curve (black dashed lines) is fitted to the mean velocity deficit profiles corresponding to $\lambda = 6$ for comparison. Close to the turbine, in the upper plane, 5 inflection points are observed (figure 3.4(a)). The mean velocity/velocity deficit profiles in the wake of a single scale bluff body contain only one inflection point on each side of the wake. The existence of multiple inflection points in the wake of the wind turbine essentially shows its multiscale nature. Baj and Buxton (2017) observed mean velocity profiles of a similar nature in the near wake of a multiscale array of prisms having unequal widths. Note that the qualitative nature of the wake deficit profiles are similar for both tip speed ratios considered. In the upper plane, at $x/D = 0.5$, there is an inflection point at $y/D \approx 0.1$ (shown by the **x** symbol) which corresponds to the wake of the nacelle. The other inflection point, corresponding to the nacelle's wake, is present below the symmetryline ($y = 0$) but inflection points are only shown for the upper plane ($y > 0$). The second pair of inflection points, shown by the (●) symbols, occurs at $0.2 < y/D < 0.4$. These inflection points appear most likely due to the sheet-like vortices shed

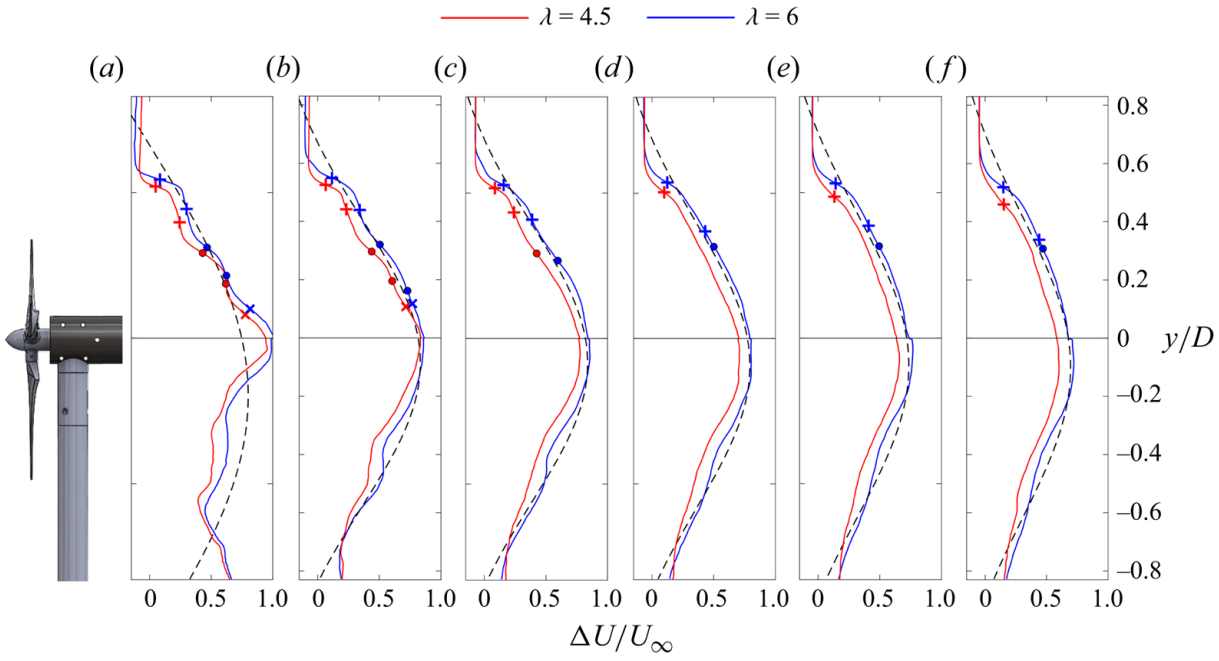


Figure 3.4: Mean velocity deficit at (a) $x/D = 0.5$, (b) $x/D = 1.0$, (c) $x/D = 1.5$, (d) $x/D = 2.0$, (e) $x/D = 2.5$, and (f) $x/D = 3.0$ for $\lambda = 4.5$ and 6. The black dashed lines represent a Gaussian fit to the mean velocity deficit profiles corresponding to $\lambda = 6$.

from the blades as seen in figure 3.1 and figure 3.2. The third pair of inflection points (shown by the + symbols) occurs around $y/D \approx 0.5$ and corresponds to the tip vortices. The first inflection point is the least spatially persistent (until $x/D \approx 1$) indicating a small spatial extent of the nacelle wake, while the other inflection points are observed further downstream due to the persistent nature of the vortices shed from the blades. Note that such inflection points in wake profiles have also been observed in previous studies (Lignarolo et al., 2015; Yang et al., 2012). If observed carefully, 5 inflection points can be observed in Yang et al. (2012)'s data as well (see the curve corresponding to $\lambda = 4.5$ in figure 4 of Yang et al. (2012)), however the curvature of the mean velocity profile was much milder as the experiments were conducted inside a turbulent boundary layer. Additionally, based on the design of the turbine, a separate pair of inflection points may or may not be observed for the blade wake and nacelle wake. Alternatively, there could be one combined wake of the two forming a single pair of inflection points, which we see further downstream (from $x/D = 1.5$) in our case in figure 3.4.

Important observations can be made if we compare the mean velocity deficit profiles with standard wake models used in industry. Standard models like Jensen (Jensen, 1983) or Frandsen (Frandsen et al., 2006) assume that the velocity deficit has a symmetric top hat shape. Although

the aim of these models is not to produce the correct wake profile, the discrepency between the assumed wake profile and the actual wake profile in figure 3.4 should be noted. The far-wake model proposed by Bastankhah and Porté-Agel (2014) assumes a Gaussian distribution of the velocity deficit profile, which is a more realistic assumption but still has its limitations. As can be seen from figure 3.4, even at $x/D = 3$, the wake deficit profile is not exactly Gaussian. Sharp gradients exist near the wake edge as coherent tip vortices are still present. In the presence of freestream turbulence, however, the wake profile approaches a Gaussian nature earlier (Wu and Porté-Agel, 2012; Vahidi and Porté-Agel, 2022), leading to a better agreement with the model. Another important thing to note is that the wake centreline, defined as the location where the velocity deficit is maximum, drifts from the geometric centreline ($y = 0$) towards $y < 0$. This downward drift in the mean wake centreline is caused by the asymmetry induced by the turbine's tower (Pierella and Sætran, 2017). Such asymmetry in the wake is not accounted for in the aforementioned models in use.

3.4 Important frequencies

The temporal fluctuation in the wake of a wind turbine is important as that determines the nature of the fluctuating loads induced on downstream turbines exposed to the wake of the wake-producing machine. Due to the inherent multiscale nature of the wake, multiple frequencies can be expected to characterise the wake dynamics. First the important frequencies towards the outer edge of the wake for different tip speed ratios are identified. For that, a new length scale termed as the convective pitch is introduced as $L_c = \pi D/\lambda$. This length scale can physically be interpreted as the distance travelled by a fluid element at velocity U_∞ in the time taken for the rotor to complete one full rotation. Note that L_c is not exactly the same as the pitch of the tip vortices as the tip vortices propagate at a velocity slightly smaller than the freestream velocity. For the present configuration $L_c = 0.70D$ and $0.52D$ for $\lambda = 4.5$ and 6 respectively. Fast Fourier transforms are evaluated at selected points (shown by $+$ in figure 3.1) based on the fluctuating transverse velocity component and are shown in figure 3.5. The Strouhal number, St_C is calculated based on U_∞ and L_c. Figures 3.5(a) and 3.5(e) show the transverse velocity spectra at $x/L_c = 1$ for $\lambda = 4.5$ and $\lambda = 6$ respectively. Apart from an energetic low frequency

region near the nacelle ($y \approx 0$), a number of distinct frequencies are observed which are close to integer multiples of St_C. These frequencies and their relative strengths can be more clearly observed from figures 3.5(b) and 3.5(f) (for $\lambda = 4.5$ and $\lambda = 6$ respectively) which show the frequency spectra at $x/L_c = 1$ and $y/D = 0.55$, *i.e.* near the outer wake. Note that, the spectra look qualitatively similar for both tip speed ratios. Here, the dominant frequency is $St_C \approx 3$, which corresponds to the blade passing frequency (henceforth denoted as $3f_r$, where f_r is the rotor frequency). This similarity holds up the possibility to demarcate the very near field of the turbine wake (where the influence of the blade passing frequency is significant) based on the convective pitch, L_c, which is discussed further in the next section. Although the dominant frequency is the same for both λ at this location, there are subtle differences in the spectra. Especially, for $\lambda = 6$, the rotor frequency f_r ($St_C \approx 1$) as well as other harmonics of f_r are more pronounced compared to $\lambda = 4.5$. Comparing figure 3.1(a) and 3.1(b), it can be seen that for $\lambda = 6$ at $x/L_c = 1$ there is a waviness at the edge of the wake owing to the early merging process for $\lambda = 6$. This is not present at $x/L_c = 1$ for $\lambda = 4.5$. This wavy nature has a frequency of f_r. As a result f_r and its harmonics are much stronger in the near field for $\lambda = 6$.

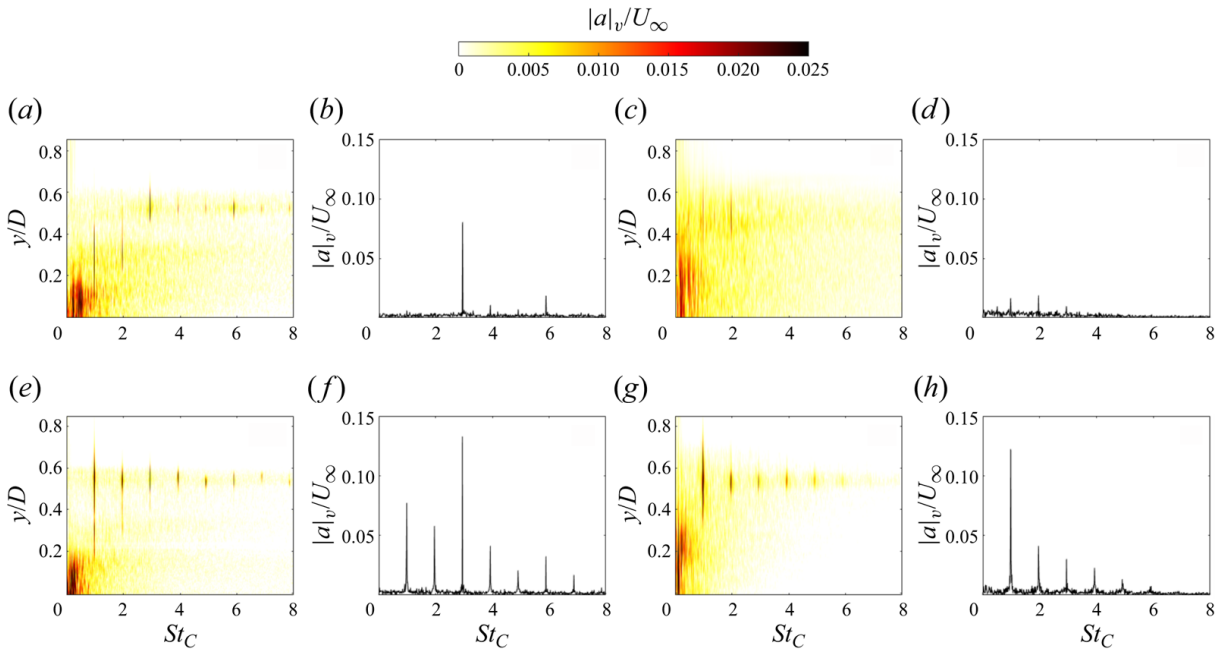


Figure 3.5: Transverse velocity spectra obtained at $x/L_c = 1$ for (a) $\lambda = 4.5$ and (e) $\lambda = 6$. Subfigures (b) and (f) show the same at $x/L_c = 1$, $y/D = 0.55$ for the two tip speed ratios. Similarly, subfigures (c) and (g) show the spectra at $x/L_c = 4$ for $\lambda = 4.5$ and $\lambda = 6$ respectively. The corresponding spectra at $x/L_c = 4$, $y/D = 0.55$ are shown in (d) and (h). Strouhal numbers St_C and St_D are defined based on L_c and D as the length scales, respectively, and U_∞ as the velocity scale.

The difference between the two tip speed ratios becomes more significant in the far field as can be seen from figures 3.5(c) and 3.5(g) which show the transverse velocity spectra at $x/L_c = 4$. Clearly f_r is much stronger for $\lambda = 6$ here. The corresponding spectra at $x/L_c = 4$ and $y/D = 0.55$ are shown in figures 3.5(d) and 3.5(h). It can be seen that the blade passing frequency ($3f_r$) is no longer dominant. For $\lambda = 4.5$, the dominant frequency is $2f_r$, while the strength of the f_r and $2f_r$ peaks is similar. For $\lambda = 6$ however, f_r is by far the dominant frequency at this location, which implies that the merging process for $\lambda = 6$ is different from $\lambda = 4.5$. The presence of both rotor frequency and blade passing frequency has been previously reported in the near wake (Felli et al., 2011; Chamorro et al., 2013; Okulov et al., 2014; Toloui et al., 2015). Different modes of tip vortex merging have been reported in experiments (Sherry et al., 2013a; Felli et al., 2011) and theory (Widnall, 1972). The merging process is known to be primarily driven by mutual inductance of the tip vortices and it has been shown to depend on vortex strength, vortex core size and pitch of the vortices (Widnall, 1972). In addition, disturbances from the freestream or rotor geometry such as slight imperfections in the blade construction can influence the merging and break down of the tip vortices (Ivanell et al., 2010; Toloui et al., 2015; Ramos-García et al., 2023; Abraham and Leweke, 2023). The tower is another source of disturbance to the tip vortices as seen in figure 3.1 here. Felli et al. (2011); Sherry et al. (2013a) argued that the merging of the tip vortices is a two-step process, where two vortex filaments get entangled first and thereafter merge with the third filament further downstream leading to a single vortical structure. The dominance of $2f_r$ in the far field for $\lambda = 4.5$ is believed to be the result of such a two-step merging process. However, this is not very evident from supplementary video 1[†], as the vortex cores of the tip vortices for $\lambda = 4.5$ are weaker compared to $\lambda = 6$ and they quickly get diffused. For $\lambda = 6$, the vortex cores are stronger and their separation is shorter, as a result of which there is a stronger and earlier interaction.

By calculating the circulation around the phase-averaged tip vortices, it can be shown that the tip vortices for $\lambda = 6$ are $\approx 5\%$ stronger than those for $\lambda = 4.5$, while there is a $\approx 25\%$ reduction in separation between the vortices for the higher λ. From the nature of the Biot-Savart law, that governs the mutual inductance instability, the growth of the instability can be vaguely expected to be directly proportional to the strength of the vortices and inversely proportional to the square

[†]Please find the supplementary videos here.

of the separation (Sørensen et al., 2015). Combining these two facts, it can be said that the reduced separation is the main factor for the earlier tip vortex interaction for $\lambda = 6$ compared to $\lambda = 4.5$ observed here. However, note that the growth rate of the instability also strongly depends on the nature of disturbances/asymmetries available or introduced to the system at a given λ as discussed in chapter 1. Abraham and Leweke (2023) used the leapfrogging distance (defined as the distance from the rotor where adjacent vortex loops swap positions) to quantify the effect of blade asymmetry. The authors reported that an axial displacement of $0.013D$ in one of the blade's tip reduced the leapfrogging distance by 17% at $\lambda = 3$ for a three bladed rotor. The current study did not have any dynamic forcing on the rotor, however a small axial displacement of around $0.5mm$ or $0.0025D$ at the tip of the blades was observed as discussed in chapter 2. Note that this is not unexpected as the tip thickness was quite small ($\approx 0.5mm$) in the present case unlike works that categorically studied the effects of blade asymmetry using much thicker blades (Ramos-García et al., 2023; Abraham and Leweke, 2023). The blade eccentricity observed most likely resulted in the tip vortices being of slightly unequal strength as can be seen from figure 3.1(b) for $\lambda = 6$. For the same reason, for $\lambda = 4.5$ in figure 3.1(a) one of the tip vortices looked slightly different. Some degree of eccentricity is inevitable in any experimental setup and an asymmetry of around $0.0025D$ is not large. This is particularly evident from the tip vortices being prevalent beyond $x \approx 2D$ for $\lambda = 4.5$ for the present case, which is similar to the leapfrogging distance of the baseline case of Abraham and Leweke (2023) for a lower tip speed ratio ($\lambda = 3$), although their Reynolds number was higher. This is further discussed in the following section.

From supplementary video 2[†] it can be noted that, for $\lambda = 6$, two tip vortices start revolving around the third tip vortex and eventually merge into a single vortical structure beyond $x/D \approx 1.5$. This hints at a single-step merging process for the tip vortices unlike that observed for $\lambda = 4.5$. This observation indicates that the merging process may or may not be a multistage process as proposed in previous studies (Felli et al., 2011; Sherry et al., 2013a). Instead, the process could depend on the tip speed ratio as well as the design of the turbine blades. It can also change with Reynolds number, as that would change the $C_l - C_d$ characteristics of the blade's section airfoils, hence changing the strength of the tip vortices.

[†]Please find the supplementary videos here.

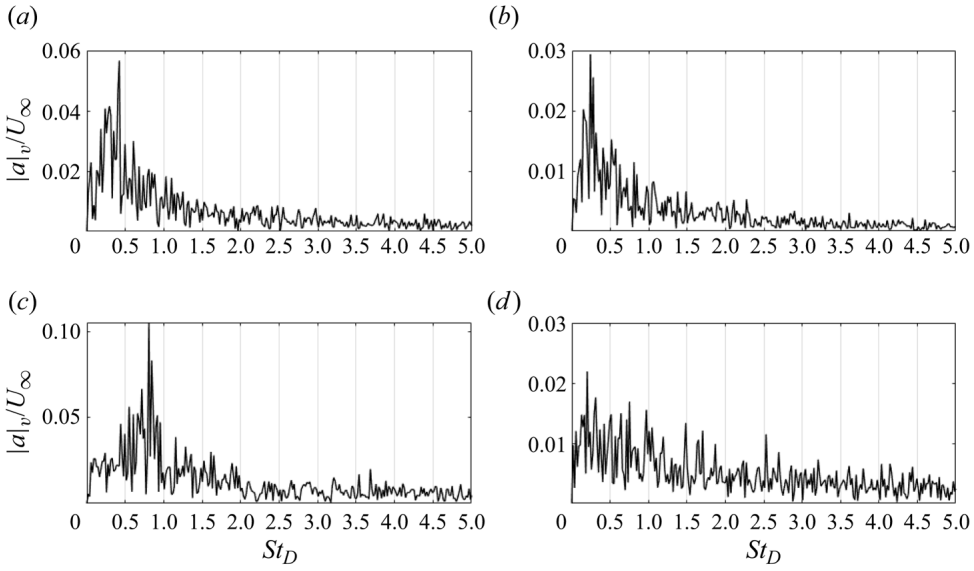


Figure 3.6: Transverse velocity spectra obtained at (a) $x/D = 0.5$, $z/D = 0$ and (b) $x/D = 1.5$, $z/D = 0$ in the plane $y = 0$ (experiment 2A). The same is shown at an offset plane (experiment 2B) at (c) $x/D = 0.5$, $z/D = 0$, and (d) $x/D = 1.5$, $z/D = 0$. All the spectra are shown for $\lambda = 6$ only.

Next, the frequencies near the central region of the wake are investigated. For that, fast Fourier transforms are performed at selected points from experiment 2, which are shown by the + signs in figure 3.2. The results are shown in figure 3.6 and are only for $\lambda = 6$, as the corresponding results for $\lambda = 4.5$ were similar. Hence, unlike figure 3.5, the Strouhal number is calculated only based on diameter D. Figures 3.6(a) and 3.6(b) are obtained from experiment 2A ($y = 0$ plane) at $x/D = 0.5, z/D = 0$ and $x/D = 1.5, z/D = 0$ respectively. Near the nacelle (figure 3.6(a)) the dominant frequency is at $St_D = 0.42$. Note that the nacelle diameter for this study is close to 6 times smaller than the rotor diameter. Hence, if the nacelle diameter is used to scale the frequency instead, the Strouhal number comes to around 0.069. Abraham et al. (2019) and Howard et al. (2015) reported a similar nacelle shedding frequency $St \approx 0.06$ for a utility-scale turbine. Accordingly, this frequency is believed to be related to vortex shedding from the nacelle and henceforth it is denoted as f_n. Interestingly, away from the nacelle, at $x/D = 1.5, z/D = 0$ (figure 3.6(b)), an even lower dominant frequency is observed at $St_D \approx 0.23$. This Strouhal number correlates well with the wake meandering frequencies reported in several previous studies (Okulov et al., 2014; Chamorro et al., 2013) and is henceforth denoted as f_{wm}. The origin of f_{wm} is discussed in more detail in section 3.6.

Figures 3.6(c)-(d) are obtained from experiment 2B, *i.e.* at an offset plane ($y = -0.35D$),

away from the nacelle and downstream of the tower. In the near wake ($x/D = 0.5, z/D = 0$, figure 3.6(c)), a dominant frequency is found at $St_D \sim 0.8$. This frequency was expected to correspond to the vortex shedding from the tower and hence, was denoted as f_T. However, upon non-dimensionalisation based on tower diameter (d_T) and U_∞, the Strouhal number (St_{d_T}) was found to be around 0.084, which is significantly lower than the expected value of $St \approx 0.2$ for vortex shedding from a cylinder in this Reynolds number range (Williamson, 1996). It is speculated that a combination of two main factors resulted in such a reduction in the tower's vortex shedding's Strouhal number. Firstly, note that the Strouhal number was calculated based on the freestream velocity. The incoming velocity just ahead of the tower was not measured in the experiments. Nonetheless, a velocity reduction of $\approx 20\%$ relative to the freestream value is expected using the blade element momentum method as the flow crosses the rotor disk. Secondly, the tower is exposed to a complex rotational flow containing frequencies such as f_r and $3f_r$. These factors strongly influence the tower's vortex shedding which can be clearly seen from supplementary videos 5 and 6[†]. Note that a similar reduction in the Strouhal number corresponding to vortex shedding from the upper portion of the tower was also reported recently by De Cillis et al. (2021).

To demonstrate this further, the transverse velocity fluctuations' signals just behind the tower from experiment 2B are shown in figure 3.7 for $\lambda = 6$ and $\lambda = 4.5$ respectively. Observing the red line (filtered signal), it can be sensed that the dominant frequency is < 1 Hz. The corresponding spectra based on the unfiltered signals are shown in figures 3.7(b) and (d). The Strouhal number of the dominant frequency based on tower diameter (d_T) is ≈ 0.085 and ≈ 0.071 for $\lambda = 6$ and $\lambda = 4.5$ respectively. The fact that for $\lambda = 4.5$, St_{d_T} slightly reduced to 0.071 is interesting. Note that the shedding frequencies for both λs are close to half of the turbine's rotational frequency (f_r). This could happen due to a lock on between the tower's vortex shedding frequency and f_r similarly to that observed in vortex shedding exposed to oscillatory flows (Barbi et al., 1986). Further downstream, at $x/D = 1.5$ (figure 3.6(d)), f_T is no longer found to be prominent. The wake meandering frequency is still observed, but is weaker compared to the central plane ($y = 0$), indicating a stronger influence of wake meandering in the central region of the wake.

[†]Please find the supplementary videos here.

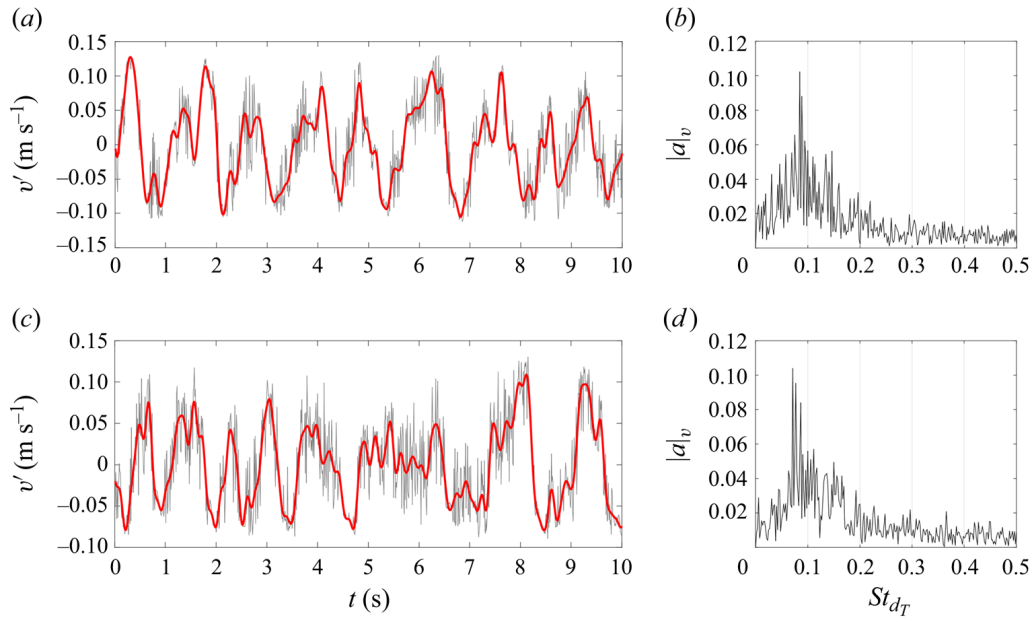


Figure 3.7: (a) Transverse velocity fluctuations just behind the tower and (b) corresponding spectra for $\lambda = 6$. The gray line in (a) is the unfiltered signal and the red line is the filtered signal. The spectra are obtained based on the unfiltered signal. (c) and (d) show the same for $\lambda = 4.5$.

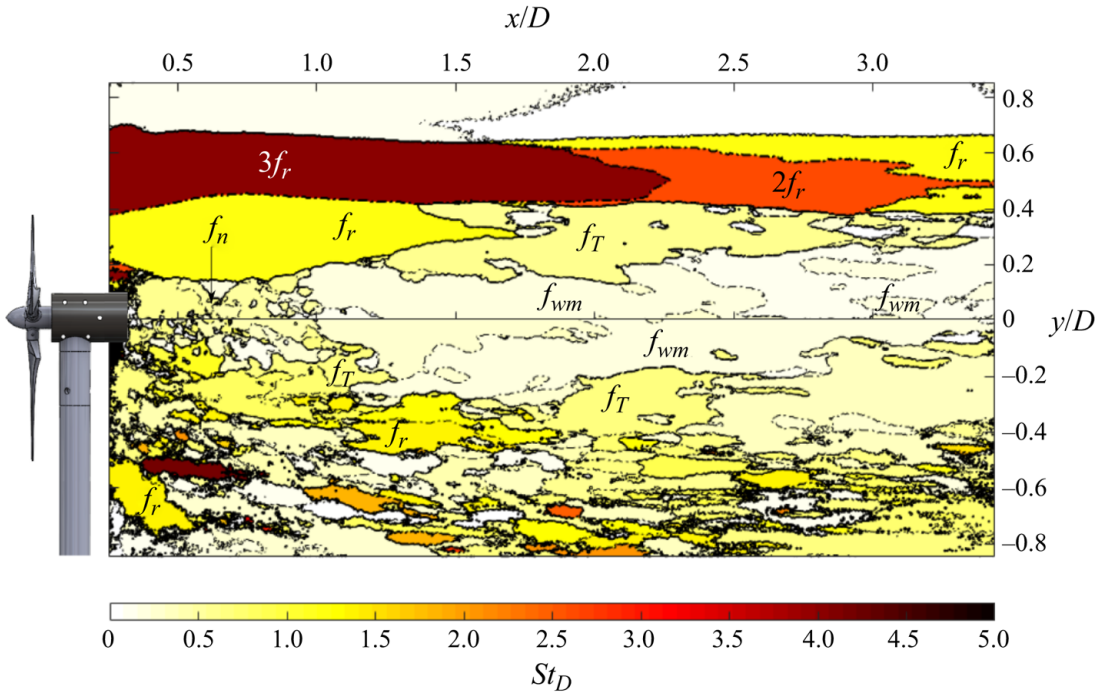


Figure 3.8: Zones of dominant frequencies for $\lambda = 4.5$

3.4.1 Frequency maps

The previous section showed the presence of multiple frequencies in the near wake of the turbine. These frequencies are stronger at a specific region depending on the nature of the frequency. In this section the spatial region where a particular frequency stays dominant is identified. At a particular location, the dominant frequency is defined to be that at which the transverse velocity spectrum attains its maximum value. For instance, in figures 3.5(b) and 3.5(f), *i.e.* in the near field and in the tip region, the dominant frequency is $3f_r$, while relatively far from the rotor, near the central region (see figure 3.6(b)), it is the wake meandering frequency (f_{wm}), which is dominant. The dominant frequencies at all the spatial locations are obtained and frequency maps are generated demarcating zones where a particular frequency is dominant. The dominant frequency map for $\lambda = 4.5$ in the xy plane is shown in figure 3.8.

In the top plane, large zones with distinct boundaries are observed where a particular frequency is dominant. Near the rotor in the tip region, $3f_r$ is dominant until around $x/D \approx 2.25$, beyond which $2f_r$ and f_r become important. Therefore it is identified that the merging process initiates at $x/D \approx 2.25$ which correlates well with the earlier observation from the instantaneous vorticity field in section 3.2. At similar Re, Sherry et al. (2013b) observed merging at $x/D \approx 2.5$ for $\lambda = 4$ and at $x/D \approx 1.5$ for $\lambda = 5$ (see figure 5 of Sherry et al. (2013a)). Since the merging location observed here lies between these two values, it can be stated that the current results match well with Sherry et al. (2013a) in spite of the differences in turbine design. Sherry et al. (2013a) also observed distinct root vortices (having a frequency of $3f_r$) in the vicinity of the root of the blade. Although a small region was observed in the vicinity of the root region where $3f_r$ was dominant (see figure 3.8), root vortices were not clearly observed in the present study, which can be seen from figure 3.1 (see also supplementary videos 1 and 2[†]). This is believed to be related to the specific design of the blades in the root region that produce only very weak root vortices that are sustained only very briefly. The relatively large size of the nacelle in the present study could also be a factor.

Interestingly, near the root region of the blade, until around $x/D \approx 1.5$, there is a large region where f_r is dominant. f_r is formed here most likely due to the merging of the unstable root

[†]Please find the supplementary videos here.

vortices and the trailing sheet vortices which can be seen from figure 3.1(a) and figure 3.2(a). Very close to the nacelle, there is a small region of nacelle shedding frequency (f_n). Further downstream a large region is seen where the dominant frequency is close to the tower frequency (f_T). However, at this location there were no high magnitude spectral peaks so that the mode associated with the tower's shedding frequency was simply identified as the dominant frequency in relation to a relatively incoherent region of the flow. Nevertheless, the observation of f_T in the xy plane is interesting and it indicates the inherent three-dimensionality of the vortex shedding from the tower.

In the lower plane ($y < 0$), the tip vortices break down earlier due to their interaction with the tower's vortex shedding. Patches of high frequency regions can be seen near the tip region in the lower plane, which are the remains of the blade passing or rotor frequencies. Apart from that, a number of other frequencies are also observed, making it look more broadband and turbulent like. The wake meandering frequency (f_{wm}) is found to be dominant only near the central region in the near wake. The entire wake looks like a shell of high-frequency dynamics surrounding the central region dominated by the low frequencies. The scenario remains qualitatively similar for $\lambda = 6$ as can be seen in figure 3.9, however, the streamwise/transverse extents of the dominant zones clearly look different. In the upper plane, the zones where $3f_r$ and $2f_r$ are dominant are quite small, and f_r is dominant in a large portion of the upper plane.

From figure 3.1(b) as well as from supplementary video 2[†] it can be noted that for $\lambda = 6$ merging occurs beyond $x/D \approx 1.5$. Sherry et al. (2013a) observed merging to occur at a closer distance of $x/D \approx 1.2$ for $\lambda = 6$ at a similar Re. Okulov et al. (2014) observed merging of tip vortices at $x/D \approx 1$ for $\lambda = 6$, although their Reynolds number was higher. This variability in the merging location could be related to the specific design of the blades and possible blade eccentricities. It also bolsters the fact that the observed blade eccentricity of around $0.0025D$ has a relatively small impact on the merging of the tip vortices. Nevertheless, it is safe to say that the specific design of the blades and the presence of any asymmetry in the blades can alter the frequency zones reported here, especially near the tip shear layer (Ramos-García et al., 2023; Abraham and Leweke, 2023).

In the lower plane, for $\lambda = 6$, traces of the tip vortices are still observed but again there are

[†]Please find the supplementary videos here.

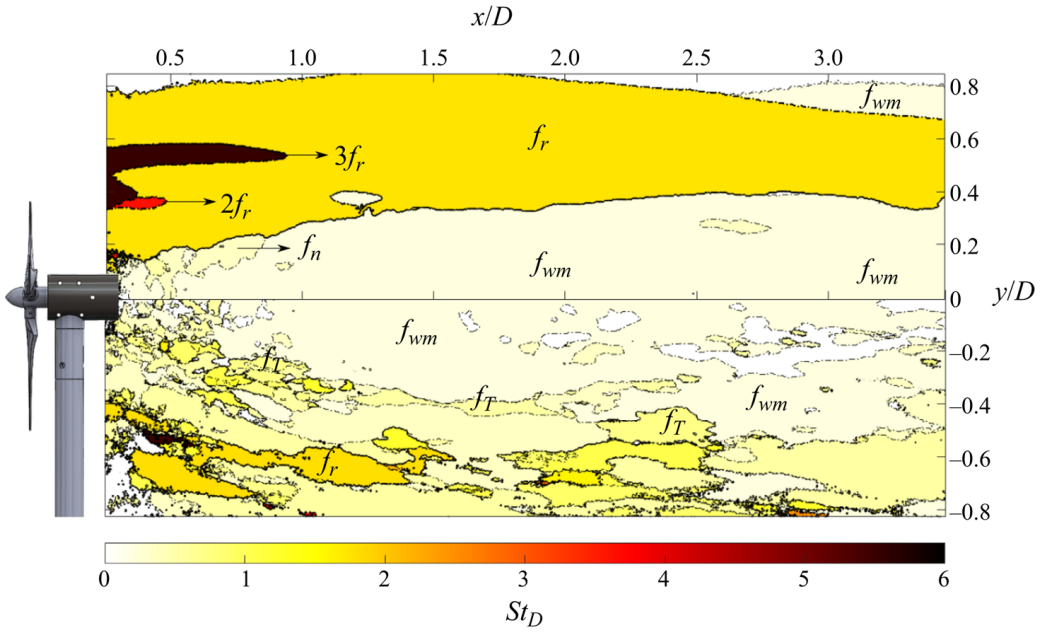


Figure 3.9: Zones of dominant frequencies for $\lambda = 6$.

several new frequencies present and it is more broadband. In the central region wake meandering is dominant and the transverse extent of the region where it is dominant grows with downstream distance. In fact, f_{wm} remains dominant over a larger region at $\lambda = 6$ compared to $\lambda = 4.5$, which shows a possible dependence of wake meandering on the tip speed ratio. This dependence is further discussed in section 3.6.

Next, the frequency zones obtained from experiment 2 are discussed. Figures 3.10(a) and 3.10(c) correspond to $\lambda = 4.5$ and $\lambda = 6$ respectively at the central plane ($y = 0$) and are similar to the upper plane in figures 3.8 and 3.9. This offers reassurance that the results of the experiments are reproducible. The wake meandering frequency remains dominant over a larger region for $\lambda = 6$ compared to $\lambda = 4.5$. The difference between the two tip speed ratios is more pronounced at the offset plane (experiment 2B). For $\lambda = 4.5$, the tower frequency (f_T) dominates the central part of the wake (see figure 3.10(b)). Contrastingly, for $\lambda = 6$, f_T has a sole dominance only before $x/D \approx 1$, beyond which the strengths of f_T and f_{wm} become comparable. This evidence further indicates that the strength of wake meandering depends on the tip speed ratio. Note that for $\lambda = 6$, the wake appears to be slightly deflected towards the side $z > 0$ which is most likely related to the rotation of the turbine and the altered vortex shedding from the tower as discussed earlier.

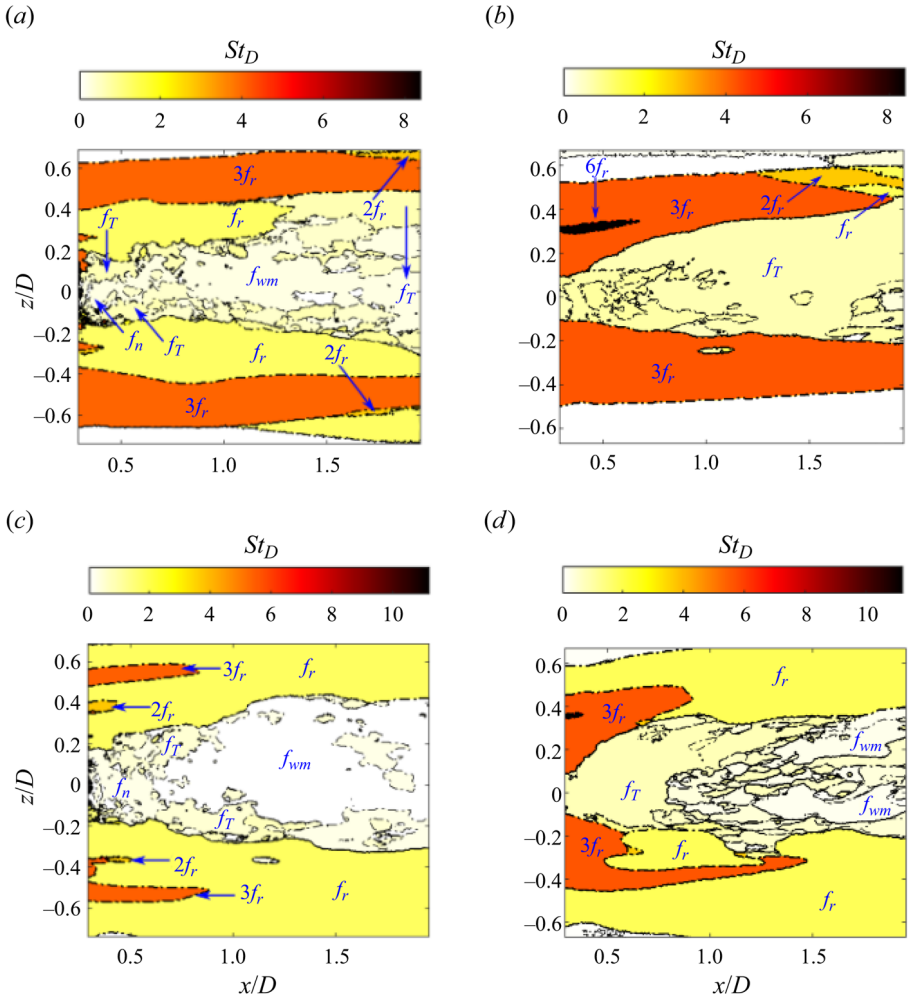


Figure 3.10: Zones of dominant frequencies for $\lambda = 4.5$ in the plane (a) $y = 0$ and (b) $y = -0.35D$. Subfigures (c) and (d) show the same for $\lambda = 6$.

Figures 3.11(a-b) show the frequency maps obtained from experiments 1E and 1F for $\lambda = 6$. These experiments were performed at a higher freestream velocity ($U_\infty = 0.3$ m/s and $U_\infty = 0.4$ m/s respectively). The maps look qualitatively similar to figure 3.9.

3.4.2 Strength of frequencies

The 'strength' of a frequency can be measured locally by taking the maximum amplitude in the transverse velocity spectra of a particular frequency at a particular streamwise distance, which is denoted as $|a|_v$. For instance, in figure 3.5(g), see that the signature of the frequency f_r is present over a range of y (from $y/D \approx 0.35$ - $y/D \approx 0.75$) at a particular x. However, its amplitude is maximum at $y/D \approx 0.5$ at this x location. This maximum value of f_r's amplitude

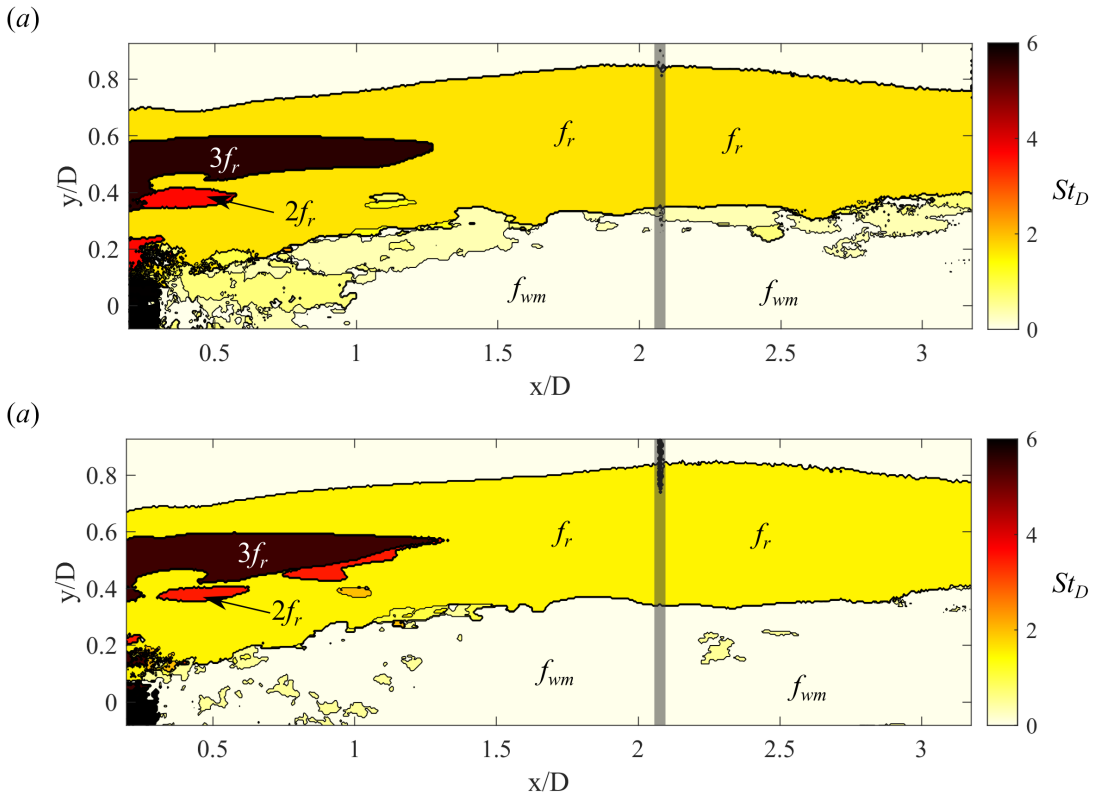


Figure 3.11: Zones of dominant frequencies for $\lambda = 6$ in the plane $z = 0$ for (a) $U_\infty = 0.3$ m/s and (b) $U_\infty = 0.4$ m/s.

is denoted as the strength ($|a|_v$) of f_r at this particular x location. $|a|_v$ for each of the important frequencies are obtained in a similar way at each x location. In figure 3.12(a), $|a|_v$ is shown over streamwise distance in the upper plane (experiment 1A) for $\lambda = 4.5$. In the near field, the blade passing frequency ($3f_r$) dominates over other frequencies and corresponds to the passage of tip vortices. At $x/D \approx 2.25$, $2f_r$ surpasses $3f_r$ and at $x/D \approx 3.2$, f_r surpasses $2f_r$, which is indicative of the two-step merging process. The higher harmonics are comparatively damped and less important beyond $x/D \approx 1.5$.

Figure 3.12(b), shows $|a|_v$ for $\lambda = 6$. Similarly to $\lambda = 4.5$, the dominant frequency in the near field is $3f_r$. However, owing to the higher tip speed ratio, the tip vortices interact much earlier. As a result, f_r surpasses $3f_r$ much closer to the turbine, at $x/D \approx 0.92$ and remains dominant even beyond 3 rotor diameters. Although $2f_r$ is present, it never becomes dominant. The strength of wake meandering shows a trend similar to $\lambda = 4.5$ and remains roughly constant throughout the domain of investigation. However, the strength of wake meandering is markedly increased for $\lambda = 6$. The wake meandering frequency, although not dominant, is present in the

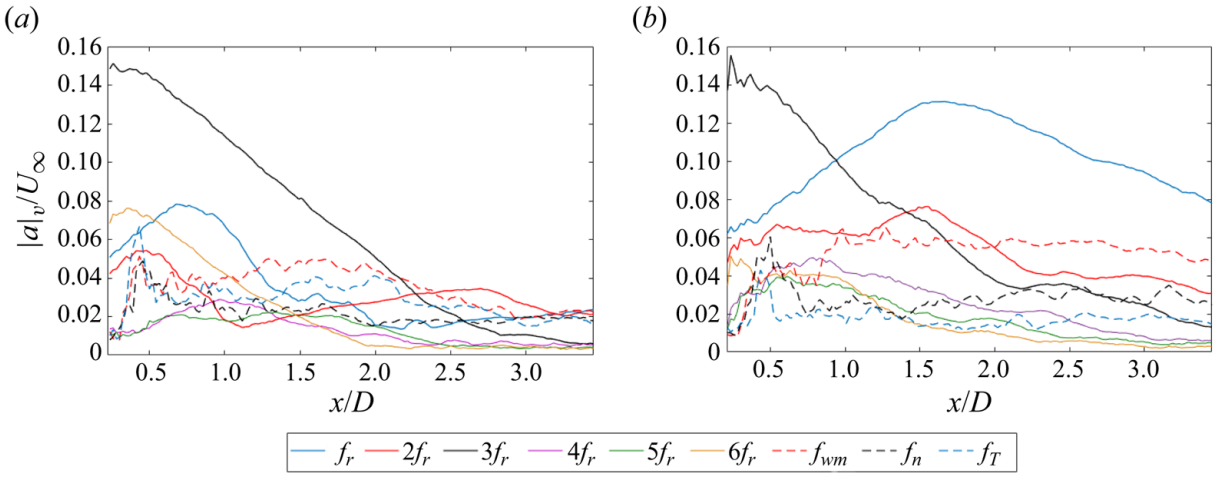


Figure 3.12: The evolution of the 'strength' of different frequencies with streamwise distance for (a) $\lambda = 4.5$ (a) and (b) $\lambda = 6$. The strength is calculated as the magnitude of the largest peak in the spectra of transverse velocity at a particular streamwise location.

near wake, and in fact it exists close to the nacelle in the central region which hints at the fact that the nacelle has an important role in the genesis of wake meandering. This is explored in more detail in section 3.6.

In the lower plane (experiment 1B), the frequency spectrum is more broadband and turbulent like, as can be seen from figure 3.8 and figure 3.9. As a result, a similar analysis for the lower plane revealed a large number of frequencies of comparable strengths making it difficult to draw firm conclusions hence it is not discussed any further. The same analysis is also performed for experiment 2 and the strengths of the different frequencies are shown in figure 3.13. The results from experiment 2A (*i.e.* in the plane $y = 0$) are shown in figures 3.13(a) and 3.13(c) for $\lambda = 4.5$ and $\lambda = 6$ respectively, and they closely resemble figure 3.12 despite being different experiments. Note that, for $\lambda = 6$ f_{wm} surpasses $3f_r$ exactly at $x/D \approx 1.7$ similarly to figure 3.12(b). The nacelle frequency f_n is important only in the very near field and the tower frequency is rather weak. Figures 3.13(b) and 3.13(d) show the strength of frequencies at the offset plane (experiment 2B). The tower frequency (f_T) now becomes important and can even be the dominant frequency in the near field. The streamwise evolution of f_T is similar in figures 3.13(b) and 3.13(d), showing minimal dependence on λ. Similarly to figure 3.12, the strength of wake meandering for $\lambda = 6$ is higher than $\lambda = 4.5$ for both the planes considered, which firmly establishes the fact that the strength of wake meandering is a function of the tip speed ratio.

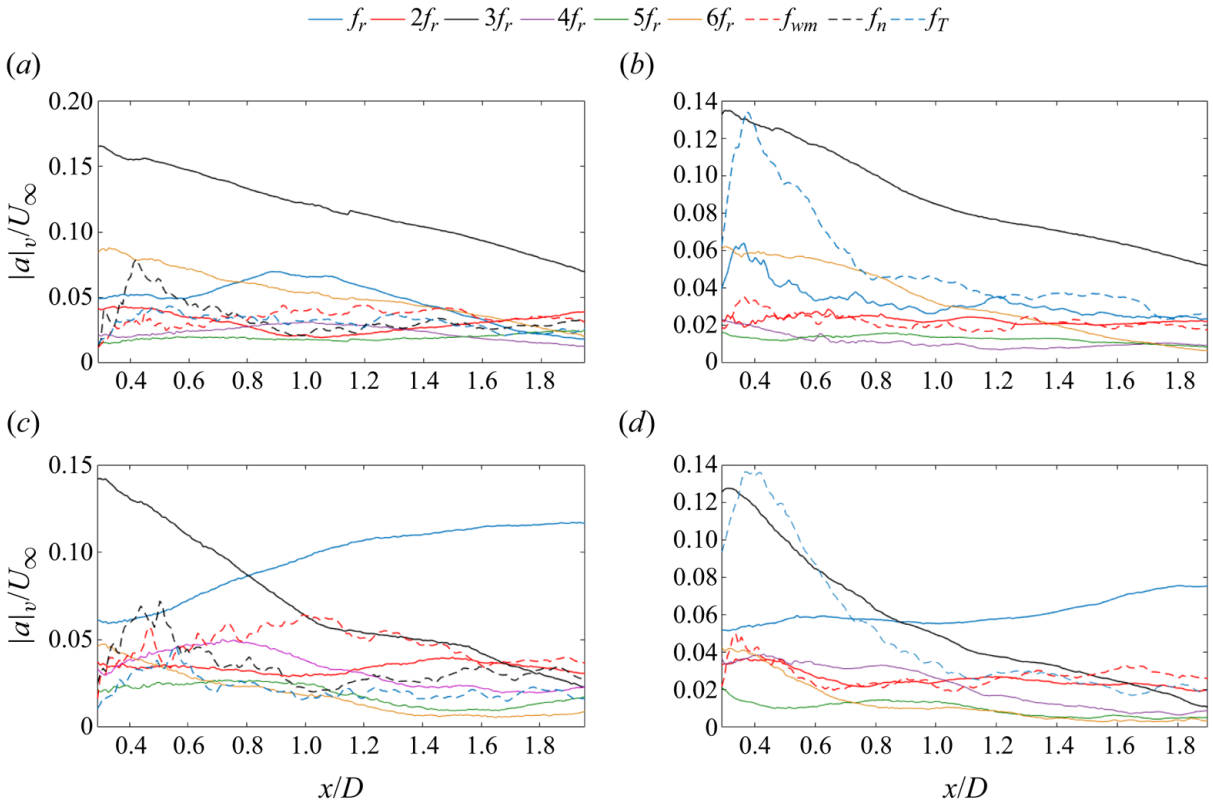


Figure 3.13: Strength of different frequencies in the $xz(y = 0)$ plane for (a) $\lambda = 4.5$ and (c) $\lambda = 6$ respectively. Sub figures (b) and (d) show the same in an offset plane $y = -0.35D$.

3.5 The definition of near wake

The near wake is coarsely defined as the region where the effect of the coherent structures shed from the turbine is pronounced. Contrastingly in the far wake the mean wake velocity profile starts to resemble a Gaussian owing to wake recovery. The distinction between the two is generally not trivial and depends on several factors including turbine geometry, operating condition, as well as inflow condition. The transition between the near and far wake is thus often vaguely defined to be in the range $2D - 4D$ from the rotor (Vermeer et al., 2003).

In the presence of freestream turbulence the tip vortices break down earlier and the wake recovers faster leading to a shorter near wake (Chamorro and Porté-Agel, 2009; Wu and Porté-Agel, 2012). Gambuzza and Ganapathisubramani (2023) recently studied the effect of both freestream turbulence intensity (T_i) and integral time scale. They tested T_is from 3% to 12% and integral time scales from $0.1 - 10$ times the convective time scale based on turbine diameter. They reported a shorter near wake for higher T_i and short integral time scale. The extent of the near

wake would thus depend on several factors and it is safe to say that an unambiguous definition of the near wake simply based off the turbine diameter may not be possible (Howard et al., 2015). Various attempts have been made to systematically define the near wake. Sørensen et al. (2015); Vahidi and Porté-Agel (2022) defined the near wake as the distance from the rotor at which the mean velocity profile becomes approximately Gaussian. De Cillis et al. (2021) defined the near wake's extent as the distance where the time-averaged coherent kinetic energy dropped to a certain level. Gambuzza and Ganapathisubramani (2023) defined the near wake to be the region where the material derivative of turbulent kinetic energy is positive.

Unlike these approaches, an attempt is made here to demarcate the near wake based on the frequency dynamics. Note that, the dominant frequency signature in the immediate vicinity of the turbine is that of the tip vortices, while in the far wake the dominant frequency is expected to be that of wake meandering. Therefore, a sensible definition for the near wake could be the location where the strength of wake meandering (lets call it S_{wm}) surpasses the strength of the blade passing frequency (S_{3fr}). Note that this idea of defining the near wake is similar to that proposed by Howard et al. (2015). The authors made a qualitative distinction between the near and far wake based on the importance of the hub vortex (signature of the near wake) and the wake meandering (signature of the far wake). In this work a more quantitative approach is adopted and the strength of the tip vortices is used as the near wake signature instead of the hub vortex.

Note from figure 3.12 that the crossover between S_{wm} and S_{3fr} happens at $x/D \approx 2.2$ and $x/D \approx 1.7$ for $\lambda = 4.5$ and $\lambda = 6$ respectively. Although these locations are far apart in terms of turbine diameter D, they are found to be close in terms of convective pitch L_c and correspond to $3.15L_c$ and $3.24L_c$ respectively. To further investigate the effectiveness of L_c as a length scale in the near wake, a series of experiments are performed in experimental campaign $1D$ (see table 2.1 for details) at tip speed ratios different from the two main tip speed ratios. The evolution of the relative strength of the tip vortices and wake meandering (defined as S_{3fr} - S_{wm}) with both turbine diameter, D and the convective length scale, L_c for all the tip speed ratios tested are shown in figure 3.14. A better collapse is observed for different λs when x is non-dimensionalised using L_c. Further, the relative strength becomes zero, *i.e.* the strength of wake meandering surpasses that of $3f_r$ in the vicinity of $x \simeq 3L_c$. The blue shaded region in

figure 3.14 shows the scatter in the location where the relative strength becomes zero in terms of D and L_c. Based on this experimental evidence it is proposed that a distance of $3L_c$ from the rotor plane can be a good estimate of the near wake of a three-bladed turbine when the freestream turbulence level is low.

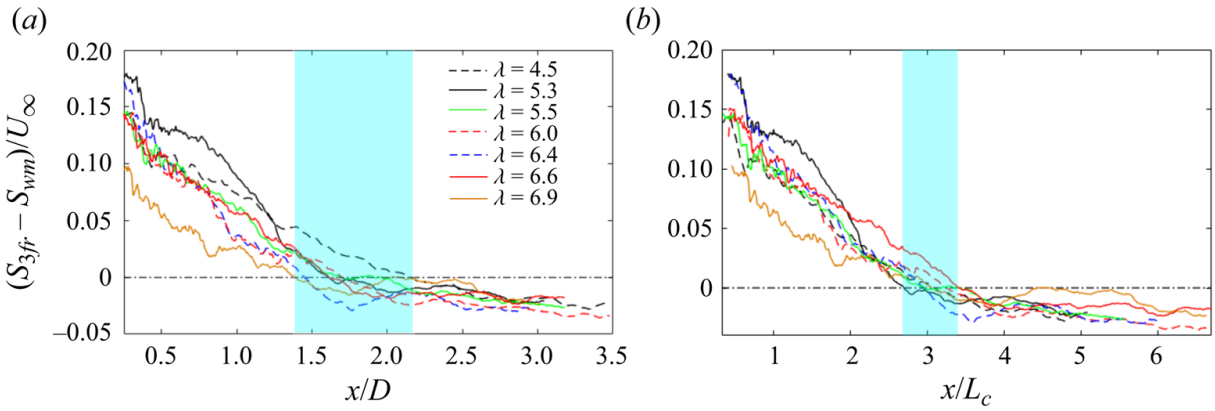


Figure 3.14: Variation of relative strength of $3f_r$ and f_{wm} with streamwise distance scaled by (a) turbine diameter D and (b) convective length scale L_c for different tip speed ratios.

To further understand if the near wake length changes with U_∞, the data from experiments 1E and 1F are used which had higher freestream velocities (0.3 m/s and 0.4 m/s respectively) for $\lambda = 6$. The amplitudes of the modes at frequencies $3f_r$ and f_{wm} for the two cases are shown in figure 3.15. The crossover between the two is again found to occur close to $3L_c$. In figure 3.15(a) and (b) the strength is obtained using an FFT of the transverse velocity fluctuation, whilst (c) and (d) are based on Welch's PSD estimation. Similar results are obtained using the two techniques. Nevertheless, the near wake length may still depend on U_∞ or Re_D in general as real wind turbines operate at much higher Re_D. The near wake can also depend on C_T differently from λ. It is not trivial to separate out the effects of changing λ and C_T as both change simultaneously. In the current study only a single wind turbine model was used and force measurement was not available. Future works can consider blades of different designs that operate at a considerably different C_T at the same λ. Otherwise, the number of blades can be changed to see how the near wake is affected in terms of L_c. In addition, in the presence of freestream turbulence, the extent of the near wake might be expected to be shorter than $3L_c$ due to the earlier breakdown of the tip vortices as discussed earlier. This will be explored in chapter 4.

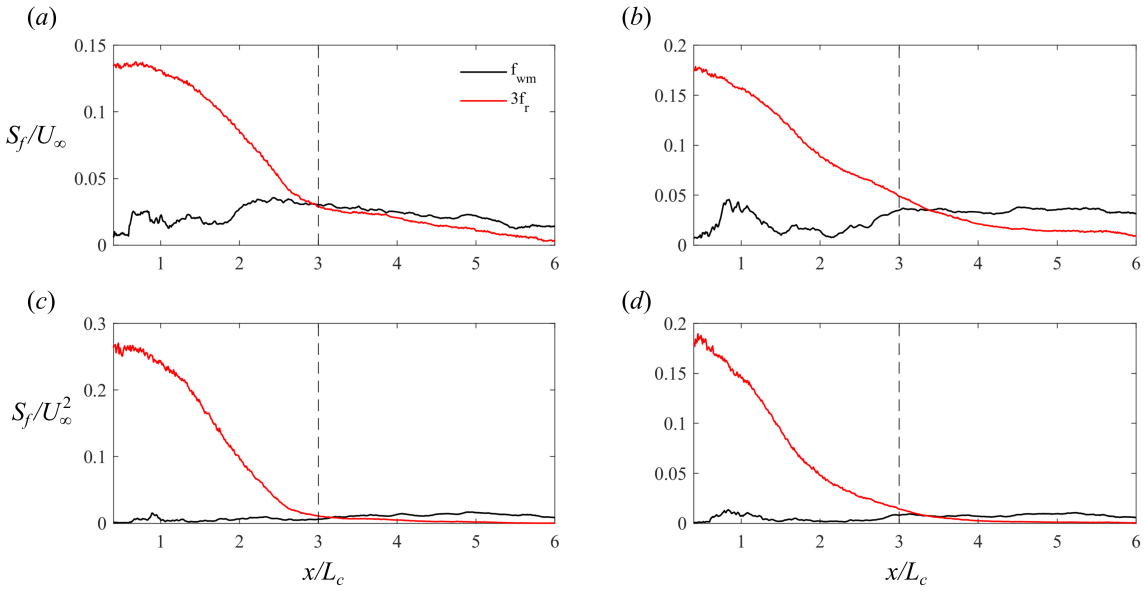


Figure 3.15: Streamwise variation of the amplitudes of the modes at frequencies $3f_r$ and f_{wm} for $\lambda = 6$ when (a, c) $U_\infty = 0.3$ m/s and (b, d) $U_\infty = 0.4$ m/s. In (a) and (b) the strength is obtained using an FFT of the transverse velocity fluctuation, whilst (c) and (d) are based on Welch's PSD estimation.

3.6 The nature and origin of wake meandering

Wake meandering has been described as the large scale motion that dominates the 'far wake' dynamics of a wind turbine. However, there exists varied opinions about the exact causes of wake meandering (Larsen et al., 2008; Espana et al., 2011; Okulov et al., 2014; Foti et al., 2018). For example, wake meandering has been described as large intermittent displacements of the entire wake due to passive advection by large scale turbulence in the incoming flow (Espana et al., 2011; Porté-Agel et al., 2020). On the other hand, a well defined low frequency has been obtained in the far wake, which has been associated with wake meandering when the freestream turbulence is negligible (Medici and Alfredsson, 2006, 2008; Okulov et al., 2014; Howard et al., 2015). These authors argued that wake meandering observed in the absence of freestream turbulence is associated with vortex shedding from the turbine, similar to large scale helical vortical structures found behind porous or solid disks (Berger et al., 1990; Medici and Alfredsson, 2005). The wake meandering observed in the present study is of the latter type which is induced by the wake-generating body itself, as opposed to any inflow turbulence.

Figures 3.8 and 3.9 reveal that the wake meandering frequency is dominant in the central region,

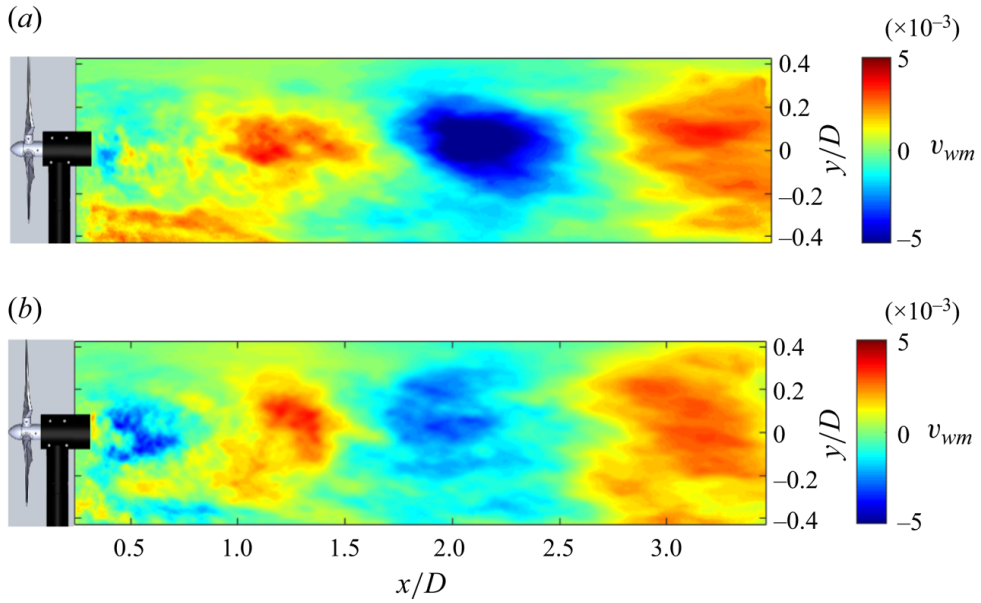


Figure 3.16: Transverse velocity components of the phase-averaged wake meandering modes for (a) $\lambda = 4.5$ and (b) $\lambda = 6$.

within $-0.4D < y < 0.4D$. Accordingly, experiment 1C focused on this region (see figure 2.6(a)) to capture the centreline dynamics and the nature of the wake meandering. To understand the nature of wake meandering, phase averaging is utilised (see for instance Reynolds and Hussain (1972); Cantwell and Coles (1983)) based on the frequency of the wake meandering observed for the two tip speed ratios. 48 phase bins were used to obtain the phase-averaged flow fields. Thereafter the second Fourier mode of the phase-averaged flow field was obtained. More details about this method can be found in Baj and Buxton (2017). The limited total acquisition time ($\approx$ 10-15 cycles of wake meandering) in experiment 1C, however, yielded poorly converged modes. Nevertheless, to have a qualitative idea, the transverse velocity component of the phase-averaged modes are shown in figures 3.16(a-b) for $\lambda = 4.5$ and $\lambda = 6$ respectively. Note that the modes are qualitatively similar and they resemble vortex shedding modes from a bluff body (for instance see DMD or OMD modes associated to vortex shedding behind cylinders (Chen et al., 2012; Baj et al., 2015)) of characteristic diameter D (albeit a porous body) which initiates from the vicinity of the nacelle. In fact, the wavelength of the mode is also similar to helical vortex shedding modes found behind a solid circular disk (Berger et al., 1990) at similar $O(Re_D)$. Note that wake meandering behind a turbine is inherently 3 dimensional (Medici and Alfredsson, 2006; Foti et al., 2016) whereas only a planar slice of the mode is presented in figure 3.16.

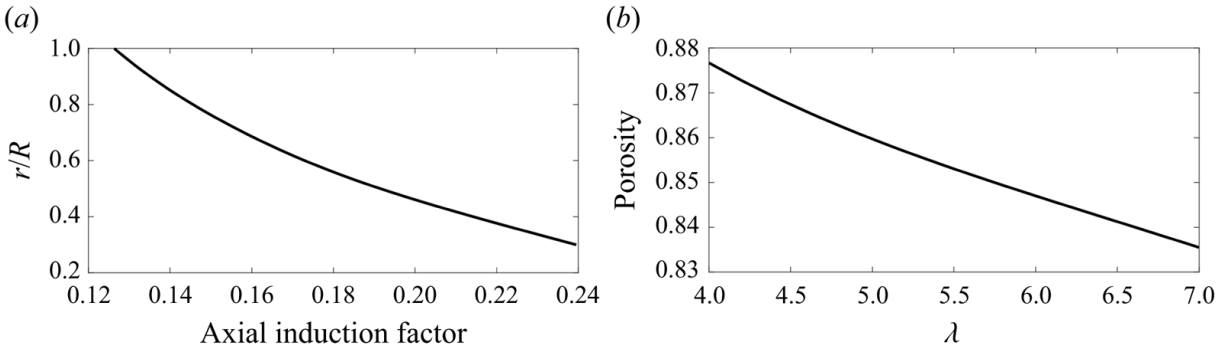


Figure 3.17: (a) Axial induction factor obtained from the blade element momentum method for $\lambda = 6$. (b) Variation of rotor porosity with λ.

Parallels have previously been drawn between a rotating turbine and a non-rotating porous disk (Lignarolo et al., 2016; Neunaber et al., 2021; Vinnes et al., 2022). It has been shown in several works that the wake characteristics of a porous disk can be similar to those of a turbine, at least in the far field, weakly agreed upon as $x \gtrsim 3D$ (Aubrun et al., 2013; Neunaber et al., 2021). Indeed the effective porosity of a wind turbine changes if λ is changed. If λ is increased, a greater area is swept by the blades in the time taken for a parcel of fluid to convect across the rotor disk, thus increasing the effective blockage, or reducing the porosity. Through a simple calculation, it can be shown how the effective 'porosity' of the turbine reduces with λ. First, using the blade element momentum method the axial induction factors are calculated at different λ. As an example the variation of the induction factor with radial distance r is shown in figure 3.17(a) for $\lambda = 6$. This gives the streamwise velocity at the rotor plane as a function of r. Next, using the knowledge of the chord and twist variation of the blades, the projected thickness of the blades in the xy plane (see figure 2.2) is calculated as a function of r. Using the two, a time scale, $t(r)$ is obtained which tells how much time a fluid parcel would take to cross the rotor disk at a particular radial location. Next, a blade element is taken at radial distance r and the area covered by the element in the yz plane (normal to freestream) in time $t(r)$ is calculated for a particular λ. Integrating the area covered over the blade an estimate of the effective blockage or porosity is obtained. The variation of effective porosity with λ is shown in figure 3.17(b). As can be expected, porosity of the turbine reduces as λ is increased. The porosities in figure 3.17(b) are higher than the actual values as the blockage caused by the nacelle, tower as well as the connecting part below the root of the blades were ignored. Nevertheless, the calculation serves the motivation to show how porosity depends on the turbine's operation.

The seminal work of Castro (1971) showed that the Strouhal number of vortex shedding from a 2D porous plate decreases if porosity is reduced and it asymptotes to ≈ 0.14 for a solid plate. A similar trend of wake meandering Strouhal number reducing with λ was reported by Medici and Alfredsson (2006, 2008). Further, Castro (1971) didn't observe vortex shedding for low porosity. On a similar note, Medici and Alfredsson (2006) did not observe wake meandering at lower λ ($\lambda < 3$ for a two bladed turbine). This motivated a further investigation on the potential link between wake meandering and vortex shedding. Medici and Alfredsson (2008) reported the reducing trend of St with λ only at a distance $1D$ downstream of the rotor which can be said to be well within the near wake of a turbine. An interesting question to ask was does the wake meandering frequency show a similar dependence on λ even in the far field? Okulov et al. (2014) reported that the wake meandering frequency was a function of operating condition for $1.5 < x/D < 2.5$, beyond which it was found to be invariant of operating condition. However, if wake meandering is to be related to the vortex shedding of the turbine disk, its characteristic frequency should scale similarly with λ or effective porosity everywhere in the wake. To answer this question, a series of experiments (termed as experiment 3 in figure 2.6 and table 2.1) were performed which focused on thin strip-like fields of view at different locations in the flow.

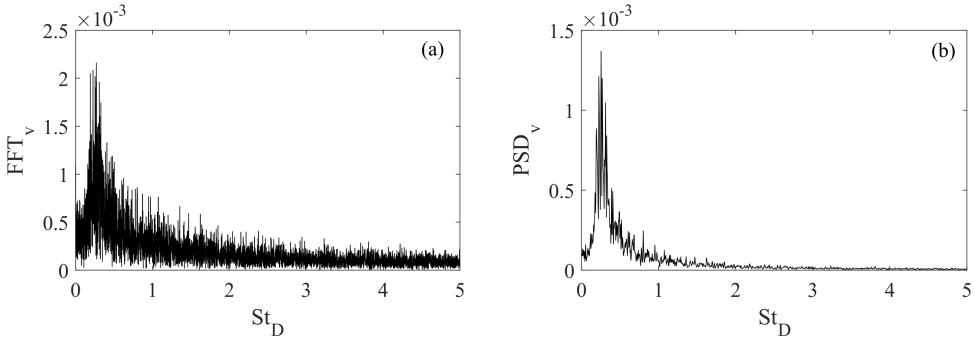


Figure 3.18: Transverse velocity spectra obtained at $x/D = 2$ and $z/D = 0$ for $\lambda = 5.2$ using (a) FFT and (b) Welch's PSD estimation.

For a precise measurement of the wake meandering frequency, a large time series of data was required as wake meandering involves rather slow dynamics. A strip FOV was therefore deployed which allowed a long time series ($\approx$ 15 minutes or $\approx$ 180 wake meandering cycles) of data considering the storage constraints of the cameras used. The FOVs were centred at three different locations, $x/D = 2$, 3 and 5. Experiments were conducted at 16 tip speed ratios from 4.5 to 6 in steps of 0.1. The acquisition frequency (f_{aq}) of the experiments was reduced

to 10 Hz. The spectra were obtained at the local geometric centreline. As was seen from the frequency maps, the centreline region was dominated by low frequency dynamics and the effect of the tip vortices was negligible in this region. Therefore, the lower f_{aq} was believed to be large enough to properly capture the dynamics of the wake in this region. This is further verified in the following section. To reduce noise, the spectra were obtained using Welch's PSD estimator (Welch, 1967). The number of windows used in Welch's PSD estimator was varied for each λ tested to ensure that there was a robust detection of a single spectral peak that could be ascribed to the wake meandering. As an example, the spectrum for $\lambda = 5.2$ at $x/D = 2$ and $z/D = 0$ is shown in figure 3.18. The Strouhal numbers of wake meandering, St_{wm} (defined based on D and U_∞) obtained at different locations are shown in figure 3.19. A decreasing trend of wake meandering Strouhal number with λ is observed at all three locations. This result establishes that wake meandering in a wind turbine wake is related to the global vortex shedding mode of a porous bluff body, the frequency of which depends on λ (*i.e.* porosity). It is however possible that background turbulence can significantly affect wake meandering (this will be discussed in chapters 4 and 7). Nevertheless, wake meandering is shown to exist even in the absence of freestream turbulence. The fact that Okulov et al. (2014) found wake meandering St to be invariant to operating condition beyond $x/D \approx 2.5$ could be due to the long arm like nacelle (which was longer than the turbine diameter) in their turbine (see figure 1.4 in chapter 1), which could have significantly altered the far field boundary conditions around the central wake region where wake meandering is found to be the strongest in the present study. It could also be that their frequency resolution was not good enough to capture minute changes in the wake meandering frequency (they could only capture ≈ 23 wake meandering cycles at the highest U_∞ considered, while the current work used data corresponding to ≈ 180 wake meandering cycles).

To check if reducing f_{aq} to 10 Hz had an aliasing effect on the spectra, data from other experiments at higher f_{aq} was used. Experiment 4 obtained data in a strip region in the central region of the wake (see figure 2.6). The acquisition frequency was 100 Hz and the data was available for $\approx 219s$ (≈ 44 wake meandering cycles). The data is undersampled at frequencies down to 10 Hz and the corresponding power spectra at $x/D = 4$ and $y/D = 0$ are shown in Figure 3.20 for $\lambda = 6$. The dominant wake meandering peak (and the nature of the spectrum in general) remains unchanged even at the lowest f_{aq} (10 Hz). Note that the data used to produce figure

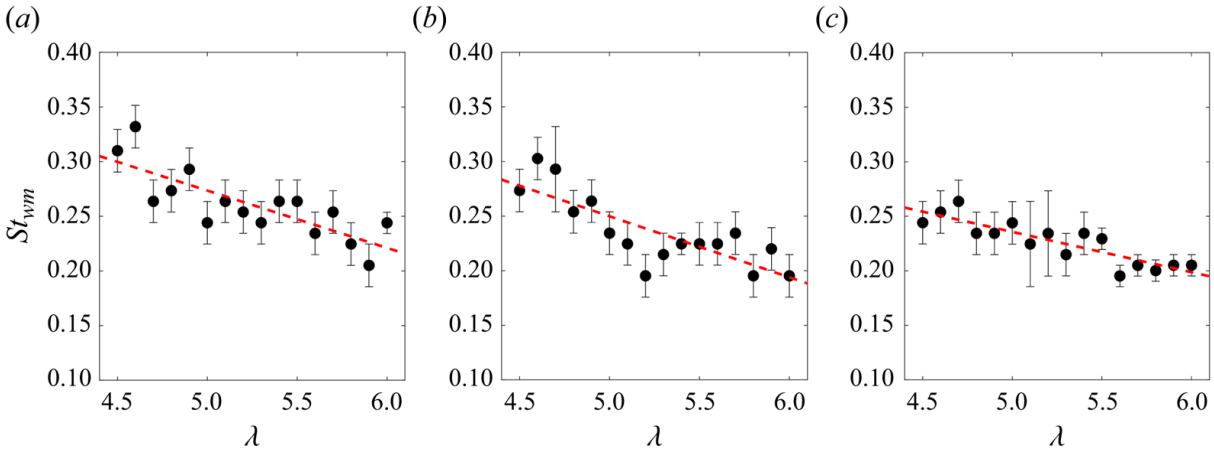


Figure 3.19: Variation of wake meandering Strouhal number with λ at (a) $x/D = 2$, (b) $x/D = 3$, and (c) $x/D = 5$. '- -' shows the linear best fit lines.

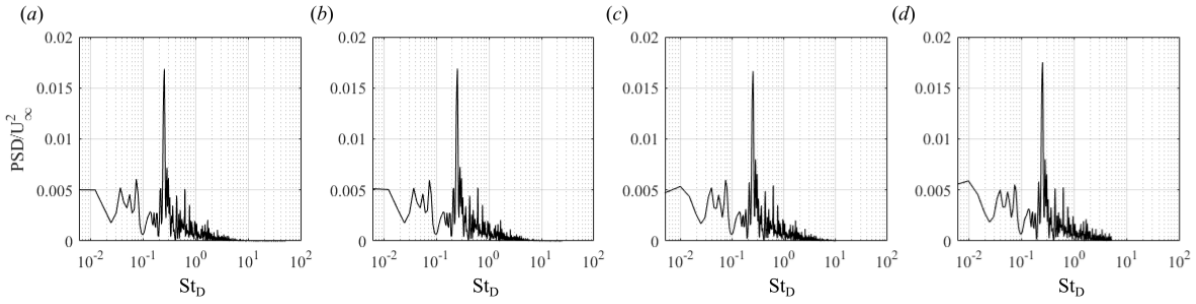


Figure 3.20: Power spectra obtained using the Welch's PSD estimation at $x/D = 4$ and $y/D = 0$ from experiment 4 for $\lambda = 6$. (a) is obtained using the entire time series *i.e.* with the data sampled at 100 Hz. In (b-d) the data is down sampled at (b) 50 Hz, (c) 20 Hz and (d) 10 Hz. The length of the windows used in the PSD estimation was fixed to $N/2$ for all the cases, where N is the time series length in the corresponding case.

3.19 (experiment 3) were acquired at $f_{aq} = 10$ Hz for a much longer period ($\approx 900s$) suggesting that there were no significant effects of aliasing on the spectra.

The importance of the nacelle in the genesis of wake meandering has rather recently been highlighted in several works (Howard et al., 2015; Foti et al., 2016, 2018). Howard et al. (2015) noted the nacelle provides an important perturbation to initiate wake meandering. The importance of the nacelle is also realized in the present study as wake meandering initiates from the vicinity of the nacelle. Wake meandering therefore seems to be a global instability mode akin to regular vortex shedding from a porous body of characteristic length scale D that may require initiation via a perturbation wrought by the vortex shedding from the nacelle (i.e. a region of 0% porosity in the centre of the wake-generating body).

Another interesting question to ask is, upon what does wake meandering depend more: the porosity of the turbine disk or the thrust coefficient, or both? It is not trivial to distinguish the separate effects of blockage of mass (porosity) and momentum (C_T) as both change with λ. Medici and Alfredsson (2008) showed that wake meandering frequency depends on C_T. They performed experiments on turbines with different numbers of blades. Interestingly, for the turbine with a single blade, they did not observe wake meandering at all, although the corresponding thrust coefficient was high. At similar thrust coefficients they however observed wake meandering for 2 and 3 bladed turbines. Accordingly, for wake meandering to be present both porosity and C_T are likely important.

To further understand the nature of wake meandering, especially in the absence of freestream turbulence, linear stability analysis (e.g. (Iungo et al., 2013)) could be a useful tool. Determining the growth rate of the wake meandering mode could aid in understanding the observed dominance of wake meandering over $3f_r$ beyond $x \approx 3L_c$. However, as shown in figure 3.4 the mean velocity field in the near wake is complex, non-axisymmetric, and spatially varying meaning that linear stability analysis of such a base flow is non-trivial. Modelling the wind turbine as a porous object could be useful but this would require matching of both the porosity and the thrust coefficient, as both are likely important parameters. Additionally, the radial distribution of the inhomogeneous porosity likely plays an important role since the nacelle has been shown to be important in the genesis of wake meandering (Howard et al., 2015).

3.7 Conclusion

The near field of the wind turbine model was found to be dominated by several frequencies, such as the ones related to the tip vortices, vortex sheddings from the tower and nacelle as well as large scale wake meandering motion. The array of the coherent tip vortices along the outer edge of the wake appeared to be inhibiting mixing with the outer non-turbulent fluid in the immediate near wake, before they ultimately merged. The merging and the breakdown process of the tip vortices was found to be strongly dependent on λ. To be precise, for $\lambda = 4.5$, a two-step merging process was observed as reported in previous studies (Felli et al., 2011; Sherry et al., 2013a). For $\lambda = 6$ however, there was an earlier and stronger interaction between the tip

vortices and the vortices appeared to merge directly in a one-step process.

A new way of defining the near wake based on the relative strength of the tip vortices (signature of the near wake) and wake meandering (signature of the far wake) was proposed. A length scale termed as the convective pitch ($L_c = \pi D/\lambda$, D being the diameter) was proposed that varies with λ and is related to the pitch of a helical vortex filament. The distance from the rotor plane to the location where the strength of the wake meandering surpassed that of the tip vortices was found to be close to $3L_c$ for all the tip speed ratios tested. This indicates that a distance of $3L_c$ from the rotor disk could be used as a robust definition of the immediate near wake (where the effect of tip vortices are important) of the turbine irrespective of tip speed ratio, at least when freestream turbulence level is low.

The tower frequency was observed over a broad region and it could even be the dominant frequency in the near field for the present experimental condition. Below the nacelle ($y < 0$), the interaction of the tip vortices with the tower resulted in an earlier breakdown of the tip vortices and increased levels of turbulence and mixing. Indeed, the tower acted as the major source of asymmetry in the wake also evident by a deflection of the wake centerline towards the tower side ($y < 0$).

The nacelle frequency was important only very close to the nacelle and was not particularly energetic. However, the nacelle was found to be important in 'seeding' wake meandering, indicated by the presence of the wake meandering frequency close to the nacelle ($x/D < 0.5$). A plausible role of the nacelle in aiding wake meandering, combined with the fact that free stream turbulence levels were negligible in the present experiments, uphold wake meandering as a global instability of the turbine wake, the characteristic of which should vary with operating condition. In order to justify this, separate experiments were performed to calculate the wake meandering frequency at three different streamwise locations, $x/D = 2, 3$ and 5 for $4.5 \leq \lambda \leq 6$. The Strouhal number of wake meandering was found to decrease when λ was increased (or effective porosity was decreased) at all three streamwise stations probed in a similar fashion. Interestingly, a similar decreasing trend of Strouhal number with porosity was observed for vortex shedding behind a porous plate (Castro, 1971). This similarity bolsters the notion that wake meandering is a global instability of the wake generating body, *i.e.* a 'porous' turbine with characteristic length

scale D and is in contrast to the previous works who found wake meandering frequency to be invariant to operating condition in the far wake (Okulov et al., 2014).

Chapter 4

Effect of freestream turbulence on the near wake coherent dynamics

4.1 Introduction

In chapter 3 the frequencies in the near wake of a wind turbine model were discussed in the absence of any added freestream turbulence (FST). In this chapter, the effects of FST on the dynamic properties of the wake are discussed. 9 FST cases were explored including a non-turbulent case for the tip speed ratio based on U_∞, $\lambda_\infty = 6$. The specifications of these experiments are detailed in chapter 2 (see table 2.2).

4.1.1 Test cases

Different FST test cases were obtained by using different passive turbulence generating grids. Separate PIV experiments were conducted to characterise the variation of turbulence intensity (T_i), integral length scales (L_v) and the mean streamwise velocity as a function of streamwise distance from the grids (see chapter 2 for details). The parametric space (spanned by T_i and L_v) in this study is shown in figure 4.1(a). Specific symbols are used for certain types of grids. The symbols represent the value of T_i and L_v at the hub height, while the error bars show the maximum and minimum values observed within the transverse span of the field of view which

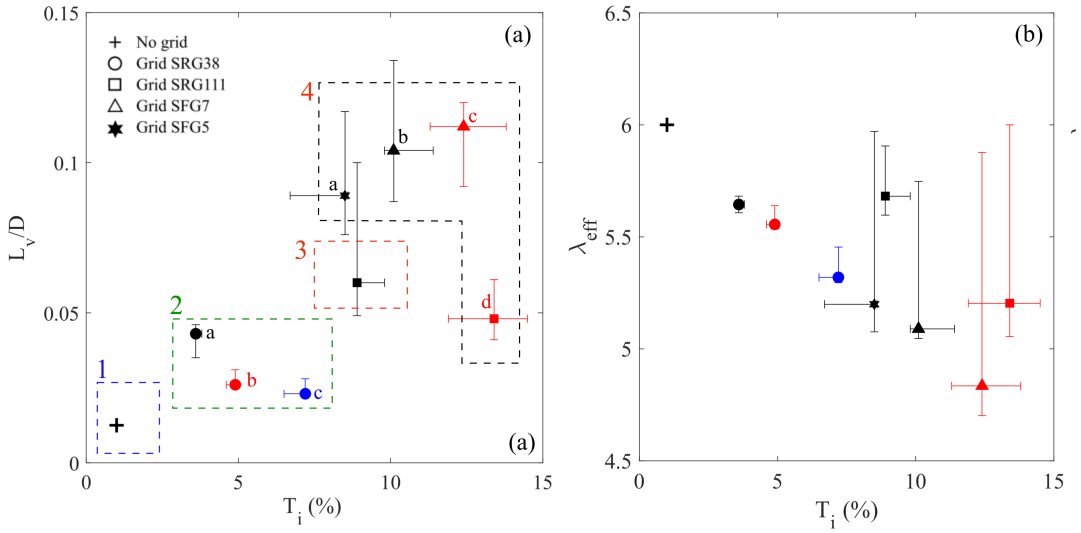


Figure 4.1: (a) Parameter space of turbulence intensity (T_i) and integral length scale (L_v) produced by different turbulence generating grids. (b) shows the effective tip speed ratios (λ_{eff}) for $\lambda_\infty = 6$.

was close to the rotor diameter (see the transverse variations of T_i and L_v in figures 2.10 and 2.12 respectively). Similarly, the grids introduce a blockage to the freestream, resulting in an acceleration of the incoming flow. The variation of mean streamwise velocity behind the grids was shown in figure 2.9. Although the tip speed ratio based on U_∞ (denoted as λ_∞) was kept constant at 6 for all the FST cases, due to the blockage induced increment of the freestream velocity, the effective tip speed ratio (λ_{eff}) reduced for all the FST cases. λ_{eff} for the different cases are shown in figure 4.1(b). The test cases are divided into 4 subgroups, primarily based on turbulence intensity. These groups are enclosed in figure 4.1(a) with the dashed lines. Group 1 has negligible T_i while groups 2, 3 and 4 have low, mild and high T_i respectively. This classification will be further justified in the upcoming sections based on the strength of the frequencies observed in the near wake.

4.2 Vorticity field

Instantaneous vorticity fields for 4 cases from each subgroup (increasing turbulence intensity) are shown in figure 4.2 for $\lambda_\infty = 6$ (see also supplementary videos 7-10[†]). For case 1, the tip vortices undergo merging at $x/D \approx 1.5$ similarly to that observed in chapter 3 through different

[†]Please find the supplementary videos here.

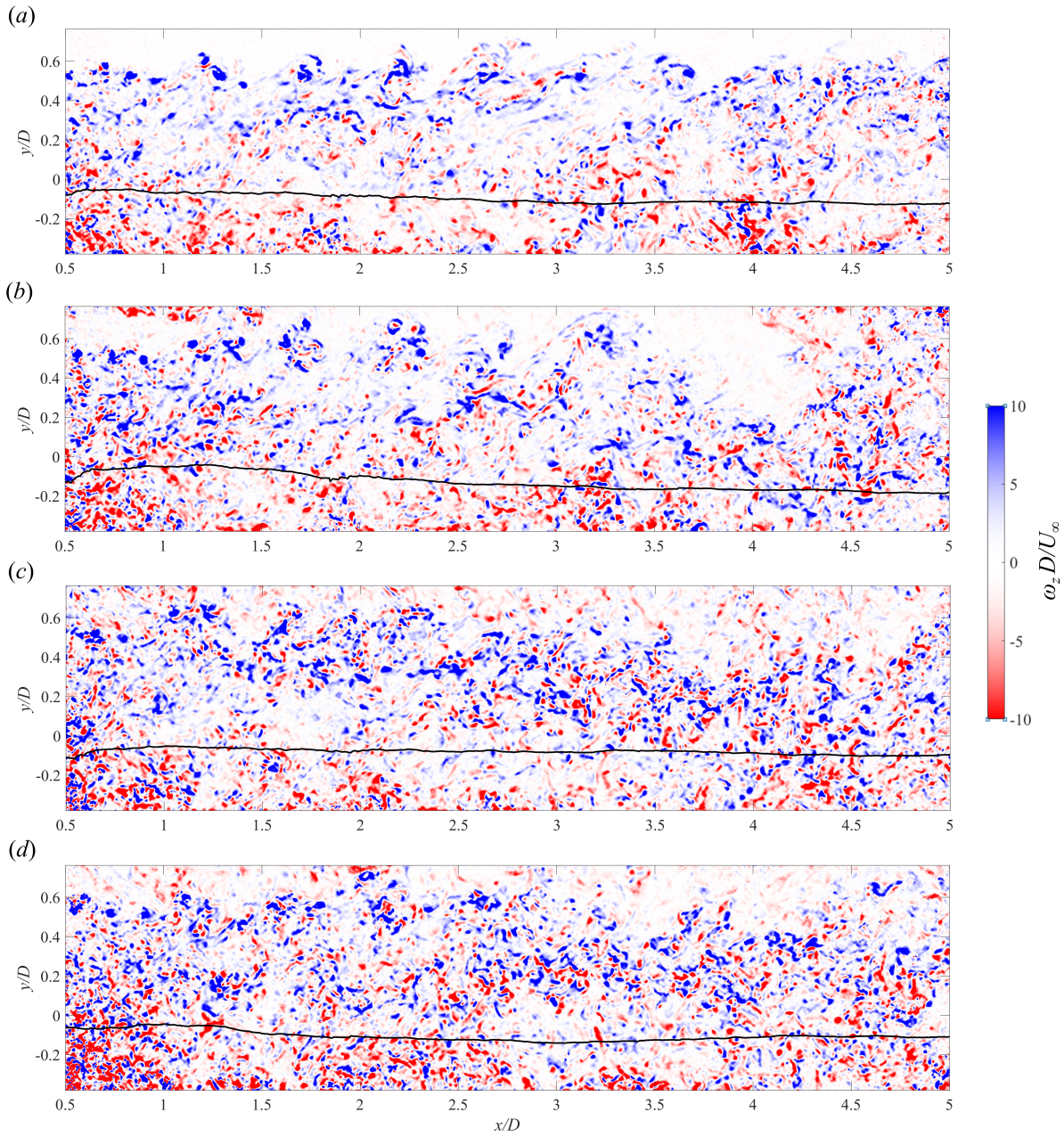


Figure 4.2: Vorticity field for the cases (a) 1, (b) 2a, (c) 3, and (d) 4b.

experiments. Due to the outer fluid being non-turbulent, the wake edge is clearly marked by vorticity in case 1. The solid black line shows the mean wake centreline $y = y_c$ obtained by averaging over instantaneous wake centrelines (the loci of the minima in the instantaneous streamwise velocity profiles). The centreline bends towards the $y < 0$ side due to the presence of the tower as was also discussed in chapter 3. For low T_i (case 2), tip vortices and their merging are still observed, however the trajectories of both the individual and merged vortices appear more erratic. Large scale structures from the freestream penetrate deep into the wake,

close to the wake centreline (see supplementary video 8). As T_i is increased further, the tip vortices break down much closer to the turbine as reported in previous studies (Chamorro and Porté-Agel, 2009; Wu and Porté-Agel, 2012; Gambuzza and Ganapathisubramani, 2023). The presence of background turbulence makes it difficult to visually identify the wake edge for both medium and high T_i cases.

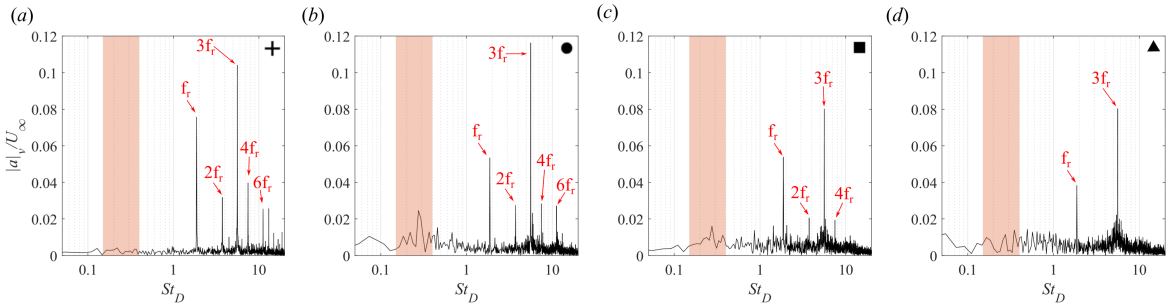


Figure 4.3: Spectra at $x/D = 0.5$ and $y/D = 0.55$ for the cases (a) 1, (b) 2a, (c) 3, and (d) 4b.

4.3 Effect of freestream turbulence on the important frequencies

In order to further understand the effect of FST on the different frequencies, the transverse velocity spectra (obtained using FFT) in the tip region of near wake ($x/D = 0.5$, $y/D = 0.55$) are first shown in figure 4.3(a-d). The symbols in the top right corner correspond to the different FST cases shown in figure 4.1(a). For all the FST cases, the dominant frequency is $3f_r$, where f_r is the turbine's rotational frequency. $3f_r$ therefore denotes the frequency of the tip vortices for a three-bladed turbine. Apart from $3f_r$, f_r is also found to be important and is observed in all cases. In chapter 3 multiple harmonics of f_r were reported in the tip region in the absence of freestream turbulence. These harmonics up to $6f_r$ and even beyond are clearly observed for case 1. The orange band in the low frequency region $0.15 \leq St_D \leq 0.4$ shows the typical frequency range of wake meandering reported in previous studies (Medici and Alfredsson, 2008; Okulov et al., 2014; Chamorro et al., 2013). Note from figure 4.3(a) that without any freestream turbulence, the spectral energy content in this wake meandering frequency band (WMFB) is negligible in the tip region of the near wake. Contrastingly, for all the FST cases (case 2-4) non-negligible spectral peaks are observed in the WMFB even in the tip region. Especially, for the case 2a, there is a

clear peak at $St_D \approx 0.27$. This difference highlights the fact that the nature of wake meandering for case 1 is different from the cases with significant levels of freestream turbulence. In chapter 3 the role of the nacelle in the genesis of wake meandering was reported. It was argued that the nacelle's vortex shedding provided an important perturbation that triggered wake meandering in the absence of freestream turbulence (Howard et al., 2015). The phase-averaged mode associated with wake meandering in the absence of freestream turbulence was shown in figure 3.16(b) of chapter 3 for $\lambda_\infty = 6$. From the mode shape as well as from the dominant frequency zones in figure 3.9 it was deduced that wake meandering remains important in the central region of the wake. Although the wake meandering mode grows radially with downstream distance, it does not reach the tip region before $x \approx 3D$. This justifies the absence of spectral peaks in the WMFB observed in figure 4.3(a). In the presence of freestream turbulence (cases 2-4), perturbations are available everywhere unlike case 1 where the nacelle's vortex shedding is the main source of the perturbation. Therefore with FST, wake meandering likely initiates closer to the turbine and the associated mode reaches the tip region earlier. As a result, a non-negligible amount of energy content is present in the WMFB for the FST cases. This will be further discussed in the subsequent paragraphs.

For low T_i (case 2a), most of the harmonics of f_r are observed in the tip region similar to case 1. However, the amplitudes at these frequencies are weaker except $3f_r$, which shows a slightly stronger peak. This could be due to the fact that the freestream velocity for case 2a was slightly higher due to the blockage caused by the grid (see figure 2.9 in chapter 2), therefore bringing λ_{eff} closer to the optimum tip speed ratio (yielding maximum C_p) as can be seen from figure 2.3. For case 3, the harmonics such as $2f_r$ and $4f_r$ are observed, although their amplitudes are significantly diminished. $6f_r$ is no longer observed for case 3. Finally, for the highest T_i case, no distinct frequencies other than f_r and $3f_r$ are observed within the field of view considered here ($x/D \geq 0.5$). These frequencies can however still be present very close to the turbine blades.

Figures 4.4(i,a-d) show the transverse velocity spectra obtained using FFT at $x/D = 4$ and $y/D = 0$ for the same four cases of increasing turbulence intensity. The spectra obtained using FFT looked noisy and it was not directly evident if the spectra in the WMFB were discrete or continuous. Therefore, the power spectra were computed at the same locations using Welch's PSD estimator to reduce the noise. The length of the overlapping windows (w) was varied

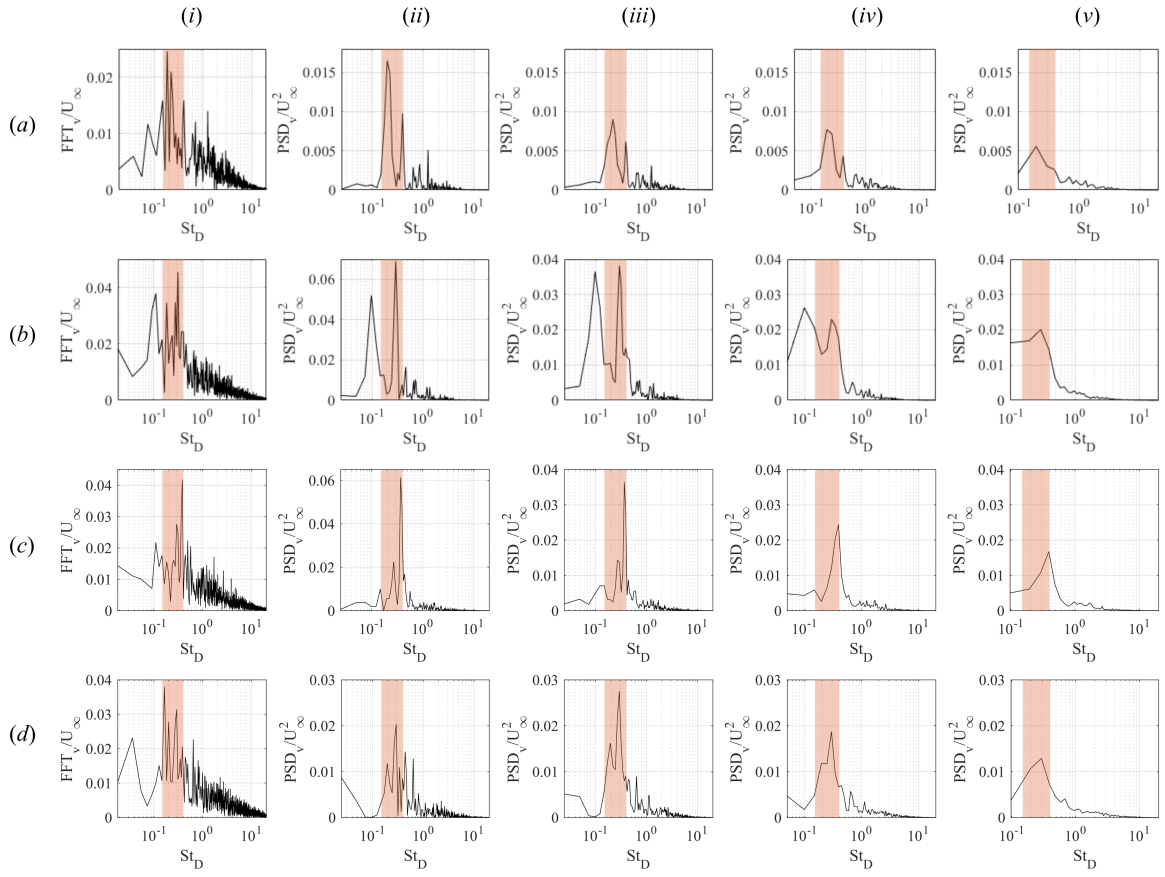


Figure 4.4: Spectra at $x/D = 4$ and $y/D = 0$ for the cases (a) 1, (b) 2a, (c) 3, and (d) 4b. The transverse velocity spectra stacked in column (i) are obtained using FFT. The power spectra in columns (ii) - (v) are obtained using the Pwelch PSD estimator having window lengths (ii) 4000, (iii) 3000, (iv) 2000 and (v) 1000. The total length of the data was 5455 snapshots. The windows had 50% overlap in each case.

during the process to obtain a smoother spectrum. For $w = 4000$ (column *ii* in figure 4.4) and $w = 3000$ (column *iii* in figure 4.4), discrete peaks are clearly observed in and around the WMFB. A smaller window size oversimplified the spectra (see columns *iv* - *v* in figure 4.4). Therefore, further work concerning spectral analysis around WMFB was carried out with a window length of 3000 having a 50% overlap. The no grid case showed a distinct peak in the WMFB at $St_D \approx 0.2$ (figure 4.4(a,*ii-iii*). Another peak was observed at $St_D \approx 0.4$ which is likely a harmonic of the wake meandering mode. Similar peaks were also observed for the cases with FST. In fact, the amplitudes of the peaks were stronger in the presence of FST compared to the case without FST (see columns *ii-iii* in figure 4.4). This is further discussed in the subsequent paragraphs

For a global view of the important frequencies in different parts of the wake, a dominant fre-

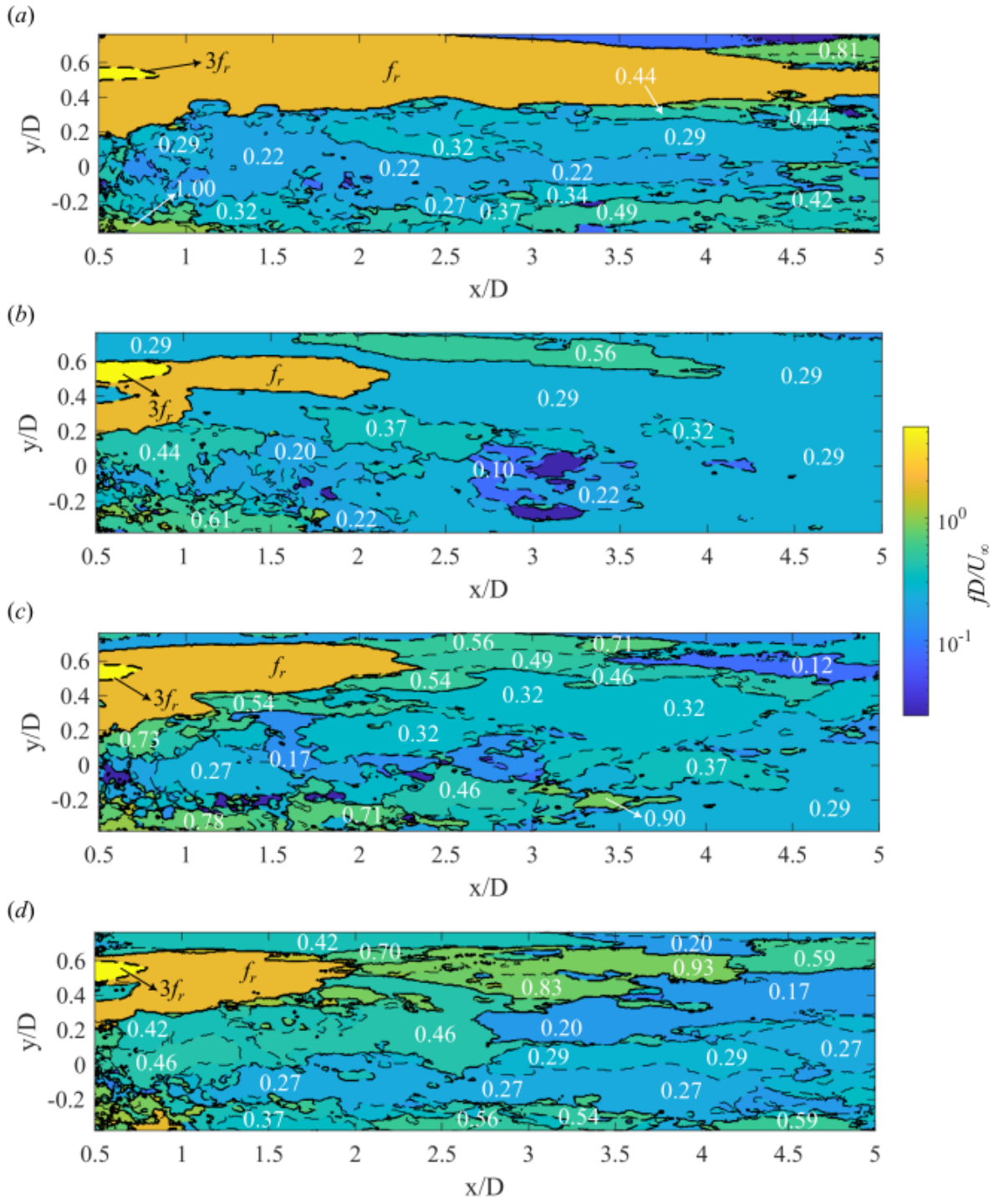


Figure 4.5: Dominant frequency maps for the cases (a) 1, (b) 2a, (c) 3, and (d) 4b obtained from the power spectra. The power spectra are obtained using Pwelch's PSD estimation with a window length of 3000.

quency map is created similar to those in chapter 3. These maps are produced after obtaining the power spectra at all the spatial locations. The window length used in the PSD estimation

was 3000. The map of the non-turbulent case for $\lambda = 6$ is shown in figure 4.5(a). There is a small region close to the tip near the rotor where the tip vortices ($3f_r$) are the strongest. However, they soon interact with each other producing f_r, which remains the dominant frequency in the wake edge even beyond $5D$. The frequencies related to the tip vortices, especially f_r remains dominant in a nearly axisymmetric (apart from the region behind the tower) shell type region which demarcates the inner region from outer background fluid. In the core region, multiple low frequencies dominate in large patches and these frequencies fall in the accepted frequency range of wake meandering. Among these, the largest patch has a Strouhal number ≈ 0.22 and it initiates from near the nacelle. The low frequency zone as a whole expands radially with the downstream distance, similarly to the map shown earlier in chapter 3 through a different experimental campaign.

For the low T_i case, the high frequency shell breaks down much earlier and a connection between background turbulence and the inner core is established beyond $x/D = 2.25$. Although, large patches of frequencies in the WMFB are observed in the wake, the far wake is dominated by a single frequency $St_D \approx 0.29$. The frequency is also available close to the rotor in the tip region. This frequency is the same as the frequency identified as 0.27 using FFT in figure 4.3(b). The slight difference in the frequency is due to the compromised frequency resolution in Welch's PSD estimation. For the cases with medium and high turbulence intensity, the shell gets punctured at a similar location, but many other low frequencies appear in smaller patches, making it look more broadband and turbulent like in the core region as well as at the wake's outer edge.

To elucidate the nature of wake meandering in the presence of FST, power spectra are shown in figure 4.6 with and without the turbine. In each figure set, the first sub figure shows the spectrum in the freestream where the turbine would be placed. The second subfigure shows the spectrum in the turbine wake at a distance of $x/D = 0.5$ from the turbine. The spectra correspond to the same cases as discussed earlier. The energy content in the freestream spectra is the lowest for the no grid case and it increases for the high T_i cases as can be expected. For all the cases in the turbine wake, low frequency peaks can be observed in the central region (near $y = 0$) that correspond to frequencies associated with the nacelle's vortex shedding (f_n) and wake meandering (f_{wm}). For the no grid case, no signature of wake meandering is found in the wake near the tip region. If looked at closely, some non-negligible energy content can

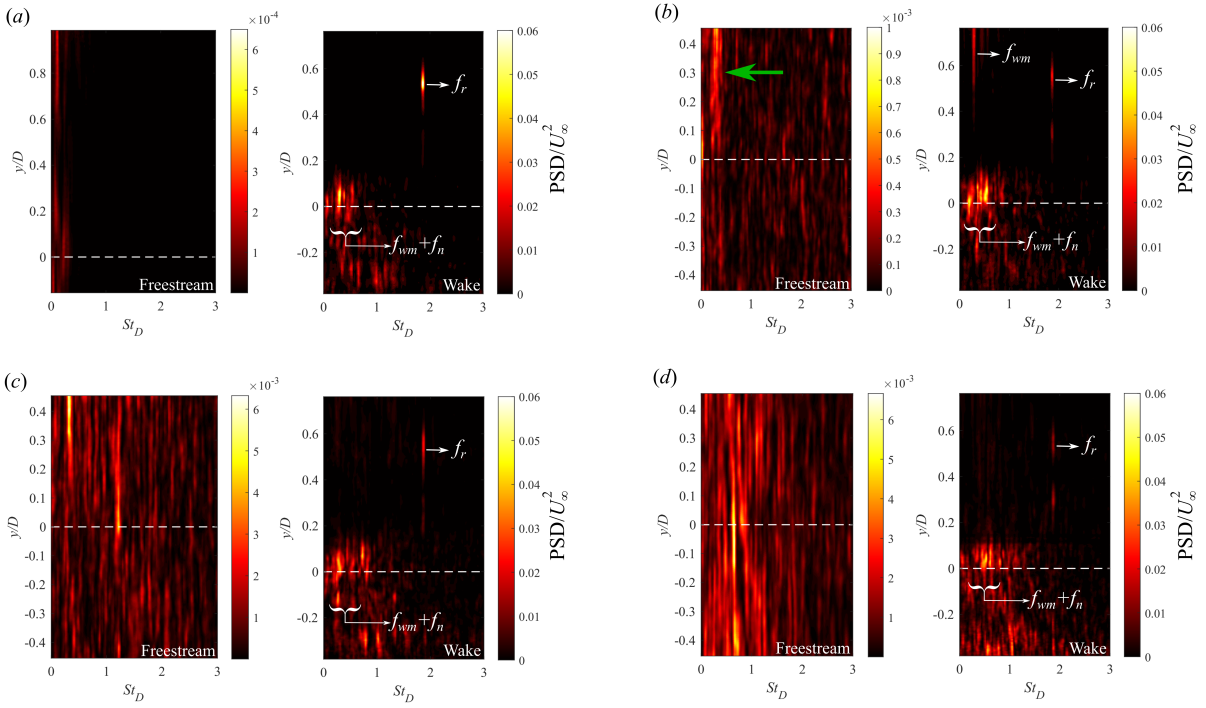


Figure 4.6: Power spectra in the freestream (without the turbine) and in the wake, $0.5D$ downstream of the turbine for (a) no grid case, (b) case 2a, (c) case 3 and (d) case 4b obtained using Pwelch's PSD estimation with a window length of 3000.

be observed in the tip region for cases 3 and 4b. Interestingly, the low T_i case 2a showed the strongest signature of wake meandering in the tip region. When considering the freestream spectrum for case 2a, a significant energy content can be observed in a similar frequency range and at a similar spatial location (see the green arrow in figure 4.6(b)). It appears that these frequencies in the freestream are amplified in the turbine wake. The f_{wm} peak in the tip region was nearly 6 times larger than the strongest peak in the similar frequency range available in the freestream for case 2a. Further, it seems that the turbine does not equally amplify all the frequencies since energy is available over a broader frequency range in the freestream, while in the wake, the peak is narrower. This is in line with the observations of some recent works (Mao and Sørensen, 2018; Heisel et al., 2018; Gupta and Wan, 2019). A similar amplification of the freestream frequencies was also made for another low T_i case 2b (not shown here for brevity). Interestingly, however, such amplification is weak if not non-existent for the medium or high T_i cases although a significant energy content is present in the freestream in the WMFB. Such an effect of elevated T_i is not clearly understood and deserves further investigation.

Another interesting observation from figure 4.6(b) is that there is a spatial discontinuity between

two wake meandering frequencies. One of them is energised by FST towards the outer edge of the wake, and the other one is induced by the nacelle's vortex shedding in the central region. These two different wake meandering frequencies remain separated by the shear layer of the tip vortices in the near wake as can be seen from figure 4.5(b). Only the latter can be observed for the no grid case.

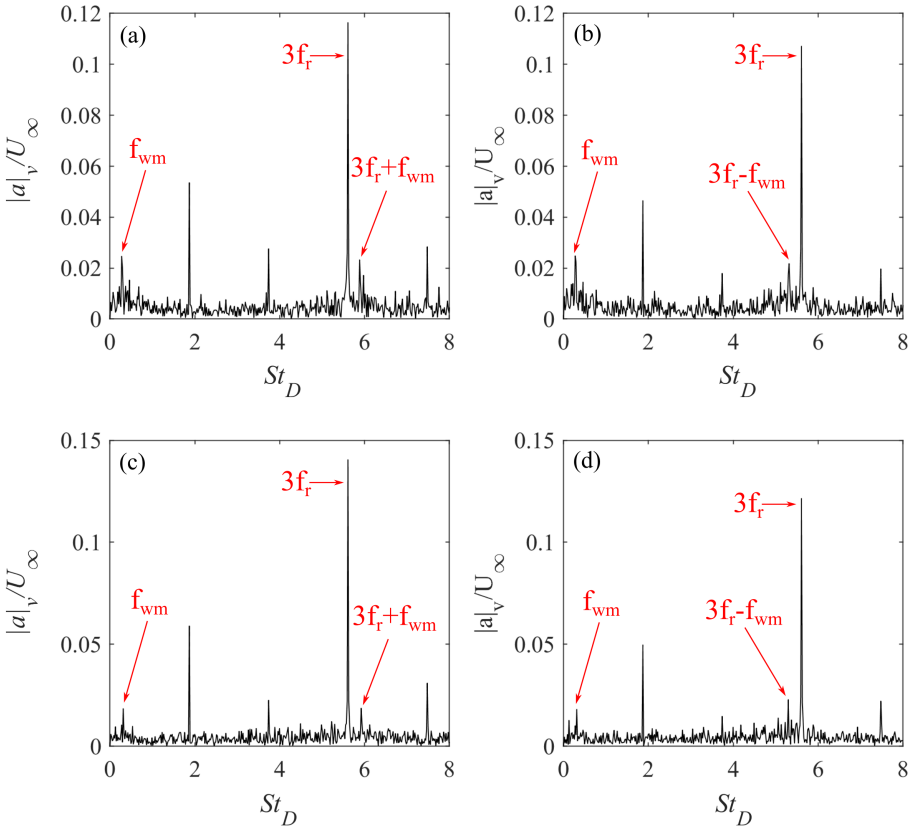


Figure 4.7: Spectra for case 2a at $x/D = 0.5$ and (a) $y/D = 0.55$ and (b) $y/D = 0.53$. Subfigures (c) and (d) show the same for the case 2b.

If looked closely at figure 4.3(b), *i.e* that for the case 2a at $x/D = 0.5$ and $y/D = 0.55$, a new peak can be observed at a frequency slightly higher than $3f_r$. To understand the origin of this peak, the spectra are reproduced on a linear scale in figure 4.7(a). This new frequency was found to be numerically equal to $3f_r + f_{wm}$, where $f_{wm} = 0.27$ is the wake meandering frequency energized by FST. Similarly at $x/D = 0.5$ and $y/D = 0.53$, another new frequency was found which was numerically equal to $3f_r - f_{wm}$. A similar observation was also recorded for the case 2b as shown in figures 4.7(c-d). These frequencies are similar to the secondary frequencies observed in previous studies on multiscale flows involving cylinders/prisms of unequal diameters

(Baj and Buxton, 2017; Cicolin et al., 2021). The secondary frequencies were numerically equal to the sum and difference of the primary shedding frequencies of the two cylinders and were shown to be produced due to the non-linear triadic interaction between the primary frequencies. Whether the same is true for the new frequencies observed here will be explored in chapter 7.

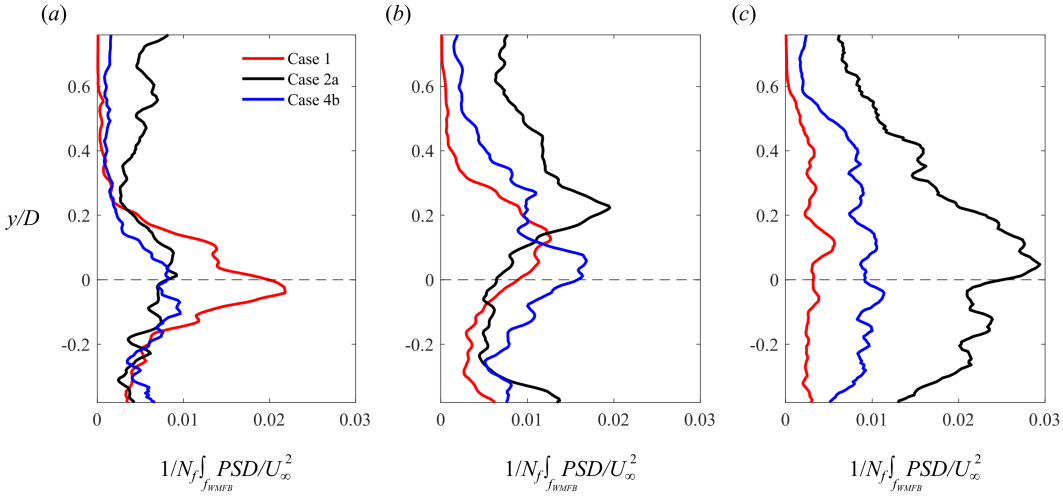


Figure 4.8: Transverse variation of PSD amplitude averaged over WMFB for different FST cases at (a) $x/D = 1$, (b) $x/D = 3$ and (c) $x/D = 5$. Here N_f denotes the number frequencies in the WMFB.

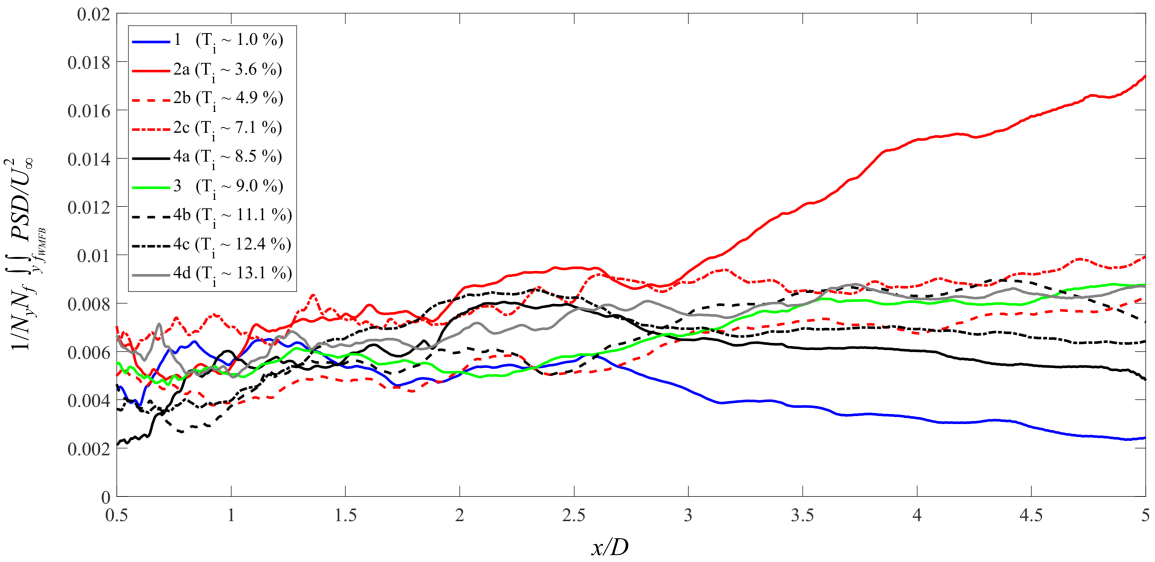


Figure 4.9: PSD amplitudes averaged over WMFB and transverse distance y for different FST cases.

To further understand how the average amplitude of wake meandering varies with FST, the power spectrum at a spatial location is averaged over the frequencies in the WMFB. In chapter 3 the nacelle's shedding frequency at $\lambda = 6$ was found to be around $St_D \approx 0.42$. Therefore, in

order to avoid unwanted contribution from the nacelle's shedding frequency, the averaging was performed over a frequency rage $0.15 \leq St_D \leq 0.37$ (containing $N_f = 10$ resolved frequencies) only. The average wake meandering profiles hence created is first shown at $x/D = 1$ in figure 4.8 for selected cases. In the central part of the wake, where wake meandering is induced by the nacelle's vortex shedding, the wake meandering profile for the no grid case shows the strongest peak. The amplitude thereafter decays in the freestream. For the other cases with FST, the profiles still show a peak in the central region, although diminished, highlighting that wake meandering in the central part is still induced by the nacelle's shedding. Unlike the no grid case however, the FST cases show significant wake meandering amplitudes in the freestream due to the amplification of frequencies from the freestream as discussed earlier. Furthermore, note that in the freestream, the amplitude is the strongest for the low T_i case 2a, not for case 4b which had a higher T_i and higher L_v. This again indicates that T_i and L_v are not the only important parameters, rather the specific nature of the freestream spectrum is important. Further downstream, wake meandering for the no grid case gets weaker while for the other two cases it gets stronger.

To compare all the cases simultaneously, the profiles are further averaged over y and the average amplitudes are shown for all the cases considered here in figure 4.9. Note that nearer the turbine, for $x/D \leq 2.5$, the average wake meandering amplitudes are comparable for all the cases. Beyond $x/D = 2.5$, the differences become more discernible. Wake meandering is the weakest for the no grid case. Further, the amplitude does not increase monotonically with T_i. At the farthest streamwise location, case 2a shows almost twice stronger wake meandering compared to most of the other cases. The other cases showing stronger wake meandering are identified as cases 2c, 4d and 3.

4.4 Extent of the near wake

In chapter 3, the end of the near wake was defined as the location where the strength of wake meandering surpassed that of the tip vortices ($3f_r$). To obtain the strength of a particular frequency f (denoted as S_f) at a particular streamwise location, first the spectra are obtained at all the y locations for the given x location. This gives the amplitudes of a certain frequency f

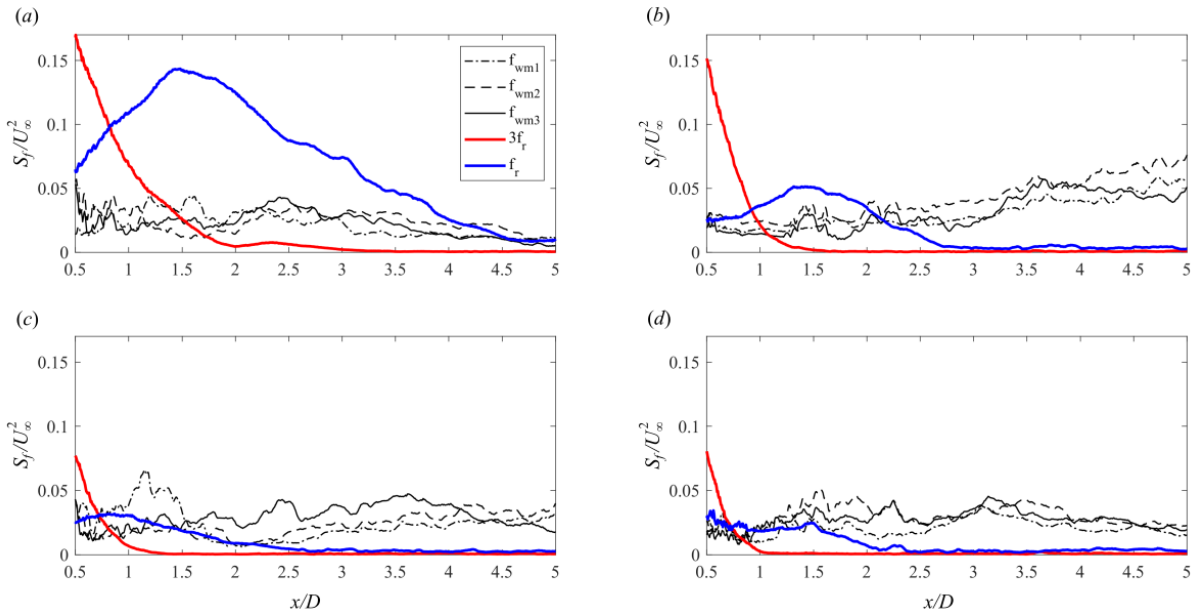


Figure 4.10: Variation of the strength of frequencies for the cases (a) 1, (b) 2a, (c) 3 and (d) 4b.

at all the y locations. The maximum of these amplitudes is denoted as the strength of frequency f or S_f at that particular x location. In this chapter, the spectra were obtained using Welch's PSD estimator (with a window length of 3000) for all the cases unlike chapter 3 where FFT spectra were used. Therefore S_f here is normalised with U_∞^2. As an example, the streamwise variation of S_f for cases 1, 2a, 3 and 4b is shown in figure 4.10. For the tip vortex related frequencies, only the variation of $3f_r$ and f_r is shown. For all the cases, $3f_r$ is the strongest immediately close to the rotor but quickly gets overtaken by f_r. The strength of $3f_r$ reduces with increasing T_i. In the same plot, the strengths of the three strongest wake meandering frequencies in the WMFB are shown. These are identified after summing the amplitude of a particular frequency (obtained from power spectra) everywhere in the domain beyond a cutoff location $x/D = 2$. The cutoff location was so chosen to prioritize the frequencies that contribute the most in the far wake. Nevertheless, the frequency process was verified to be invariant of small changes of the cutoff location.

The strength of three major wake meandering frequencies shown in figure 4.10 surpass that of $3f_r$ at three slightly different locations. From these, the maximum and minimum near wake length is obtained. The average of the two is used as the near wake length and the difference is shown by the error bars in figure 4.11. In chapter 3 the near wake length is measured in terms of the convective pitch L_c defined as $L_c = 2\pi R/\lambda$. This length could be physically interpreted

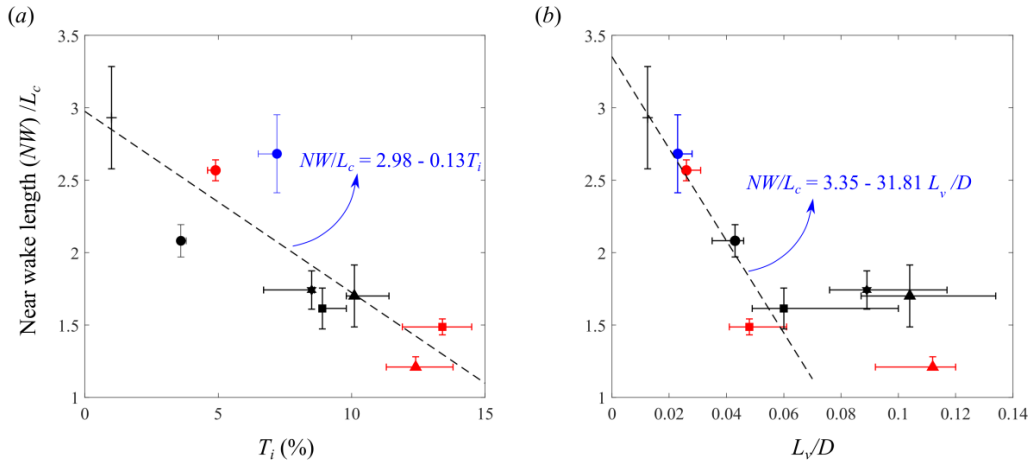


Figure 4.11: Variation of the near wake length with (a) T_i and (b) L_v. The near wake is scaled by L_c. For each case L_c is calculated based on λ_{eff}.

as the distance traveled by a fluid parcel in the freestream in the time taken by the turbine to complete a single revolution. Here L_c is calculated for the FST cases based on λ_{eff}. Through a different experiment, a near wake length of $\approx 3L_c$ is again observed for case 1 (see figure 4.11(a)). Although some scatter is present in the data, a near monotonic reduction in the near wake length can be observed as T_i is increased. In fact, the near wake length seems to scale better with T_i for the higher T_i cases.

The variations with the integral length scales (L_v) are shown in figures 4.11(b) with L_c being calculated based on λ_{eff}. Initially, the near wake length reduces almost linearly as L_v is increased up to a certain threshold, beyond that the rate of reduction slows down and some non-linear trend is observed. It was observed that this threshold length scale was close to the average size of the tip vortices near the turbine. To show this, a phase averaged vorticity field of the tip vortices for the no grid case is shown in figure 4.12. The best fit circle has a diameter $\approx 0.07D$. A best fit line is therefore drawn in figure 4.11(b) up to $L_v/D = 0.07$. This implies that freestream structures smaller than the tip vortices likely hasten the breakdown. In fact, for the cases with $L_v < 0.07D$, the near wake length appears to scale better with L_v than with T_i (see the cases marked by a 'o'). This observation is similar to that observed by Gambuzza and Ganapathisubramani (2023). The authors reported that, for FST with very large length scales, the near wake length increased back to a value close to the non-turbulence case. The authors argued that very large scales modulated the tip vortices rather than breaking them down.

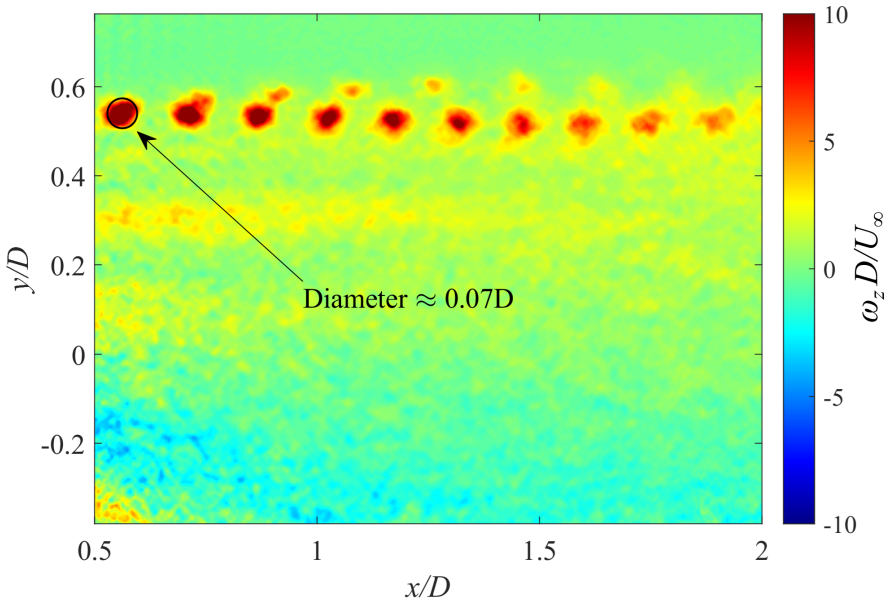


Figure 4.12: Phase averaged vorticity field for $3f_r$ for the no grid case. The fitted circle shows the average size of the tip vortices.

4.5 Conclusions

The effect of freestream turbulence (FST) on the multiscale coherent dynamics in a wind turbine wake was discussed. A total of 9 cases were studied that had varying turbulence intensity (T_i) and integral length scales (L_v). In general the tip vortices were found to break down closer to the turbine in the presence of FST. The nature of wake meandering with and without FST was shown to be different. The amplitudes of wake meandering frequency increased with FST. New secondary frequencies were reported for the first time that were likely produced through non-linear triadic interaction between the tip vortices and wake meandering induced by FST similar to previous studies on multiscale wakes (Baj and Buxton, 2017; Cicolin et al., 2021). This will be further explored in chapter 7. The near wake length was found to depend on both T_i and L_v. On an average, it reduced monotonically with T_i. Interestingly, a stronger dependence of the near wake length on L_v was observed when L_v was smaller than the tip vortices.

Chapter 5

Multiscale triple decomposition and energy budget analysis: a simple flow

5.1 Introduction

An wind turbine wake is inherently multiscale in nature due to the presence of multiple length/time scales that are shed into the flow from the blades, nacelle, tower etc. In chapters 3 and 4 this multiscale nature of wind turbine wakes was discussed in depth and the presence of a large number of important frequencies was shown. Understanding the energy exchanges to and from these frequencies can help develop a deeper understanding of the spatio-temporal development of the wake. To study the energy exchanges, a framework needs to be developed which is best done through a simple (two dimensional) flow. This chapter therefore uses a simple multiscale flow to establish a foundation that will be useful to understand the energy exchanges in a more complex wind turbine wake. The results of this chapter were published in Biswas et al. (2022).

5.2 The simple multiscale flow

The simple multiscale flow consisted of a main cylinder of diameter $D = 0.05$m with a control rod of diameter $d = 0.1D$ mounted at a radial position (R) of $0.7D$ giving a gap of $0.15D$ between the cylinder and the control rod. The PIV data set for this flow was originally obtained by Cicolin

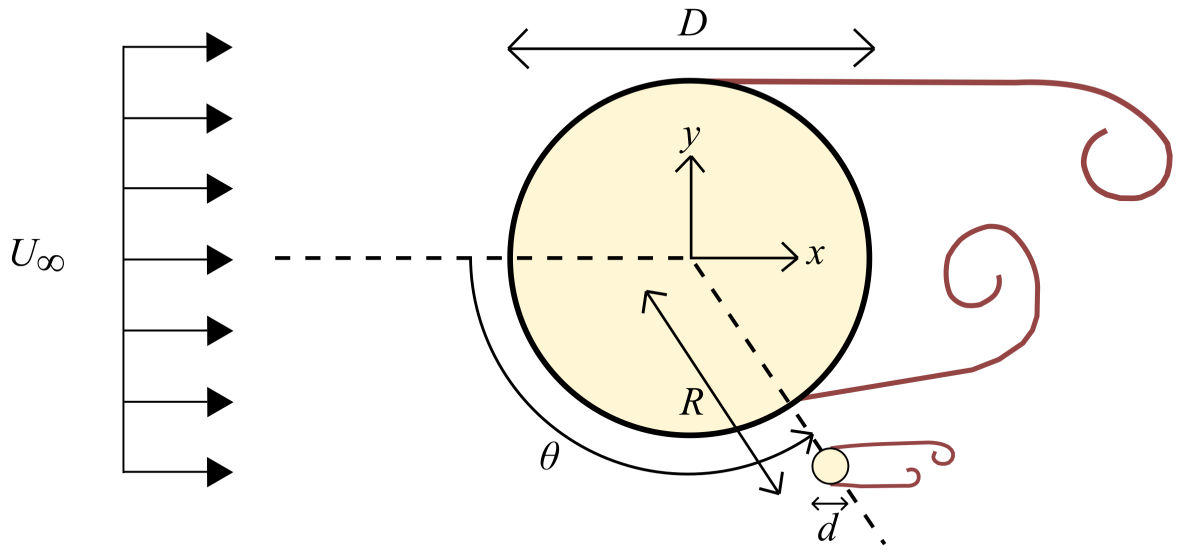


Figure 5.1: A schematic of the main cylinder and control rod assembly.

et al. (2021). A schematic of the main cylinder and control rod assembly is shown in figure 5.1. The freestream velocity (U_∞) was fixed at 0.4m/s giving a Reynolds number $Re_D = 20 \times 10^3$ for the cylinder and $Re_d = 2 \times 10^3$ for the control rod. The PIV measurements were conducted in the mid-sectional plane of the cylinder - control rod assembly. Cicolin et al. (2021) varied the control rod angle (θ) between 90° to 140° and reported three flow states, alongside a bi-stable flow state. Qualitative representations of the flow states are shown in figure 5.2. In state I, *i.e.* $90° \leq \theta \leq 115°$, the main cylinder and the control rod form their own individual wakes. As the main motivation of this chapter is to understand the interaction between the distinct wakes of the cylinder and the control rod, only State I is considered. The data used here was obtained at an acquisition frequency of 70Hz and the total acquisition time was around 42.86s (a total of 3000 snapshots) which is close to 70 and 840 cycles of the main cylinder and control rod shedding respectively. The spatial resolution of the experiments, δ_x is approximately $1.88mm = 0.037D$. This spatial resolution is verified to be sufficient to resolve the coherent structures produced from the control rod (see appendix A.1).

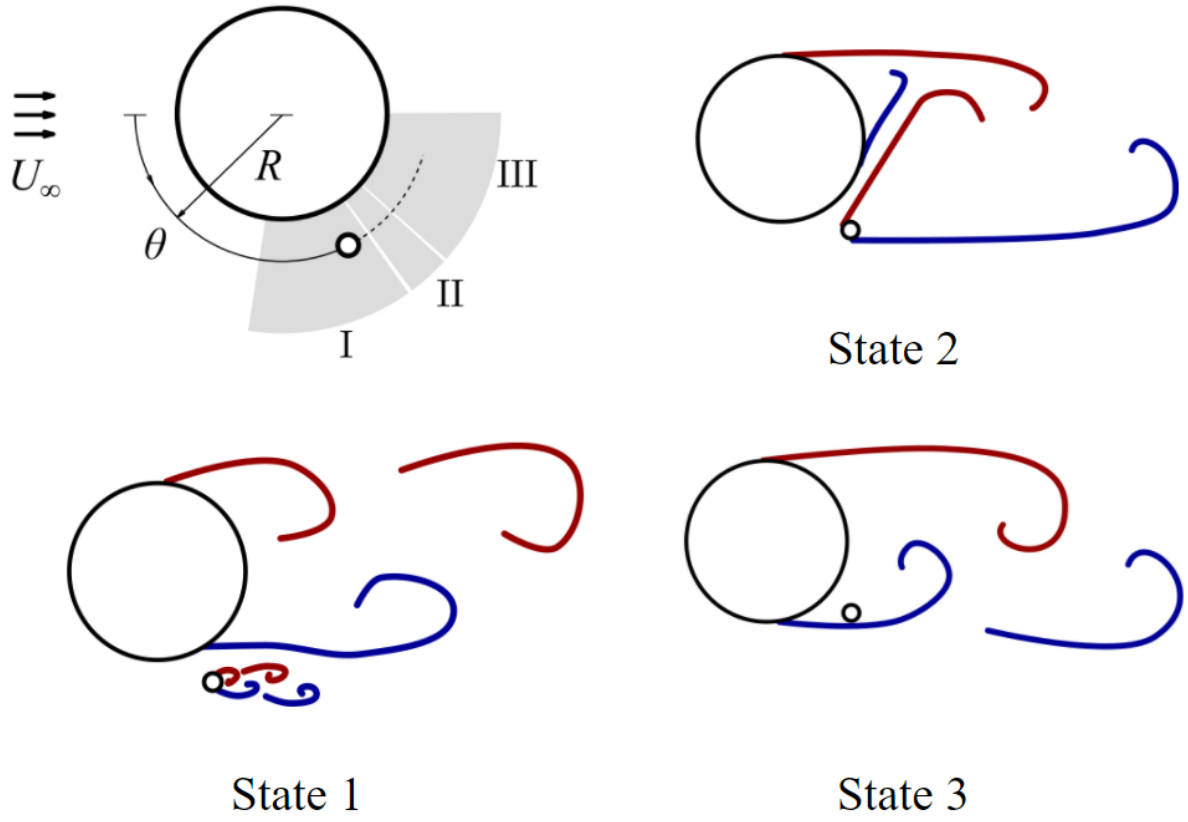


Figure 5.2: Flow states adopted from Cicolin et al. (2021) for the flow past a circular cylinder and a control rod in the range $\theta = 90° - 180°$ and for a fixed radial position $R/D = 0.7$. State I occurs for $90° \leq \theta \leq 115°$, State II for $120° \leq \theta \leq 125°$, and State III for $135° \leq \theta \leq 180°$ at this particular Re. At $\theta = 130°$ the flow develops a bistability between states II and III.

5.2.1 Mean flow properties

First the mean quantities of the flow field are investigated for different control rod positions (θ) in state I. The variation of the mean streamwise velocity field with θ is shown in figure 5.3(a - c). As discussed previously, both the main cylinder and the control rod form distinct wakes. The large recirculating region behind the main cylinder is evident from the region of negative mean streamwise velocity. The wake of the control rod appears to be slightly deflected downwards due to a biased gap flow (Song et al., 2013; Alam et al., 2003) between the control rod and the main cylinder. Similar wake deflections of small and medium rectangular prisms adjacent to another large rectangular prism have been reported by Baj and Buxton (2017). In spite of the broadly similar wake structure at different θ, subtle differences can be seen as θ is varied. To facilitate the differences, the extent of the recirculation region defined as $x : \bar{U}(x) = 0$ ($\bar{U}$ being the mean streamwise velocity component) is estimated and is shown by the dashed

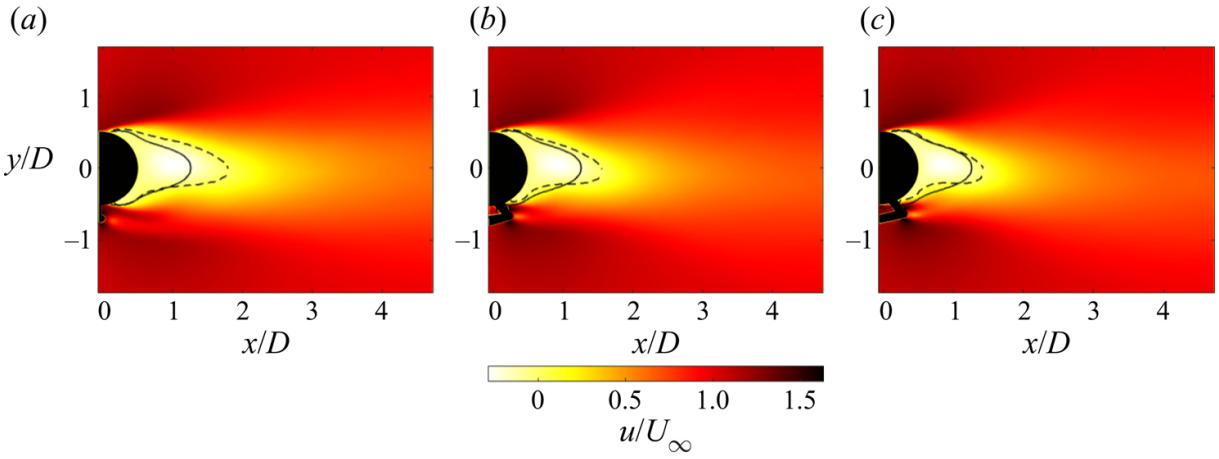


Figure 5.3: Mean streamwise velocity field for (a) $\theta = 90^o$ (b) $\theta = 110^o$ (c) $\theta = 115^o$. The dashed lines depict the extent of the recirculation region for the main cylinder wake in the presence of a control rod, whilst the solid line represents the same for a bare cylinder.

lines for different values of θ. For comparison, the same for the bare cylinder is also shown as a solid line. The recirculation region of the main cylinder wake with a control rod appears elongated compared to the bare cylinder at all control rod angles considered, an observation also reported in previous studies (Bingham et al., 2018; Dalton et al., 2001). Dalton et al. (2001) reported that in the presence of a control rod, the vortex shedding from the main cylinder was shifted slightly downstream, plausibly explaining the longer extent of the recirculation region observed. Additionally, note from figure 5.3 that the streamwise extent of the recirculation region decreases with increasing θ similar to the observation of Dalton et al. (2001). This shortening of the main cylinder's wake at higher θ is interesting as it translates to the fact that increasing θ slightly, changes the location where the wakes interact, which in turn changes the dynamics of the interaction significantly.

To quantify the location of the wake interaction, wake intersection points are defined as the locations where the rms transverse velocity fluctuation field (v_{rms}) forms a saddle, similarly to Baj and Buxton (2017). Wake intersection points have been found to be an important parameter in multiscale generated turbulence (Gomes-Fernandes et al., 2012; Mazellier and Vassilicos, 2010). Mazellier and Vassilicos (2010) showed that the downstream evolution of turbulence statistics scales with the wake intersection length scale for the fractal grids tested. Further, wake intersection points were found to be important in the space scale unfolding (SSU) mechanism first proposed by Laizet and Vassilicos (2012) which yields an enhanced scalar transport in multi-

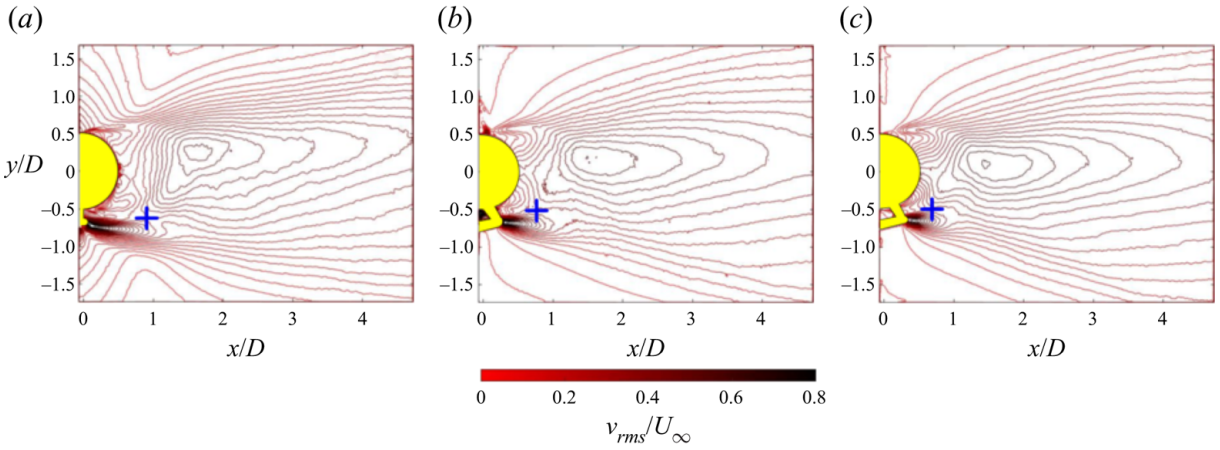


Figure 5.4: Normalised v_{rms} field for (a) $\theta = 90°$ (b) $\theta = 110°$ (c) $\theta = 115°$

scale flows (Laizet and Vassilicos, 2012; Baj and Buxton, 2019). Figures 5.4(a - c) shows the normalised v_{rms} fields for different θ. The wake intersection points are shown as a + sign. The shortening of the main cylinder's wake at larger θ results in an earlier interaction between the two wakes, which is evident from the wake intersection points moving closer to the cylinder - control rod assembly with increasing θ. The streamwise position of the wake intersection points are found to be around $x/D = 0.97, 0.76$ and 0.72 for $\theta = 90°, 110°$ and $115°$ respectively.

5.2.2 Dominant frequencies in the flow field

In order to identify the frequencies of importance, first the evolution of the transverse velocity spectra is presented in figures 5.5 for different θ, at two streamwise positions $x/D = 1$ and $x/D = 2$. The spectra for different θs are also compared with that of the bare cylinder. For the bare cylinder at $x/D = 1$ (figure 5.5(a)), a strong peak can be seen at Strouhal number ($S_t = fD/U_\infty$) around 0.195 (corresponding frequency, $f_b \approx 1.56Hz$) that correlates well with S_t reported in the literature for vortex shedding behind a cylinder at high subcritical Reynolds numbers (Roshko, 1961; Prasad and Williamson, 1997). When a control rod is placed at $\theta = 90°$, the intensity of the main cylinder's shedding mode drops slightly (see figure 5.5(c)) at $x/D = 1$. Further, the Strouhal number reduces to 0.166 (corresponding frequency, $f_m \approx 1.3Hz$), which is around 15% smaller than the bare cylinder's Strouhal number. Such a reduction in the frequency of the main cylinder in the presence of a control rod, or in general another cylinder of comparable diameter, has been reported in the past (Parezanović and Cadot, 2012; Alam et al.,

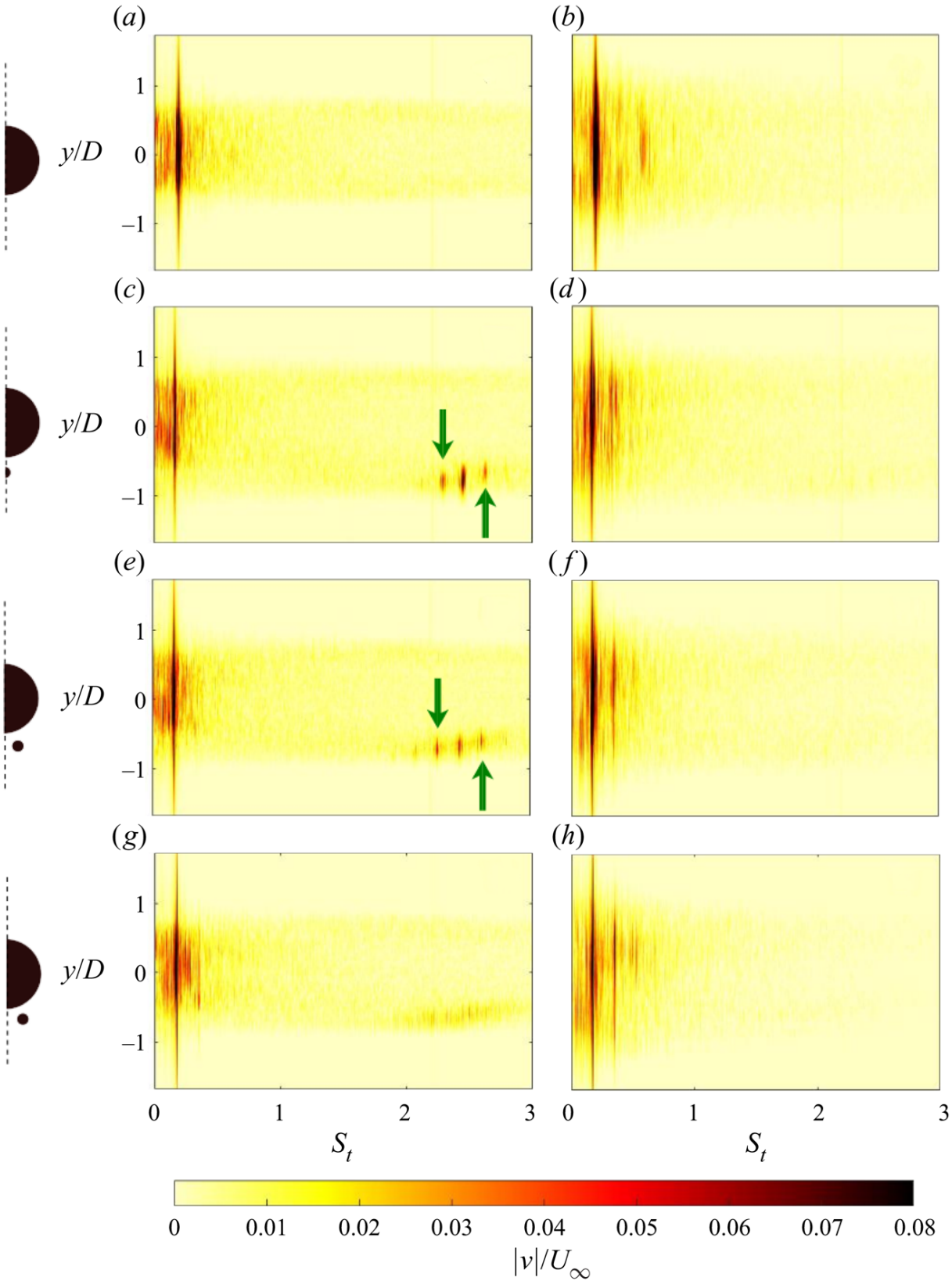


Figure 5.5: Frequency spectra of the transverse velocity fluctuation at $x/D = 1$ (a,c,e,g) and $x/D = 2$ (b,d,f,h) for the bare cylinder (a,b), $\theta = 90°$ (c,d), $\theta = 110°$ (e,f) and $\theta = 115°$ (g,h). Here S_t is the Strouhal number calculated based on the main cylinder's diameter (D) and the freestream velocity (U_∞).

2003; Bearman and Wadcock, 1973; Song et al., 2013; Strykowski and Sreenivasan, 1990). In fact, Parezanović and Cadot (2012) reported a drop of around 15% in the shedding frequency when a control rod of a similar size to the present study was placed at a similar radial and azimuthal position. However, the authors did not report the Strouhal number of the control rod shedding mode for the configuration. A strong peak is observed at $S_t = 2.45$ (corresponding frequency, $f_c \approx 19.6Hz$) in figure 5.5(c) which corresponds to the fundamental shedding mode of the control rod. If S_t is calculated based on the control rod diameter d instead of main cylinder diameter D, then the Strouhal number of the control rod shedding mode comes to around 0.245. This Strouhal number is higher than is typical for a bare cylinder at the control rod-based Reynolds number 2000 (Prasad and Williamson, 1997) as the shedding frequency can be a strong function of the shear of the oncoming flow. Such an increase in the control rod's shedding mode's frequency was also reported by previous studies on two side-by-side cylinders (Alam et al., 2003; Bearman and Wadcock, 1973; Song et al., 2013) who found that a decrease in the frequency of one cylinder was associated with an increase in the other (smaller) cylinder's frequency. However, note that the streamwise velocity upstream of the control rod is higher than U_∞ due to the acceleration of the flow past the cylinder. Hence, the actual Strouhal number of the control rod's shedding mode could be lower than the estimated value if the approach velocity is used to calculate the Strouhal number instead of U_∞.

Interestingly, around the frequency of the control rod's shedding mode, two additional prominent peaks are observed (indicated by green arrows) which correspond to the frequencies $f_c \pm f_m$. These two frequencies are believed to be generated by nonlinear interaction between the main cylinder's and control rod's fundamental frequencies. Whether the modes associated with these two frequencies can be termed "secondary modes" will be justified in section 5.4. Nevertheless, for now these are termed as secondary modes until such a justification is presented. Note that the appearance of secondary frequencies in the wake of a two-circular-cylinder system of unequal yet comparable diameters has been reported in the past (Song et al., 2013; Lam et al., 1993), but their formation mechanisms have not been given much attention until recently (Baj and Buxton, 2017, 2019; Cicolin et al., 2021). In the work by Lam et al. (1993), the secondary frequencies were found to appear in the vicinity of the smaller cylinder wake (see figure 6 of Lam et al. (1993)) which is similar to the current observation. Further, it is noted that the higher

secondary mode (f_c+f_m) is located near the separated shear layer between the main cylinder and the control rod whereas, the lower secondary mode ($f_c - f_m$) resides more towards the opposite separated shear layer of the control rod. Baj and Buxton (2017) recently studied the flow past a multiscale array of rectangular prisms and found exactly the same spatial configuration of secondary modes. This similarity in the spatial organisation of the secondary modes in $f - y$ space (f being frequency and y being transverse distance) in two very different classes of flow, is a remarkable finding and hints at a possible universality in their process of generation.

As θ is increased to 110°, the main cylinder's and the control rod's shedding frequencies remain almost the same as for $\theta = 90°$. The secondary modes are observed at precisely the same combination of frequencies but their intensity (as well as that of the control rod's shedding mode) drops at $x/D = 1$. Finally, the spectral signature of the secondary modes almost disappears at $\theta = 115°$ at $x/D = 1$. This reduction of the intensity of the control rod's shedding mode at higher θ can be expected, as the control rod gets closer to the separated shear layer from the main cylinder at a higher θ, thus facing a reduced oncoming flow velocity. In addition to that, if the rod approaches the separated shear layer, there is limited space and time for the control rods' vortex street to develop before interacting with the main cylinder's wake. Considering these two effects, the shedding modes for the rod at $\theta = 115°$ are expected to be the weakest among all the currently considered cases. Further, the wake formed with the rod at $\theta = 115°$ is on the verge of changing from flow state I to II (see figure 5.2), where the control rod does not present its own vortex street with a distinct frequency. At $x/D = 2$, the spectral signature of the control rod's shedding and the secondary modes disappears for all control rod angles considered and the harmonics of the main cylinder's shedding mode (f_m) become important. These harmonics have been commonly observed in several other studies as well (Parezanović et al., 2015; Parezanović and Cadot, 2012; Jin et al., 2021). It might be possible to observe traces of even higher harmonics at further downstream distances, but only the first two harmonics are considered as most of the energy is contained in them (Jin et al., 2021).

For the sake of completeness a sample time series of data of transverse velocity, and the corresponding spectrum at sample spatial locations, are shown in figure 5.6. The time series in figure 5.6(a) is obtained at $x/D = 1, y/D = -0.7$, which is close to the control rod's wake. The corresponding spectrum in figure 5.6(b) shows f_m, f_c and $f_c \pm f_m$. Figure 5.6(c) shows the time

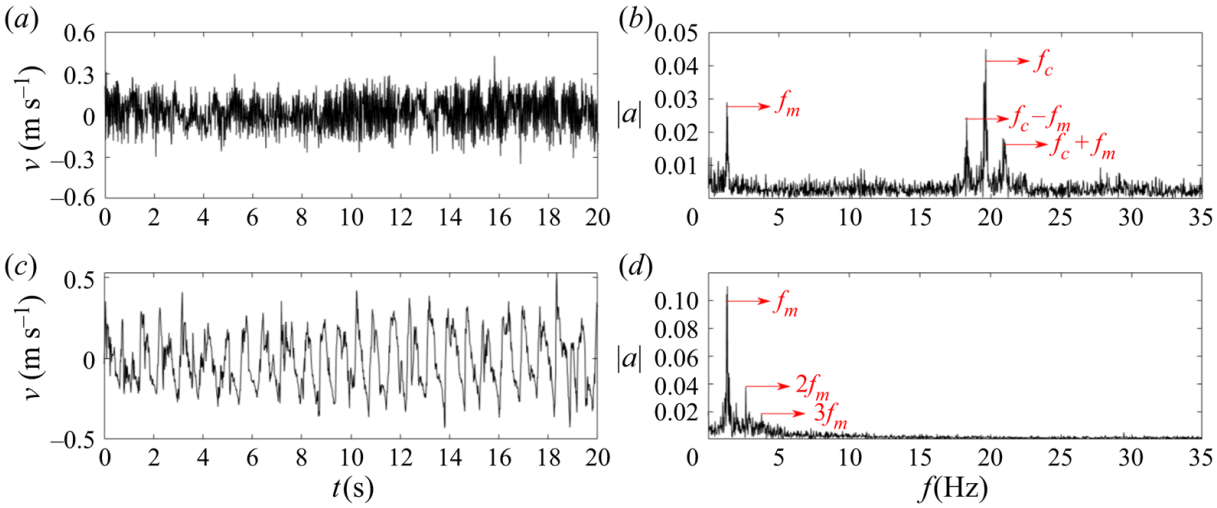


Figure 5.6: (a) transverse velocity time series and (b) corresponding transverse velocity spectra at $x/D = 1, y/D = -0.7$ showing the primary and secondary modes for $\theta = 90°$. (c) transverse velocity time series and (d) corresponding fft spectra at $x/D = 3.5, y/D = 0.35$ showing the main cylinder's shedding mode and the harmonics at the same θ.

series at $x/D = 3, y/D = 0.35$, *i.e.* far from the control rod. The corresponding spectrum in figure 5.6(d) shows f_m and its harmonics.

To quantify the spatial extent and relative importance of the frequencies, the strength of the different frequencies are obtained similar to what was presented in chapter 3 and chapter 4. The spatial evolution of all the frequencies of interest is shown in figure 5.7 for $\theta = 90°$ and 110°. Figure 5.7 reveals a qualitatively similar picture for $\theta = 90°$ and 110°. Close to the main cylinder, at $x/D \approx 0.5$, the amplitudes of f_c and f_m are comparable to each other but f_c quickly falls off as streamwise distance is increased. At $x/D \approx 0.5$, the secondary modes are significantly weaker compared to f_c and f_m and their amplitudes are significant only up to $x/D \approx 1.5$. The short spatial persistence of the secondary modes might explain why they were not observed in many previous experimental studies with similar control rod size to the present case. For instance, Parezanović and Cadot (2012) obtained a frequency spectrum of the flow field at a fixed streamwise distance of $6D$, whilst Parezanović et al. (2015) probed data at $x/D = 1.5$ hence, it is not surprising that the spectral signature of the secondary modes was not captured. Moreover, the bulk of the previous studies on a cylinder with a control rod have been performed at relatively low Reynolds numbers (Strykowski and Sreenivasan, 1990; Yildirim et al., 2010; Mittal and Raghuvanshi, 2001) where vortex shedding from the control rod does not initiate at all. At $\theta = 90°$, a clear dominance of the lower secondary mode ($f_c - f_m$) can be seen over

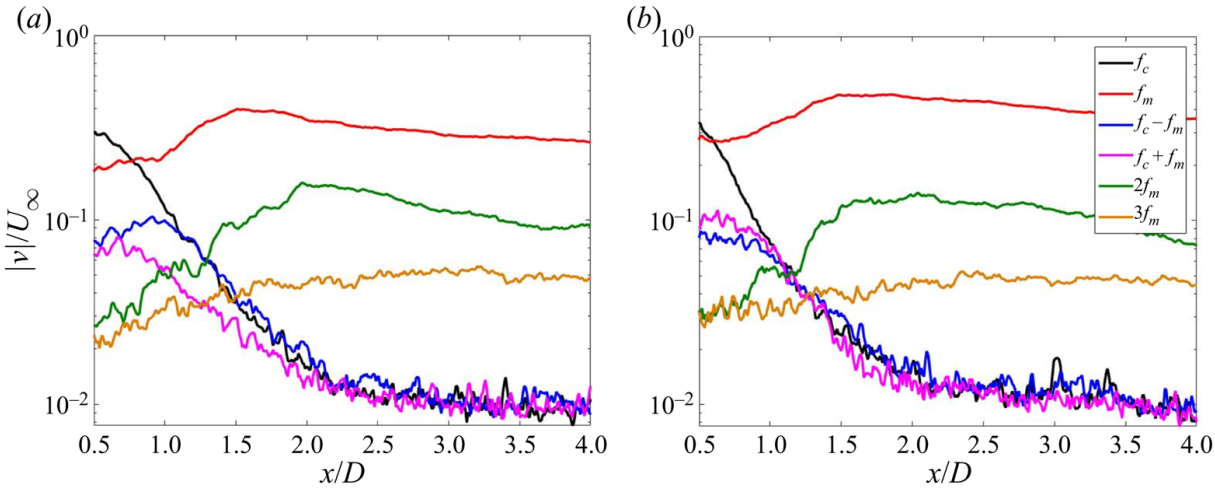


Figure 5.7: Streamwise evolution of the maximum normalised spectral peak of the transverse velocity associated with different modes for (a) $\theta = 90°$ and (b) $\theta = 110°$.

the higher secondary mode ($f_c + f_m$). This observation correlates well with the observations of Baj and Buxton (2017), who found that the low-frequency secondary modes were more spatially persistent than their high-frequency counterpart. Although $f_c - f_m$ has a lower amplitude than $f_c + f_m$ for $\theta = 110°$ at $x/D < 1$, $f_c - f_m$ does remain more persistent. Unlike f_c and the secondary modes, the amplitudes of f_m and its harmonics grow with streamwise distance. f_m reaches its peak at $x/D \approx 1.5$ for both values of θ, which correlates well with the streamwise location of maximum turbulence intensity reported by Cicolin et al. (2021). However, note that the amplitude of the main cylinder's shedding mode is almost twice as large for $\theta = 110°$ compared to $\theta = 90°$. This observation ties well with the reduced fluctuating forces observed for $\theta = 90°$ compared to $\theta = 110^o$ (Cicolin et al., 2021). In the next sections, the spatio-temporal structure of the modes associated with each of the frequencies discussed above is identified and their formation, relative strength, spatial extent and mutual interaction is studied using the coherent kinetic energy budget equations.

5.3 Multiscale triple decomposition: extraction of coherent structures

The dynamics of the length/time scales in a multiscale flow can be better understood by distinguishing the coherent modes associated with each of them. As was discussed in chapter 1, this

can be achieved through a multi-scale triple decomposition of the velocity field $\boldsymbol{u}(\boldsymbol{x},t)$ (where $\boldsymbol{x}$ and t denote space and time respectively) in the following form

$$\boldsymbol{u}(\boldsymbol{x},t) = \bar{\boldsymbol{u}}(\boldsymbol{x}) + \sum_{l} \tilde{\boldsymbol{u}}_l(\boldsymbol{x},t) + \boldsymbol{u}^{''}(\boldsymbol{x},t) \tag{5.1}$$

Here $\bar{\boldsymbol{u}}(\boldsymbol{x})$ is the mean component, $\boldsymbol{u}^{''}(\boldsymbol{x},t)$ is the stochastic component and $\sum_l \tilde{\boldsymbol{u}}_l(\boldsymbol{x},t)$ represents the sum of velocity fields corresponding to individual coherent structures in the flow. The coherent modes ($\tilde{\boldsymbol{u}}_l$) are extracted using Optimal Mode Decomposition (OMD) (Baj et al., 2015; Baj and Buxton, 2017). As the flow field is real valued, the OMD modes are either real or appear in a complex conjugate pair, say ϕ_{OMD} and ϕ^T_{OMD}. The spatio-temporal velocity field associated with a mode is then obtained by a linear combination of ϕ_{OMD} and ϕ^T_{OMD}, both multiplied by the associated time varying complex coefficients (see Baj and Buxton (2017); Baj et al. (2015) for details). The coefficients are obtained by projecting the snapshots onto ϕ_{OMD} and ϕ^T_{OMD} and it is worth noting that the projection method is not trivial. For the present problem in particular, where there are coherent motions quite closely spaced in the frequency domain (see the control rod's shedding mode and secondary modes in figures 5.5(c),(e)), projecting the snapshots onto a single mode corrupted the spectrum of the coefficient with the spectral signature of other closely spaced modes. The issue could be resolved by projecting onto all of the modes of physical relevance simultaneously. Finally, the coefficients are filtered using a band pass filter similar to Baj et al. (2015). Baj et al. (2015) also compared the performance of OMD with proper orthogonal decomposition (POD) which has also been extensively used to extract coherent modes (Berkooz et al., 1993; Dipankar et al., 2007). The authors found that POD was incapable of correctly identifying the mode shapes further downstream from a multiscale wake-generating body while OMD could identify the modes correctly. Although for the present analysis OMD and POD produce similar mode shapes, to be consistent with the previously published work, OMD is utilised to perform the multiscale triple decomposition.

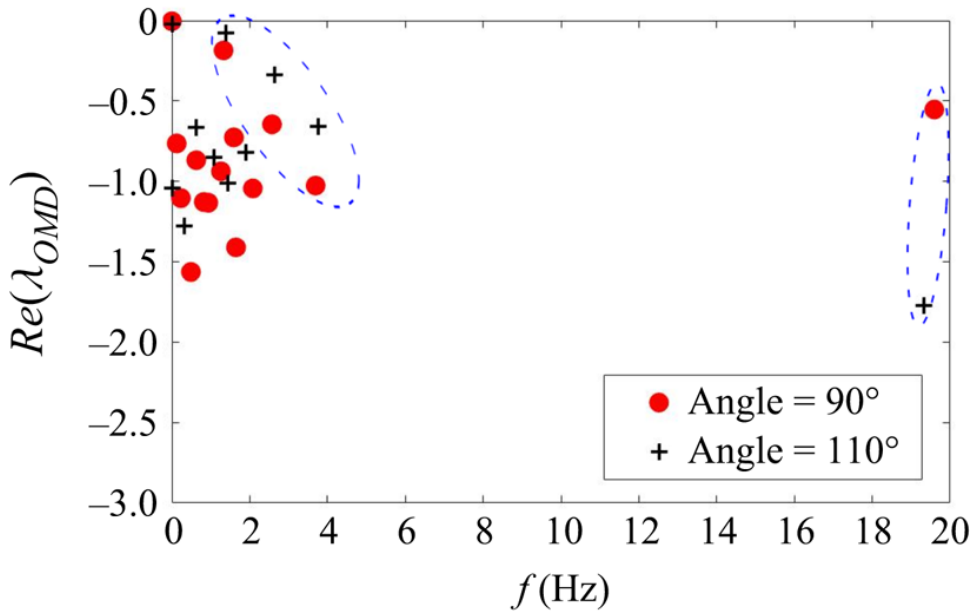


Figure 5.8: OMD spectra for $\theta = 90^o$ and $\theta = 110^o$

5.3.1 Extraction of primary coherent structures

The multiscale triple decomposition technique using OMD is successfully applied to the present data set to obtain the coherent motions associated with the sheddings of the main cylinder and the control rod and also the harmonics of the main cylinder. The OMD spectra for $\theta = 90°$ and $\theta = 110°$ is shown in figure 5.8. The least damped modes that correspond to the control rod's, and the main cylinder's, fundamental shedding modes and also the harmonics of the main cylinder's shedding mode are highlighted in the plot. Note that the frequencies of the modes remain more or less the same for both values of θ considered.

Hussain (1986) defined a coherent structure as a connected turbulent fluid mass of phase-correlated vorticity (hence velocity). The same ideology is followed here to represent the coherent structures identified in the flow. In figure 5.9 the modes associated with f_c, f_m and its harmonics are shown for the case $\theta = 90°$. The filled contours show the time averaged kinetic energies (defined as $\frac{1}{2}(\overline{\tilde{u}_l\tilde{u}_l + \tilde{v}_l\tilde{v}_l})$) of the modes, while the contour lines represent the iso-phase lines of transverse velocity component obtained from complex ϕ_{OMD} for each of the modes. The iso-phase lines are shown from $-\pi$ to π at steps decreasing with the frequency of the modes so that the spatial separation of the lines remains more or less the same for the different modes.

For the mode shown in figure 5.9(a), the iso-phase lines show a localised phase-correlated re-

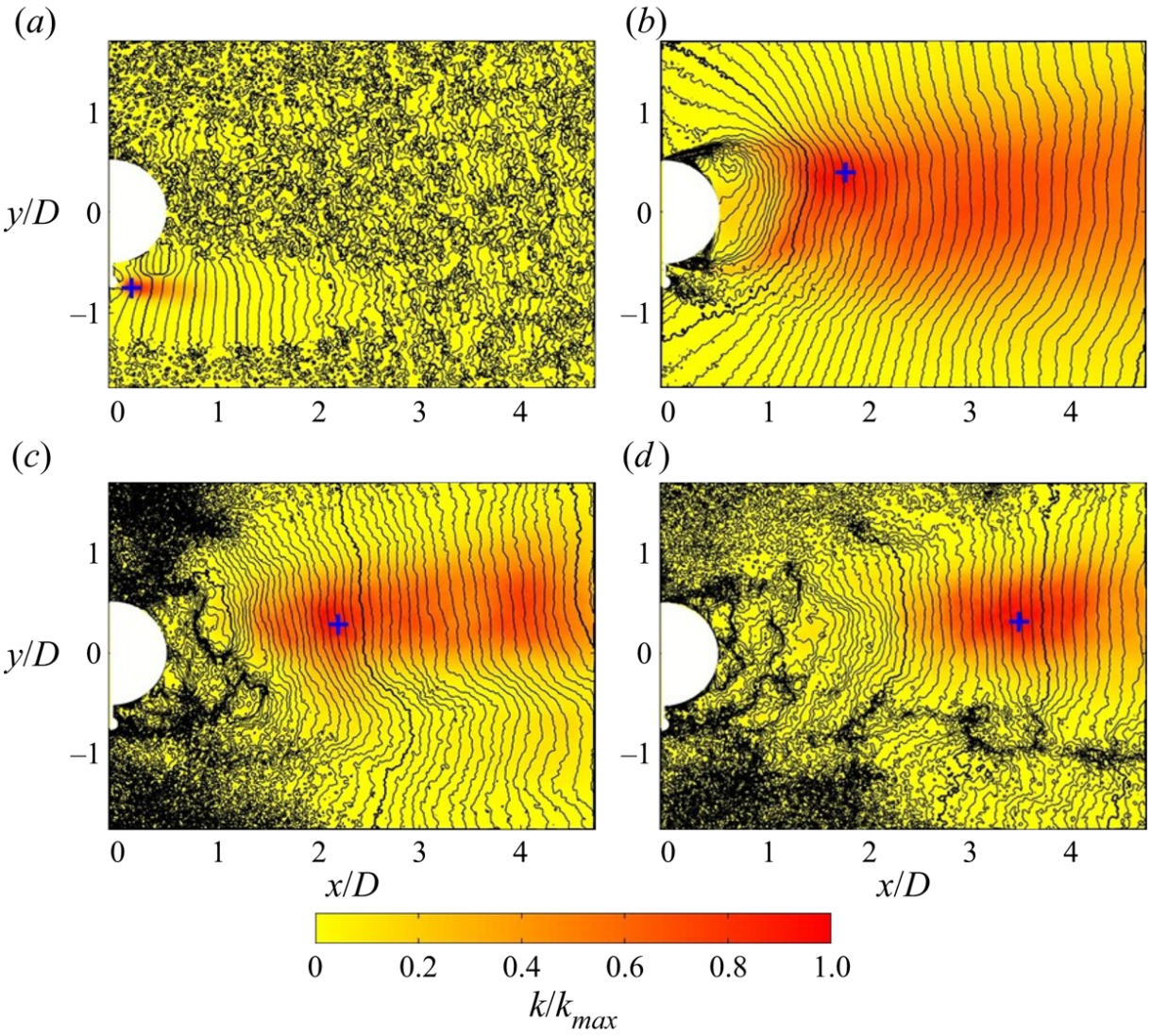


Figure 5.9: Modes associated with (a) the control rod shedding frequency and (b) the cylinder shedding frequency at $\theta = 90°$. (c) and (d) shows the second and third harmonics of the main cylinder shedding mode respectively. The filled contour shows the energy of the modes while the contour lines represent iso-phase lines of transverse velocity fluctuation of the modes. The contour lines are shown from $-\pi$ to π at step size (a) $\pi/2$ (b) $\pi/15$ (c) $\pi/10$ and (d) $\pi/7$. The '+' sign shows the location where the kinetic energies of the modes attain a maximum.

gion in the vicinity of the wake of the control rod where most of the energy of the mode is concentrated. Thus the multiscale triple decomposition method successfully identifies coherent structures associated with the shedding mode of the control rod (at the associated frequency f_c). Interestingly, a relatively small phase-correlated region is also observed towards the upper shear layer of the main cylinder. However, the energy content in this region is negligible and as a consequence no signature of the frequency is observed towards the upper shear layer of the main cylinder in the corresponding frequency spectra (see figure 5.5(c,e)). Therefore, this phase

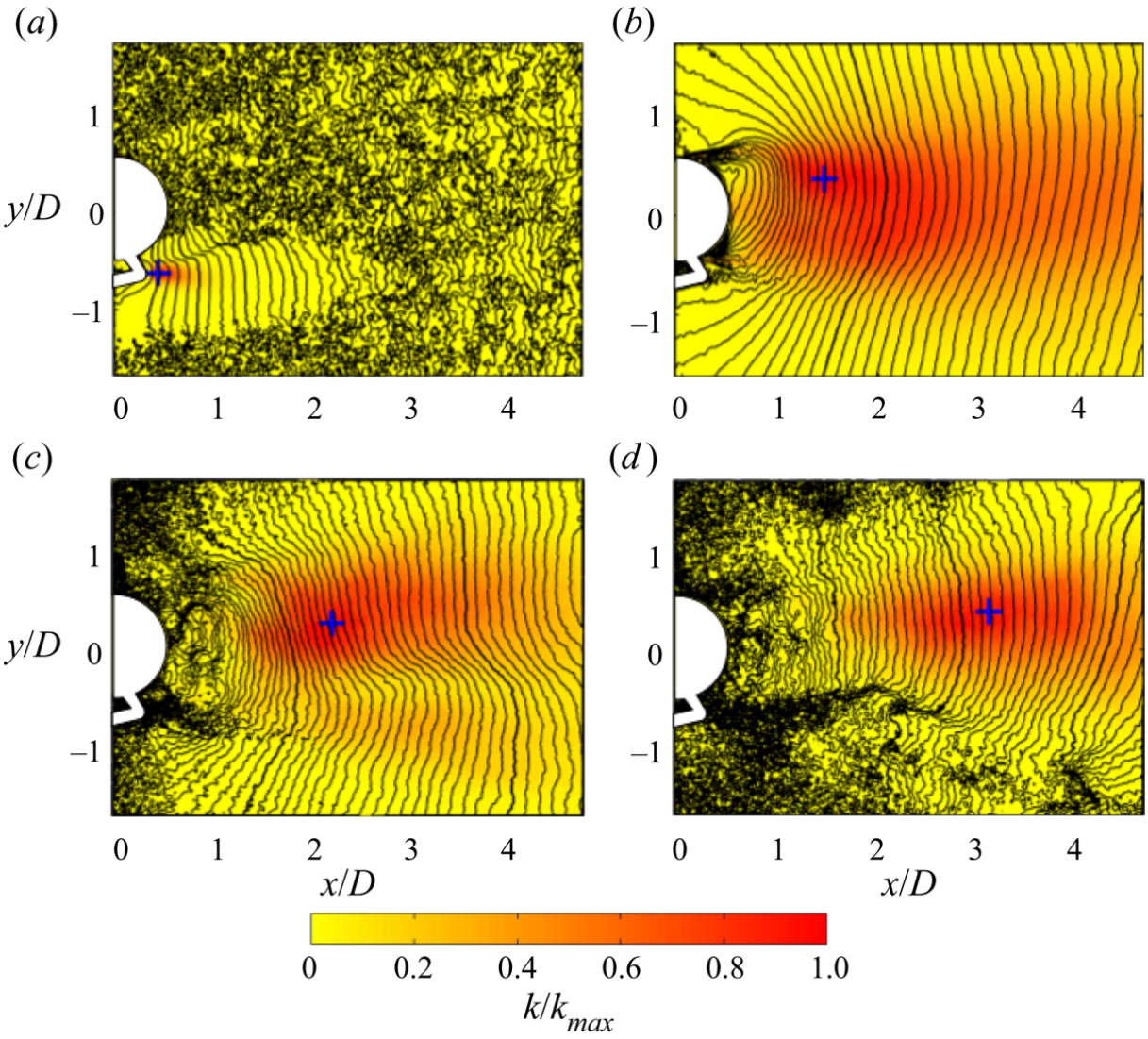


Figure 5.10: Modes associated with (a) control rod shedding frequency and (b) cylinder shedding frequency at $\theta = 110°$. (c) and (d) shows the second and third harmonics of the main cylinder's shedding mode respectively. The filled contour shows the energy of the modes while the contour lines represent iso-phase lines of transverse velocity fluctuation of the modes. The contour lines are shown from $-\pi$ to π at step size (a) $\pi/2$ (b) $\pi/15$ (c) $\pi/10$ and (d) $\pi/7$. The '+' sign shows the location where the kinetic energies of the modes attain a maximum.

correlated region is not considered to be a part of the control rod's shedding mode. The energy of the mode is maximum very close to the control rod as shown by the + sign. For the main cylinder's shedding mode, associated with frequency f_m in figure 5.9(b), the phase correlated region encompasses almost the entire field of view under investigation which is expected due to the large scale vortices shed from the main cylinder. Again note that the mode associated with f_m does not show any energy content immediately downstream of the control rod. In fact, at the near wake of the control rod, a small but clear uncorrelated region can be seen. Due to the

presence of the control rod, the energy content in the vicinity of the lower shear layer of the main cylinder is diminished. As a result, the maximum of kinetic energy for the main cylinder's shedding mode occurs more towards the upper shear layer of the main cylinder. Figures 5.9(c-d) show the second and third harmonics of the main cylinder's fundamental shedding mode, respectively. The modes are energetic further downstream compared to f_m which correlates well with figure 5.7(a) where the spectral peaks for the harmonics were found to attain maximum values further downstream compared to f_m. Similarly to f_m, the harmonics also show higher energy content in the vicinity of the upper shear layer of the main cylinder. The shedding modes and the harmonics obtained for $\theta = 110^\circ$ are shown in figure 5.10 and are qualitatively similar to $\theta = 90^\circ$.

5.3.2 Secondary modes and phase averaging

Although the fundamental shedding modes of the control rod, the main cylinder and its harmonics were captured in the OMD spectrum, the secondary modes (as shown in figures 5.5 (c, e)) were not captured by the OMD spectrum (see figure 5.8). Similar observations were reported by Baj and Buxton (2017) where OMD was incapable of identifying modes in and around the secondary frequencies even when the rank of the projection/dynamic matrices was set to very high values. However, since the phase reference of the secondary modes is available, *i.e.* $f_c \pm f_m$, phase averaging (see for instance Reynolds and Hussain (1972); Cantwell and Coles (1983)) can be used to extract the modes associated with the secondary frequencies. Essentially, phase averaging is applied separately for the two secondary modes with corresponding phase references. In order to obtain the phase averaged flow field at the reference frequencies $f_c \pm f_m$, the snapshots are divided into 16 phase bins with phases ranging from $-\pi$ to π. Subsequently, the second Fourier mode of the phase-averaged flow field is taken in order to produce a complex spatial mode that mimics the OMD modes. Thereupon, the complex coefficients of the secondary modes are obtained in a similar fashion to the OMD modes. A more extensive description of identification of the secondary modes using phase averaging can be found in Baj and Buxton (2017).

The secondary modes identified for $\theta = 90^\circ$ and 110° are shown in figure 5.11. Note that both

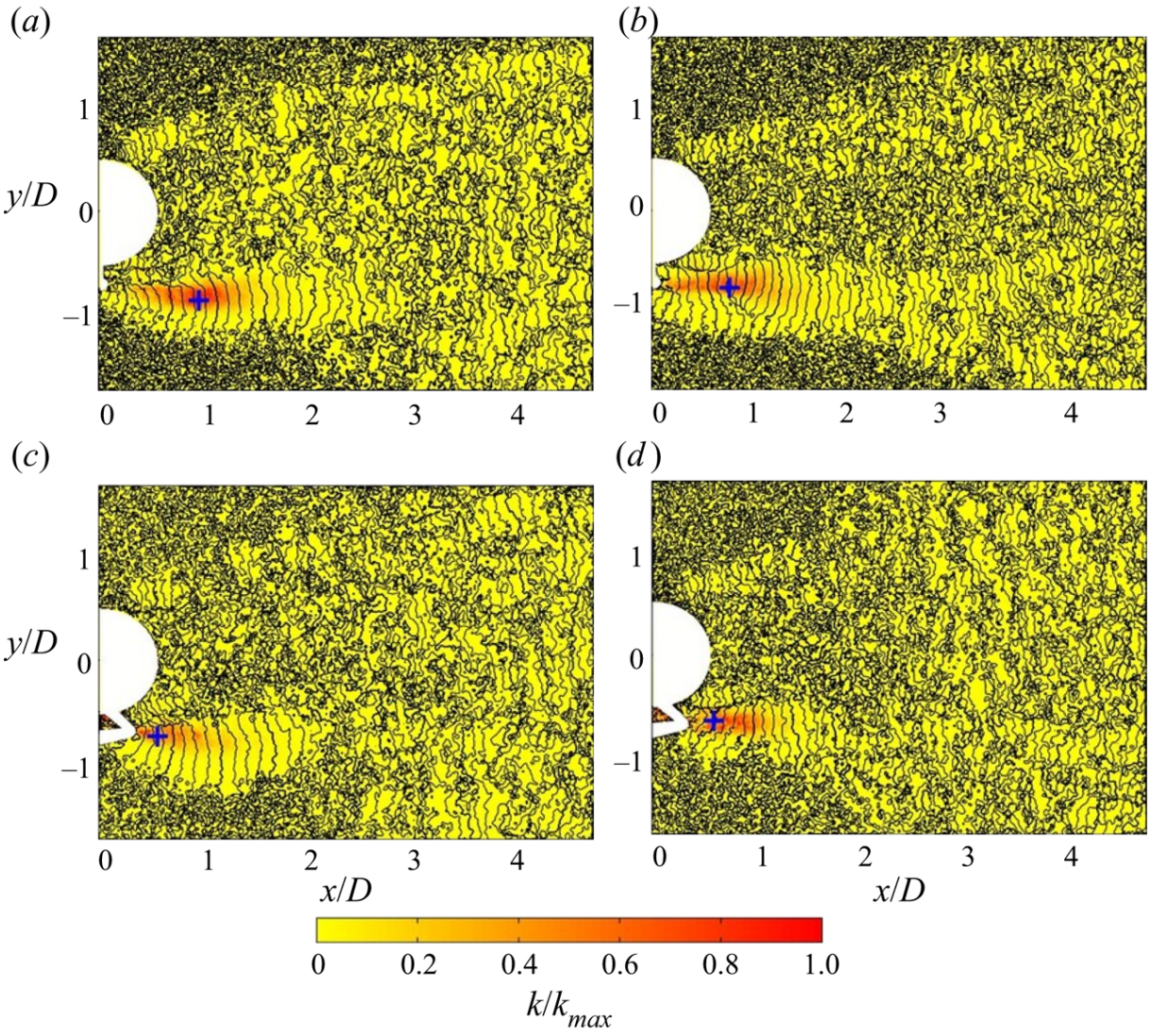


Figure 5.11: Energy and iso-phase lines associated with (a) low-frequency ($f_c - f_m$) and (b) high-frequency ($f_c + f_m$) secondary modes for $\theta = 90°$. The corresponding modes for $\theta = 110°$ are shown in fig (c) and (d). The contour lines are shown between $-\pi$ to π at a step size of $\pi/2$ for all the modes. The '+' sign shows the location where kinetic energy is maximum.

modes present a large phase-correlated region in the vicinity of the control rod, although they are not as prominent as the modes shown in figure 5.9 or figure 5.10. Similar to the control rod's shedding mode, a small phase correlated region is observed towards the upper shear layer of the main cylinder for all the secondary modes. However, the energy content in this region is again negligible and hence not considered for further analysis. Note that the strength and the spatial extent of the modes depends on the control rod angle. Recall from figures 5.5(c,e), that the secondary modes were more prominent for $\theta = 90°$ compared to $\theta = 110°$. The same observation can be made from figure 5.11. The energy content and the spatial extent of both

modes diminishes for $\theta = 110°$ compared to $\theta = 90°$. Similarly to figure 5.9, the location of maximum kinetic energy of the secondary modes is also shown by a '+' sign. The location of peak kinetic energy, as well as the spatial orientation of the modes, reveals some interesting facts. Recall from figure 5.5(c) and (e) that the high-frequency secondary mode was located more towards the separated shear layer between the main cylinder and the control rod whereas the lower secondary frequency was more towards the lower shear layer. The orientation of the spatial region where most of the energy of the modes is concentrated in figure 5.11 reveals similar trends, *i.e.* most of the energy of the lower secondary mode is concentrated towards the lower shear layer of the control rod and vice versa. The kinetic energy of the secondary modes peaks further downstream compared to the control rod's fundamental shedding mode, for which the peak was located very close to the control rod. This difference in the location of peak kinetic energy was also noted by Baj and Buxton (2017) and it hints at the fact that a different mechanism is involved behind the formation of the secondary modes. Interestingly, the kinetic energy of the secondary modes at $\theta = 110°$ peaks much earlier in comparison to $\theta = 90°$ and it correlates well with the closer wake intersection points observed for $\theta = 110°$ in figure 5.4(b). This correlation between the location of wake intersection points and kinetic energy maxima implies that the secondary modes ought to be related to the interaction between the main cylinder's and control rod's fundamental shedding modes. However, the locations of the kinetic energy maxima of the secondary modes do not exactly coincide with the corresponding wake intersection points and are located slightly upstream (see figure 5.4). For a deeper understanding of the formation of the modes, the kinetic energy budget for each of the modes is evaluated in the next section.

5.4 Energy budget analysis

Turbulent kinetic energy (TKE) transport in free shear flows has been the subject of numerous studies (Liu and Thomas, 2004; Panchapakesan and Lumley, 1993; Morris et al., 2021) using a generic TKE transport equation (for instance see Hinze (1975)). However, for a multiscale flow like a wind turbine wake, a separate TKE transport equation is required for each of the coherent motions present in the flow to track energy exchanges to/from them (as well as the mean flow and stochastic fluctuations). Reynolds and Hussain (1972) derived separate TKE

transport equations for the mean, coherent and stochastic part of the flow. Here, the average kinetic energy per unit mass in the flow was represented as

$$\frac{1}{2}\overline{u_i u_i} = \frac{1}{2}\bar{u}_i\bar{u}_i + \frac{1}{2}\overline{\tilde{u}_i\tilde{u}_i} + \frac{1}{2}\overline{u_i'' u_i''} \tag{5.2}$$

This assumes that the decomposition is energy preserving. Along similar lines, Baj and Buxton (2017) derived the kinetic energy budget equations identified using the multiscale triple decomposition technique discussed earlier. The average kinetic energy at a point is then described as

$$\frac{1}{2}\overline{u_i u_i} = \frac{1}{2}\bar{u}_i\bar{u}_i + \frac{1}{2}\sum_l \overline{\tilde{u}_i^{f_l}\tilde{u}_i^{f_l}} + \frac{1}{2}\overline{u_i'' u_i''} \tag{5.3}$$

where $\tilde{u}_i^{f_k}$ is the i^{th} velocity component of the coherent motion with characteristic frequency f_k. Using the OMD based multiscale triple decomposition, Baj and Buxton (2017) showed that the correlations such as $\overline{\tilde{u}_i^{f_l} u_i''}$ and $\overline{\tilde{u}_i^{f_l}\tilde{u}_i^{f_m}}$ were negligible compared to the terms on the right hand side of equation 5.3 (see appendix D of (Baj and Buxton, 2017)). The authors derived separate TKE transport equations for the mean and stochastic component of the flow as well as for each of the coherent motions present in the flow. The TKE transport equation for the mean component and the coherent motions are shown symbolically in equation 5.4 and equation 5.5 respectively. The full derivation of these equations and the various terms contained therein can be found in Baj and Buxton (2017).

$$-\bar{C} - \sum_l \tilde{P}_l - P'' - \bar{\epsilon} + \bar{D} = 0 \tag{5.4}$$

$$\frac{\partial \tilde{k}_l}{\partial t} = -\tilde{C}_l + \tilde{P}_l - \hat{P}_l + \tilde{T}_l^{+} - \tilde{T}_l^{-} - \tilde{\epsilon}_l + \tilde{D}_l \tag{5.5}$$

In equation 5.4, the term $-\bar{C}$ is the convection term and $-\sum_l \tilde{P}_l$ denotes the net coherent energy production term (from the mean flow) which is the sum of the energies transferred to the individual coherent motions from the mean flow (*i.e.* $\tilde{P}_l$ for the l^{th} coherent motion). Here,

$\tilde{P}_l$ is defined as $-\sum_{f_s} \overline{\tilde{u}_i^{f_s} \tilde{u}_j^{f_l} \frac{\partial \bar{u}_i}{\partial x_j}}$, where s can be any coherent motion including the l^{th} coherent motion. The terms P'', $\bar{\epsilon}$ and $\bar{D}$ represent the production of stochastic turbulent kinetic energy directly from the mean flow, direct dissipation from the mean flow and the mean diffusion terms respectively.

Contrastingly to equation 5.4, in equation 5.5 $\tilde{P}_l$ appears with a positive sign, *i.e,* it acts as a source for the l^{th} coherent motion. The term $\hat{P}_l$ is the production of stochastic turbulent kinetic energy from the l^{th} coherent motion and appears as a sink. $\tilde{\epsilon}_l$ and $\tilde{D}_l$ represent the dissipation of kinetic energy (by the l^{th} coherent motion) and diffusion terms respectively. Note that two new terms appear in the kinetic energy budget equation for coherent structures, $\tilde{T}_l^+$ and $\tilde{T}_l^-$, which are referred to as the triadic energy production terms. These terms account for the energy transfer between different coherent structures through non-linear interactions. For instance, the term $\tilde{T}_l^+$ accounts for the energy gained by the l^{th} coherent motion from other coherent modes and is defined as

$$\tilde{T}_l^+ = -\frac{1}{2} \sum_{f_s, f_t} \overline{u_i^{f_l} u_j^{f_t} \frac{\partial u_i^{f_s}}{\partial x_j}}. \tag{5.6}$$

Baj and Buxton (2017) argued that this term could be non-negligible only when the coherent structures involved in the energy exchange process formed a triad, *i.e.* $f_l \pm f_s \pm f_t = 0$. Similarly, $\tilde{T}_l^-$ represents the energy lost by the l^{th} mode to other coherent motions and is defined as

$$\tilde{T}_l^- = -\frac{1}{2} \sum_{f_s, f_t} \overline{u_i^{f_s} u_j^{f_t} \frac{\partial u_i^{f_l}}{\partial x_j}}. \tag{5.7}$$

Note that, in both $\tilde{T}_l^+$ and $\tilde{T}_l^-$, the t^{th} mode acts merely as a catalyst and does not take part in the energy transfer process directly. Baj and Buxton (2017) grouped these two terms together and represented them as a single triadic energy transfer term. Note that in a wind turbine wake, there exist multiple harmonics of the rotor frequency (f_r) and blade passing frequency ($3f_r$) which form a large number of triads. Therefore, the triadic energy exchange term can have a significant role in governing the dynamics of these frequencies.

The energy budget terms shown in equations 5.4 and 5.5 are first applied to the simple two-dimensional multiscale flow discussed above. The knowledge gained from this analysis will elucidate a number of interesting physical phenomena in a wind turbine wake as will be discussed

in chapters 6 and 7. Note that, the spatial resolution of the experimental data corresponding to the simple multiscale flow as well as that for the wind turbine wake discussed in chapters 3 and 4 was insufficient to resolve the dissipation rate of TKE, which is a major contributor to the budget for the stochastic fluctuations. Therefore, the stochastic energy budget was not considered here. Nevertheless, the main motivation of this thesis was only to study the energy exchanges between the mean flow and the coherent motions, and also between different coherent motions.

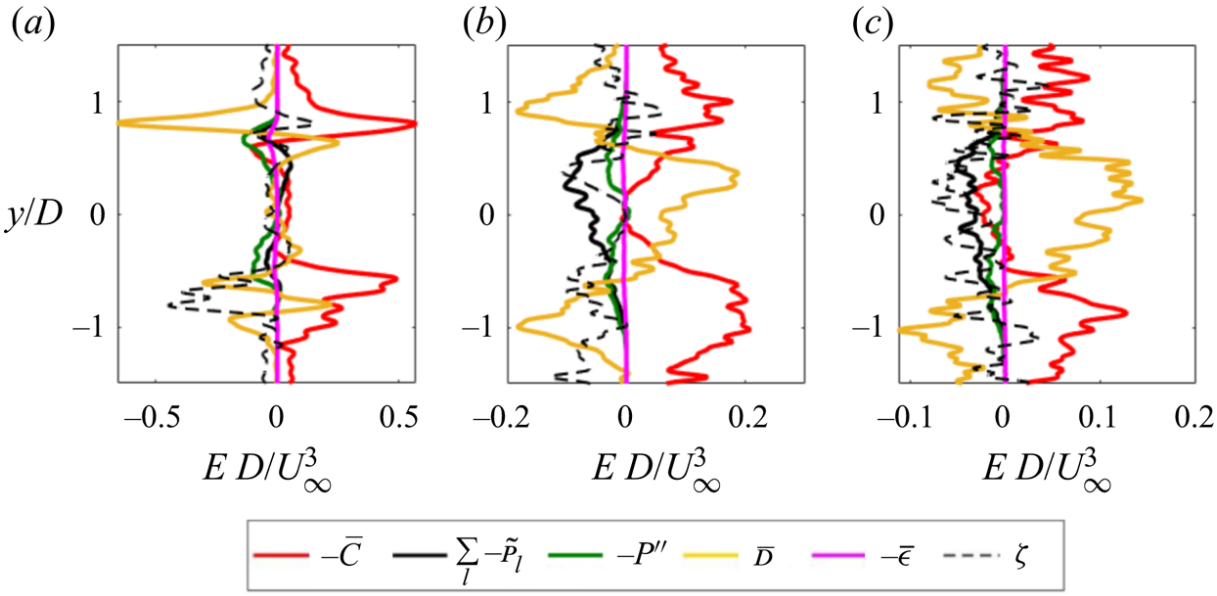


Figure 5.12: Terms of the mean kinetic energy budget for $\theta = 90°$ at (a) $x/D = 1$, (b) $x/D = 2$ and (c) $x/D = 3$. The energy budget terms (denoted by E in the figure) are non-dimensionalised by U_∞^3/D.

5.4.1 Mean energy budget

First the terms of the mean TKE buget equation (equation 5.4) are investigated. As the flow is primarily two dimensional, the contribution of the out-of-plane component of velocity can be expected to be small (Baj and Buxton, 2017; Portela et al., 2017). Therefore, the terms containing the out-of-plane velocity component as well as out-of-plane velocity gradients are ignored while evaluating the TKE budget terms. These are expected to be small but will (in part) appear in the residual ζ, alongside other inaccessible terms such as the pressure-diffusion term. The pressure-diffusion term has been neglected in several other works on free shear flows and its contribution has been estimated from a balance of the budget (for example see Browne

et al. (1987) for a self-similar wake and Panchapakesan and Lumley (1993) for an axisymmetric jet). Baj and Buxton (2017) ignored the pressure - velocity coupling while calculating the diffusion term and argued that the high residuals observed in the near field of their multiscale geometry was largely due to the neglected contribution of pressure.

The different terms of equation 5.4 for $\theta = 90°$ are presented in figure 5.12 at different streamwise stations. The energy terms are normalised by U_∞^3/D. At $x/D = 1$, the convection term $(-\bar{C})$ appears to be the dominant source term, while diffusion partly acts to counter it. The magnitude of the convection term is small but positive near the centreline of the main cylinder implying a slow spatial decay of kinetic energy in the vicinity of the centreline. This can be expected in the recirculation region as the magnitude of the streamwise velocity (which is negative) reduces as one approaches the end of the recirculation region. The magnitude of the convection term however is large and positive outside the separated shear layers of the main cylinder implying a quick decay of the flow at this position. Note from figure 5.3(a) that at around $x/D = 1$, the accelerated flow past the main cylinder quickly adjusts to the free stream value (*i.e.* a decay of mean kinetic energy) outside the separated shear layers, hence explaining the positive peaks observed in the convection term. Comparing the sink terms at this location, it can be discerned that a considerable amount of energy is transferred to the stochastic motion from the mean flow. However, further downstream, at $x/D = 2$ (see figure 5.12(b)), the major energy sink is the coherent energy production term. Note from figure 5.7 that at this location, the fundamental shedding mode of the main cylinder as well as its harmonics are significantly stronger compared to $x/D = 1$. As a result, a higher coherent energy production at $x/D = 2$ can be expected. The convection term is nearly zero at the centreline as the location is close to the edge of the recirculation region. The peaks of the convection terms are now milder and appear further apart from the centreline. At $x/D = 3$, the terms show the same qualitative trends as for $x/D = 2$, however the convection term becomes positive near the centreline implying a spatial accumulation of kinetic energy or wake recovery. The $(\sum_l -\tilde{P}_l)$ term at this location is lower compared to $x/D = 2$ implying a decrease in the strength of the coherent motions also observed in figure 5.7(a). Energy lost due to direct dissipation from the mean flow is negligible at all of the streamwise locations considered as expected.

In order to obtain a clearer picture, the profiles of the different terms of equation 5.4 are

integrated w.r.t. transverse distance y and their evolution with streamwise distance is shown for $\theta = 90°$ and the bare cylinder in figure 5.13. The corresponding figure for $\theta = 110°$ is not shown for brevity due to its qualitative similarity with $\theta = 90°$. The limits of integration ($y1$ and $y2$) are taken to be $-1.65D$ and $1.65D$ respectively which are slightly smaller than the limit of the field of view. The integrated terms remain apparently insensitive to slight variation in $y1$ and $y2$. Figure 5.13 shows that the convection term is dominant everywhere for both $\theta = 90°$ and the bare cylinder. The coherent energy production term is the main sink of energy for both cases, however this term also shows two minima for $\theta = 90°$ (unlike the bare cylinder) due to the presence of two distinct wake-generating bodies. The minimum in the coherent energy production term associated with the main cylinder's shedding mode is significantly reduced for $\theta = 90°$ compared to the bare cylinder, showing the effectiveness of the control rod in controlling the main cylinder's shedding mode. Apart from the primary shedding modes, the coherent energy production term includes a contribution from the harmonics of the main cylinder's shedding mode as well. Note that although the evolution of the $\sum -\tilde{P}_l$ term is shown from close to the control rod surface, the second and third harmonics are largely incoherent before $x/D \approx 1.3$. As a result, the $\sum -\tilde{P}_l$ term can be expected to be slightly noisy close to the main-cylinder-and-control-rod-assembly. Nevertheless, since the $\tilde{P}_l$ terms for the harmonics are an order of magnitude weaker than those of the primary shedding modes (as will be shown in section 5.4), they do not affect the $\sum -\tilde{P}_l$ term significantly in this region. Apart from the $\sum -\tilde{P}_l$ term, some amount of energy is also lost through the stochastic energy production and dissipation terms, however their relative contribution in both cases is hard to assess from figure 5.13.

The sink terms shown in figure 5.13(a-b) are further integrated w.r.t. x to obtain the net contribution of each of the terms across the whole field of view. The results are shown in figure 5.13(c) for $\theta = 90°$, $\theta = 110°$, and the bare cylinder. The domain of integration is taken from $x1 = 0.1D$, which is close to the control rod or the left limit of the field of view to $x2 = 4.5D$. Note from figure 5.13(c) that for all cases, the major energy loss is due to the coherent energy production term followed by stochastic energy production and direct dissipation. Interestingly, the net energy lost to the coherent motions for $\theta = 90°$ is the least among the three cases, followed by the bare cylinder and $\theta = 110°$. It indicates that the coherent motions on an

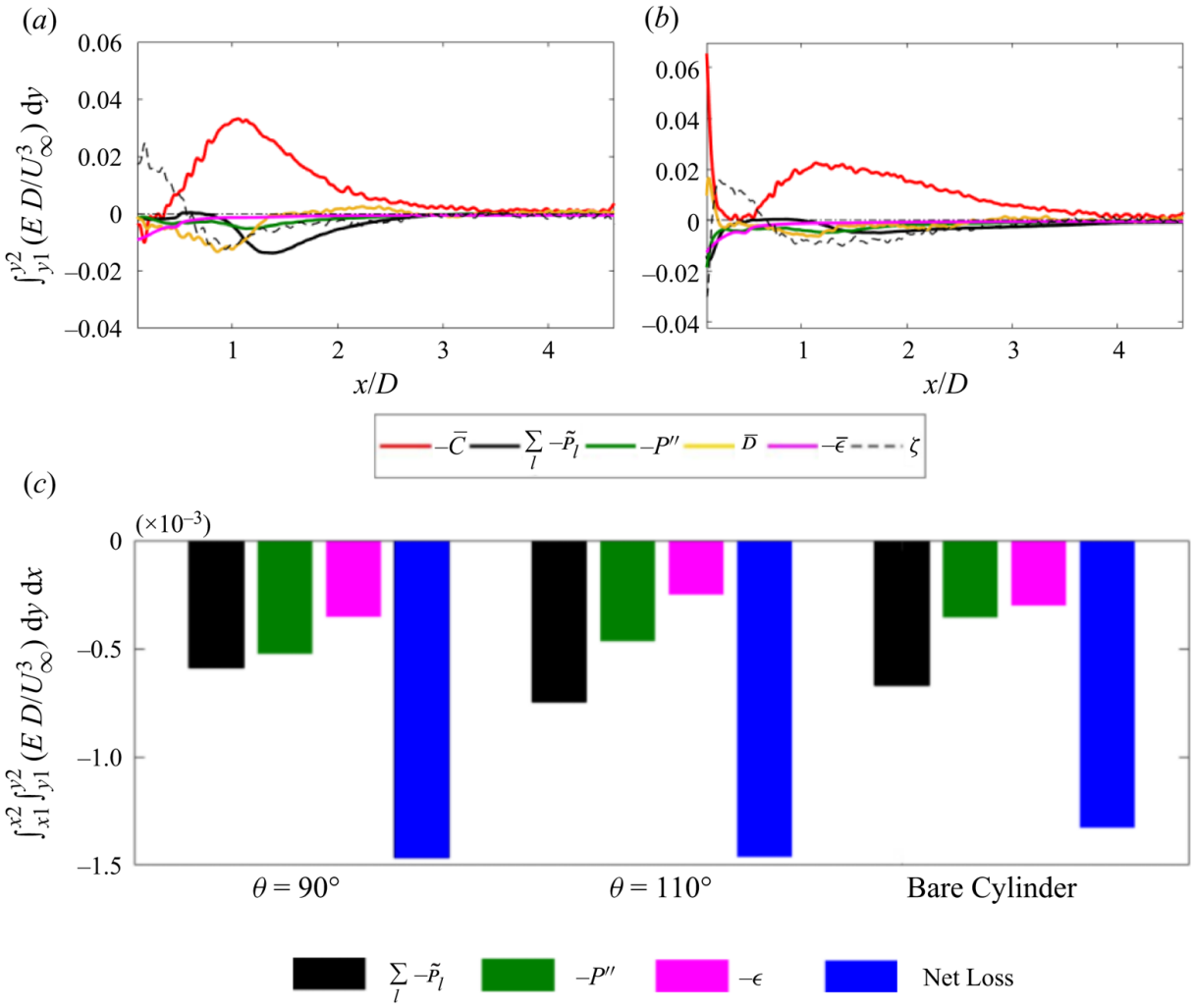


Figure 5.13: Streamwise evolution of the integrated kinetic energy budget terms for (a) bare cylinder and (b) $\theta = 90°$. The horizontal $(- \cdot -)$ line shows the 0 level for a reference. (c) Net contribution of different sink terms. The energy budget terms are denoted by the generic E letter.

aggregate are the most energetic for $\theta = 110°$ and least energetic for $\theta = 90°$. This observation correlates well with the finding of Cicolin et al. (2021) that the fluctuating loads acting on the main cylinder at $\theta = 90°$ were lower than the bare cylinder, while for $\theta = 110°$ they were higher. Further, the authors reported that the net drag acting on the combined assembly of the main cylinder and control rod was close for $\theta = 90°$ and $\theta = 110°$, while both were nearly 10% larger than the drag on the bare cylinder. A remarkably similar trend is revealed by the blue bars representing the net losses in figure 5.13(c), *i.e.*, the net losses suffered by the mean flow for both $\theta = 90°$ and $\theta = 110°$ are similar and both are 10% larger than that of the bare cylinder. Note that drag must be thermodynamically linked to total dissipation and the pink columns

represent the energy dissipated directly from the mean flow only. Considering the cascade of energy, the energy transferred to the coherent motions and stochastic motion from the mean flow is ultimately dissipated. Hence, figure 5.13(c) essentially shows that, although the total dissipation might be similar for both $\theta = 90°$ and $\theta = 110°$ (hence similar total drag), the path leading to total dissipation is different.

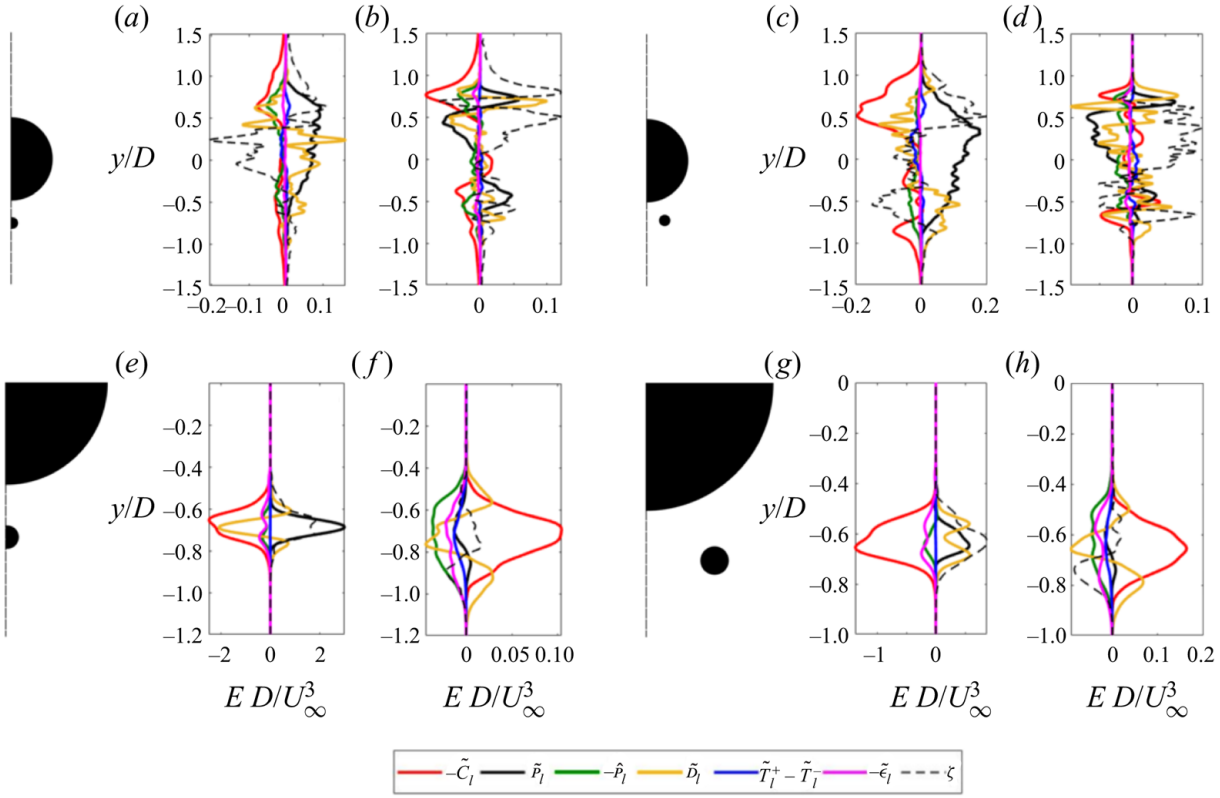


Figure 5.14: Coherent energy budget terms of the main cylinder's shedding mode at (a) the location where the peak in the spectrum of transverse velocity component of the mode attains a maximum, *i.e.* $x/D \approx 1.51$ (b) wake intersection point ($x/D \approx 0.97$) for $\theta = 90°$. The same plots for $\theta = 110°$ are shown in fig. (c) at $x/D \approx 1.48$ and (d) at $x/D \approx 0.76$ respectively. The corresponding budget terms for the control rod's fundamental shedding mode for $\theta = 90°$ are shown in fig. (e) for $x/D \approx 0.1$ and in (f) for $x/D \approx 0.97$. The same plots for $\theta = 110°$ are shown in fig. (g) at $x/D \approx 0.3$ and (h) at $x/D \approx 0.76$ respectively.

5.4.2 Energy budgets of primary shedding modes

The terms of the coherent energy budget equations are first calculated for the main cylinder's (f_m) and control rod's shedding (f_c) modes and are shown in figure 5.14 for $\theta = 90°$ and 110°. Figure 5.14 (a) shows the energy budget terms in the near wake of the main cylinder at $x/D \approx 1.51$. Note from figure 5.7(a) that at this location the peak in the spectrum of the

transverse velocity component attains its maximum value. At this location, the production term ($\tilde{P}_l$) is the main source of energy and is largely positive around the centreline. The convection term is largely negative in the vicinity of the shear layers of the main cylinder wake and acts as the major sink. It also shows that the energy of the mode is still building up and is yet to start decaying. Note that the $\tilde{P}_l$ and convection terms (which are the dominant source and sink terms respectively) are asymmetric about the wake centreline ($y = 0$) due to the presence of the control rod which alters the energy content in the lower shear layer of the main cylinder wake significantly, as observed in figure 5.9(b). Apart from the convection term, the other major contributor to the energy losses is the stochastic energy production term which is almost 30% of the production term.

Figure 5.14(b) shows the energy budget terms for f_m at the wake intersection point ($x/D \approx 0.97$) which is upstream of figure 5.14(a). The difference between the two stations is most pronounced in the $\tilde{P}_l$ term. The magnitude of the production term is much lower and it is positive only in the separated shear layers of the wake as the formation of the von Kármán vortex street behind the main cylinder is not complete at $x/D \approx 0.97$. Similarly, figure 5.14(c-d) show the kinetic energy budget terms for the main cylinder wake at the point of transverse velocity peak ($x/D \approx 1.48$) and the wake intersection point ($x/D \approx 0.76$) at $\theta = 110°$. The qualitative nature of the terms are very similar to $\theta = 90°$ although slight differences are seen in the magnitude of the terms. In particular, the $\tilde{P}_l$ term is almost twice larger for $\theta = 110°$ compared to $\theta = 90°$, which correlates well with the twice larger spectral peak for the transverse velocity at f_m for $\theta = 110°$ observed in figure 5.7(b).

Figure 5.14(e) shows the kinetic energy budget terms for the control rod's fundamental shedding mode for $\theta = 90°$ at $x/D = 0.1$. This location is close to the point where the mode is the most energetic. At this location, the mode is primarily energised by the mean flow through the $\tilde{P}_l$ term, whilst energy is mainly lost through convection and direct dissipation. All other terms are relatively small at this station. At the wake intersection point (figure 5.14(f)) however, the convection term is positive showing that the mode is now spatially decaying. This observation correlates well with the fast decaying transverse velocity amplitude of the control rod's shedding mode in figure 5.7(a). The production term is negligible and a significant amount of energy is drained by the stochastic energy production and dissipation terms at this location. Interestingly,

at the wake intersection point, the triadic energy production term is non-negligible and acts as a sink for the control rod's shedding mode. The qualitative trends of the kinetic energy budget terms for f_c remain very similar for $\theta = 110°$ (see figure 5.14(g-h)) apart from slight variation in the magnitudes. Figure 5.14(g) is shown at $x/D = 0.3$, *i.e.* close to the point where f_c is most energetic for $\theta = 110°$. Notably, the coherent energy production term ($\tilde{P}_l$) is weaker compared to that found in figure 5.14(e). The magnitude of the convection term at this location is also small indicating a relatively slow build up of energy. However, the magnitude of the convection term is higher compared to $\theta = 90°$ at the wake intersection point (figure 5.14(h)) indicating faster decay of the mode. All these points together agree well with the shorter extent of the control rod's wake seen in figure 5.4(b) for $\theta = 110°$.

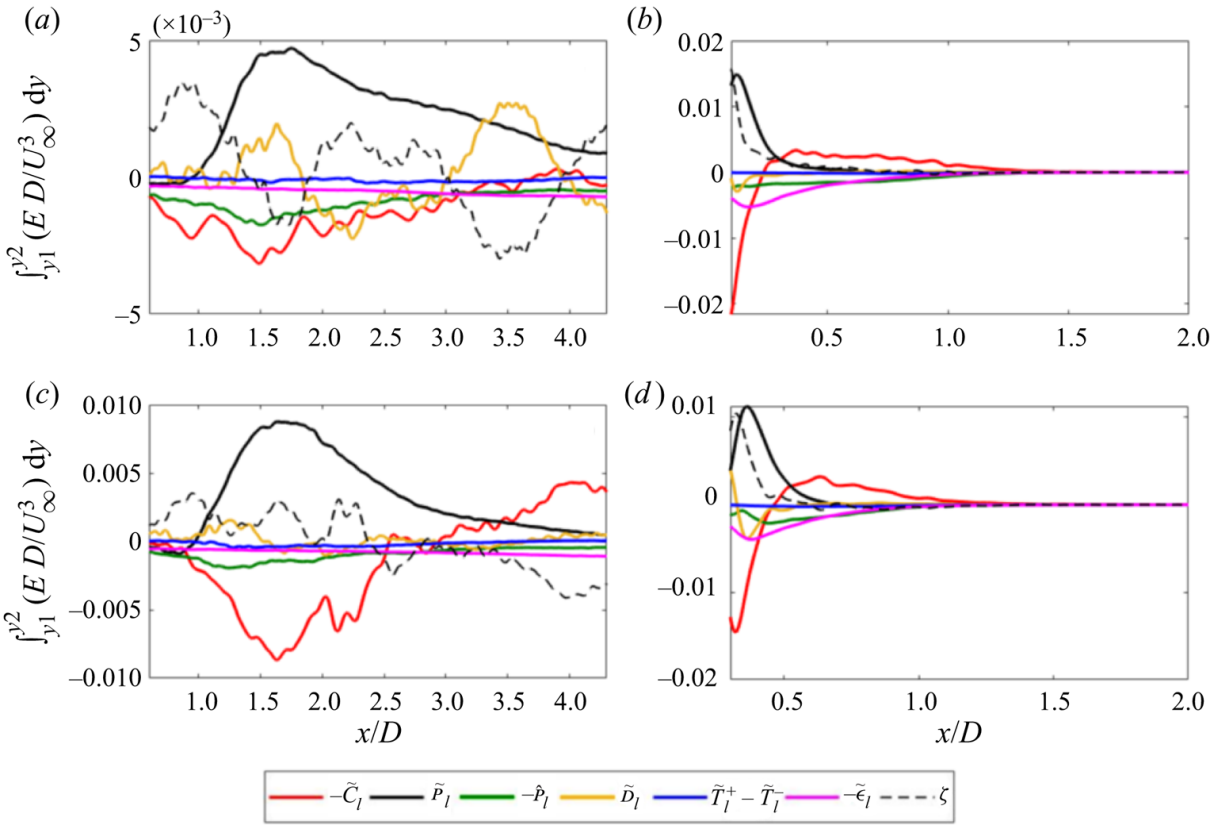


Figure 5.15: Streamwise evolution of the kinetic energy budget terms for (a) the main cylinder's and (b) the control rod's fundamental shedding modes at $\theta = 90°$. Plots (c) and (d) show the same $\theta = 110°$. The horizontal $(- \cdot -)$ line shows the 0 level for a reference.

A clearer picture of the dynamics of each of the modes can be revealed by tracking the contribution of the terms with spatial distance in a continuous fashion. The different terms in the kinetic energy budget equation of the coherent motions are therefore integrated w.r.t. y and

their evolution with streamwise distance is shown in figure 5.15. Note that the dynamics of the modes at both values of θ are primarily governed by the $\tilde{P}_l$ and convection terms. The convection term shows a sign change for all the modes, implying an energy buildup and subsequent decay of the modes, although the rate of growth/decay is different for the modes and it also varies with θ. For the main cylinder's shedding mode at $\theta = 90°$ (figure 5.15(a)), the main source of energy for the mode is the $\tilde{P}_l$ term everywhere in the domain, while the convection term and the $-\hat{P}_l$ term combined nearly balances the net gain due to it. The evolution of the $\tilde{P}_l$ term looks quite similar to the evolution of the mode's spectral peak in figure 5.7(a) and it peaks around $x/D = 1.5$ which is where the amplitude of transverse velocity of the mode is also maximum.

The fact that the vortex shedding modes are primarily energised by the $\tilde{P}_l$ term implies that this term could be an important source of energy to a number of modes in a wind turbine wake. In chapter 3, distinct frequencies associated to vortex sheddings from the nacelle and tower were identified. A positive contribution of the $\tilde{P}_l$ term to energise these modes can be expected. Furthermore, the wake meandering mode was shown to behave similarly to a global vortex shedding mode from the wind turbine as a whole considered as a porous bluff body. If the wake meandering mode is found to be positively energised by the $\tilde{P}_l$ term, this would further evidence to the argument that wake meandering is a bluff body type rotor scale instability. These aspects will be further discussed in chapters 6 and 7.

For $\theta = 110°$, although figure 5.15(c) shows a trend qualitatively similar to figure 5.15(a), note that the production term then drops off much earlier. The convection term also becomes positive much earlier, implying that the mode starts to decay much earlier in comparison to $\theta = 90°$. This result correlates well with the shorter recirculation region observed for $\theta = 110°$ in figure 5.3(b) compared to $\theta = 90°$. Further, note that the peak of the production term at $\theta = 110°$ is almost twice that compared to $\theta = 90°$ which explains the twice higher spectral peak observed for f_m at $\theta = 110°$ in figure 5.7(b). Similarly the streamwise evolution of the kinetic energy budget terms for the control rod's fundamental shedding mode at $\theta = 90°$ and $\theta = 110°$ is shown in figures 5.15(b) and 5.15(d) respectively. The trends look very similar to each other apart from slight differences in the amplitudes. The production term falls off sharply within a short streamwise distance and correlates well with the short streamwise extent of the modes seen in figure 5.7 and figure 5.9(a). The contribution from all the other terms as a whole is

relatively small compared to the convection and $\tilde{P}_l$ term.

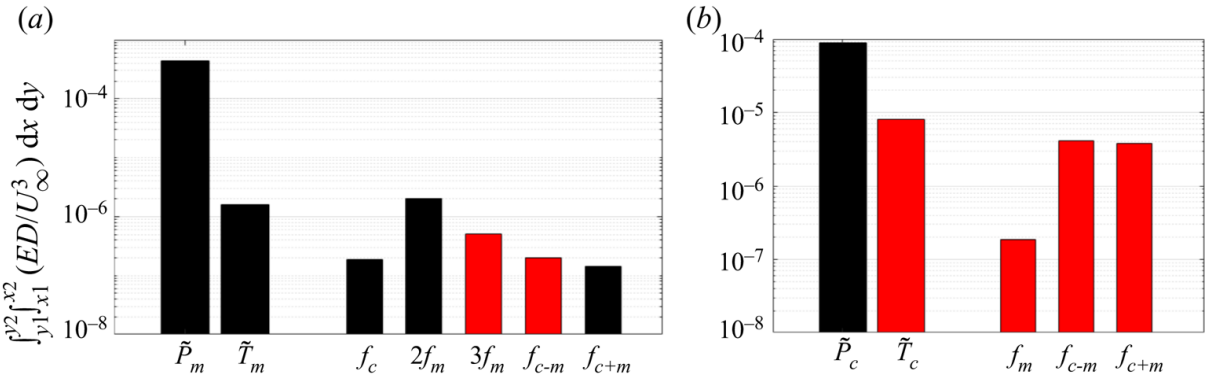


Figure 5.16: Net energy transfers through coherent energy production and non-linear triadic energy transfer terms for (a) the main cylinder's fundamental shedding mode, and (b) the control rod's fundamental shedding mode for $\theta = 90°$. Black bars show a gain of energy and red bars show a loss of energy for the respective mode.

Next the nature of the non-linear triadic interaction term is explored. Note that the evolution of the triadic interaction term shown in figure 5.15 is the sum of contributions from all other modes forming a triad with that respective mode. For instance, for a triad containing f_p, f_q, and f_r, the net triadic energy transfer to mode f_p (denoted by $\tilde{T}_p^+ - \tilde{T}_p^-$) is essentially the sum of two non-negligible transfers as shown in equation 5.8

$$\tilde{T}_p^+ - \tilde{T}_p^- = \frac{1}{2}\Big(-\overline{u_i^{f_p} u_j^{f_q} \frac{\partial u_i^{f_r}}{\partial x_j}} + \overline{u_i^{f_r} u_j^{f_q} \frac{\partial u_i^{f_p}}{\partial x_j}}\Big) + \frac{1}{2}\Big(-\overline{u_i^{f_p} u_j^{f_r} \frac{\partial u_i^{f_q}}{\partial x_j}} + \overline{u_i^{f_q} u_j^{f_r} \frac{\partial u_i^{f_p}}{\partial x_j}}\Big) \tag{5.8}$$

Here, the first term on the RHS accounts for the net energy exchange between f_p and f_r, while the second term captures the same between f_p and f_q. The overall contributions of each of these individual energy transfers (integrated over the entire domain of interest) between two modes is studied. The main cylinder's shedding mode forms three triads with the other modes, which are $[f_m, f_c, f_{c-m}]$, $[f_m, f_c, f_{c+m}]$ and $[f_m, 2f_m, 3f_m]$. Hence, a non negligible non-linear energy transfer between f_m and all the other modes can be expected. The control rod's shedding mode (f_c) can interact only with f_m and the secondary modes, however. While integrating these non-linear energy transfers as well as the $\tilde{P}_l$ term of the modes over the entire domain, care must be taken for the selection of the left limit of the domain ($x1$) for each of the terms. For instance, for the $\tilde{P}_l$ term of the main cylinder's shedding mode, $x1$ must be set to $0.5D$ in order to avoid the spatially incoherent region of the mode adjacent to the cylinder. For the control

rod's shedding mode however, $x1$ must be set close to the control rod (*i.e.* $< 0.5D$) to capture the contribution of the $\tilde{P}_l$ term (see figure 5.15(b)). Hence, for the control rod's shedding mode as well as the secondary modes at $\theta = 90°$, $x1$ is set to be $0.1D$. Similarly, for $\theta = 110°$ the corresponding $x1$ is chosen to be $0.3D$ which is sufficiently close to the control rod. The harmonics of the main cylinder's shedding mode are energetic further downstream and shows a large spatially incoherent region at $x/D \lesssim 1.3$. Therefore, for the harmonics at $\theta = 90°$, $x1$ is chosen to be $1.3D$. A sensitivity analysis is performed by varying $x1$ around $1.3D$ and obtaining the integrated energy terms for the harmonics which is discussed in section 5.4.4. It is found that lowering $x1$ below $1.3D$ does not introduce appreciable changes to the energy terms of interest.

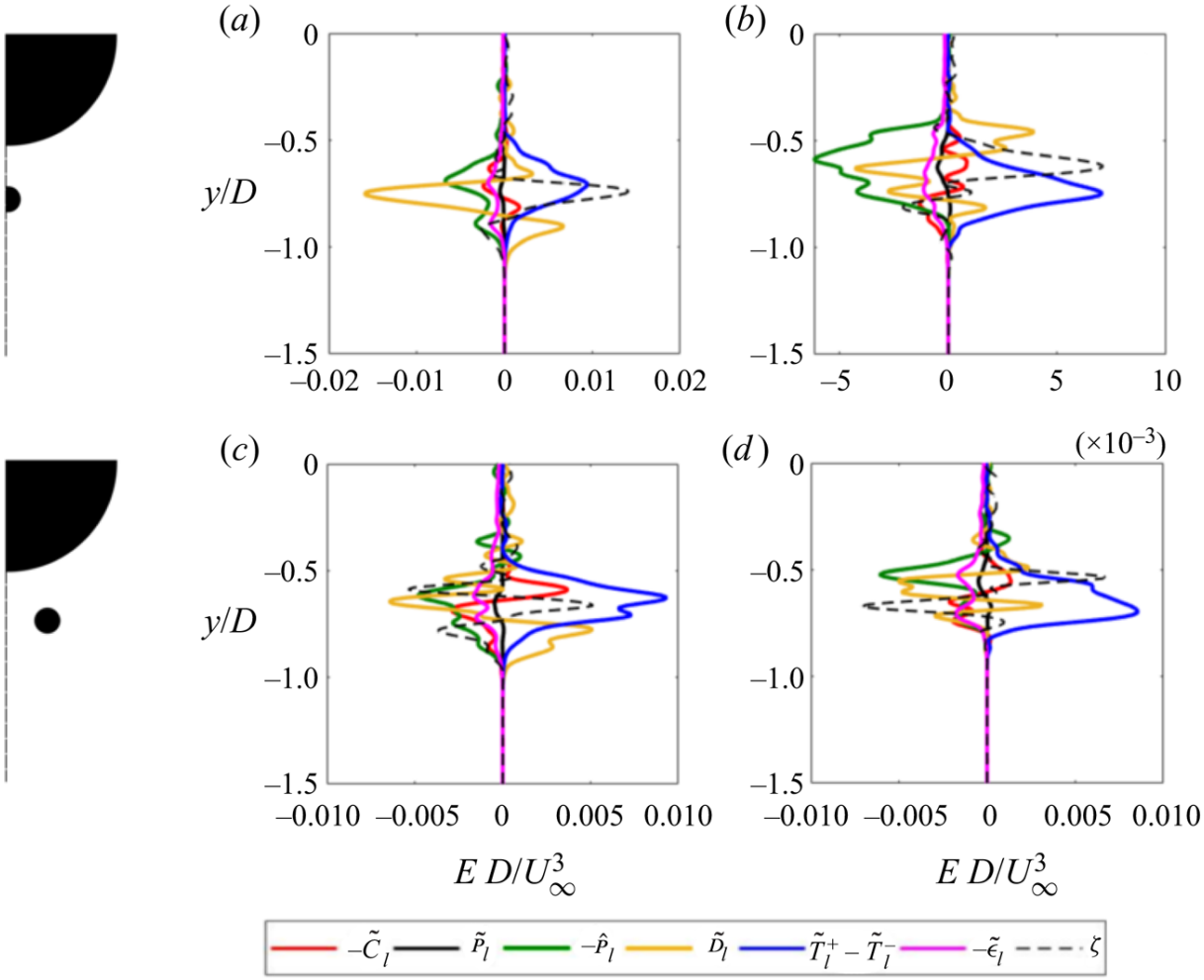


Figure 5.17: Kinetic energy budget terms for (a) low- and (b) high-frequency secondary coherent modes for $\theta = 90°$ at the wake intersection point. Figure (c-d) shows the same for $\theta = 110°$ at the corresponding wake intersection point.

In figure 5.16, the two thick bars on the left show the net contribution from $\tilde{P}_l$ and the triadic

interaction term ($\tilde{T}_l$) respectively to the l^{th} mode, whilst the thinner bars towards the right break down the contributions from different modes to the overall triadic interaction term. All energy terms are obtained by performing integration over the domain spanned by $[(x1, y1), (x2, y2)]$, with $x1$ varying depending on the particular mode as discussed previously and $x2, y1$ and $y2$ set close to the edge of the domain avoiding spurious vectors towards the boundary. In figure 5.16, a positive contribution (*i.e.* energy is gained by the mode) is shown with a black bar whilst red bars signify a loss of energy. For the main cylinder's fundamental shedding mode (figure 5.16(a)) the net triadic production is positive, though negligible in comparison to production from the mean flow. The main source of triadic energy gain of f_m is the second harmonic ($2f_m$), while the energy transfers with the other modes is an order of magnitude smaller. This energy transfer between the main cylinder's fundamental shedding mode and its harmonics differs significantly from the findings of Jin et al. (2021). However the authors reported the energy transfers between the modes at a Reynolds number 2 orders of magnitudes lower than the present study and hence a significant difference can be expected in the energy transfer processes.

It is also interesting to note from figure 5.16(a) that the two secondary modes behave in an opposite fashion to one another, *i.e.* the low-frequency mode (f_{c-m}) gains some energy from f_m whilst the high-frequency mode (f_{c+m}) transfers almost the same amount of energy to f_m. Unlike the main cylinder's fundamental shedding mode, the control rod's shedding mode (f_c) is solely energised by the mean flow (figure 5.16(b)). This mode gives away an almost equal amount of energy to both the secondary coherent structures.

5.4.3 On the origin of the secondary coherent structures

Next the kinetic energy budget terms are obtained for the secondary coherent motions shown in figure 5.11. Figure 5.17 shows the energy budget terms for the secondary modes at the wake intersection points for $\theta = 90°$ and $110°$. Note that the qualitative trend for the modes is remarkably similar for both values of θ, although subtle differences do exist. Unlike the primary shedding modes discussed earlier, the main source of energy for the secondary modes is the triadic energy production term whereas the energy production from the mean flow is negligible, and even slightly negative; similar to the findings of Baj and Buxton (2017). This fundamental

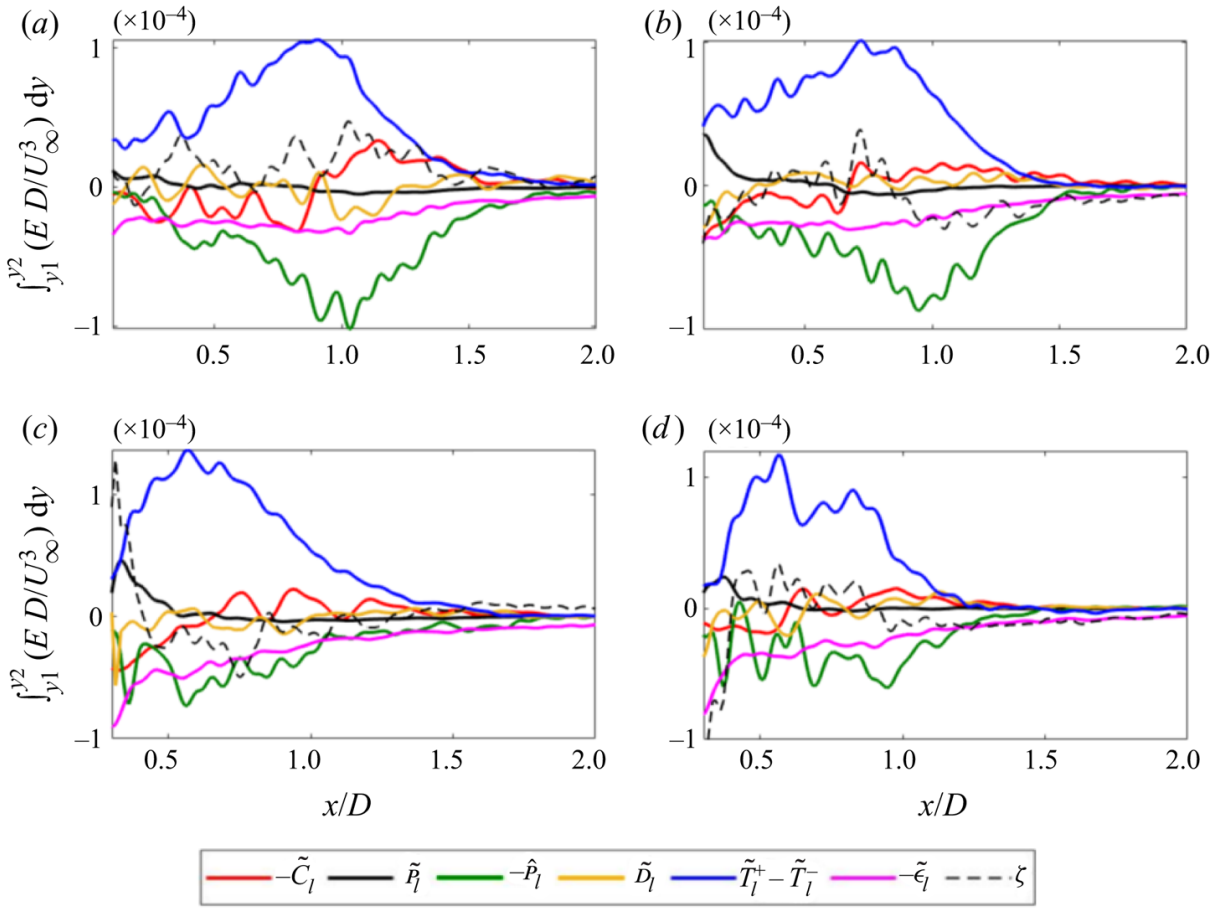


Figure 5.18: Streamwise evolution of the integrated kinetic energy budget terms for (a) low- and (b) high-frequency secondary modes for $\theta = 90°$. Figure (c-d) shows the same for $\theta = 110°$.

difference in the primary energy source of the mode justifies naming them as "secondary" since they are not directly energised by the mean flow. Note that the secondary modes play a major role in the energy cascade as a significant amount of energy is drained into stochastic turbulent motion through them. The net contribution of the diffusion and convection terms at this station for both the modes is small and is rather inconclusive.

A clearer picture is obtained by looking at the streamwise evolution of the various integrated kinetic energy budget terms in figure 5.18. For both the low-frequency and high-frequency secondary modes, the major source of energy is the triadic production term everywhere in the domain whereas production from the mean flow is negligible. Further, note that the triadic production term of the secondary modes at $\theta = 90°$ peaks further downstream than for $\theta = 110°$. Recall from figure 5.11 that the maximum of the kinetic energy of the secondary modes indeed appeared slightly downstream for $\theta = 90°$ compared to $\theta = 110°$, and the evolution of the

triadic energy production term explains this observation. This is also in line with the nearer wake intersection point observed for $\theta = 110°$ compared to $\theta = 90°$. Baj and Buxton (2017) found that the low-frequency secondary mode was more spatially persistent compared to the high-frequency one. A similar observation is recorded here. At $\theta = 90°$, the convection term becomes positive earlier for the high-frequency secondary mode, implying that the high-frequency secondary mode starts to decay earlier compared to its low-frequency counterpart. A similar trend, although not pronounced, is observed for $\theta = 110°$ as well. Moreover, see that for both values of θ, the triadic energy production term drops off earlier for the high-frequency secondary mode. It is believed that a combination of both of these effects results in a more spatially persistent low-frequency secondary mode compared to the high-frequency one.

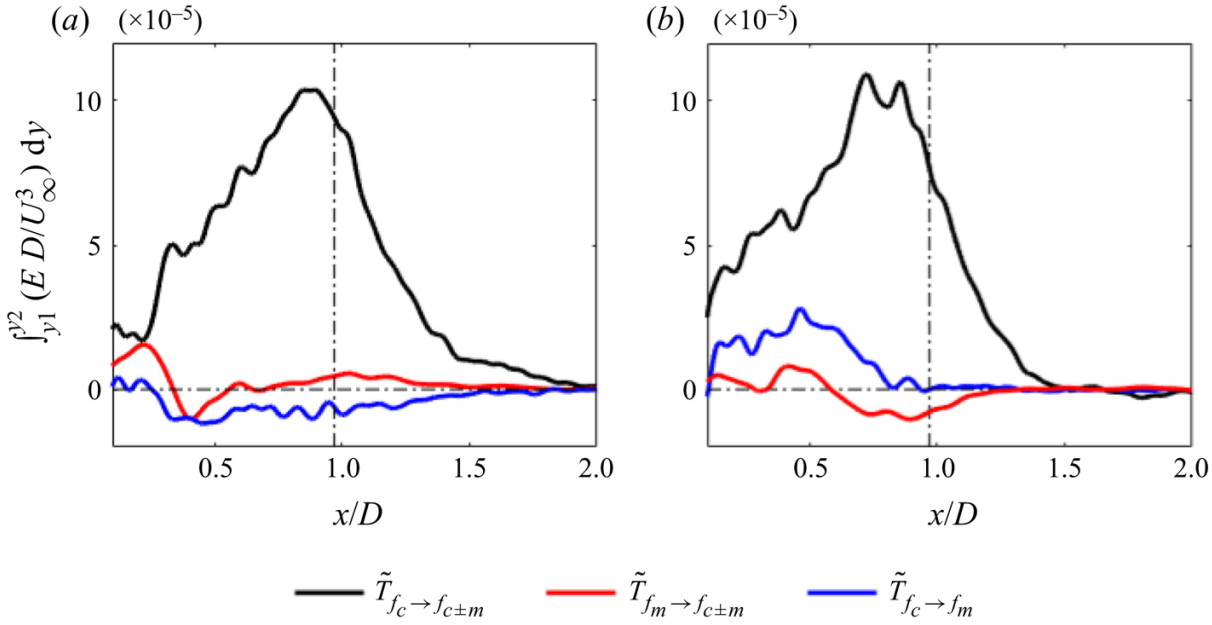


Figure 5.19: Streamwise evolution of certain triadic energy transfer terms for (a) low- and (b) high-frequency secondary modes at $\theta = 90°$.

Next, the non-linear energy transfers between two modes in the triads $[f_m, f_c, f_{c\pm m}]$ are compared. The spatial evolution of the non-linear energy transfer terms for $\theta = 90°$ are shown in figure 5.19(a-b) for the low-frequency and high-frequency secondary modes respectively. The solid black curve shows the non-linear energy transfer from f_c to $f_{c\pm m}$, $\tilde{T}_{f_c \to f_{c\pm m}}$ defined as

$$\tilde{T}_{f_c \to f_{c\pm m}} = -\frac{1}{2}\overline{u_i^{f_{c\pm m}} u_j^{f_m} \frac{\partial u_i^{f_c}}{\partial x_j}} + \frac{1}{2}\overline{u_i^{f_c} u_j^{f_m} \frac{\partial u_i^{f_{c\pm m}}}{\partial x_j}}. \tag{5.9}$$

Here the main cylinder's shedding mode (f_m) acts as the catalyst. The net non-linear energy gain for both the secondary modes almost entirely comes from the control rod's shedding mode (f_c). The dashed vertical line shows the location of the wake intersection point. In the vicinity of the wake intersection point, the low-frequency secondary mode (f_{c-m}) receives a small amount of energy from f_m, while the high-frequency secondary mode (f_{c+m}) loses some energy to f_m. Further, f_m receives some energy from f_c in the presence of f_{c-m}, whilst the direction of the energy transfer gets reversed in the presence of f_{c+m}. The exact same sequence of energy transfers was reported by Baj and Buxton (2017) near the wake intersection points in the wake of a multiscale array of rectangular prisms.

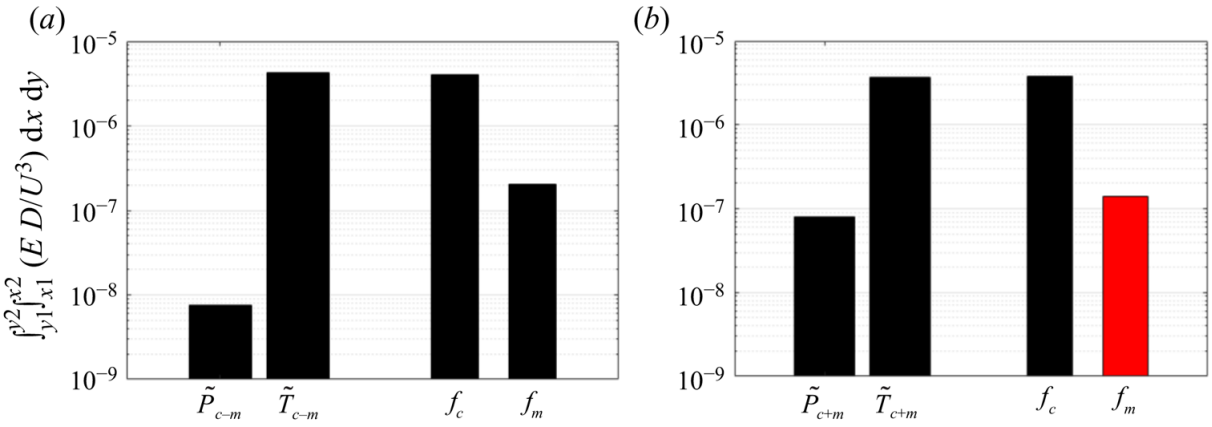


Figure 5.20: Net energy transfer through coherent energy production and non-linear triadic energy transfer terms for (a) low- and (b) high-frequency secondary modes at $\theta = 90°$. The colours of the bars bear the same meaning as in figure 5.16.

Similar to figure 5.16, the production terms and the triadic energy transfer terms from other modes are integrated over the whole domain for the secondary modes, starting from $x/D = 0.1$. The results are shown in figure 5.20. As expected the main source of energy for both the secondary modes is the non-linear energy transfer from f_c and production from the mean flow is negligible. The net energy transfer between f_m and the secondary modes is almost equal in magnitude and opposite in direction. Hence, it can be said that the sequence of energy transfers first reported by Baj and Buxton (2017) not only applies locally near the wake intersection points, but also applies globally when the net energy transfer in the domain is considered. Indeed, such similarity in the energy transfer process observed in two different flows is remarkable and it further strengthens the notion that this pattern of energy exchange in a triad of primary and secondary coherent motions is universal in two dimensional multiscale flows. Note that the flow

considered in the present work is different from the flow investigated by Baj and Buxton (2017) in 2 major aspects: 1) for the present case the spectral separation of the two primary modes is much larger (see figure 5.5(c,e)). 2) The sizes of the control rod and the cylinder differ by an order of magnitude in the present case hence the energy difference between the two primary coherent modes is quite large compared to Baj and Buxton (2017). The fact that similar energy exchanges are found in two fundamentally different flows is both fascinating and significant for further understanding multiscale flows.

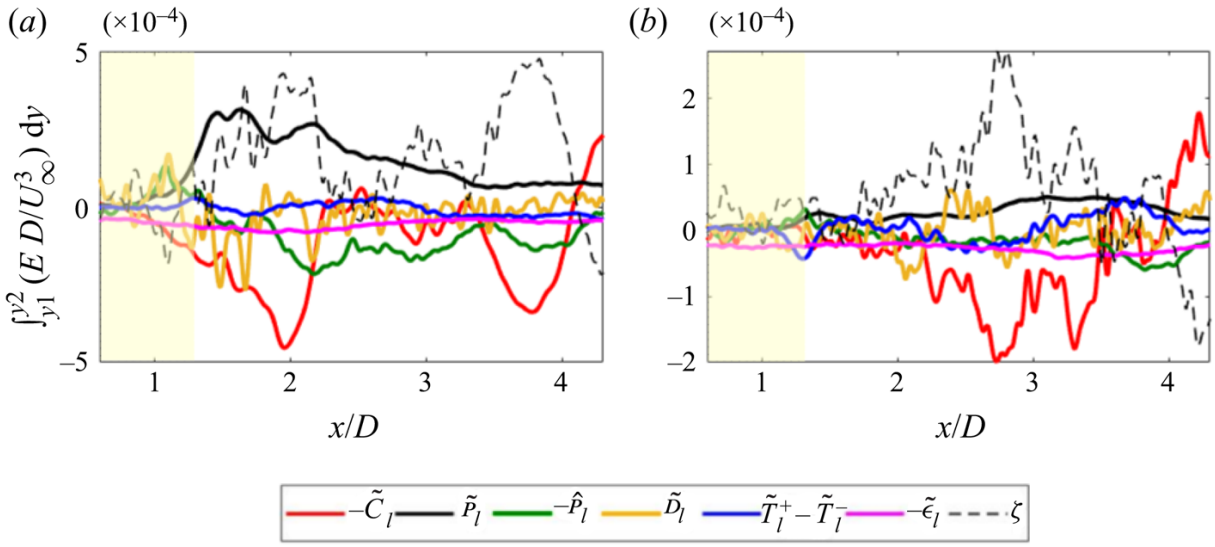


Figure 5.21: Streamwise evolution of the kinetic energy budget terms for (a) the second harmonic ($2f_m$) and (b) the third harmonic ($3f_m$) of the main cylinder shedding mode for $\theta = 90°$. The region highlighted in yellow color is excluded in further analysis to avoid spatially incoherent region of the modes.

5.4.4 Energy exchanges for the harmonics

The same analysis is also applied for the harmonics of the main cylinder's shedding mode (f_m) to better understand the nature of the modes. The evolution of the integrated TKE budget terms are shown in figure 5.21 for $\theta = 90°$. Due to qualitative similarity of the modes for $\theta = 90°$ and $\theta = 110°$, the analysis is restricted to $\theta = 90°$. As discussed earlier, the second and third harmonics of the main cylinder's shedding mode being spatially coherent beyond $x/D \approx 1.3$, the region highlighted with a yellow colour in figure 5.21 is excluded for further analysis. The terms in figure 5.21 look much noisier compared to the corresponding ones for the primary modes (f_c, f_m) and even the secondary modes ($f_c \pm f_m$) seen earlier. Nevertheless,

several insightful conclusions can be drawn from the plots. First of all, note that unlike the secondary modes observed in figure 5.18, the main source of energy for both the harmonics is still production from the mean flow. This is in contrast to the observation of Jin et al. (2021) who found that the primary source of energy for the harmonics was the fundamental shedding mode at a $Re = 100$. This fundamental difference in the primary energy source of the harmonics is believed to be a manifestation of the larger Re in the present case. However, the contribution of the non-linear triadic interaction term is not negligible as observed for the primary modes in figure 5.15. Therefore, the harmonics can neither be termed as "primary" modes which feed from the mean flow nor "secondary modes" which derive their energy from the primary modes alone. The harmonics rather behave as "intermediate" or "mixed" modes at this Re. The modes drain a significant amount of energy to stochastic turbulent kinetic energy and dissipation as can be seen from figure 5.21. The trends of the convection and diffusion terms however are comparatively noisy and hard to draw conclusions from.

Figure 5.22 shows the total contribution from the production term and triadic interaction terms for the harmonics. The terms are integrated from $x1 = 1.3$. Note that the magnitude of the triadic energy transfer term is smaller compared to the production term as expected. However, the triadic interaction term can still be significantly important and in fact, it is a significant source of energy for the third harmonic. The third harmonic is positively energised by both the fundamental mode and the second harmonic, while the non-linear energy gain of the fundamental mode is mainly due to the second harmonic.

In order to understand the effect of the selected domain of integration on the net contribution from coherent energy production and triadic interaction terms for the harmonics of the main cylinder (as shown in figure 5.22), the starting point of the domain of integration ($x1$) is varied and the variation in the terms are shown in figure 5.23. It is found that for both the second and third harmonics, the net coherent energy production does not alter significantly if $x1$ is reduced below $1.3D$. Hence, for both the harmonics $x1$ is set to be $1.3D$.

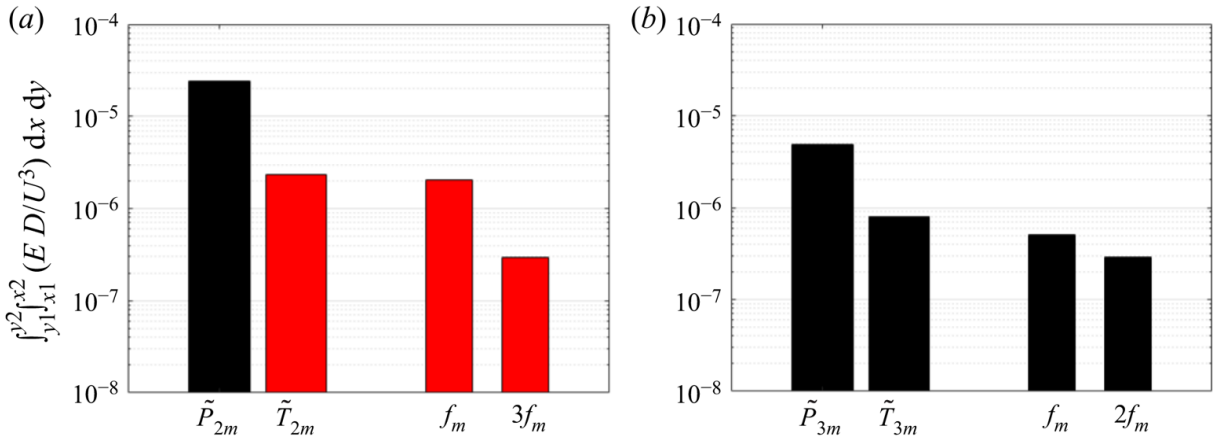


Figure 5.22: Net contribution from the production and triadic interaction terms for (a) the second harmonic ($2f_m$) and (b) the third harmonic ($3f_m$) of the main cylinder. The colours of the bars bear the same meaning as in figure 5.16.

5.4.5 Summarising the energy cascade

The entire energy transfer process from the mean flow to the coherent motions, and also between the different coherent motions is shown through a flow diagram in figure 5.24. The 6 modes identified in the flow, namely $f_m, 2f_m, 3f_m, f_{c-m}, f_c, f_{c+m}$, are shown as yellow circles. For visual representation, the modes are placed from bottom to top in increasing order of frequency, although not to scale. Further, the lower frequencies are shown as a larger circle as a representation of their larger spatial extent. The full headed arrows show the net energy transfer between the mean flow and the coherent motions. The full headed black arrows show energy gain of the modes, whilst red arrows show loss of energy. The half-headed arrows on the other hand represent non-linear energy transfer between two modes. Solid arrows represent energy transfer from low-frequency to high-frequency whilst dashed arrows represent energy transfer from high-frequency to low-frequency, or an inverse energy cascade. Note that the primary modes, f_m and f_c, draw the largest amount of energy from the mean flow, whilst the energy transfer to the secondary modes ($f_{c\pm m}$) from the mean flow is negligible and negative in the domain of investigation similar to the findings of Baj and Buxton (2017). The primary energy source of the harmonics is also the mean flow, however the energy received by the harmonics is significantly lower compared to the primary modes. The three triads (each triad consisting of three different frequencies whose linear combination sum to zero) formed by the half-headed arrows can be identified as the regions shaded with different colors. In triad 1 and triad 2 (shaded by

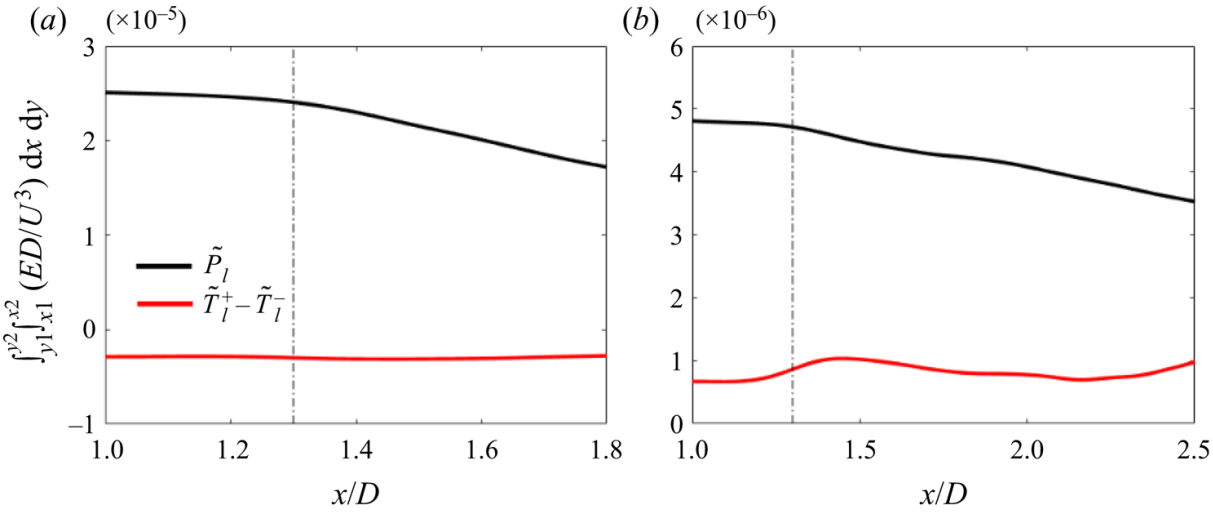


Figure 5.23: Effect of changing the domain of integration on the coherent energy production and triadic interaction terms of the (a) second and (b) third harmonics of the main cylinder's shedding frequency for $\theta = 90°$.

pink and green colours respectively), f_c shares almost the same amount of energy to f_{c+m} and f_{c-m}. During both of these transfers, f_m acts as the mediator. In triad 1, f_{c+m} then transfers some of its energy to f_m. Interestingly, f_m then transfers almost the same amount of energy to f_{c-m}. As a consequence, the net non-linear energy gain of the low-frequency secondary mode is higher than the high-frequency secondary mode and this is consistent with the greater spatial persistence of the lower secondary mode observed in our current work and by Baj and Buxton (2017). The energy transfers between f_c and f_m in the two triads are of similar magnitude and opposite in sign. These energy transfer trends in triad 1 and triad 2 are qualitatively identical to the findings of Baj and Buxton (2017).

The third triad formed by the main cylinder's fundamental shedding mode and its harmonics is shown in a blue color. $2f_m$ shares just around 8% of the total energy it receives from the mean flow to f_m, nearly 34% of which f_m shares to f_{3m}. Note that almost half the non-linear energy transfer for the present flow takes place from a high-frequency mode to a low-frequency mode, implying a significant amount of inverse energy cascade. Such inverse energy cascades have also been observed in the near wake of a multiscale (Gomes-Fernandes et al., 2015; Baj and Buxton, 2017) or single scale geometry (Jin et al., 2021) and are important in understanding the inter-scale dynamics in flows consisting of several length/time scales.

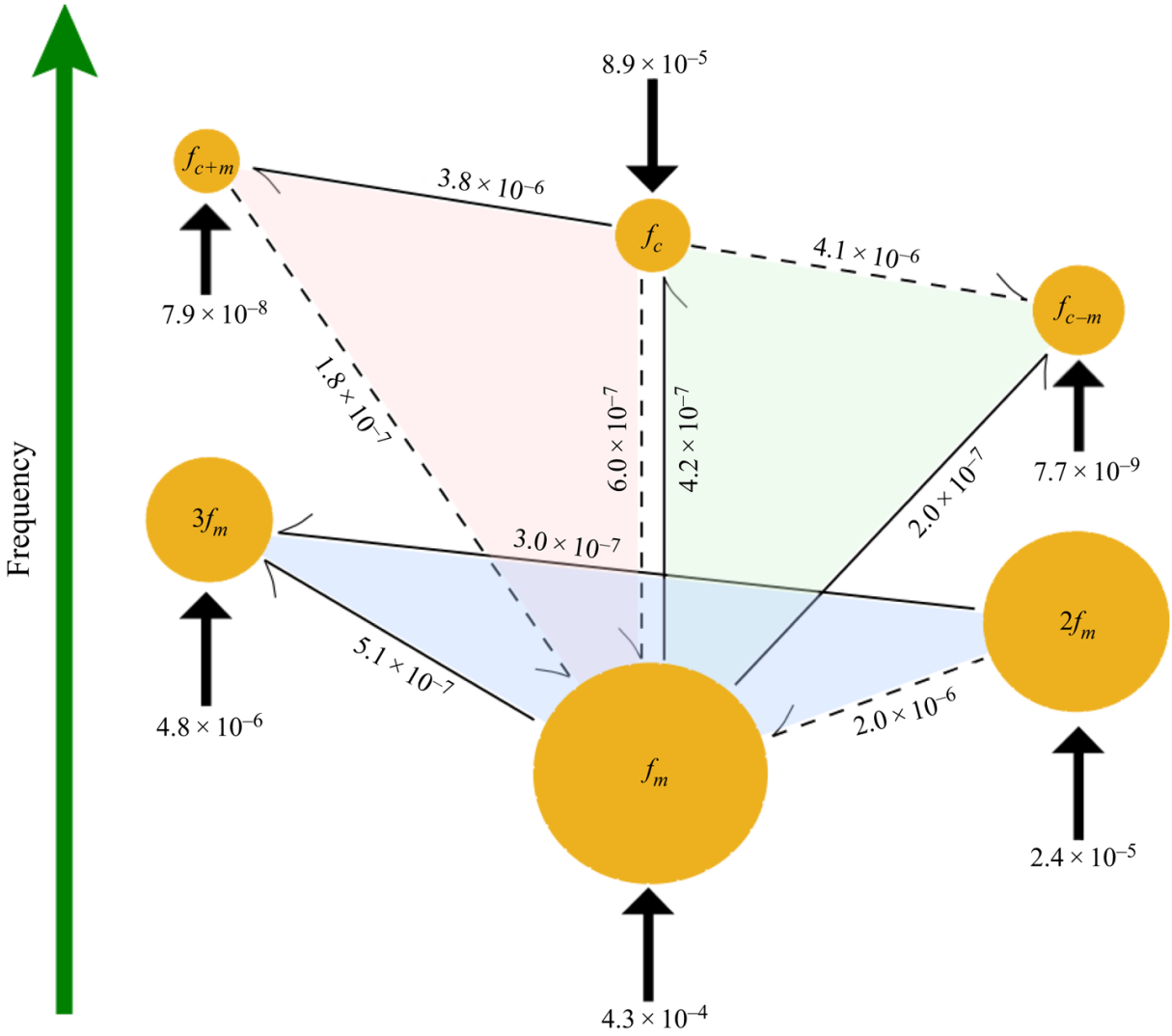


Figure 5.24: Combined schematic energy transfer diagram for the different modes identified within the flow. The modes are arranged such that characteristic frequency of the modes increases from bottom to top. The thick full headed arrows show the net energy transfer between the various modes and the mean flow. The single headed arrows show the non-linear triadic energy transfer between two modes. A solid line shows non-linear energy transfer from low-frequency to high-frequency, whilst the dashed lines show energy transfers from high-frequency to low-frequency - an inverse cascade.

5.5 Conclusion

In this chapter a simple multiscale flow is studied using multiscale triple decomposition and coherent kinetic energy budget analysis. The multiscale flow consisted of a main cylinder and control rod and the data was originally obtained Cicolin et al. (2021). Aside from the frequencies associated with the fundamental shedding modes of the control rod and the main cylinder (and its harmonics), new secondary frequencies are observed in the spectra of the transverse velocity

component that correspond to the sum and difference of the control rod's and main cylinder's fundamental shedding frequencies. The spatial configuration of these secondary frequencies observed at two different control rod angles reveals a remarkable similarity to the findings of Baj and Buxton (2017) in the near wake of a multiscale array of rectangular prisms, hinting at a possible universality of the flow physics that generate these secondary modes. Specifically, the high-frequency secondary mode is found to position itself near the separated shear layer between the two wake-generating bodies, whilst the low-frequency secondary mode resides towards the opposite shear layer separating from the control rod. The multiscale triple decomposition method proposed by Baj et al. (2015) is applied to identify all of the coherent modes associated with each of the distinct frequencies identified within the flow. The secondary modes show a pronounced region of phase-correlated velocity (vorticity) that correlates well with the definition of a coherent structure proposed by Hussain (1986).

The energy exchanges taking place between the mean flow and the coherent motions is studied, as well as the energy exchanges taking place between the various coherent motions in the context of the multiscale triple-decomposed energy budgets. The increase in the net energy losses suffered by the mean flow in the presence of the control rod compared to a bare cylinder (cylinder without control rod) is found to correlate remarkably well to the overall increase of mean drag for the main-cylinder-and-control-rod-assembly reported by Cicolin et al. (2021) for the same control rod positions. Further, the net energy lost to the coherent motions ($\sum_l \tilde{P}_l$) in the presence of the control rod agrees well with the relative changes in the fluctuating loads when compared to the bare cylinder, as reported by Cicolin et al. (2021).

Assessing the kinetic energy budgets of the individual coherent motions, it is found that the fundamental shedding modes of the control rod and the main cylinder are energised by the mean flow. Contrastingly, the secondary coherent modes are found to be primarily energised by the non-linear triadic energy transfer from the control rod's fundamental shedding mode. Although both secondary modes receive a nearly equal amount of energy from the control rod's fundamental shedding mode, the high-frequency secondary mode transfers some amount of energy to the main cylinder's fundamental shedding mode. This energy is subsequently transferred to the low-frequency secondary mode thereby forming a net inverse cascade. This sequence of energy transfers results in a more spatially persistent low-frequency secondary coherent mode compared

to its high-frequency counterpart, a similar result to Baj and Buxton (2017) for a different multiscale flow. The similarity between the secondary modes and their formation mechanisms, reported in two different studies consisting of markedly different wake-generating bodies further strengthens the notion of universality of these structures, and the nature of the energy transfers that feed them, in a general multiscale flow. Note that Baj and Buxton (2017) tracked the energy exchanges for the secondary modes at selected spatial locations *only*. Unlike them, the detailed spatial evolution of the non-linear energy fluxes involving the secondary modes are reported here. It is found that the non-linear energy flux from the control rod's shedding mode to the secondary modes, which is the main driver for the secondary modes, peaks in the vicinity of the wake intersection points, hence firmly establishing the importance of the wake intersection points in multiscale flows also identified by previous works (Gomes-Fernandes et al., 2012; Mazellier and Vassilicos, 2010; Baj and Buxton, 2017). Integrating the non-linear energy fluxes over the entire domain, it is deduced that the sequence of energy transfers between the primary and the secondary modes first reported by Baj and Buxton (2017) not only applies locally at the wake intersection points, but also it applies for the net non-linear energy transfers in the entire domain in which the secondary coherent structures are energetic. Interestingly, unlike the primary modes (the main cylinder's and control rod's shedding modes) and the secondary modes, it is shown that harmonics can be energised by both the mean flow and non-linear triadic energy exchanges at our Re, implying a *mixed* or *intermediate* character of the modes at this Re.

Another facet of the work is that a significant amount of non-linear energy transfer from high-frequency modes to low-frequency modes is observed, a phenomenon commonly referred to as an inverse energy cascade in turbulent flows (Gomes-Fernandes et al., 2015; Biferale et al., 2012; Jin et al., 2021). The recent study by Jin et al. (2021) showed that resolvent analysis (which is only based on the mean flow) failed to correctly capture the non-linear energy transfers in a cylinder wake. Accordingly, the present analysis not only improves our understanding of the complex energy exchanges taking place in a widely studied flow, but it also offers an opportunity to better model the non-linear energy transfers in flows of practical relevance such as the wake of a wind turbine.

Chapter 6

Coherent energy budgets in wind turbine wake

6.1 Introduction

In chapter 3 a large variety of length scales (and associated time scales/ frequencies) contained in a wind turbine wake were discussed. The important scales included the turbine's rotational frequency (f_r), blade passing frequency or the frequency associated with the passage of the tip vortices (which is numerically equal to three times the rotational frequency for a three-bladed turbine, $3f_r$). Other harmonics of f_r and $3f_r$ were also observed which although not as energetic as the former, can have an important role in the energy exchange processes as will be discussed. Distinct frequencies associated with vortices shed from the nacelle and the tower were observed. The far wake was found to be dominated by large scale wake meandering. In this chapter, the origin and evolution of these scales are further understood by assessing their kinetic energy budgets. The analysis is performed based on the data from experiment 1G. Most of the results reported in this chapter were published in Biswas and Buxton (2024b).

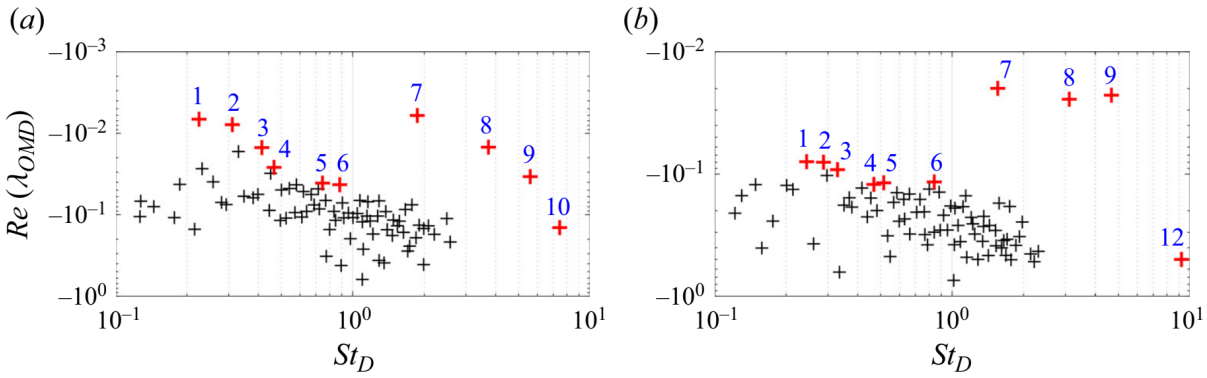


Figure 6.1: OMD spectra obtained for (a) $\lambda = 6$ and (b) $\lambda = 5$ from experiment 1G. The modes shown by a + sign are selected for a lower order representation of the flow. The high frequency modes with $St_D > 1$ are related to the tip vortices. The low frequency modes ($St_D < 1$) are associated with wake meandering, and the sheddings from the nacelle and the tower.

6.2 Coherent modes in the wake

The modes corresponding to individual coherent structures in the flow, $\tilde{\boldsymbol{u}}_l(\boldsymbol{x}, t)$ are extracted using Optimal Mode Decomposition (OMD), the details of which can be found in chapter 5. OMD is first performed on the large FOV obtained from experiment 1G (see chapter 2 for details). Example OMD spectra are shown in figures 6.1(a) and 6.1(b) for $\lambda = 6$ and $\lambda = 5$ respectively. The rank of the OMD matrices (r) was set to 175. A sensitivity study was performed before selecting this r and the results were found to be largely invariant to the selection of r. This is discussed in detail in appendix A.2. In figure 6.1, the x axis shows the Strouhal number ($St_D = fD/U_\infty$) associated with the modes, while the y axis shows the growth rates of the modes. The less damped modes have a growth rate closer to zero and are likely to represent a physically meaningful coherent motion in the flow. A total of 12 modes were selected for both λs based on the observed growth rates from the OMD spectra and knowledge of important frequencies present in the wake based on the experimental results presented in chapter 3. The selected modes are highlighted with + signs in figure 6.1. Among them the modes on the top right branch of the spectra ($St_D > 1$) correspond to the tip vortices and their harmonics. Mode 7 has a frequency equal to the turbine's rotation, henceforth denoted as f_r. Similarly the other two modes (modes 8 and 9) represent frequencies $2f_r$ and $3f_r$ (blade passing frequency) respectively. In chapter 3, the presence of higher harmonics of the tip vortices was verified up to a frequency of $6f_r$. However, not all the higher harmonics ($4f_r - 6f_r$) could be

captured for a particular λ as can be seen from figure 6.1. This is because the higher harmonics are generally weaker in nature and most of their energy can be expected to be concentrated near the rotor. For $\lambda = 6$, only $4f_r$ (mode 10) was captured, while for $\lambda = 5$, $6f_r$ (mode 12) could be captured for $r = 175$. For $\lambda = 6$, OMD was performed with a higher $r = 250$ (see appendix A.2) but the frequencies $5f_r$ and $6f_r$ were still absent. Any larger rank would overly populate the spectra especially in the low frequency ($St_D < 1$) region making it harder to identify the physically meaningful modes. Therefore, r was fixed to 175. To obtain the full set of tip vortex related modes ($f_r - 6f_r$) in the full domain (x up to $5D$), the remaining modes were obtained using phase averaging similar to that discussed in chapter 5. For the low-frequency modes, six modes were retained with $St_D < 1$ that were found to be physically meaningful. The modes in the range $1 < St_D < 3$ (other than f_r) were found to be much weaker in nature and they did not show any significant energy exchanges. Accordingly, these modes were excluded. A more detailed discussion on this can be found in appendix A.2.

6.2.1 Tip vortices

The spatial nature of the modes associated with the tip vortices obtained from experiment 1G are first discussed. The transverse velocity components of the modes associated with the frequencies $f_r - 6f_r$ are shown in figures 6.2(a-f) for $\lambda = 6$ and in figures 6.2(g-l) for $\lambda = 5$. The '+' sign shows the location where the time-averaged kinetic energy of the modes is maximum. Figures 6.2(c) and 6.2(i) show the modes associated with the tip vortices ($3f_r$) and the modes are qualitatively similar for both λs. The modes can be expected to be the most energetic near the rotor plane and hence are found to monotonically decay within the field of investigation. The modes associated with the frequency f_r are shown in figures 6.2(a) and 6.2(g) for the two λs which represent large-scale structures associated with the merging of the tip vortices as discussed in chapter 3. Note that the spatial organisation of the mode is significantly different for different λ unlike the tip vortices. For $\lambda = 6$, the mode is stronger and its energy content peaks nearer to the turbine which reaffirms a stronger and earlier interaction between the tip vortices for a higher λ (Felli et al., 2011; Sherry et al., 2013a). Furthermore, for $\lambda = 5$, there is a region near the root of the blades where f_r is energetic, which is believed to have resulted from an earlier interaction of the unstable root vortices. The variation of angle of attack (AOA) along

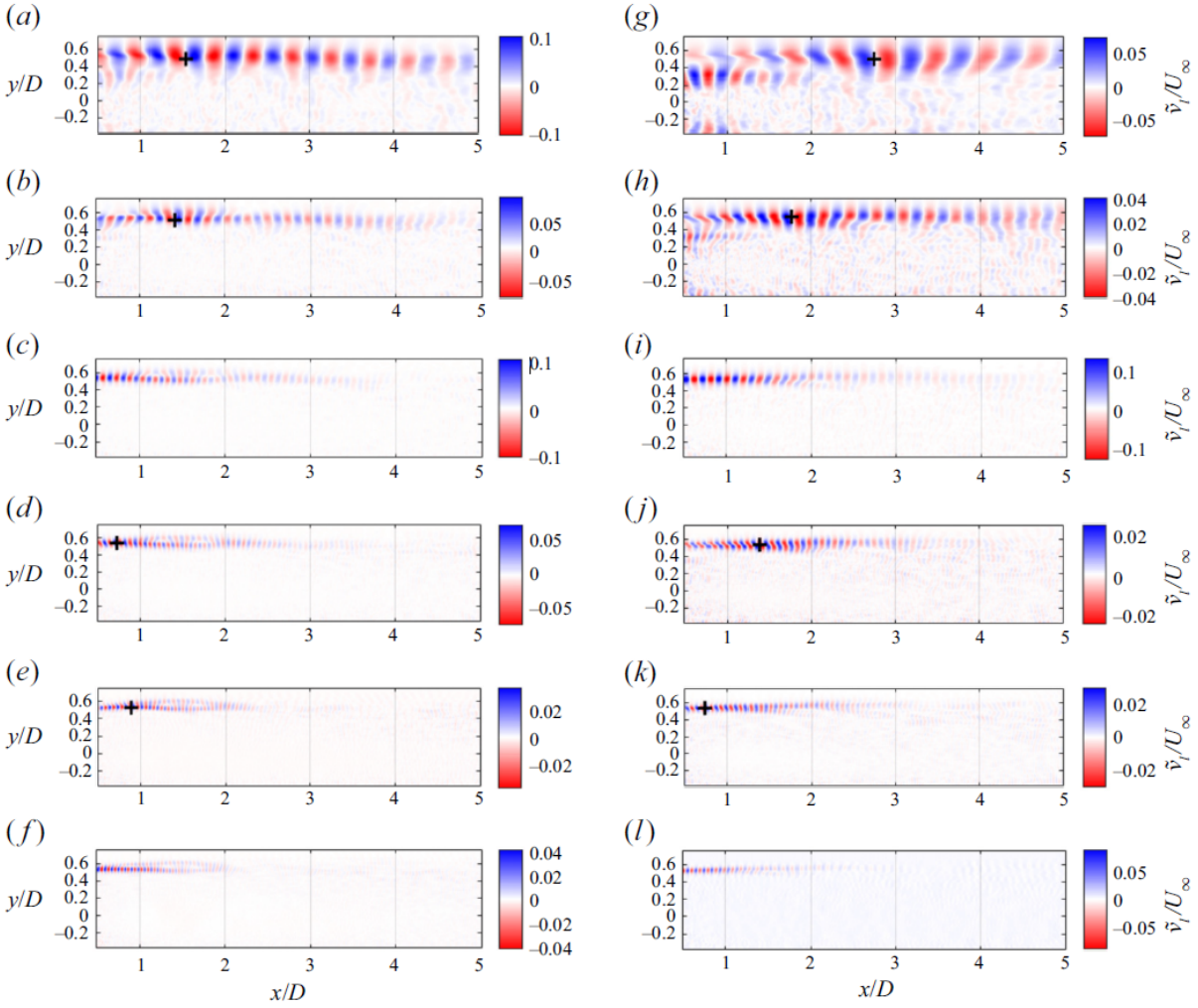


Figure 6.2: Transverse velocity component of the OMD modes associated with f_r - $6f_r$ for $\lambda = 6$ (a - f) and $\lambda = 5$ (g - l). The + sign shows the location where the kinetic energy associated with the individual modes is maximum.

the blades for different λ was estimated using the blade element momentum (BEM) method. The local AOA near the root for $\lambda = 5$ was estimated to be $\approx 8^o$, significantly higher than that for $\lambda = 6$ ($\approx 5^o$) which is in line with the observation of stronger root vortices for the lower λ.

A similar dependence on λ is observed for $2f_r$, *i.e.* the mode peaks at an earlier streamwise location for $\lambda = 6$ (note the '+' sign), and there is a region near the root where the mode is energetic for $\lambda = 5$. Note that $2f_r$ forms a triad with f_r and $3f_r$, suggesting possible triadic energy exchanges between these three modes. Another interesting observation is that the kinetic energy of $2f_r$ peaks at a streamwise location which is between that of f_r and $3f_r$. This is reminiscent of the secondary modes observed for the simplified multiscale flow discussed in chapter 5. These secondary modes arose from the non-linear triadic interaction between two

primary modes of different characteristic frequencies. The downstream streamwise location at which a secondary mode was the most energetic laid between the corresponding locations of the interacting high and low frequency primary modes. Whilst the secondary modes were produced due to triadic interactions, the primary modes were primarily energised by the mean flow. The nature and the origin of the modes will be understood in more detail in section 6.3 where the kinetic energy budgets associated with each individual mode will be assessed.

The modes associated with $4f_r - 6f_r$ are comparatively weaker and the energy of the modes peaks between the corresponding locations of a number of other modes. For instance, for $\lambda = 6$, $5f_r$ peaks between the corresponding locations for $2f_r$ and $3f_r$ and also between that of f_r and $4f_r$, both pairs summing to $5f_r$. Accordingly, a number of modes might contribute to the formation of these high frequency modes. For $\lambda = 5$ on the other hand, the peak of $5f_r$ lies only between that of $2f_r$ and $3f_r$, showing an interesting dependence with the tip speed ratio.

6.2.2 Low-frequency modes

Apart from the high-frequency modes related to the tip vortices, there are a number of low-frequency modes observed in the OMD spectra (modes 1-6) in figure 6.1. For $\lambda = 6$, modes 1 and 2 have St_D around 0.22 and 0.31 respectively, which matches well with the range of Strouhal numbers associated with large-scale oscillations due to wake meandering reported in past studies (Chamorro et al., 2013; Okulov et al., 2014). Indeed the corresponding transverse velocity fields for modes 1 and 2 presented in figures 6.3(a) and 6.3(b) show large-scale structures similar to wake meandering. For $\lambda = 5$ in figure 6.1(b), a number of modes are observed in the accepted Strouhal number range for wake meandering. They are shown in figure 6.3(g-i) and they again show large-scale coherence. Note that for both the tip speed ratios, the wake meandering mode starts from close to the nacelle and grows radially in the streamwise direction. The wavelength of the mode is shorter near the nacelle and stretches to around $1.5D - 2D$ further downstream which matches well with previous experimental and numerical studies (Howard et al., 2015; Foti et al., 2016).

A number of modes are also observed in the OMD spectra at $0.4 < St_D < 0.5$ and $0.7 < St_D < 0.9$. The former when nondimensionalised by the nacelle's diameter instead of turbine diameter

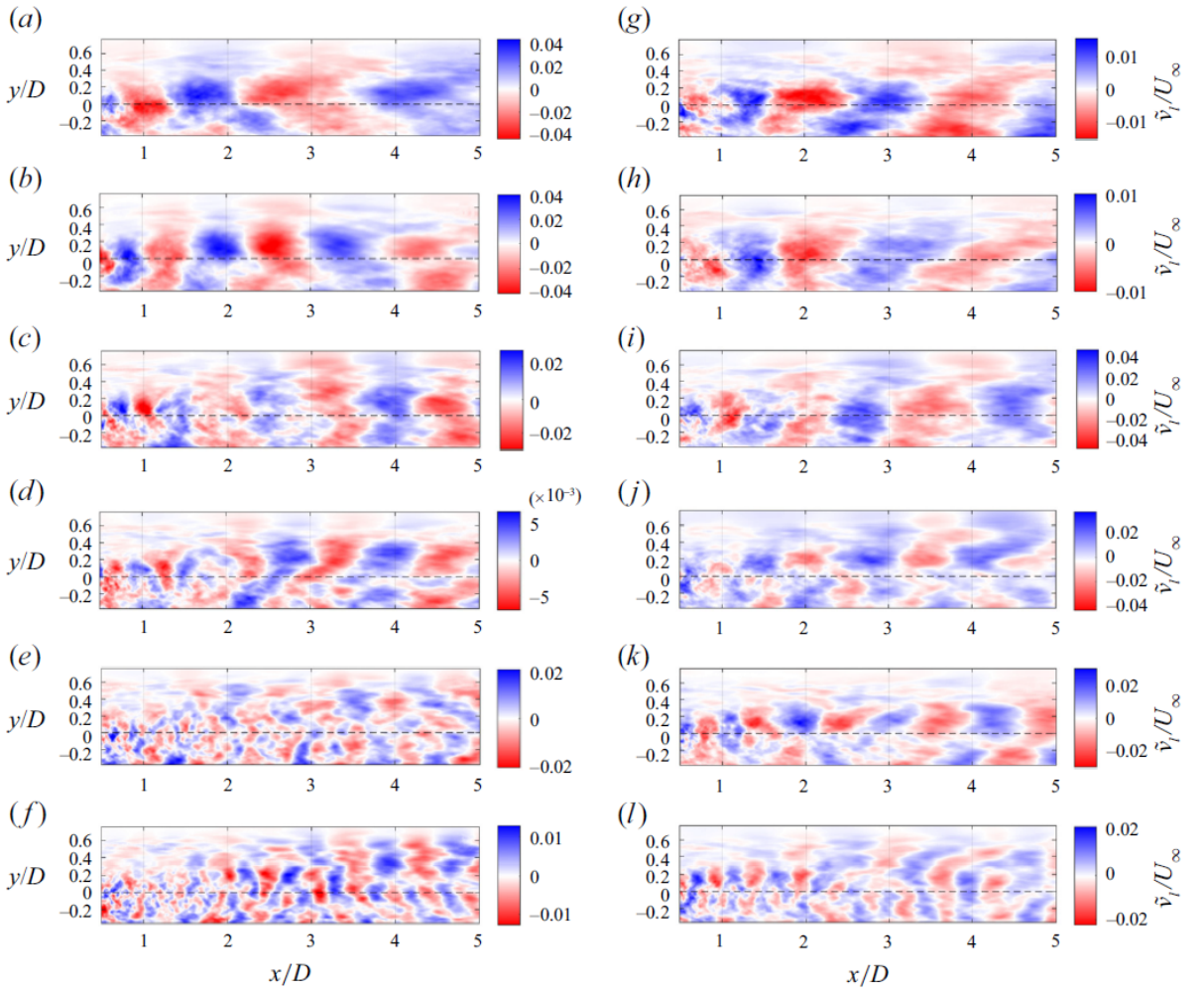


Figure 6.3: Transverse velocity component of the low frequency modes (labeled as 1-6 in figure 6.1) for $\lambda = 6$ (a - f) and $\lambda = 5$ (g - l).

yields a Strouhal number around 0.066 – 0.083 which is similar to the nacelle's vortex shedding frequency reported in previous studies (Abraham et al., 2019; Howard et al., 2015). These modes are numbered as modes 3-4 for $\lambda = 6$ (figure 6.1(a)) and as modes 4-5 for $\lambda = 5$ (figure 6.1(b)). These modes are however weaker compared to the wake meandering mode and are not spatially as coherent. A potential reason that the nacelle's shedding was not captured well could be due to the fact that the FOV in experiment 1G did not start from immediately downstream of the nacelle's rear face.

Similarly the modes in the Strouhal number range $0.7-0.9$ are most likely related to the shedding from the tower, although the corresponding Strouhal numbers based on the tower's diameter, around $0.074 - 0.095$ are much lower than the expected value of ≈ 0.2 for vortex shedding

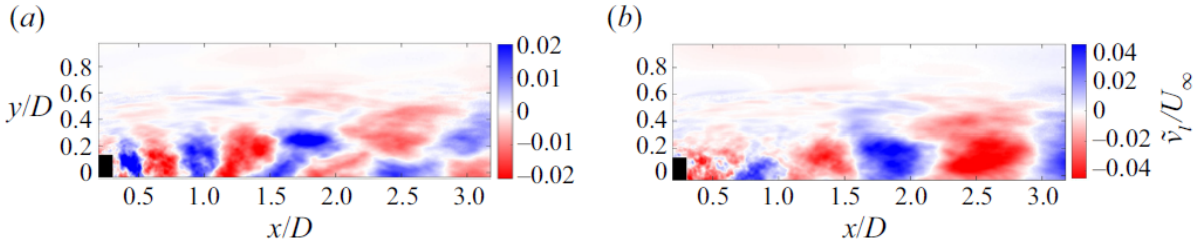


Figure 6.4: Transverse velocity components of the OMD modes associated with frequencies (a) f_n and (b) f_{wm} for $\lambda = 5.5$ obtained from experiment 1D.

behind a 2D circular cylinder at a similar Reynolds number ≈ 4000 based on the tower's diameter (Williamson, 1996). Such a reduction in the tower's vortex shedding frequency has been observed earlier (De Cillis et al., 2021) and was also discussed in chapter 3. In chapter 3, a number of factors were identified that could play a role such as the reduction of the freestream velocity as the flow passes through the rotor, shear induced on the incoming flow, the unsteadiness in the flow due to the passage of tip and trailing sheet vortices and other three-dimensional effects. As a result the vortex pattern is significantly distorted from the regular vortex street pattern one might expect. The modes which are expected to be associated with the tower's vortex shedding are shown in figures 6.3(e-f) for $\lambda = 6$ and in figure 6.3(l) for $\lambda = 5$. The modes are much weaker and are not as coherent as the other modes discussed here. This is firstly because of the altered vortex shedding pattern. Secondly, note that only the velocity fluctuation parallel to the tower's axis is considered here which only arises from the three dimensionality in the vortex shedding pattern and hence is not the dominant velocity component associated with the mode.

Unlike experiment 1G, the FOV of experiment 1D included the rear face of the nacelle (see figure 2.6). OMD was performed for all the λs obtained from experiment 1D keeping the rank r fixed to 175. The OMD spectra were similar to those obtained from experiment 1G, consisting of the modes related to the tip vortices and an assortment of low-frequency modes ($St_D < 1$). However, the nacelle's shedding mode obtained from experiment 1D was much more coherent than that observed from experiment 1G, as the FOV for the former included part of the nacelle. As an example, the nacelle's shedding mode for $\lambda = 5.5$ obtained from experiment 1D is shown in figure 6.4(a) which shows energetic structures near the nacelle that decay downstream. For a comparison, the wake meandering mode obtained for the same λ is shown in figure 6.4(b) which shows structures of a larger spatial extent that grow downstream and the mode is similar to

those observed for experiment 1G.

The OMD modes were also obtained from experiment 2, which considered planes perpendicular to the tower's axis. A selected number of modes are shown in figure 6.5 for $\lambda = 6$. Figures 6.5(a-c) show the modes $f_r - 3f_r$ in the $y = 0$ plane which are similar to those observed in figures 6.2(a-c). In the same plane, figure 6.5(d) shows the nacelle's shedding mode with a Strouhal number based on nacelle's diameter of around 0.069. The tower's shedding mode was not captured in the $y = 0$ plane. However, it was captured in the offset plane ($y = -0.35D$) and is shown in figure 6.5(e). The mode had a Strouhal number based on tower's diameter of around 0.08. Note that the mode is much more organised spatially and is more energetic than that observed in the xy plane. Interestingly, no modes could be captured from experiment 2 that resembled the wake meandering modes observed in figure 6.3. This is probably because the streamwise extent (up to $x/D \approx 1.85D$) of the field of view was not large enough to capture the structures associated with wake meandering which can have wavelengths as large as $1.5D - 2D$ (Howard et al., 2015). Additionally, the wake meandering mode can be expected to be more energetic beyond $x/D \approx 2$ (see figure 6.4(b)), making it highly unlikely to be captured in the short field of view.

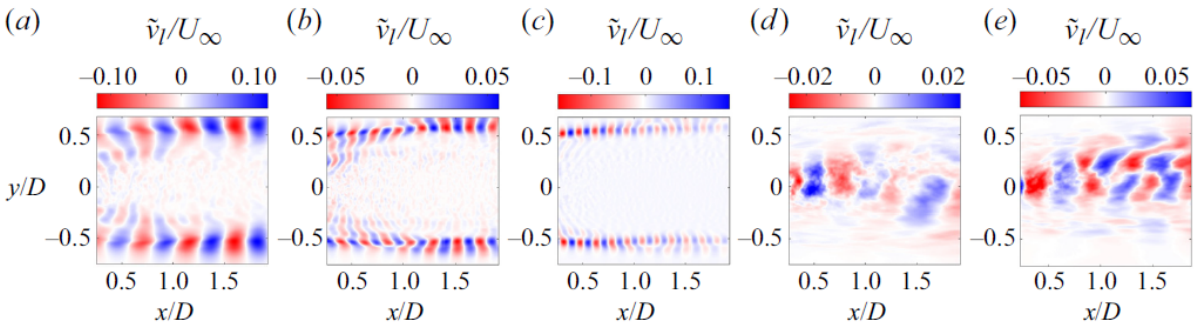


Figure 6.5: Transverse velocity components of the OMD modes associated with frequencies (a) f_r, (b) $2f_r$, (c) $3f_r$, (d) f_n obtained in the xz ($y = 0$) plane. Sub figure (e) shows the tower's vortex shedding mode at an offset plane $y = -0.35D$. The modes are shown for $\lambda = 6$ only.

6.3 Energy exchanges

The energy exchanges to and from the coherent modes present in the turbine's wake are explored using the multiscale triple decomposed coherent kinetic energy (CKE) budget equation discussed

in chapter 5 (equation 5.5). Note that the frequencies $f_r - 6f_r$ form a large number of triads, implying the triadic energy exchange term can play a significant role. The kinetic energy budgets of the modes obtained from experiment 1G are first assessed for the tip speed ratios 6 and 5. Since only planar data is available, the terms containing out of plane velocity and velocity gradients have to be ignored in the energy budget equation. The contribution to the diffusion term from the pressure is also ignored. However, as will be shown, this simplification does not alter the conclusions of the energy budget analysis. For both $\lambda = 6$ and $\lambda = 5$, the 12 modes shown in figures 6.2 and 6.3 are selected and the stochastic component of the flow is obtained by subtracting these modes from the mean-subtracted velocity field. It is worthwhile mentioning that this process leaves the spectrum of the stochastic turbulence continuous (Baj et al., 2015; Baj and Buxton, 2017). Please note that the energy budget terms reported here were previously reported in Biswas and Buxton (2024b). However, due to a bug in the post processing script, the terms were wrongly non-dimensionalised with D/U_∞^2 instead of D/U_∞^3. The error has been rectified here. This, however, does not change any of the conclusions drawn from the energy budget analysis.

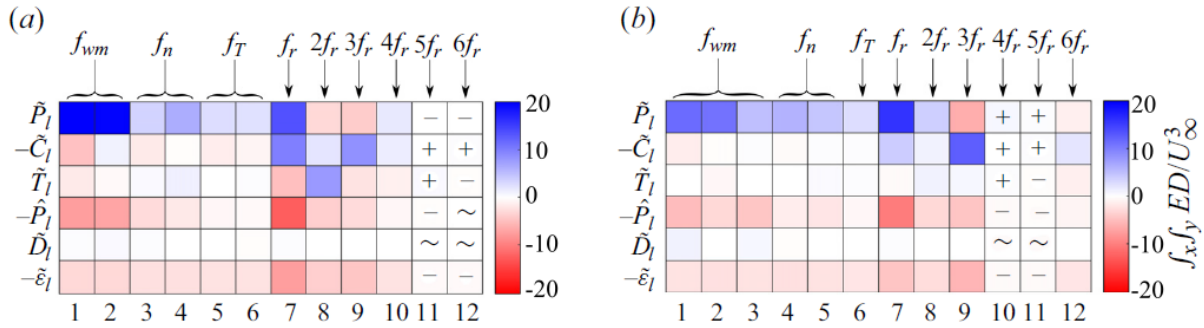


Figure 6.6: Energy budget terms of equation 5.5 summed over the domain of investigation for different modes for (a) $\lambda = 6$ and (b) $\lambda = 5$.

For an overall understanding, the terms from the CKE budget are first integrated over the entire domain of investigation for all the modes. The results are shown in figures 6.6(a) and 6.6(b) for $\lambda = 6$ and $\lambda = 5$. For the low-frequency modes ($St_D < 1$) including the wake meandering and nacelle or tower's vortex shedding, the primary energy source is the $\tilde{P}_l$ term or energy production from the mean flow, similar to the primary modes discussed in chapter 5. Among these primary modes, the wake meandering mode draws the highest amount of energy from the mean flow for both λs. The wake meandering mode for $\lambda = 6$ is more strongly energised than for $\lambda = 5$. A

similar dependence of the strength of the wake meandering mode on λ was reported in chapter 3. A link between λ and the effective porosity of the turbine was established. As λ increased, the effective porosity reduced, resulting in a decrement in the wake meandering frequency and an increment in the strength of the mode. Note from figure 6.1 that for the low-frequency modes, multiple triads are possible for which the frequencies sum to ≈ 0. For instance, for $\lambda = 6$, $f_1 + f_1 - f_4 \approx 0$, where f_1 is the mode numbered as 1 or the wake meandering mode (f_{wm}) and similarly f_4 is the 4th mode in the spectrum which is believed to be related to the nacelle's shedding (f_n). Another possible triad is $f_3 + f_4 - f_6 \approx 0$, where f_3 and f_4 are related to f_n and f_6 is likely related to the shedding from the tower (f_T). However, the triadic energy production term was not found to be the dominant term for any of these low-frequency modes as can be seen from figure 6.6. The modes associated with f_n are found to be slightly energised by the $\tilde{T}_l^+ - \tilde{T}_l^-$ term, while the wake meandering mode loses some energy due to non-linear interactions. All the low-frequency modes lose energy primarily through dissipation and production of incoherent (stochastic) turbulence. Hence, it can be said that non-linear triadic interactions are possible among these modes, however they are not the driving feature of their dynamics.

The tip vortices on the other hand are energised by a variety of energy sources. For both λs, f_r is primarily energised by the mean flow, thus behaving similarly to a primary mode. $3f_r$ only shows a positive convection (-$\tilde{C}_l$) term. This is expected as the tip vortices are formed at the passage of the blades and then advected into the PIV domain where they decay monotonically. Here a contribution from pressure diffusion can be expected to energise the mode, however, this cannot be captured with the current experiments. The nature of $2f_r$ changes with λ. For $\lambda = 6$, it is solely energised by the non-linear triadic interaction term, hence it acts like a secondary mode, similar to those observed in the simplified multiscale flow discussed in chapter 5. For $\lambda = 5$, it is energised primarily by the mean flow production term, while there is also some contribution from the nonlinear triadic interaction term. $2f_r$ therefore acts like a 'mixed mode' for $\lambda = 5$, also reported in chapter 5. The modes $4f_r - 6f_r$ are weaker compared to $f_r - 3f_r$. Specifically, $5f_r$ and $6f_r$ for $\lambda = 6$ and $4f_r$ and $5f_r$ for $\lambda = 5$ exhibited only very weak energy exchanges making it hard to see them in figure 6.6. Therefore a '+' or '-' sign is added to represent gain or loss of energy for these modes. A '$\sim$' sign is shown when the contribution from a term is found to be negligible ($|\int_x \int_y ED/U_\infty^3| < 0.01$). Note that for both λs $6f_r$ behaves

similarly to $3f_r$. For $\lambda = 6$, $4f_r$ and $5f_r$ behave similarly to f_r and $2f_r$ *i.e.* like a primary and secondary mode respectively. For $\lambda = 5$ on the other hand, $4f_r$ behaves like $2f_r$ (mixed mode) and $5f_r$ behaves like f_r (primary mode).

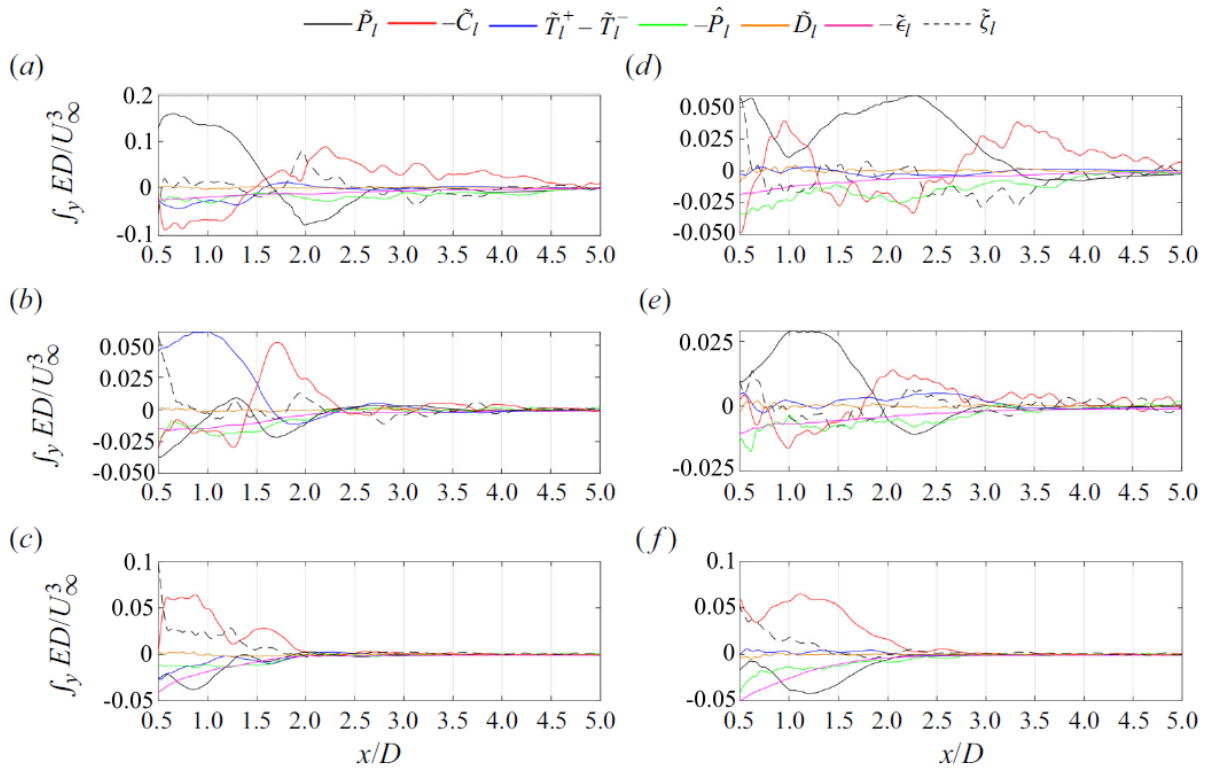


Figure 6.7: Streamwise evolution of the spanwise (along y) averaged energy budget terms of equation 5.5 for (a) f_r, (b) $2f_r$ and (c) $3f_r$ for $\lambda = 6$. Sub figures (d)-(f) show the same for $\lambda = 5$.

For a deeper understanding, the streamwise variation of the energy budget terms integrated along the spanwise (along y) direction is shown for the modes $f_r - 3f_r$ for the two λs in figure 6.7. The corresponding plots for $4f_r - 6f_r$ are not shown as their budgets were similar to one of the first three modes ($f_r - 3f_r$) as discussed earlier. Since the budget terms are considered in a time-averaged sense, $\mathrm{d}k/\mathrm{d}t$ in equation 5.5 is essentially zero, therefore, the combined effect of the various terms of the CKE budget equation is reflected in the convection term ($-\tilde{C}_l$): if the energy content of the mode is increasing with downstream distance (it is being net energised) then this term will be negative whilst it will be positive when the mode is spatially decaying.

For f_r (figure 6.7(a) and 6.7(d)), the primary source is the $\tilde{P}_l$ term, shown with a black line. Note that for $\lambda = 6$, the $\tilde{P}_l$ term changes sign at $x/D \approx 1.65$. This location is close to where

f_r was found to be the most energetic (see figure 6.2(a)). Beyond this point the mode decays monotonically as indicated by the convection ($-\tilde{C}_l$) term being positive. For brevity, the location where $\tilde{P}_l$ changes sign is denoted as x_{wr}. Note that x_{wr} is particularly important in terms of wake recovery, as beyond this point the mode transfers energy back to the mean flow. For $\lambda = 5$ (figure 6.7(d)), $x_{wr} \approx 3.2$ which implies that wake recovery starts much later. Note that for $\lambda = 5$, there is a drop in the $\tilde{P}_l$ term of f_r at $x/D \approx 1$. This is because of the presence of the merged root vortices (with frequency f_r) that decay in this region and noting that the $\tilde{P}_l$ term is essentially the sum of contributions from both the root and tip regions.

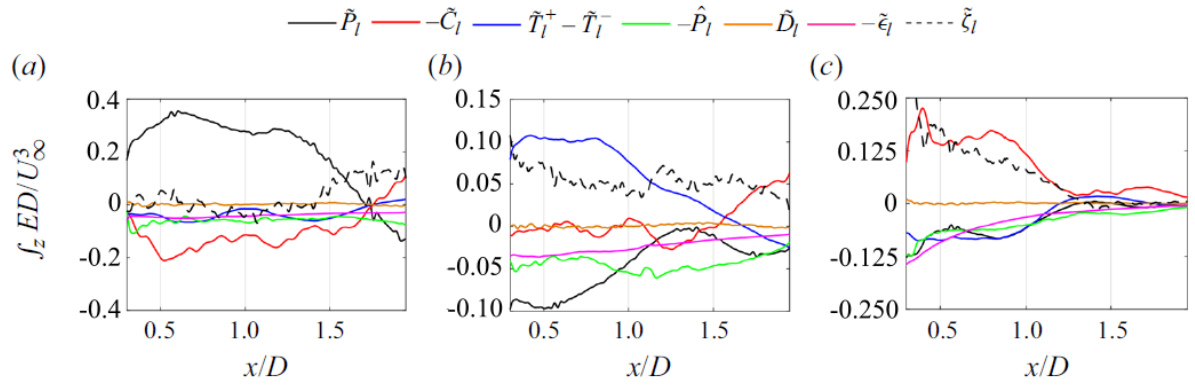


Figure 6.8: Streamwise evolution of the energy budget terms of equation 5.5 averaged along the z direction for (a) f_r, (b) $2f_r$ and (c) $3f_r$ for $\lambda = 6$.

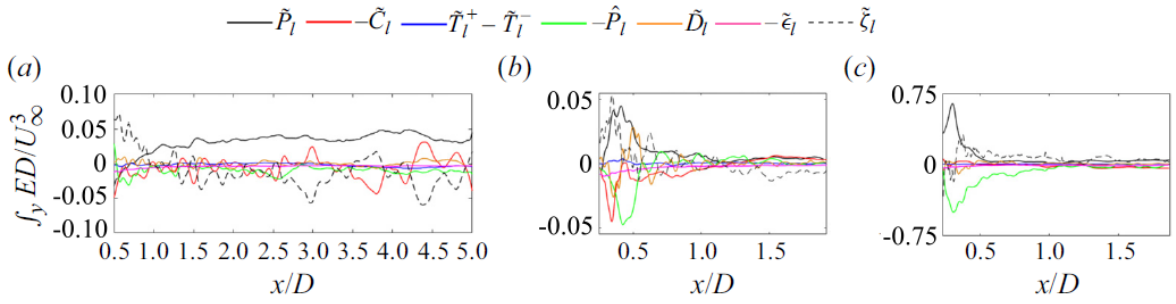


Figure 6.9: Streamwise evolution of the spanwise (along y) averaged energy budget terms of equation 5.5 for (a) f_{wm} in the xy plane. Streamwise evolution of the energy budget terms averaged along z direction for (b) f_n in the $y = 0$ plane, (c) f_T in the $y = -0.35D$ plane.

For $\lambda = 6$, $2f_r$ is primarily energised by the triadic interaction term which drops off to zero at $x/D \approx 1.6$; this is again close to the point where $2f_r$ is most energetic in figure 6.2(b). From figure 6.2 it can be seen that for $\lambda = 5$, $2f_r$ is much weaker than for $\lambda = 6$. This is corroborated by the fact that the magnitude of the energy budget terms of $2f_r$ in figure 6.7 is smaller for $\lambda = 5$, compared to $\lambda = 6$. Additionally, for the lower λ, the triadic interaction term is much

weaker due to increased separation between the tip vortices. Therefore, unlike $\lambda = 6$, for $\lambda = 5$, $2f_r$ is energised mainly by the mean flow. For $3f_r$, the convection term is positive throughout as it decays monotonically in the domain. The trends are qualitatively similar for both the λs. Note also that the residuals of the budget equation are highest for $3f_r$, especially closer to the rotor. This is probably because there is a significant role of the pressure diffusion term in this region that has been neglected in the analysis.

The same analysis is performed with the data from experiment 2A (see chapter 2 for details) which considered the orthogonal xz plane for $\lambda = 6$. The budget terms are summed in the z direction and are shown in figure 6.8 for the modes $f_r - 3f_r$. Note that the trends of the budget terms are quite similar to those observed in the xy plane earlier (in figure 6.7). The dominant source terms of the modes are the same. Moreover, the $\tilde{P}_l$ term for f_r changes sign at the same location as before, at $x/D \approx 1.65$. Similarly, the triadic interaction term for $2f_r$ changes sign at $x/D \approx 1.6$, consistent with the observation in the xy plane. This similarity of the budget terms in the two orthogonal planes shows that the budget terms are close to axisymmetric in nature and offers reassurance as to the repeatability of our results.

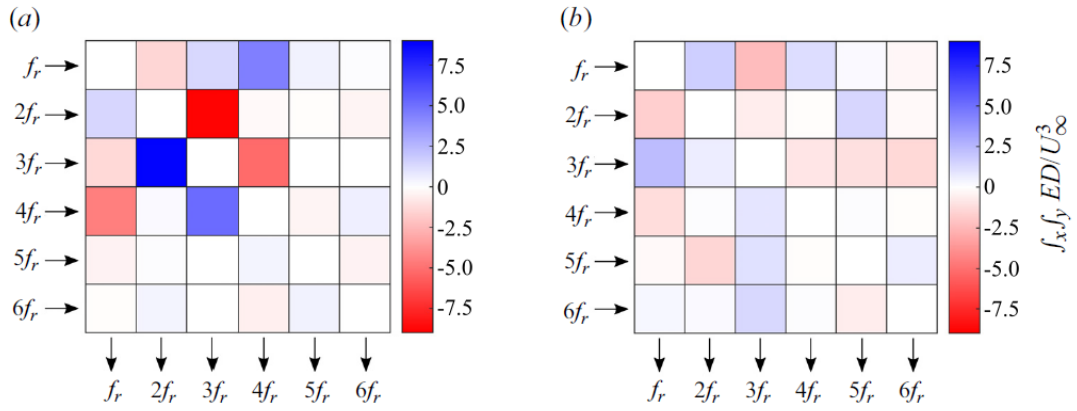


Figure 6.10: Triadic energy exchanges for (a) $\lambda = 6$ and (b) $\lambda = 5$ from experiment 1G.

Figure 6.9 shows the evolution of the CKE budget terms for selected low-frequency modes in different PIV planes for $\lambda = 6$. Figure 6.9(a) shows the terms for the dominant wake meandering mode obtained from experiment 1G (the mode shown in figure 6.3(a)). Figures 6.9(b) and 6.9(c) show the same for the nacelle's and the tower's shedding mode obtained from experiments 2A and 2B respectively. The terms appear to be noisier compared to the tip vortex system, however, the $\tilde{P}_l$ term is unambiguously the dominant source term for these modes. For the wake meandering

mode, $\tilde{P}_l$ slowly grows with streamwise distance, which is consistent with the far-wake dominance of wake meandering observed in chapter 3. The sheddings from the nacelle and the tower on the other hand quickly drop to zero, showing their relatively transient spatial nature.

6.3.1 Triadic interactions

It was shown that for $\lambda = 6$, $2f_r$ is energised primarily by the triadic energy exchange term. But, $2f_r$ forms a number of triads and the triadic energy gain of $2f_r$ is a sum of contributions from all the triads that $2f_r$ can form with the other frequencies. At this point an interesting question to ask is are there any particular triads that are more important or are there any frequencies that transfer more energy to $2f_r$? Answering these questions can help significantly simplify what would be a rather complicated network of energy transfers in the tip vortex system. The terms $\tilde{T}_l^+$ and $\tilde{T}_l^-$ in equation 5.5 indicate the net non-linear energy gain and loss respectively from the l_{th} coherent mode and are defined as follows:

$$\tilde{T}_l^+ = -\frac{1}{2}\sum_{f_s,f_t} \overline{\tilde{u}_i^{f_l}\tilde{u}_j^{f_t}\frac{\partial \tilde{u}_i^{f_s}}{\partial x_j}}, \qquad \tilde{T}_l^- = -\frac{1}{2}\sum_{f_s,f_t} \overline{\tilde{u}_i^{f_s}\tilde{u}_j^{f_t}\frac{\partial \tilde{u}_i^{f_l}}{\partial x_j}}. \tag{6.1}$$

Note that the terms consist of 3 frequencies and are non-negligible only when the frequencies form a triad (Baj and Buxton, 2017). Essentially the contributions from all possible triads are taken by summing over the two frequencies (f_s and f_t). Instead, one can fix one of these two frequencies (let's say f_s) and can take a summation over the other frequency (f_t). This would give the net triadic energy exchange between f_l and f_s. This is done for all the frequencies related to the tip vortices ($f_r - 6f_r$) and the results are shown in figure 6.10 for the two λs. The arrows show the direction of energy transfer. For instance the first row shows the net amount of energy f_r is giving away to the other frequencies. In other words, the first column shows the amount of energy received by f_r from all other frequencies. As observed earlier, the magnitude of the traidic energy transfers are much stronger for $\lambda = 6$, compared to $\lambda = 5$. Moreover, for $\lambda = 6$, most of the energy transfer is limited between $f_r - 4f_r$, while the contributions from $5f_r$ and $6f_r$ are significantly weaker in comparison. Looking at the second column in figure 6.10(a) it can be said that the main source for $2f_r$'s triadic energy gain is $3f_r$. Thereafter, $2f_r$

transfers some amount of energy to f_r, hence forming a net inverse energy cascade. Note that this sequence of energy transfer is similar to that predicted by Felli et al. (2011) (see figure 41(b) of Felli et al. (2011)) for a three bladed turbine. However, the fact that the higher harmonics can also have an important role in the energy exchange process was not highlighted in their work. Note from figure 6.10(a) that f_r transfers a significant amount of energy to $4f_r$ and $4f_r$ transfers almost the same amount of energy to $3f_r$. Therefore, although $4f_r$ does not gain energy through triadic interactions, it forms a bypass route of energy transfer allowing f_r to transfer some energy back to $3f_r$.

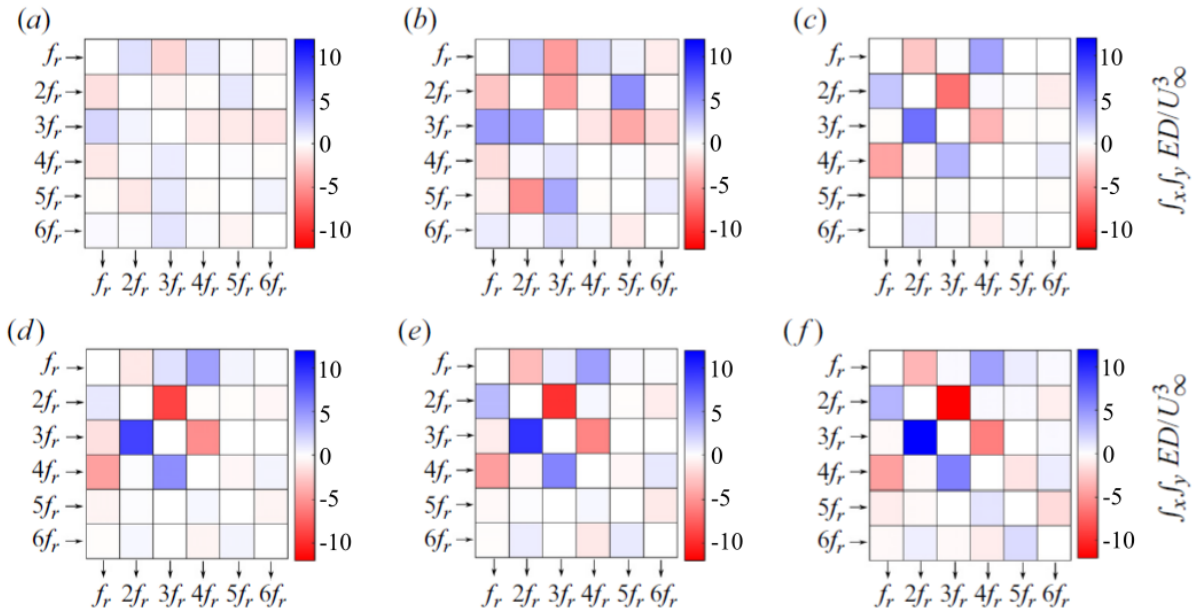


Figure 6.11: Net traidic transfers for (a) $\lambda = 5$, (b) $\lambda = 5.3$, (c) $\lambda = 5.5$, (d) $\lambda = 6$, (e) $\lambda = 6.6$, (f) $\lambda = 6.9$.

For $\lambda = 5$, figure 6.10(b) shows that not only are the magnitudes of the energy transfers weaker but the energy transfer pathways are also different. This includes the fact that the net non-linear energy gain for $2f_r$ is now quite small, as was previously shown in figure 6.6(b). Unlike for $\lambda = 6$, $2f_r$ and $4f_r$ are both energised mainly by f_r, as far as triadic interaction is concerned. To further understand the dependence of these energy transfers on λ, the analysis is repeated for other λs in experiment 1D. These are shown in figure 6.11 in combination with the results for $\lambda = 6$ and $\lambda = 5$ (from experiment 1G) for a better comparison. Note that the extents of the FOV are different for experiment 1D. Therefore, in order to be consistent across different FOV sizes, the triadic energy exchanges are integrated between $0.5 < x/D < 3D$ and $0 < y/D < 0.75D$. Note

that as we increase λ from 5 to 6, there is a clear transition in the energy exchange pathway. For $\lambda = 5.5$, the pattern looks exactly similar to that for $\lambda = 6$. For $\lambda = 5.3$, the pattern appears to be at an intermediate state between that for $\lambda = 5$ and $\lambda = 5.5$. From $\lambda = 5.5$, the energy exchange pattern remains qualitatively similar as we increase λ and the magnitude of the energy transfers increases showing a stronger non-linear interaction between the modes at higher λ.

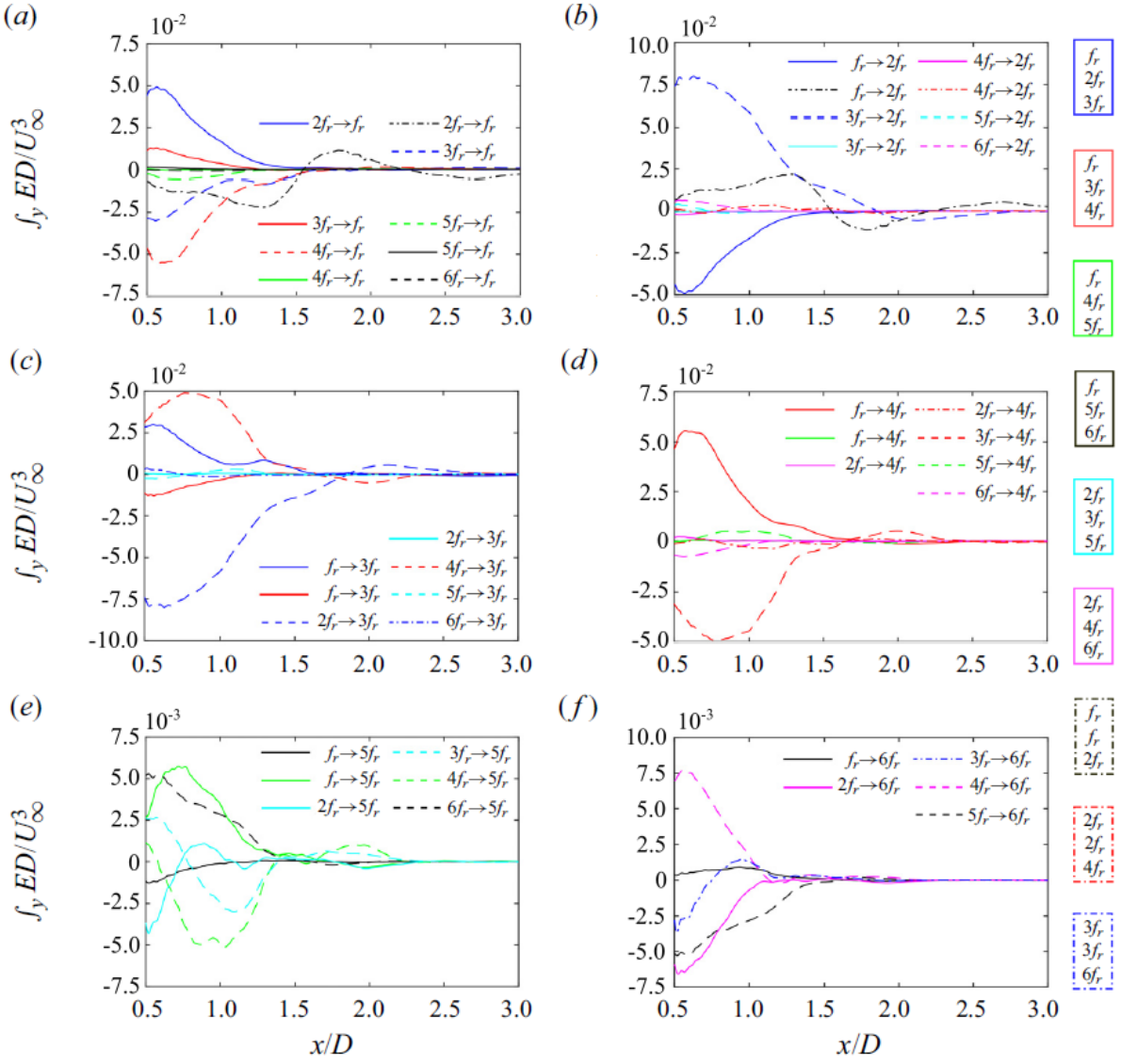


Figure 6.12: Energy transfers from different frequencies in different triads to (a) f_r, (b) $2f_r$, (c) $3f_r$, (d) $4f_r$, (e) $5f_r$ and (f) $6f_r$. The possible traids are shown on the right.

Figure 6.10(a) shows that for $\lambda = 6$, $2f_r$ gets most of its energy from $3f_r$. However, $2f_r$ and $3f_r$ can form 2 triads together, one with f_r, and another with $5f_r$, hence it is not clearly known which triad is more important. One can further split the inter-frequency energy transfers shown in figure 6.10 into contributions from different triads. For brevity, the results are only shown for

$\lambda = 6$ as it showed stronger non-linear interactions. Figure 6.12 shows the streamwise evolution of the spanwise averaged inter-frequency energy transfers that correspond to different triads. Note that there are a total of 9 triads involving the frequencies $f_r - 6f_r$. These are shown in boxes of different colours and line types in figure 6.12 for an easier interpretation. The first six triads involve 3 different frequencies and are shown in boxes with a solid line. These are denoted as triad type I. The last three triads have a repeated frequency and are shown in boxes with a dash-dotted line to distinguish them. These triads are termed triad type II. First the energy transfers to f_r from the other frequencies in different triads are shown in figure 6.12(a). Note that f_r forms 4 triads of type I and 1 triad of type II. For each triad of type I, it is possible to have two energy transfers to f_r from the other two frequencies involved in the triad. For triads of type II, there will be only one transfer. Accordingly, there are a total of 9 transfers to f_r as indicated in figure 6.12(a). The transfers corresponding to the first triad (shown in the blue solid box) are shown with blue lines. The transfer from the lower of the two frequencies of the triad (*i.e.* $2f_r$) is shown in a solid blue line and that from the higher frequency ($3f_r$) is shown in a dashed blue line. The transfer from the $7th$ triad (shown in black dash dotted box) is shown in a black dash-dotted line. This same convention is used throughout to avoid confusion. Note that for f_r, only three triads 1, 2 and 7 are important. For $2f_r$, only triad 1 and 7 are found to be important and both positively energise $2f_r$. The main source of energy for $2f_r$ is however $3f_r$ from triad 1 as discussed earlier. For $3f_r$, only triad 1 and 2 are important. As a whole, $3f_r$ loses energy, most of which goes to energise $2f_r$. For $4f_r$, only the second triad is important. The energy transfers involving $5f_r$ and $6f_r$ are an order of magnitude smaller and can be ignored.

6.4 Summary of the energy exchanges for the tip vortices

The analysis of section 6.3.1 allows a drastic simplification of the network of non-linear energy exchanges by using a fewer number of triads. To be specific, for $\lambda = 6$, only the triads 1, 2 and 7 (shown in figure 6.12) need to be retained discarding the rest. This approximated network of energy transfers is schematically shown in figure 6.13(a) and it summarises the key energy exchanges in the tip vortex system discussed above. The energy exchanges in triads 1 and 2 are shown in blue and red solid lines respectively, while the black dash dotted line represents the

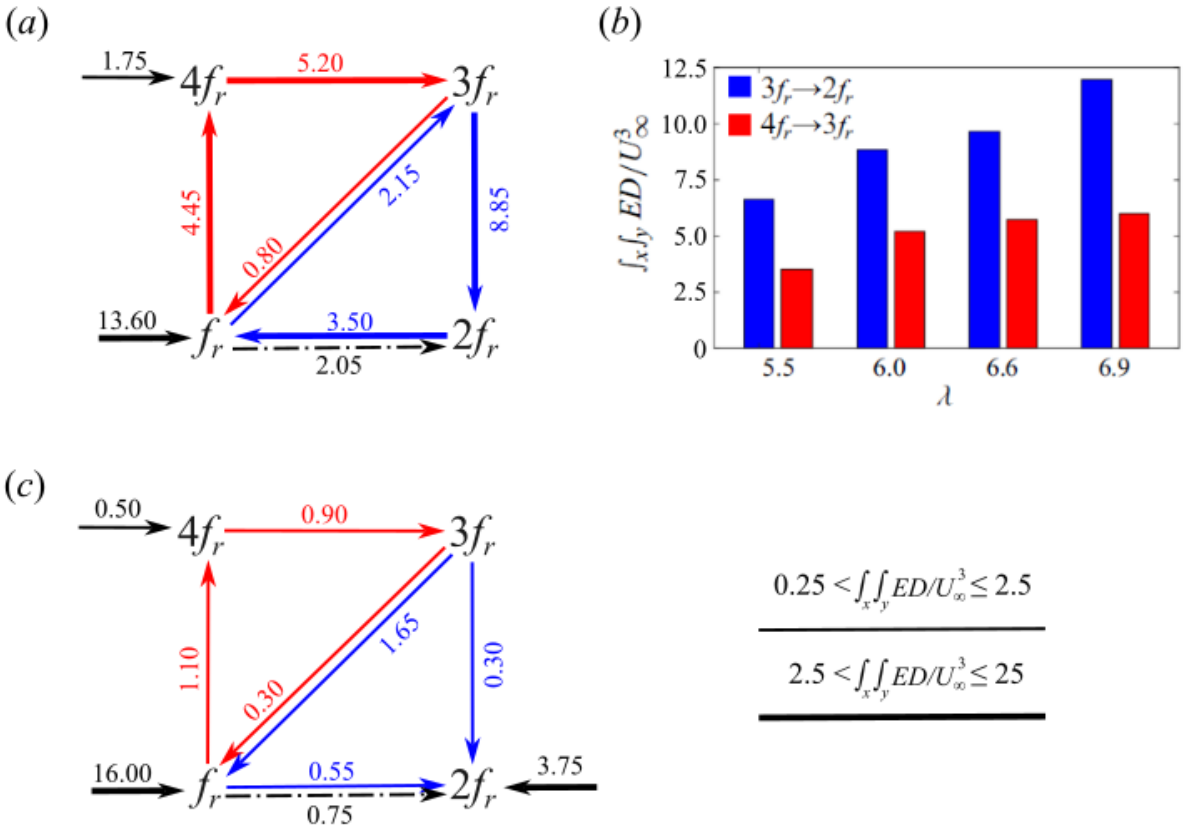


Figure 6.13: Triadic energy transfer pathways among the modes $f_r - 4f_r$ for (a) $\lambda = 6$ and (c) $\lambda = 5$. The line types and the colour of the arrows showing inter frequency energy transfers are consistent with those used to represent triads in figure 6.12. The solid black arrow show the positive contribution from the $\tilde{P}_l$ term in equation 5.5. The thickness of the arrows varies according to the magnitude of the energy transfers as indicated. (b) shows the magnitudes of the energy transfers from $3f_r$ to $2f_r$ in triad 1 and from $4f_r$ to $3f_r$ in triad 2 for different λs.

energy transfer in triad 7, similar to the convention used in figure 6.12. The values show the net triadic energy transfers. Note that triads 1 and 2 show a cyclic nature of energy transfers and form a net inverse energy cascade (*i.e.* energy transfer from high to low frequency), while triad 7 shows a forward cascade. For a comparison, the positive contributions from the mean flow production term ($\tilde{P}_l$) in equation 5.5 are also shown by solid black lines. The numbers show the magnitudes of the energy transfers and the same is also highlighted by the thicknesses of the arrows.

To summarise the energy transfer process involving the tip vortices, it can be noted from triad 1 that energy primarily flows from $3f_r$ towards f_r via the secondary mode $2f_r$ which is a nice representation of the tip vortex merging process (Felli et al., 2011). However, it is interesting to note that the net triadic energy gain of f_r is nearly zero. This is because f_r transfers most of its

triadic energy gain to $4f_r$. f_r is therefore primarily sustained by energy supply from the mean flow thus acting as a primary mode. Similarly $4f_r$ also behaves like a primary mode, transferring the energy it gains from f_r to $3f_r$. This energy feedback slows down the energy drainage of $3f_r$. It is therefore believed that the energy transfers from $3f_r$ to $2f_r$ in triad 1 and from $4f_r$ to $3f_r$ in triad 2 can be linked to the stability and sustainment of the tip vortices. These two energy transfers are compared for the four λs (5.5, 6, 6.6, 6.9) that showed similar triadic energy exchange patterns (figure 6.11) in figure 6.13(b). Note that both the energy transfers increase with λ. However, the difference of the two energy transfers also increases with λ indicating a faster decay of the tip vortices at a higher λ.

A similar schematic of energy transfers among the modes $f_r - 4f_r$ for $\lambda = 5$ is shown in figure 6.13(c). Note that for $\lambda = 5$ a simplification of the energy transfer network is not readily possible as all the modes exhibit energy transfers of similar magnitudes to/from them (see figure 6.10(b)). Therefore, the purpose of figure 6.13(c) is solely to compare the triads 1, 2 and 7 between $\lambda = 5$ and $\lambda = 6$. First of all, the energy transfers are much weaker for $\lambda = 5$. Secondly, although triad 2 is still cyclic in nature, triad 1 has become non-cyclic. The primary change has occurred around $2f_r$ which is no longer strongly energised by $3f_r$. Triads 1 and 7 contribute to some non-linear energy gain of $2f_r$ but it gets most of its energy from the mean flow.

These energy exchanges can elucidate the nature of the tip vortex merging process. Note that in chapter 3 two different merging processes were reported for two different λs. For the lower λ ($\lambda = 4.5$) the merging of the tip vortices resembled a two-step process where first $2f_r$ was formed and f_r became energetic further downstream, as also reported by Felli et al. (2011); Sherry et al. (2013a). Contrastingly, for the higher λ ($\lambda = 6$), three tip vortices appeared to combine almost directly in making it look like a one-step process. For the same λ however, a significant direct energy transfer from $3f_r$ to f_r is not observed in figure 6.13(a), as one might expect from a one-step process. The energy transfer still happens in two steps, first from $3f_r$ to $2f_r$ and then from $2f_r$ to f_r as predicted by Felli et al. (2011). However, due to the fact that f_r and $2f_r$ attain their maximum energy at almost the same streamwise location (see figures 6.2(a) and (b)), these two steps take place almost concurrently, making it look like a one-step process. For $\lambda = 5$, there is a larger streamwise separation between the points where f_r and $2f_r$ attain their maximum energy, visually indicating a two-step merging process. The increased separation

between the helices at the lower λ, however, results in a much weaker non-linear interaction. Furthermore, the injection of energy from the mean flow to $2f_r$ results in a reorganisation of the energy transfer pattern in triad 1, *i.e.* from a cyclic to a non-cyclic one.

It is worthwhile mentioning that the energy budget terms for the tip vortices may be a function of the chord based Reynolds number (Re_c). At a lower Re_c, the larger viscous effects result in a higher drag and limits the maximum lift coefficient (Lissaman, 1983). Therefore, since utility-scale wind turbines operate at a much higher Re_c, the blade sections experience a higher C_l and lower C_d. Since, C_l is directly related to the bound circulation, one can expect the strength of the tip vortices (shed circulation) to increase with Re_c. The stronger tip vortices result in an interaction that occurs earlier (further upstream) which can in turn be linked to the observed faster wake expansion and wake recovery at higher Reynolds numbers (McTavish et al., 2013; Bourhis et al., 2023). Therefore it is believed that increasing Re_c would further increase the magnitudes of the nonlinear triadic energy exchanges for the tip vortices at a given λ. It will be interesting to study and compare the separate effects of increasing Re_c and λ on the triadic interactions and the tip vortex merging process. From the nature of the Biot–Savart law, which governs the interaction between the tip vortices, one can vaguely expect the growth of the tip vortex instability to be directly proportional to the strength of the vortices, and inversely proportional to the square of the separation (Sørensen et al., 2015). Now, increasing λ results in a reduction of the separation (pitch of the helices) and can increase the strength of the tip vortices, while increasing Re is expected to only increase the strength of the tip vortices. Further, as was reported in chapter 3, the stronger interaction at the higher λ is primarily driven by the reduced separation. To summarise it can be deduced that the tip vortex merging process likely depends on Re_c, however it is more likely a stronger function of λ.

6.5 The near wake and wake recovery

For a wind turbine it is important to quantify the extent of the near wake, particularly in the context of designing wind farm layouts as the near wake contains energetic coherent structures capable of inducing fatigue damage to the subsequent turbines. The extent of the near wake depends on several factors such as the nature and intensity of the freestream turbulence level,

turbine geometry, operating condition and so on and hence it is often vaguely defined between 2-4 rotor diameters downstream of the rotor (Vermeer et al., 2003; Foti et al., 2016). Several attempts have been made to quantify the near wake for instance by observing self-similarity in the time-averaged wake profile (Sørensen et al., 2015) or by looking at the variation of time-averaged coherent or turbulent kinetic energy in the wake (De Cillis et al., 2021; Gambuzza and Ganapathisubramani, 2023). In contrast, a more dynamic point of view was endorsed in chapter 3 where the extent of the near wake was defined as the location where the strength of wake meandering or f_{wm} (dominant dynamic feature in the far wake) surpassed that of the tip vortices or $3f_r$ (dominant frequency in the near wake). Further, a convective length scale, $L_c = \pi D/\lambda$ was defined which can be physically interpreted as the distance travelled at the freestream velocity in the time taken for one complete rotation of the turbine). It was reported that the near wake location was $\approx 3L_c$ for a range of λs tested, or in other words, the near wake's extent scaled with $1/\lambda$. The strength of a frequency at a particular streamwise (x) location was however defined as the magnitude of the spectral peak at that particular frequency. As the strengths of the frequencies depended only on x, the spatial distribution of the strength or energy associated with frequencies was not taken into account in the definition of the near wake. In this section, other methods are explored to quantify the extents of the near/far wake based on the knowledge gained earlier about the nature of the different modes and the energy exchanges to/from them.

After obtaining the time-averaged kinetic energy of the modes associated with f_{wm} ($k_{f_{wm}}$) and f_r (k_{f_r}) and the relative kinetic energy $k_{f_{wm}} - k_{f_r}$ for $\lambda = 6$ and $\lambda = 5$ is shown in figures 6.14(a) and 6.14(b) respectively. The solid black line corresponding to $k_{f_{wm}} - k_{f_r} = 0$ nicely distinguishes the regions where f_{wm} or f_r is stronger than the other. Similarly, the dashed black line shows the contour corresponding to $k_{f_{wm}} - k_{3f_r} = 0$ which is always found to be located within the contour traced by $k_{f_{wm}} - k_{f_r} = 0$ for the λs tested. Similar contours can be obtained using the harmonics of f_r and $3f_r$, but they are generally weaker in nature. Therefore it is proposed that $k_{f_{wm}} - k_{f_r} = 0$ can be used to distinguish the inner wake involving low-frequency dynamics from the outer wake that contains high-frequency modes related to the tip vortices. The earlier and stronger tip vortex merging process for $\lambda = 6$ results in a quicker disintegration of the tip vortex system. The outer wake thus vanishes at $x/D \approx 4.7$ creating a path for rapid

exchange of mass and momentum between the inner wake and the non-turbulent background fluid in this case, aiding wake recovery. It is therefore further argued that the end of the outer wake can be considered as the initiation of the far wake where wake meandering is the only discernible frequency signature. The extent of the outer wake and hence the far wake depends on λ. For $\lambda = 5$, the outer wake extends beyond $x/D = 5$, therefore the far wake can also be expected to scale with λ^n (where n is a negative number) at least in the presence of low inflow turbulence, similar to the near wake.

Next, the evolution of the mean flow production term ($\tilde{P}_l$) of the tip vortex system is explored in more detail. The streamwise evolution of the spanwise averaged (along y) mean flow production term for the tip vortex system ($\sum_{l=f_r}^{l=6f_r} \tilde{P}_l$) is shown in figure 6.15(a) for 3 different λs (by the solid lines), while the dashed lines show the mean flow production term only for f_r ($\tilde{P}_{f_r}$) for the corresponding λs. Note that $\tilde{P}_{f_r}$ is close to $\sum_{l=f_r}^{l=6f_r} \tilde{P}_l$ for all λs which implies that most of the energy exchanges between the mean flow and the tip vortex system happens through f_r. As discussed earlier, disintegration of the tip vortex system is essential to re-energise the wake. Note that close to the rotor $\sum_{l=f_r}^{l=6f_r} \tilde{P}_l > 0$, *i.e.* the tip vortex system first draws energy from the mean flow as a whole. However, after some distance downstream it starts to transfer the energy back to the mean flow as indicated by $\sum_{l=f_r}^{l=6f_r} \tilde{P}_l < 0$. The streamwise location where the combined mean flow production term for the tip vortex system changes sign can be ascribed as the point of initiation of wake recovery (henceforth denoted as x_{wr}). Note that as λ increases x_{wr} moves closer to the turbine. Moreover, an estimation of x_{wr} can be obtained just by looking at the production term of f_r which again highlights the importance of f_r in the distinction of near from far wake. The variation of x_{wr} (obtained from $\tilde{P}_{f_r}$) with λ is shown in figure 6.15(b). The extent of the near wake, $\approx 3L_c$ is also shown for a comparison. x_{wr} shows a nice trend with λ. More interestingly, for higher λ, x_{wr} becomes close to $3L_c$, further highlighting the efficacy of L_c as a length scale in the near wake.

It is interesting to ask what brings about a sign change in the $\tilde{P}_l$ term for f_r after some distance downstream. Baj and Buxton (2017) defined the term as $\tilde{P}_l = -\sum_m \overline{\tilde{u}_i^m \tilde{u}_j^l} \frac{\partial \overline{u}_i}{\partial x_j}$, where m can be any coherent mode selected in the reduced order representation of the flow including the l_{th} mode. Assuming that the velocity components of the different modes are uncorrelated, *i.e.* $\overline{\tilde{u}_i^l \tilde{u}_j^m} \approx 0$ for any $l \neq m$, one can approximate $\tilde{P}_l \approx -\overline{\tilde{u}_i^l \tilde{u}_j^l} \frac{\partial \overline{u}_i}{\partial x_j}$. Next, it can be shown that the

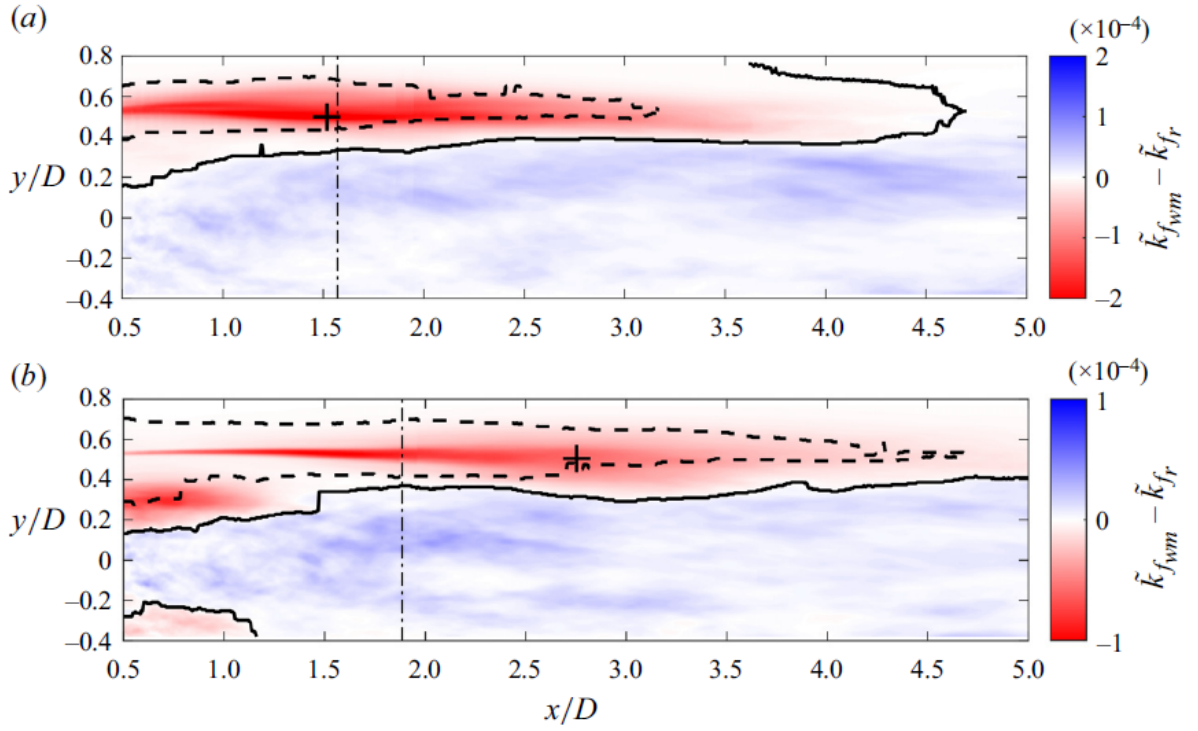


Figure 6.14: Filled contours showing relative kinetic energy of the wake meandering mode with respect to the mode associated with f_r (denoted by $\tilde{k}_{f_{wm}} - \tilde{k}_{f_r}$) for (a) $\lambda = 6$ and (b) $\lambda = 5$. The solid and dashed black lines correspond to $\tilde{k}_{f_{wm}} - \tilde{k}_{f_r} = 0$ and $\tilde{k}_{f_{wm}} - \tilde{k}_{3f_r} = 0$ respectively. The + sign shows the location where the kinetic energy corresponding to f_r is maximum. The dash-dotted vertical line shows the streamwise location corresponding to 3 convective length scales or $3L_c$ defined in chapter 3.

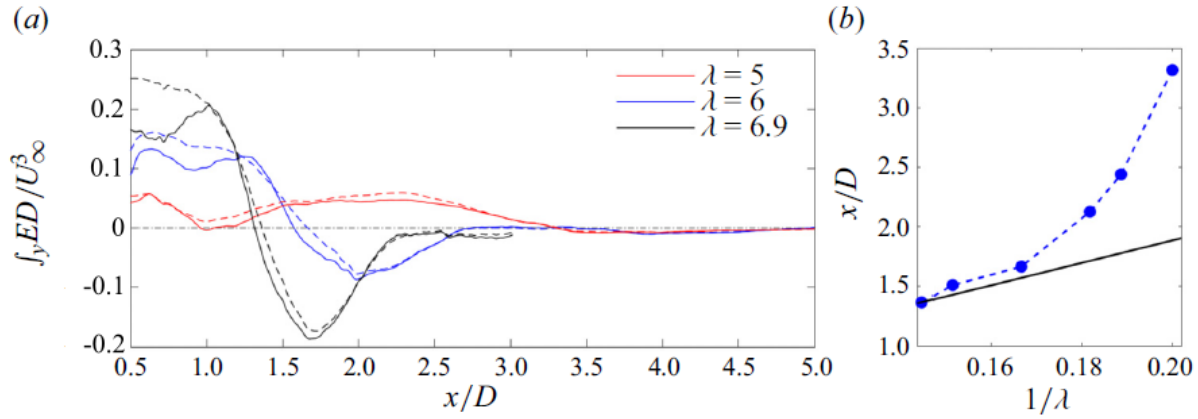


Figure 6.15: (a) Streamwise variation of spanwise averaged mean flow production term for the tip vortex system (shown by the solid lines) and f_r (shown by the dashed line) for diffrerent λs. (b) The variation of the location where wake recovery initiates or x_{wr} with λ (–●–). The solid black line shows the streamwise location $x/D = 3L_c$.

transverse gradient of the streamwise velocity ($\frac{\partial \overline{u}}{\partial y}$) is an order of magnitude stronger than the other gradients, at least in the tip shear layer region. So the term can be further approximated as $\tilde{P}_l \approx -\overline{\tilde{u}^l \tilde{v}^l} \frac{\partial \overline{u}}{\partial y}$. In figure 6.16(a), the $\tilde{P}_l$ field for f_r is shown without any approximation. As can be expected, $\tilde{P}_l$ is concentrated only in the tip shear layer region and the '+' sign shows the location where the term changes sign, *i.e.* the location of the onset of wake recovery (x_{wr}). Figure 6.16(b) shows the $\tilde{P}_l$ field only with the dominant term ($-\overline{\tilde{u}^l \tilde{v}^l} \frac{\partial \overline{u}}{\partial y}$) and it looks almost exactly similar to figure 6.16(a), hence justifying the approximation. Now, $\frac{\partial \overline{u}}{\partial y}$ is always positive in the tip shear layer region. The observed change of sign in $\tilde{P}_l$ thus requires a change in the nature of correlation (negative to positive) between the streamwise and transverse velocity components of f_r. This is similar to the observation of Lignarolo et al. (2015) for a two-bladed turbine. They argued that the net transport of kinetic energy towards the wake centreline (the component contributing to the wake recovery) due to the periodic motions can be given by the gradients of the kinetic energy flux $-\overline{\tilde{u}^l \tilde{v}^l} \overline{u}$. They further showed that at a certain distance downstream, the orientation/inclination of the tip vortex pair undergoing merging with respect to the streamwise direction changed from negative ($< 90^o$) to positive ($> 90^o$), resulting in a change in the correlation between the streamwise and transverse velocity component (see figure 17 of Lignarolo et al. (2015)). From the vorticity field for $\lambda = 6$ (see figure 3.1 in chapter 3) it can be seen that, the vortex triplet, undergoing merger, changes its inclination at $x/D \approx 1.5$. Consequently, a sign change is observed in the $\tilde{P}_l$ term for f_r at $x/D \approx 1.5$ for $\lambda = 6$.

6.6 On the choice of the modal decomposition technique

In order to understand if there are significant effects of the choice of the modal decomposition technique on the energy budget results, the analysis was repeated for $\lambda = 6$ using spectral proper orthogonal decomposition (sPOD), which is a technique fundamentally different from OMD (Towne et al., 2018; Schmidt et al., 2018). Only the data from experiment 1G was used. sPOD was performed with blocks containing 2500 snapshots that had 50% overlap. Previously, the complex coefficients of the OMD modes (and hence the associated physical velocity fields) were obtained by projecting the data on to the modes. To introduce further distinction from the earlier technique, the expansion coefficients of the sPOD modes are now obtained using the

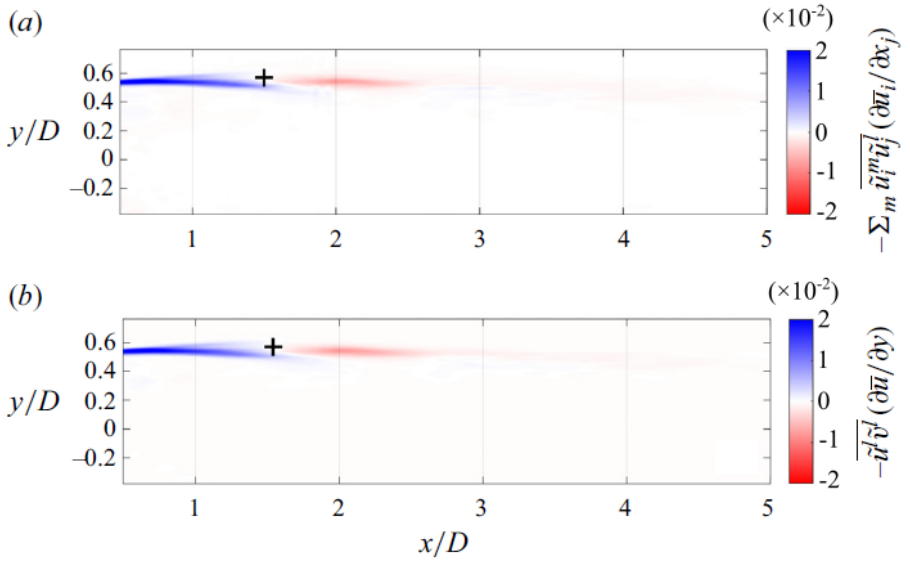


Figure 6.16: (a) Mean flow production term ($\tilde{P}_l$) of f_r for $\lambda = 6$, (b) shows the leading term of $\tilde{P}_l$. The '+' sign marks the location of the sign change.

inversion of the sPOD problem following (Nekkanti and Schmidt, 2021).

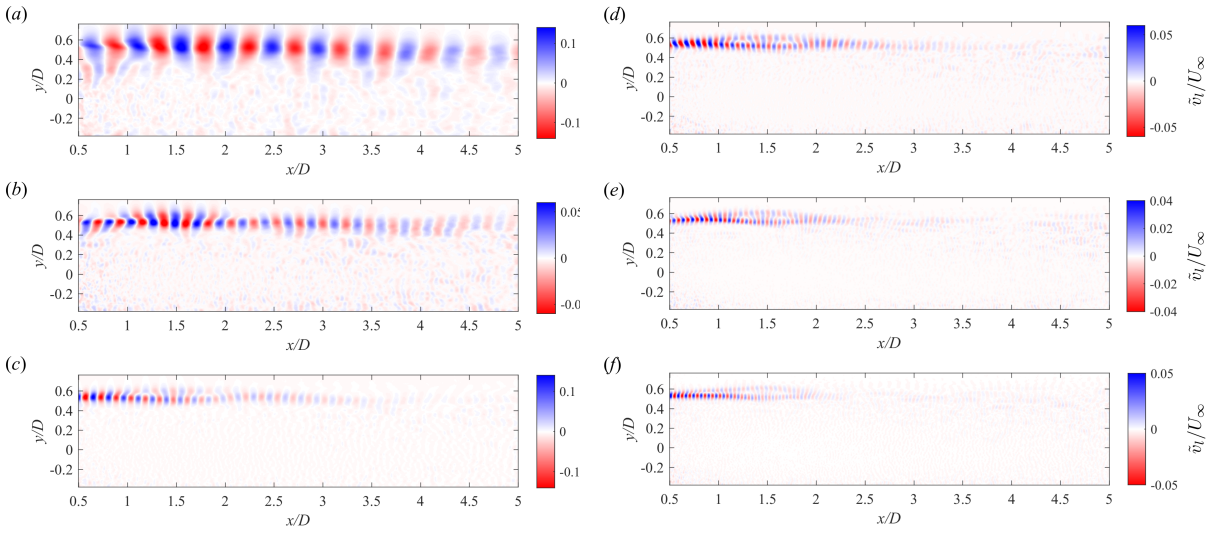


Figure 6.17: Transverse velocity components of the sPOD modes associated with frequencies (a) f_r, (b) $2f_r$, (c) $3f_r$, (d) $4f_r$, (e) $5f_r$ and $6f_r$ for $\lambda = 6$.

Figure 6.17 shows the modes f_r to $6f_r$ for $\lambda = 6$, obtained from sPOD and are almost identical to the ones shown in figure 6.2(a-f). Similarly, figure 6.18 shows the two dominant wake meandering modes which are similar to the modes shown in figure 6.3(a-b).

The energy budgets of the sPOD modes are evaluated. Figure 6.19(a) shows the energy spectrum obtained from sPOD. The selected modes are marked in circles and are also numbered according

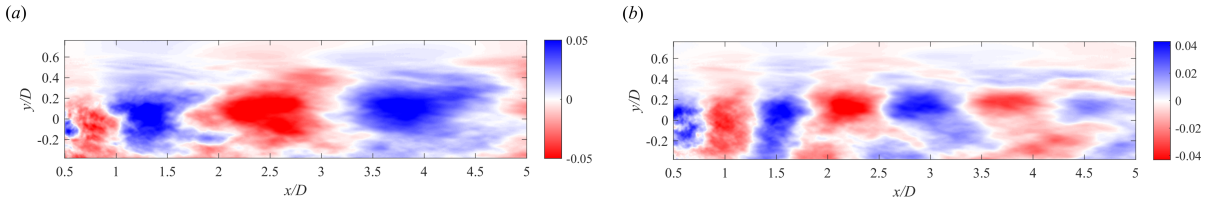


Figure 6.18: Transverse velocity components of the dominant sPOD modes associated with wake meandering.

to their Strouhal number. Note from figure 6.1 (and from the discussion in section 6.2), all the modes from $f_r - 6f_r$ could not be captured with OMD even after using a high rank. SPOD, however, detects all these modes (modes 14-19) and even the higher harmonics. Higher harmonics are not considered, since they exhibit only very weak energy exchanges. SPOD also successfully detects the modes associated with wake meandering (modes 1-3). Among these, modes 1 and 3 are shown in figure 6.18 and they resemble the dominant wake meandering modes obtained using OMD. However, using sPOD, the modes associated with the vortex sheddings from the nacelle or the tower (modes 4-13) could not be distinguished unambiguously. Nevertheless, the energy budgets of all 19 modes are evaluated and are shown in figure 6.19(b) after summing them over the entire domain. Compared with figure 6.6(a), it can be seen that the budget terms are similar in both cases, apart from slight differences in the magnitudes. This leads one to conclude that the inferences drawn from the modal decomposition/energy budget analysis do not depend on the choice of the modal decomposition technique.

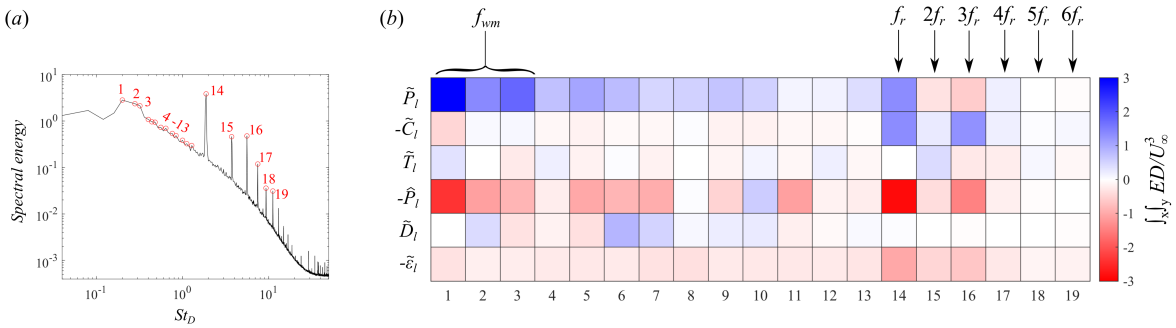


Figure 6.19: (a) sPOD spectra. The circles show the modes selected to construct the reduced order representation of the flow. (b) Energy budget terms of the sPOD modes summed over the entire domain.

6.7 Conclusion

The coherent structures in the wind turbine wake were identified using a multiscale triple decomposition of the velocity field using optimal mode decomposition or OMD (Wynn et al., 2013; Baj et al., 2015). A large number of high-frequency modes were extracted related to the tip vortices including modes with a frequency equal to the turbine's rotational frequency (f_r), blade passing frequency ($3f_r$) and their harmonics ($2f_r$ and $4f_r - 6f_r$) as well as a number of low-frequency modes which included sheddings from the tower (f_T), the nacelle (f_n) and wake meandering (f_{wm}). The spatial nature and strength of the modes depended on λ. For the higher λ ($\lambda = 6$), the modes related to the tip vortices were energetic closer to the rotor, owing to the early interaction between the tip vortices for a higher λ (Sherry et al., 2013a). For the low-frequency modes, the modes associated with f_n and f_T were similar for the two λs. Interestingly however, the wake meandering mode was found to be more energetic for the higher λ.

Further insights are gained about the nature of the different modes by studying the energy exchanges to and from them by using the multiscale triple decomposed coherent kinetic energy (CKE) budget equation derived by Baj and Buxton (2017). The low-frequency modes associated with the sheddings from the tower and the nacelle as well as the wake meandering mode were found to be primarily energised by the mean flow, hence acting similarly to a 'primary mode' (Baj and Buxton, 2017). The tip vortex system on the other hand was found to have a variety of energy sources such as energy production from the mean flow, non-linear triadic energy production or both. The mode associated with f_r behaved like a primary mode for both λs, while the nature of $2f_r$ changed with λ. For $\lambda = 6$, $2f_r$ gained most of its energy through the non-linear triadic energy production term in the CKE budget equation, hence it is akin to a 'secondary mode' (Baj and Buxton, 2017). For $\lambda = 5$ on the other hand, the mode received most of its energy through the mean flow production term, while having a non-negligible positive contribution from the triadic interaction term, therefore acting like a 'mixed mode' as discussed in chapter 5. Some triadic interaction was observed between the low frequency modes as well, but its net contribution was small compared to the energy production from the mean flow.

A complex network of triadic energy exchanges between the modes associated with $f_r - 6f_r$ is identified and discussed. For $\lambda = 6$, energy was found to flow from $3f_r$ to $2f_r$ and then from $2f_r$

to f_r via the non-linear triadic interaction term in the triad formed by $f_r, 2f_r$ and $3f_r$, similar to the observation of Felli et al. (2011). In the triad formed by $f_r, 3f_r$ and $4f_r$, f_r transfered some energy to $4f_r$. $4f_r$ then transfered almost the same amount of energy to $3f_r$, resulting in a much weaker but still dynamically important $4f_r$ mode. The same pattern of triadic energy exchanges was observed for 4 different λs ($\lambda = 5.5$, $\lambda = 6$, $\lambda = 6.6$ and $\lambda = 6.9$). The triadic energy exchanges for the lower λs were found to be much weaker due to the increased separation between the tip vortex filaments.

Finally, attempts are made to identify the boundaries between the inner/outer wake and near/far wake based on the modes and their energy contents. It is shown that the inner wake (involving low-frequency dynamics) can be distinguished from the outer wake (involving high-frequency structures) by comparing the kinetic energy associated with the turbine's rotational frequency f_r and wake meandering (f_{wm}). To identify the location of the onset of wake-recovery (defined as x_{wr}), the combined mean flow production term of the modes related to the tip vortices ($f_r - 6f_r$) is explored. Initially, the tip vortex system is found to extract energy from the mean flow, but further downstream, the combined production term became negative, implying a net energy transfer back to the mean flow. More interestingly, most of the energy exchange between the mean flow and the tip vortex system was found to happen through the turbine's rotational frequency. The sign change in the mean flow production term of f_r was shown to be related to a switch in the nature of correlation between the streamwise and transverse velocity components of the f_r mode resulting from the change of inclination of the tip vortex system undergoing merging, similar to the observation of Lignarolo et al. (2015) for a two-bladed rotor.

Chapter 7

Effect of freestream turbulence on the energy exchanges in wind turbine wake

7.1 Introduction

In chapter 4 the influence of freestream turbulence (FST) on the coherent dynamics in the wind turbine wake was discussed. Enhanced FST was shown to break up the tip vortices earlier, leading to a shorter near wake. Further, the amplitudes of frequencies related to wake meandering were shown to increase in the presence of elevated FST. More interestingly, new frequencies were observed hinting at non-linear interactions between wake meandering and the tip vortices. The origin and evolution of these coherent modes in the presence of FST are explored using the coherent kinetic energy budget equation similarly to chapters 5 and 6. The coherent modes are obtained using OMD. However, the noisy nature of the velocity spectra (especially in the low frequency wake meandering region), as reported in chapter 4 (see figure 4.4) manifested itself as a larger number of frequencies in the OMD spectra in the vicinity of the wake meandering frequency band (WMFB). An example OMD spectrum for the case 2a is shown in figure 7.1(a). To simplify the spectra, the spatially similar modes were identified and grouped together following the mode clustering algorithm proposed by Beit-Sadi et al. (2021).

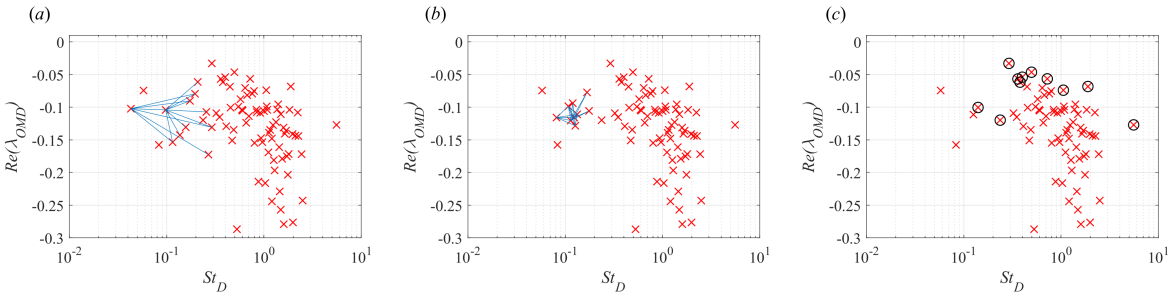


Figure 7.1: 1st, 2nd and 5th iterations of the mode clustering algorithm for the case 2a. The chosen parameters were as follows: $r = 175$, $\zeta_{spat} = 0.94$, and $\zeta_{spec} = 0.3$.

7.2 Mode clustering

Beit-Sadi et al. (2021) used graph theory to cluster the modes in an iterative process. To assess the similarity of two modes, the authors looked at the similarity between the subspaces spanned by the real and imaginary parts of the complex OMD modes. The procedure adopted there is briefly discussed here. For each OMD mode ϕ_l, they defined the metric $A_l = [\Re(\phi_l), \Im(\phi_l)]$, where $\Re$ and $\Im$ denote the real and imaginary parts of ϕ_l and are stored as column vectors. To assess the similarity between modes, the authors used the smallest angle between the subspaces of the modes. The smallest angle between two modes ϕ_l and ϕ_m was therefore measured by using the statistic $\theta_{lm} = \sin^{-1}\left(||A_l - A_m\left(A_l^T A_m\right)||_2\right)$, where $||.||$ denoted the largest singular value of the matrix. For simplicity, the spatial similarity was then represented by $\zeta = \cos(\theta_{lm})$.

A spatial similarity cutoff (ζ_{spat}) was defined, above which two modes could be considered similar and dissimilar otherwise. As an example, for the spectrum shown in figure 7.1, clustering is performed with $\zeta_{spat} = 0.94$ (note that $\zeta_{spat} = 1$ means the two modes span the same subspace). This ζ_{spat} is selected based on a convergence analysis which will be discussed in the subsequent section. Additionally, a spectral similarity cutoff ζ_{spec} was imposed such that two spatially similar modes would not be clustered if their frequencies were ζ_{spec} (or more) apart. In figure 7.1, ζ_{spec} was set to 0.3 which is of the order of the bandwidth of the WMFB. Nonetheless, the clustering process only weakly depended on ζ_{spec} as will be shown. The spatially similar modes are then connected with an 'edge' (shown by the blue lines). Note from figure 7.1(a) that there exists a large number of similar modes in the vicinity of WMFB. This is consistent with the broadband nature of wake meandering observed earlier for higher freestream turbulence cases in

chapter 4. Once the similar modes are identified, the problem of clustering becomes equivalent to finding sub groups where each mode is connected with every other mode with an edge. In graph theoretic notion, such a sub group is termed as a 'clique'. Further, a 'maximal-clique' is a subgroup or clique that is not strictly contained in any other cliques (see Beit-Sadi et al. (2021) for more details).

Once the maximal cliques are obtained, each maximal clique is represented using a single representative mode. For that, each of the modes in a maximal clique are stacked in a matrix (let us denote it as M) as column vectors multiplied by a significance parameter σ_l. If the k^{th} maximal clique has n modes, then $M_k = [\sigma_1\phi_1, \sigma_2\phi_2 ... \sigma_n\phi_n]$. Thereafter, a singular value of decomposition of M_k is performed and the first singular vector is used as the mode representing the cluster. Different statistics can be used as the significance parameter (σ). For example, one could project the snapshots on to the OMD modes to obtain the time varying coefficients of the modes. The magnitude of the coefficient at $t = 0$ or a norm of the coefficient could be used as σ. Here however, the quantity $1/|\Re(\lambda_{OMD})|$ is used as the significance, where $\Re(\lambda_{OMD})$ is the growth rate of the modes. The dominant modes (growth rate closer to zero) are therefore assigned a higher significance value. This method showed faster convergence for the current data set. The modes representing a cluster is also assigned a virtual growth rate and a frequency which is obtained by taking a weighted average of the frequencies and growth rates of the modes forming a cluster with the σ used as the weight. The whole process is repeated until no two modes are similar. The 1^{st}, 2^{nd} and the 5^{th} (final) iterations for the case 2a is shown in figure 7.1(a-c). Note that the mode clustering algorithm significantly simplifies the spectrum in the vicinity of WFMB.

The choice of the cutoff parameters ζ_{spat} and ζ_{spec} involves some subjectivity. The effects of ζ_{spat} and ζ_{spec} on the converged number of modes (N_c) for three different cases are shown in figure 7.2. The rank of OMD was set to 175 (i.e. total number of initial modes $N = 175$) for all the cases. No mode reduction is achieved for $\zeta_{spat} \geq 0.96$, while for $\zeta_{spat} \leq 0.9$ the spectra are over simplified leaving too few modes. A different ζ_{spat} was selected for each case such that $N_c/N \approx 0.9$. For the three cases shown in figure 7.2, the selected cutoffs are shown by the vertical dashed line. The different symbols in figure 7.2 correspond to different values of ζ_{spec}. Note that the mode clustering process does not depend significantly on ζ_{spec} for $\zeta_{spec} \geq 0.2$.

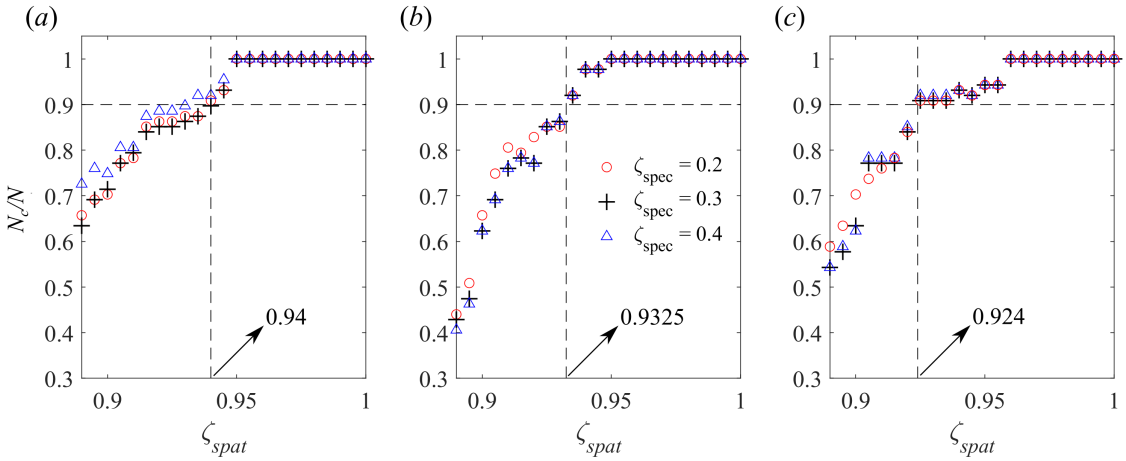


Figure 7.2: Variation of the number of converged modes (N_c) with ζ_{spat} for different ζ_{spec} for the cases (a) 2a, (b) 3 and (c) 4b.

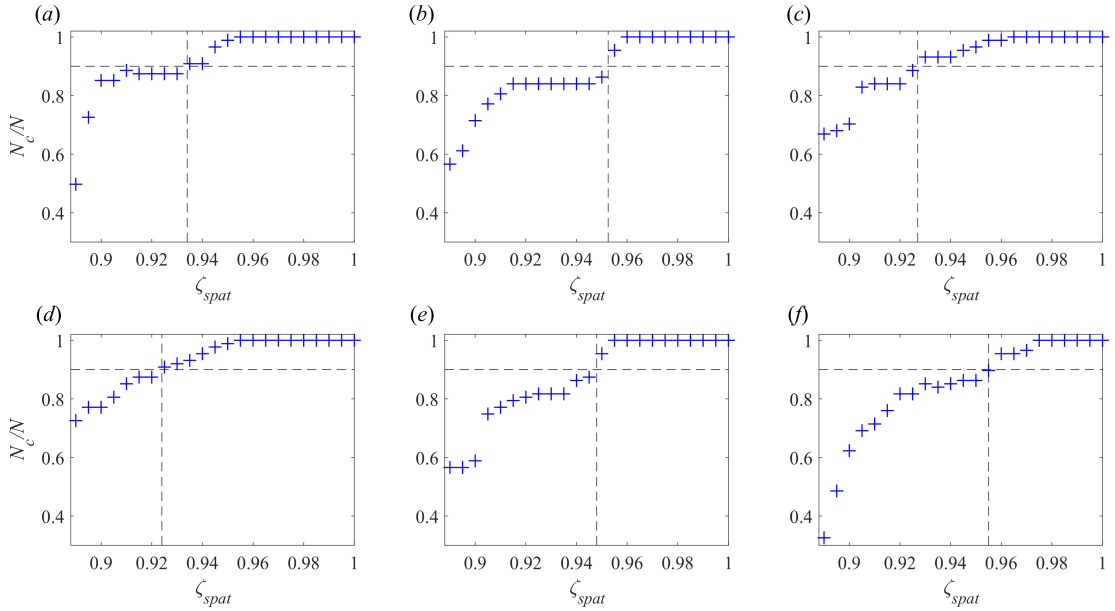


Figure 7.3: Variation of the number of converged modes (N_c) with ζ_{spat} for (a) case 1, (b) case 2b, (c) case 2c, (d) case 4a, (e) case 4c and (f) case 4d.

The analysis was therefore continued with $\zeta_{spec} = 0.3$ for all the cases. The variation of the converged number of modes for the remaining cases along with the selected ζ_{spat} (shown by the dashed vertical line) is shown in figure 7.3 for $\zeta_{spec} = 0.3$.

The first, second and the final iterations for the no grid case, case 3 and case 4b are shown in figures 7.4. Interestingly, a significant number of similar modes are observed for the no grid case as well. Note that, in chapter 6, the CKE budget analysis was performed for the same data

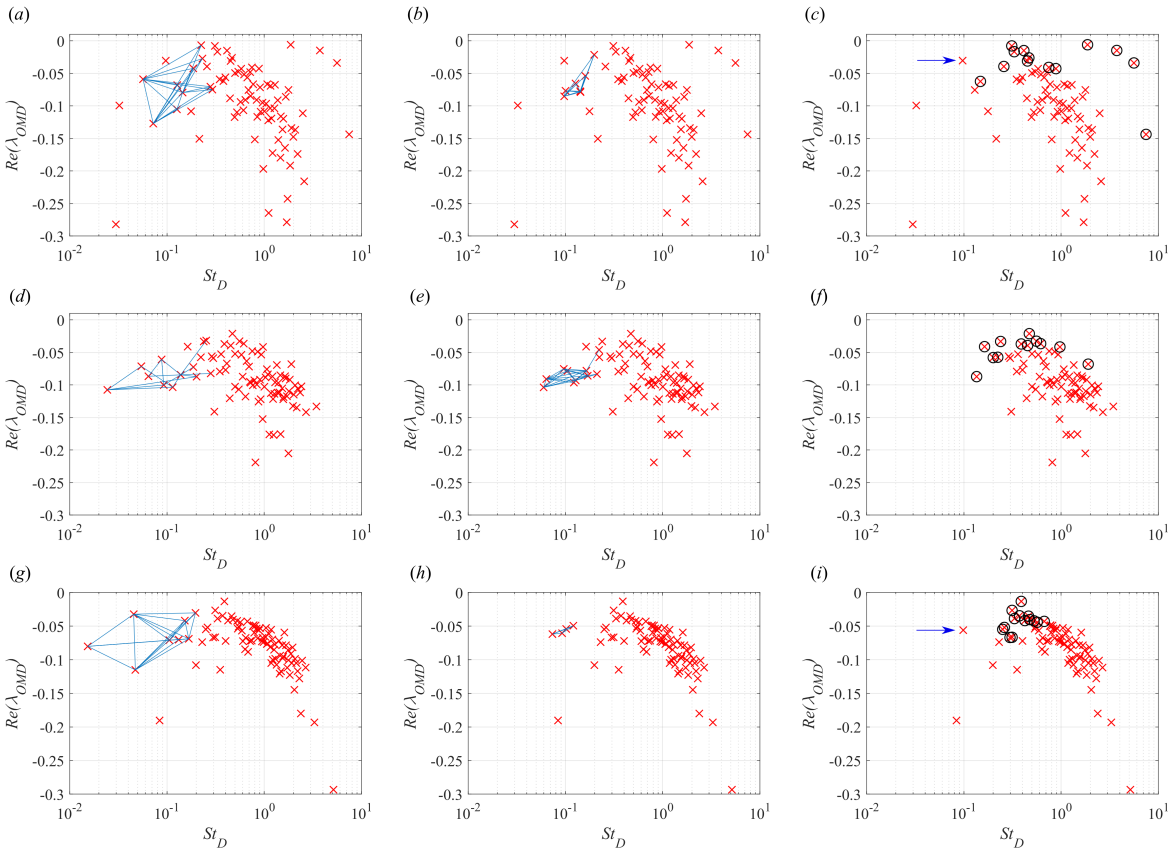


Figure 7.4: 1st, 2nd and final iterations of the mode clustering algorithm for the no grid case (a-c), case 3 (d-f) and case 4b (g-i).

set without using mode clustering. In the next section, it will be shown that the analysis for the no grid case yields similar results with/without mode clustering. Mode clustering therefore simplifies the spectrum, making it easier to select the physically meaningful modes which are used to form a reduced order representation of the coherent component of the flow. Upon clustering, the selected modes are highlighted in figure 7.4(c) with the 'o' symbols. Among the tip vortex related modes, only the frequencies $f_r - 4f_r$ could be captured in the OMD spectrum (figure 7.4(c)). The modes corresponding to $5f_r$ and $6f_r$ were therefore obtained using phase averaging similar to that discussed in chapters 5 and 6. At first glance, the number of similar modes in the first iteration for the cases with FST look comparable to that for the no grid case. However, in general, equal or more iterations were required for the cases with FST to reach convergence. This can be realised by looking at the second iterations for the cases in figure 7.4. The FST cases are left with a larger number of clusters. For all the cases, the final modes (marked by the 'o' symbols) were carefully selected by looking at the spatial mode shape and

how the clusters evolved over iterations.

7.2.1 The nature of the wake meandering mode in the presence of FST

Two dominant wake meandering modes (having a frequency in the WMFB) for four cases of increasing T_i are shown in figure 7.5. For the no grid case (figure 7.5(a,b)), regular patterned structures of wavelength $1.5-2D$ are observed. Note that, these two modes are almost exactly the same as the modes observed for the no grid case in chapter 6 without mode clustering (see figure 6.3(a,b)), apart from slight difference in the mode amplitude. This offers reassurance that the mode clustering algorithm adopted here does not alter the physical information embedded in the data set, rather it simplifies the analysis. As T_i is increased, the wake meandering modes not only show a larger wavelength, but the transverse (along y) width of the modes also increases. Note from figure 7.5(a,b) that the modes are not particularly energetic for $y \geq 0.5D$. The modes initiate from the vicinity of the nacelle highlighting the importance of the nacelle to provide the perturbation necessary to kick start wake meandering (Howard et al., 2015). For higher T_i, the modes show a significant energy content for $y \geq 0.5D$. This is primarily because in the presence of FST, perturbations are widely available and aren't limited to the region behind the nacelle. The early breakdown of the tip vortices in the presence of elevated FST can provide additional perturbations in the vicinity of the outer wake. The energy budget analysis in chapter 6 revealed that in the absence of FST, the wake meandering modes were primarily energised by the mean flow, hence acting like a primary mode. In the presence of FST, whether the dominant energy source for the mode remains the mean flow or not is an interesting question which will be discussed further in the next sections.

As highlighted earlier, care must be taken while selecting modes from the reduced spectrum (after performing mode clustering) to represent the coherent component of the flow. The lesser damped modes generally represent a physically meaningful mode, but drawing a cutoff on the growth rate ($Re(\lambda_{OMD})$) is subjective. Looking at the nature of the spectra, the modes having $Re(\lambda_{OMD}) \gtrsim -0.05$ or in the vicinity were considered. Before selecting a mode, the mode shape had to be checked manually for each of the modes to see if they show any meaningful structures at all. Sometimes a slightly more damped mode had to be selected as it showed a nice spatially

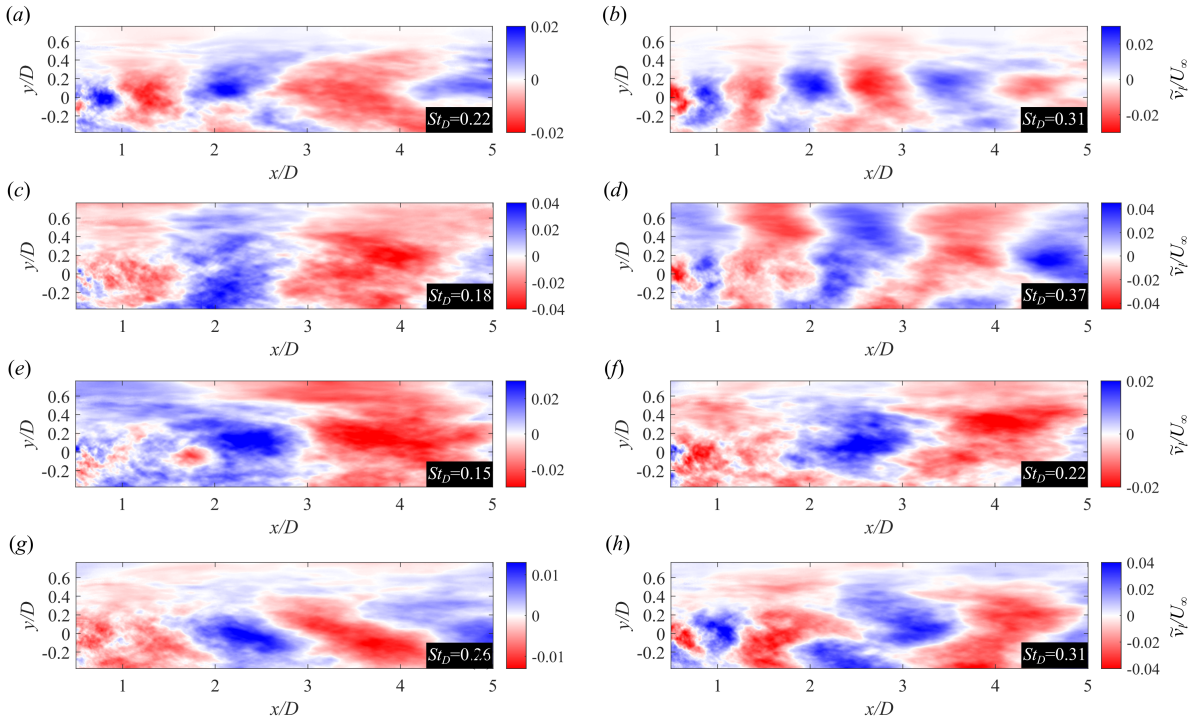


Figure 7.5: Two dominant wake meandering modes for the cases (a,b) without FST, (c,d) case 2a, (e,f) case 3, (g,h) case 4b.

coherent structure (example figure 7.4(i)). While occasionally some modes were not selected despite being less damped than some other selected modes. The spatial shape of these modes revealed very large scale smeared structures which were likely due to intermittent passage of large scale structures having a size smaller than that indicated by the mode shapes. Example of such modes are shown in figure 7.6 for the no grid case and case 4b. These modes are also highlighted with a blue arrow in the spectra shown in figures 7.4(c) and 7.4(i). Furthermore, when a mode was obtained by clustering other modes, the growth rate of the new mode was simply calculated as a weighted average of the growth rates of the modes forming the cluster. This was done just to place the new mode somewhere in the spectrum and this growth rate need not have any physical meaning. Therefore, the shape of the modes involved in clustering was always checked irrespective of their growth rates. Additionally, OMD shows the high frequency modes to be highly damped. This can be seen in figure 7.4(c) for the frequency $4f_r$.

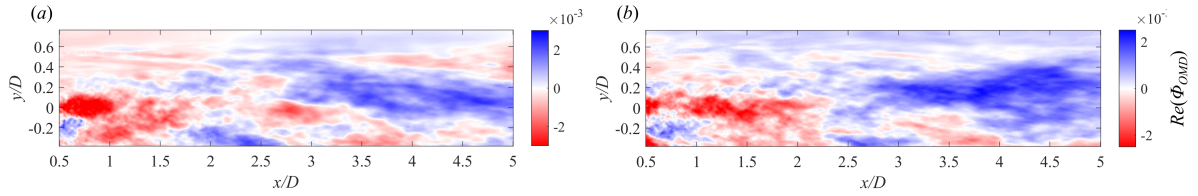


Figure 7.6: Example low frequency modes for the (a) no grid case and (b) case 4b that are not considered to be a part of the coherent component of the flow.

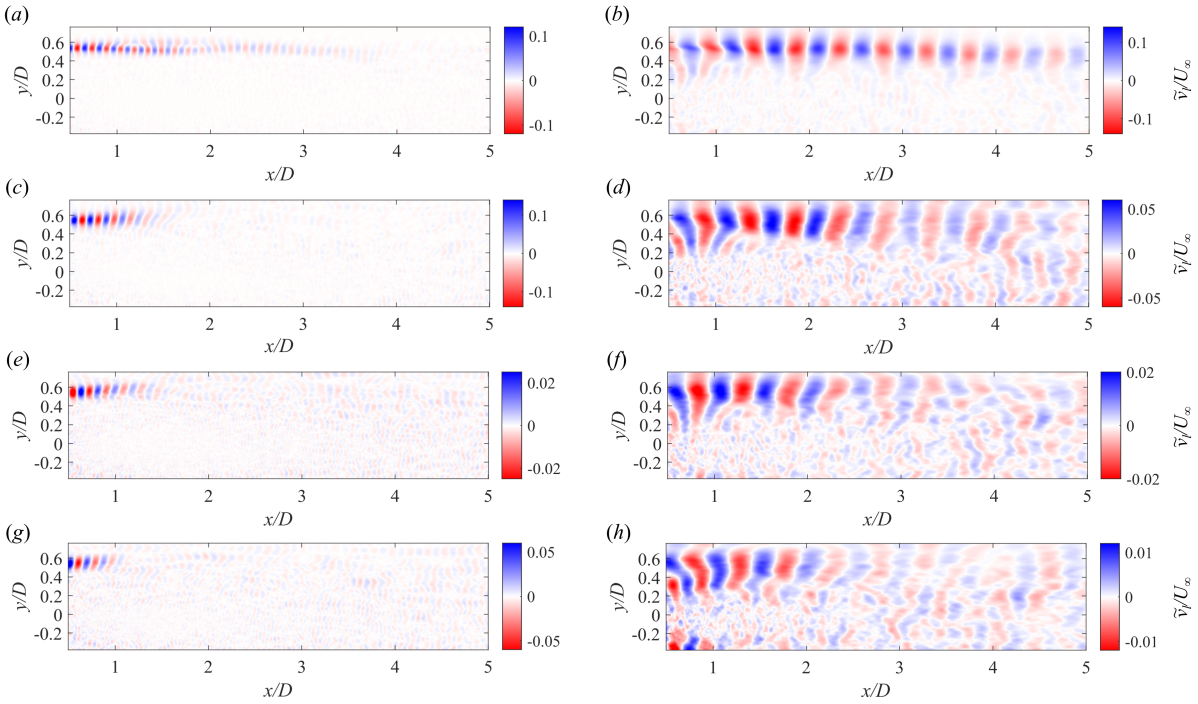


Figure 7.7: Modes associated with $3f_r$ (a,c,e,g) and f_r (b,d,f,h) for no grid case (a,b), case 2a (c,d), case 3 (e,f) and case 4b (g,h).

7.2.2 The modes related to the tip vortices

The tip vortex related modes for the four FST cases discussed earlier are shown in figure 7.7. As discussed in chapter 4, the modes associated with $3f_r$ here clearly show how the tip vortices breakdown earlier as freestream turbulence is increased. A similar pattern is observed for the modes associated with f_r as well as the harmonics of f_r and $3f_r$. In chapter 4, for the cases 2a and 2b, new frequencies were observed that corresponded to the sum and difference of $3f_r$ and a wake meandering frequency that was dominant in the freestream. These frequencies were however not present in the OMD spectrum for either of the cases. A similar observation was reported in chapter 5 where the new frequencies corresponding to the sum and difference of

the main cylinder's (f_m) and control rod's shedding frequency (f_c) were not captured in OMD. The modes associated with the new frequencies discussed in chapter 4 were therefore obtained using phase averaging as discussed in chapters 5 and 6. These are shown in figure 7.8 for the cases 2a and 2b. The spatial orientation of the modes reveal an interesting pattern. Note from figure 4.6(b) that the f_{wm} mode interacting with $3f_r$ was energetic in the freestream side ($y > 0.5D$). In order to indicate the difference in the spatial location of the modes, a black line was added in figure 7.8 showing the loci of the points where the kinetic energy of the mode $3f_r$ was maximum. It can be seen that for both the cases, the high frequency mode $3f_r + f_{wm}$ is situated more towards the freestream side, while $3f_r - f_{wm}$ resided more towards the wake side. The exact same spatial orientation of the frequencies $f_c \pm f_m$ was reported in chapter 5 where the high frequency mode resided more towards the shear layer between the two wake generating bodies, while the low frequency mode resided in the other outer side of the control rod's wake. Such similarity between a simple two dimensional multiscale flow and complex three dimensional multiscale flow involving rotation is truly remarkable.

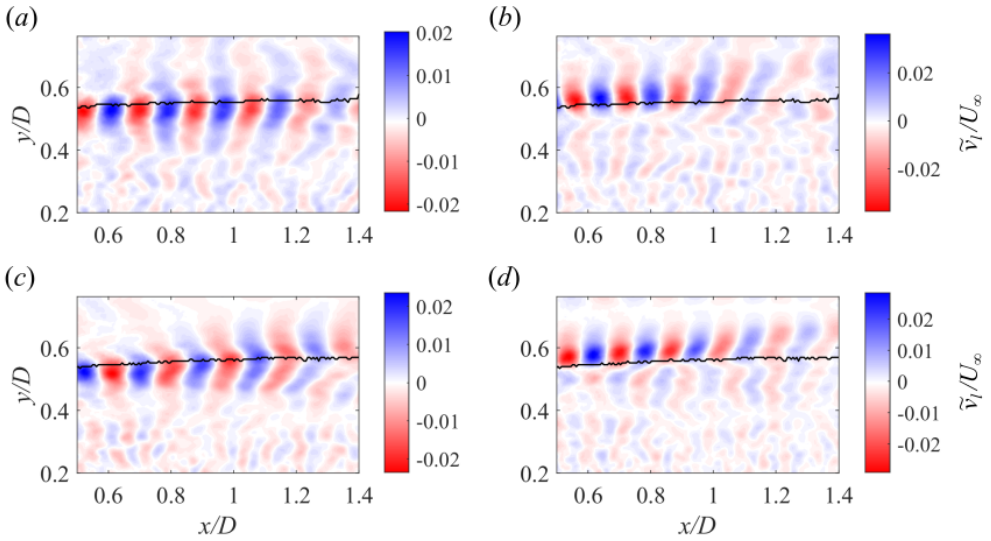


Figure 7.8: Modes associated with $3f_r - f_{wm}$ (a,c) and $3f_r + f_{wm}$ (b,d) case 2a (a,b) and case 2b (c,d).

7.3 Effect of FST on the kinetic energy budgets

The kinetic energy budget terms are first discussed for the four cases discussed earlier. The energy budget terms are summed over the entire domain and shown in figure 7.9. Since the

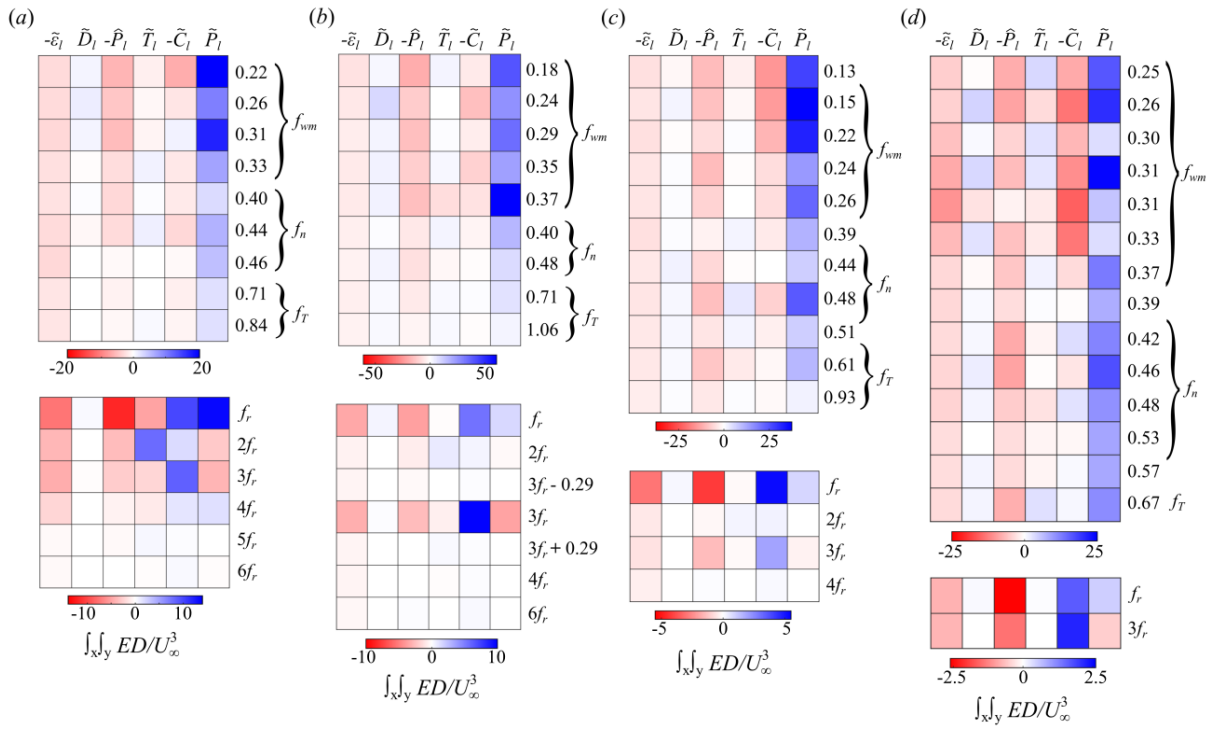


Figure 7.9: Summed budget terms for (a) no grid case, (b) case 2a, (c) case 3 and (d) case 4b.

modes related to the tip vortices show weaker energy exchanges compared to the low frequency modes (particularly for the FST cases), a separate colour bar is used for them. As a general observation, as freestream turbulence level is increased, the number of energetic low frequency modes increased. Further, the number of tip vortex related modes decreased as discussed earlier. In chapter 6 it was shown that without any freestream turbulence the wake meandering mode acted like a primary mode, extracting energy from the mean flow. In the presence of FST, the mean flow production ($\tilde{P}_l$) term is still found to be the dominant energy source for wake meandering. A larger positive contribution from triadic interaction and diffusion is observed for the cases with FST. The same was observed for the nacelle and tower's vortex shedding modes.

The tip vortex related modes in the presence of FST showed energy exchanges similar to the no grid case, however, the magnitudes of the terms decreased as T_i was increased. f_r for the no grid case was primarily energized by the mean flow production ($\tilde{P}_l$) term. For the FST cases, the relative contribution of the convection term for f_r was higher than the ($\tilde{P}_l$) term. Note from figure 6.7(a) that for the no grid case, the ($\tilde{P}_l$) term for f_r peaks at $x \approx 0.62D$. As T_i is increased, this peak moves further upstream and hence is likely not captured within the field of view resulting in a significant underestimation of the term. $2f_r$ was found to be energized by

the triadic interaction term for all the FST cases in which it could be captured. The magnitude of the term diminished with T_i. For the highest T_i cases, the harmonics of f_r and $3f_r$ were not observed within the field of view and hence no triadic interaction could be captured. The new frequencies $3f_r \pm f_{wm}$ for case 2a, although weak, showed positive contribution from the triadic interaction term, establishing the fact that these are secondary modes were produced due to the interaction between $3f_r$ and f_{wm} similar to those observed in chapter 5 for the simplified multiscale flow.

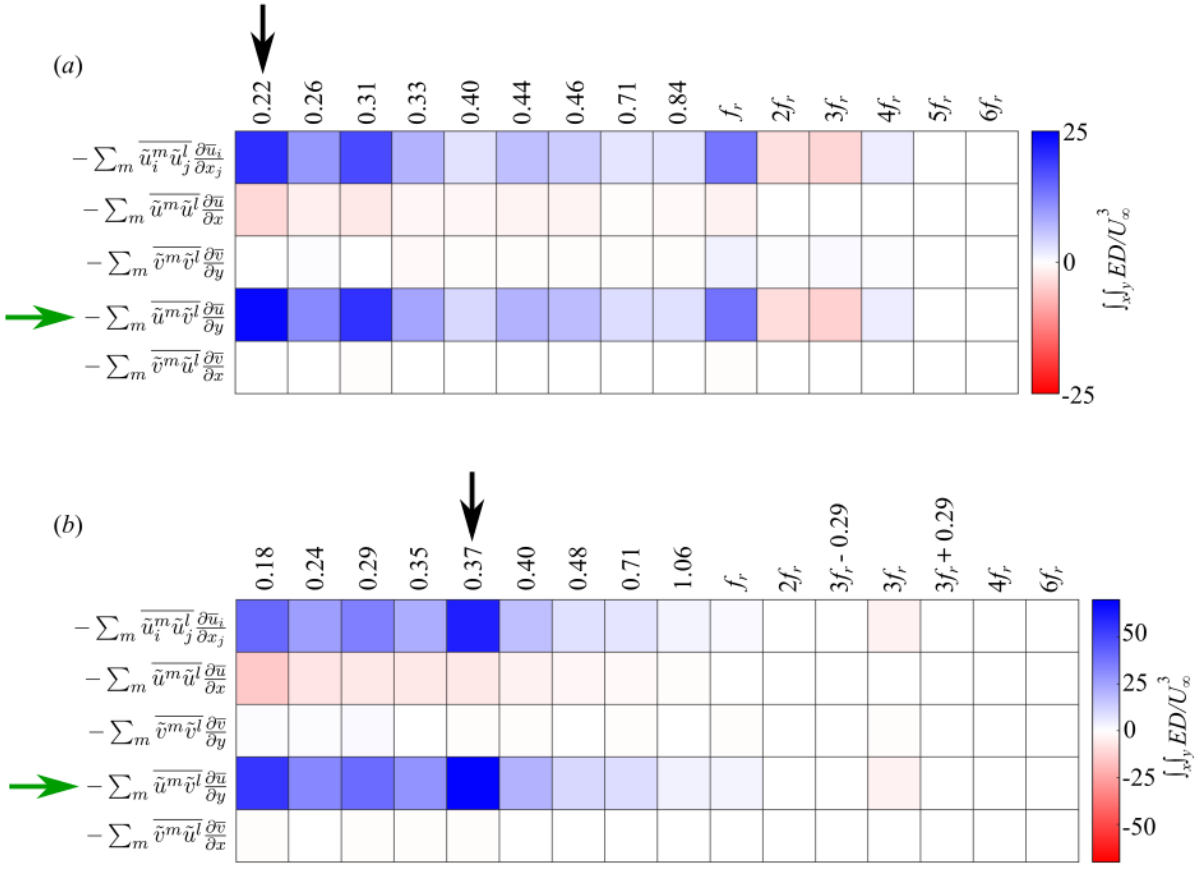


Figure 7.10: Summed $\tilde{P}_l$ term for the frequencies in the WMFB for different FST cases. The x axis on the top shows the turbulence intensity of each case.

In figure 7.10 the dominant source term for the wake meandering modes, *i.e.* the $\tilde{P}_l$ term is compared for all the cases. For a particular case, the $\tilde{P}_l$ terms for all the wake meandering related modes are stacked in a column. Among these, the frequencies of the two dominant modes are indicated. Note that these two dominant modes are the same as those highlighted in figure 7.5 for the selected cases. The net $\tilde{P}_l$ term for all the FST cases were found to be

higher than the no grid case. However, the total of the $\tilde{P}_l$ terms did not monotonically increase either with T_i or L_v, reiterating the fact that the specific details of the freestream frequency spectrum is important. This is similar to that observed in chapter 4. This offers reassurance that after a long channel of data analysis involving modal decomposition, mode clustering and energy budget analysis, the flow physics has indeed been properly captured.

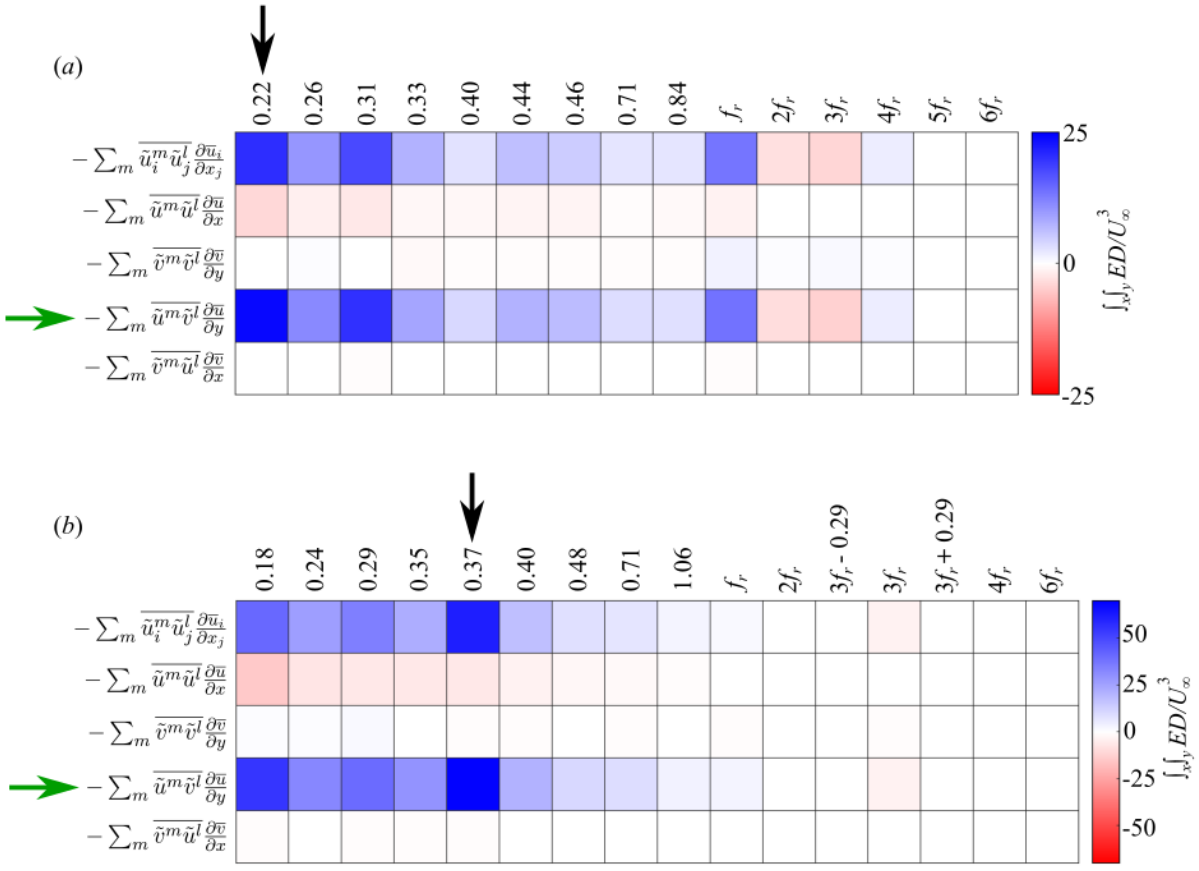


Figure 7.11: Summed components of the $\tilde{P}_l$ term for (a) case 1 and (b) case 2a.

Now the intriguing question is why at all the mean flow production term is enhanced for wake meandering in the presence of FST. Note that the $\tilde{P}_l$ term was defined as $\tilde{P}_l = -\sum_m \overline{\tilde{u}_i^m \tilde{u}_j^l} \frac{\partial \bar{u}_i}{\partial x_j}$, where m can be any coherent mode selected in the flow including the l_{th} mode. Therefore, the term is composed of four components. The contributions of these four terms towards the total mean flow production is checked for the modes for the no grid case and case 2a in figure 7.11. Note that case 2a was one of the cases that showed the strongest wake meandering modes. The first row in figures 7.11(a) and (b) show the net mean flow production term, while the next four rows show the contribution of the four constituent terms. Note that the $\tilde{P}_l$ term is essentially

driven by the single term $-\sum_m \overline{\tilde{u}^m \tilde{v}^l} \frac{\partial \overline{u}}{\partial y}$ (shown by the green arrow), similar to the arguments presented in section 6.5. This implies that for the wake meandering modes to be stronger in the presence of FST, either $-\sum_m \overline{\tilde{u}^m \tilde{v}^l}$ or $\frac{\partial \overline{u}}{\partial y}$ or both are stronger for the wake meandering modes with FST.

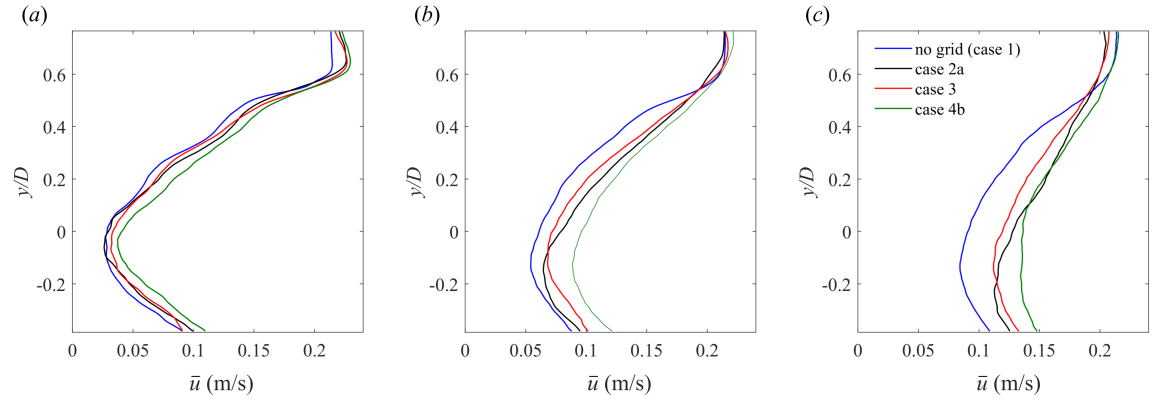


Figure 7.12: Mean streamwise velocity profiles for selected FST cases at (a) $x/D = 1$, (b) $x/D = 3$ and (c) $x/D = 5$.

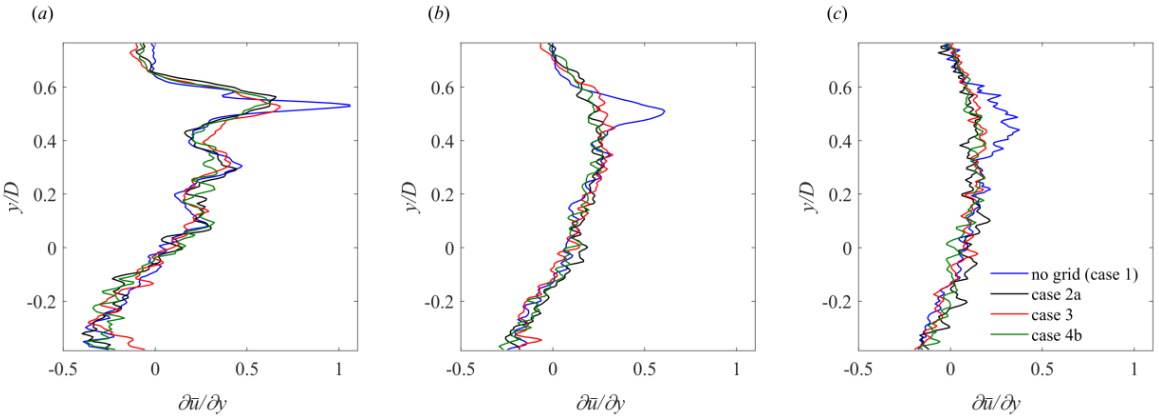


Figure 7.13: Transverse gradient of mean streamwise velocity for selected FST cases at (a) $x/D = 1$, (b) $x/D = 3$ and (c) $x/D = 5$.

To check this, first the changes in the mean flow is investigated. The mean streamwise velocity profiles and their transverse gradients for the four different FST cases are shown in figures 7.12 and 7.13. Although the mean flow profiles show some differences across different cases, the changes in the transverse gradients are not strong enough to yield the observed enhancement in the $\tilde{P}_l$ with FST. Therefore, the $-\sum_m \overline{\tilde{u}^m \tilde{v}^l}$ term must have caused the change. Following the argument in section 6.5, it can be said that $-\sum_m \overline{\tilde{u}^m \tilde{v}^l} \approx \overline{\tilde{u}^l \tilde{v}^l}$. This is verified in figure 7.14 for the two dominant wake meandering modes for case 1 and case 2a (highlighted by the

black arrows in figure 7.11). In figure 7.14, $\tilde{v}^l$ is the transverse component of the dominant wake meandering mode and $\tilde{u}^m$ can be the streamwise component of any of the modes including the dominant wake meandering mode. As was expected, the correlation is the strongest when $m = l$. Furthermore, note that the amplitude of $\overline{\tilde{u}^l\tilde{v}^l}$ (summed over the entire domain) for the case 2a is almost twice that for case 1, similar to that observed for the $\tilde{P}_l$ term. This implies that either the modes ($\tilde{v}^l$) are stronger with FST or the correlation between the transverse and streamwise components of the wake meandering mode is stronger. To further check this, the quantity $\int_x \int_y \overline{\tilde{u}^l\tilde{v}^l}$ was normalised by $\int_x \int_y \sqrt{\overline{(\tilde{u}^l)^2}\ \overline{(\tilde{v}^l)^2}}$. The normalised values were of similar magnitudes for both cases, implying that the modes themselves are stronger as was also seen in figure 7.5.

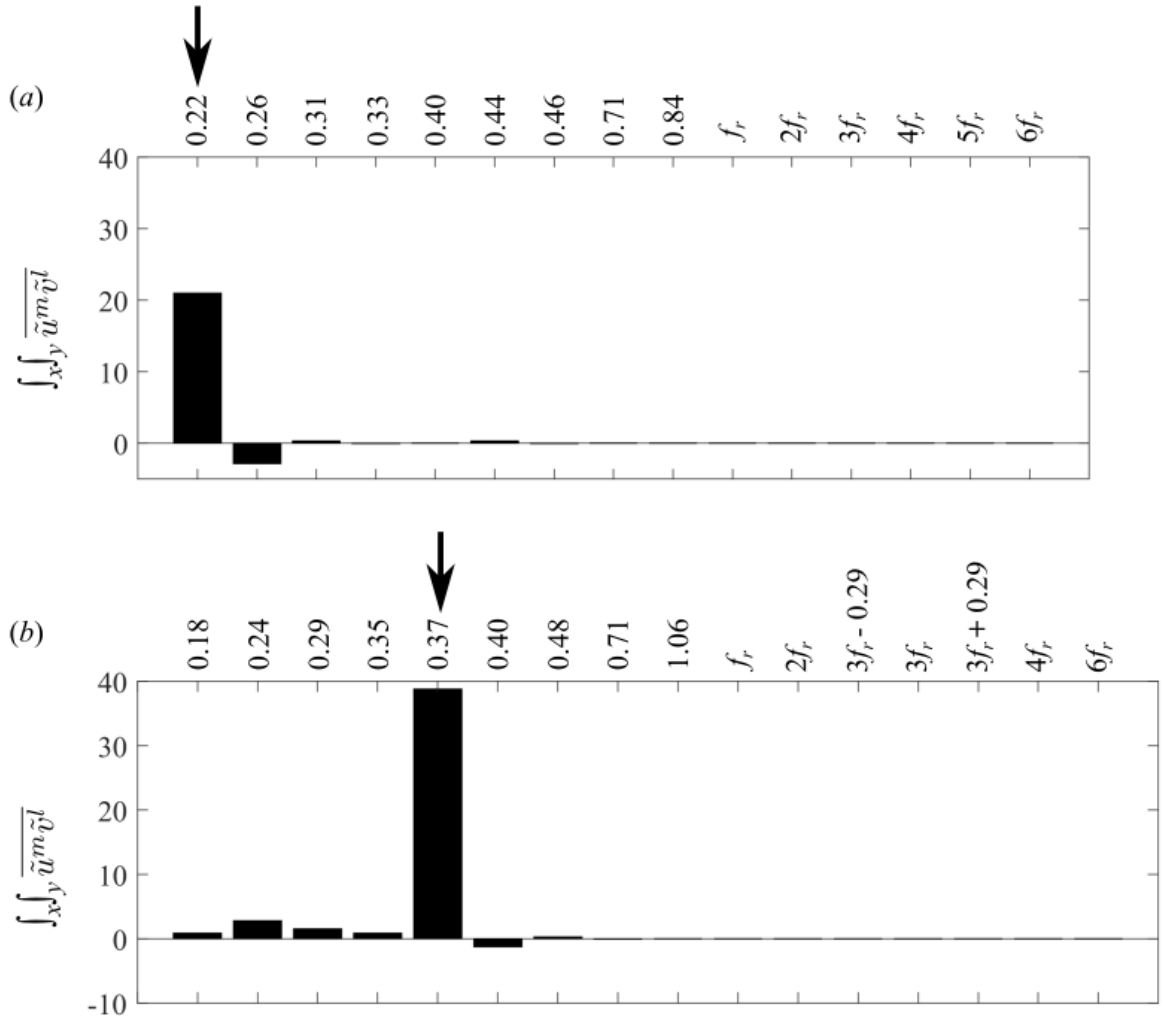


Figure 7.14: Summed correlation $\overline{\tilde{u}^m\tilde{v}^l}$ for (a) case 1 and (b) case 2a.

The above discussion however still does not physically explain how the wake meandering modes in the presence of FST are stronger. It is particularly challenging to explain the observation that the mean flow gradients do not change appreciably despite the fact that the wake meandering modes are extracting more energy from the mean flow. The problem could be due to the fact that the size of the field of view was not enough to capture the entire energy transfer process for the wake meandering modes. Note that the wake meandering modes in the presence of FST were much wider in nature (were energetic even beyond $y/D = 0.5$). Therefore, a significant proportion of the energy exchange might have been happening outside the domain and the energy got transported into the domain. As a result, the mean velocity for the cases with FST might have stronger gradients in this region outside the field of view. A hint of this can be seen from figure 7.12 here. Note that at $x/D = 1$, outside the tip region, there is a sharper decay of the mean streamwise velocity along y for the FST cases. The velocity might continue to decay in the freestream which is not captured here. The gradients reduce as one goes further downstream. One might expect stronger y gradients and even strong x gradients to be present very close to the wind turbine. Further analysis or new experiments with a larger field of view (ideally including the freestream, the turbine and the wake in the same field of view) would be necessary to properly explain the more energetic nature of the wake meandering modes in the presence of FST.

7.4 Triadic interactions

Similarly to figure 6.11 in chapter 6, the inter-frequency triadic energy transfers (summed over the entire domain) are obtained for select cases and shown in figure 7.15. Note that for the no grid case, the energy exchange pattern is the same as that observed for $\lambda = 6$ in chapter 6. The triadic energy transfers are mainly concentrated within the first 4 modes ($f_r - 4f_r$). Interestingly, the same pattern is observed for the low turbulence intensity cases (case 2). However, the transfers were an order of magnitude weaker as can be seen in figure 7.15(b) for case 2a. It can also be seen that the new frequencies $3f_r \pm f_{wm}$ are energised by $3f_r$, *i.e.* the mode having the higher frequency among the two interacting modes. This is similar to that observed for the secondary modes in the simple multiscale flow discussed in chapter 5. A similar energy exchange pattern

is observed for case 3 (figure 7.15(c)), but the transfer magnitudes were nearly two orders of magnitude weaker compared to the no grid case.

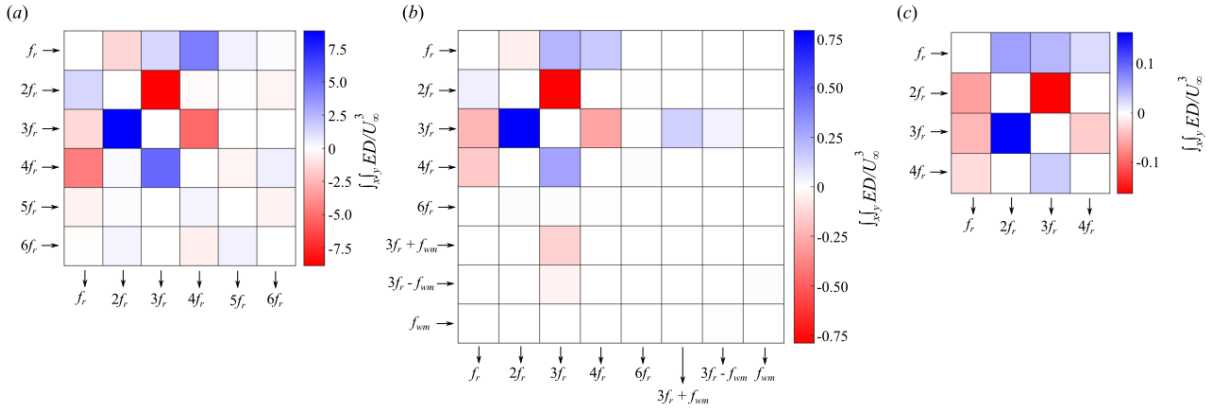


Figure 7.15: Inter frequency triadic energy transfers for (a) no grid case, (b) case 2a and (c) case 3.

7.5 Conclusions

In this chapter, the mode clustering algorithm introduced by Beit-Sadi et al. (2021) was systematically applied after performing the OMD based triple decomposition of the flow field. The algorithm significantly simplified the OMD spectra, particularly in the vicinity of the wake meandering frequency band (WMFB), $0.15 \leq St_D \leq 0.4$. Mode clustering was also performed for the no grid case for which the dominant modes with/without clustering were found to be similar, serving as a validation of the method. As the freestream turbulence (FST) level was increased, the tip vortex related modes became weaker and decayed much closer to the turbine. On the other hand, the wake meandering modes for the cases with FST were always found to be more energetic than that for the no grid case. The wake meandering modes were still primarily energised by the mean flow production term, although there were non-negligible contributions from the diffusion term and triadic interactions. Future work will considering performing the modal energy budget analysis using a different modal decomposition technique such as spectral proper orthogonal decomposition.

Chapter 8

Conclusions

8.1 Summary of Thesis Achievements

- A novel wind turbine model was designed from scratch that imitated a utility-scale wind turbine. A series of PIV experiments were performed to the capture the wake of the turbine with unprecedented spatial and temporal accuracy.
- A novel convective length scale (L_c) related to the pitch of the tip vortices was defined that is shown to be a better length scale than turbine diameter (D) to demarcate the near wake from the far wake. The near wake length was proposed to be $\approx 3L_c$ which was robust over the range of tip speed ratios (λ) tested.
- A link between the 'effective porosity' of the turbine and λ was established, and the strength and frequency of the wake meandering were found to be dependent on λ. In fact, a decreasing trend of wake meandering frequency with λ was observed, similar to vortex shedding from a porous plate at varying porosity. Such similarity upholds the notion of wake meandering being a global instability of the turbine, which can be considered as a 'porous' bluff body of diameter D.
- Considering a simple two-dimensional multiscale flow, three different types of modes were identified: (a) primary modes that draw energy from the mean flow, (b) secondary modes that are energised by other coherent modes in the flow through non-linear triadic interactions and (c) mixed modes that can be energised both by the mean flow and triadic

interactions. It was shown that such primary, secondary and mixed modes exist in the wind turbine wake as well.

- The modes related wake meandering and the sheddings from the nacelle and tower acted as primary modes extracting energy from the mean flow. The magnitude of the mean flow energy transfer term for wake meandering was higher for the higher λ showing further dependence of wake meandering on the turbine's operating condition.

- The tip vortex system (formed by the frequencies $f_r - 6f_r$) exhibited a variety of modes acting as primary, secondary or mixed modes based on λ. The triadic energy exchanges in the tip vortex system were studied in detail for the first time. Two important energy pathways were identified: a) from $3f_r$ to f_r via the frequency $2f_r$ representative of the tip vortex merging process and b) from f_r to $3f_r$ via $4f_r$, a feedback likely linked to stability of the tip vortex system.

- The tip vortex system was found to exchange energy with the mean flow primarily through the turbine's rotational frequency. In fact, the system transfers energy back to the mean flow through the turbine's rotational frequency at some distance downstream marking the onset location of wake recovery (x_{wr}). Here x_{wr} is shown to reduce with λ due to stronger interaction and earlier merging of the tip vortices at a higher λ.

- The tip vortices were shown to break down earlier as the freestream turbulence (FST) level was enhanced. On the other hand, the wake meandering modes became stronger in the presence of FST. This resulted in a shortening of the near wake length with increasing freestream turbulence intensity (T_i).

- The nature of the wake meandering mode was shown to be different in the presence of FST. The frequency peak associated with wake meandering became more broadband with FST. The wake meandering modes were not only more energetic with FST, but also they had a higher transverse width, extending beyond the tip region due to the availability of perturbations in the freestream. Interestingly, the strongest wake meandering was not observed for the case with the highest T_i. Rather, it was observed for a low turbulence intensity case (case 2a) indicating the importance of the nature of the turbulent spectrum.

- The wake meandering modes were however still found to be primarily energised by the mean flow in the presence of FST, with an enhanced contribution from diffusion and triadic interactions. The tip vortex related modes showed similar energy sources and similar triadic energy exchange pathways with/without FST. However, the magnitude of the energy exchange terms drastically reduced with FST. For the first time, new secondary modes were identified that were formed due to the triadic interactions between the tip vortices and wake meandering.

8.2 Future Work

The present work has highlighted a number of interesting physical phenomena in a wind turbine wake that deserves further research.

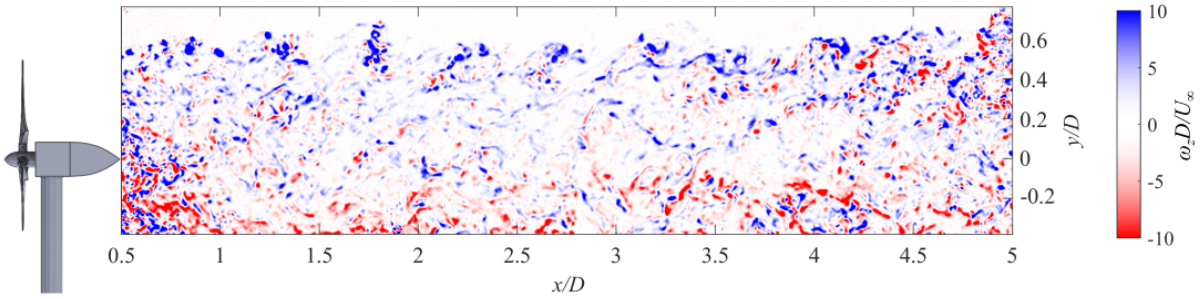


Figure 8.1: Vorticity field in the wake of a turbine with an aerodynamic nacelle for $\lambda = 6$.

- It was shown that the nacelle plays an important role in initiating wake meandering in the turbine's wake. However, the results were reported only for a single nacelle shape. It would be interesting to study if modifying the nacelle shape can modify the strength and initiation of wake meandering. Preliminary experiments were performed with a more aerodynamically shaped nacelle at different λs. The vorticity field for $\lambda = 6$ is shown in figure 8.1. However, further analysis was not performed on the data set and will be taken up as a future exercise.

- Similarly, the effect of changing the shape of the tower needs to be studied in detail. The present work has shown that the tip vortices break down earlier due to the interaction with the tower. An early breakdown of the tip vortices is beneficial in terms of wake

recovery. Therefore an interesting question to ask is, can we modify the tower geometry, at least locally where it interacts with the tip vortices, such that the growth rates of the tip vortex instability is the maximum? The nature of the disturbances that provide the highest growth rates for the instability is already known from previous linear stability works (Gupta and Loewy, 1974).

- The tower's vortex is also strongly impacted due to the unsteady sheared incoming flow. Interestingly, the vortex shedding frequency of the tower was found to be much lower than the expected Strouhal number of 0.2 for vortex shedding behind a cylinder with an undisturbed incoming flow. Even more interesting was the fact that the tower's vortex shedding frequency slightly increased as λ was increased. Is it possible to encounter a vortex lock on behind the tower as indicated by Barbi et al. (1986)? Further experiments can confirm this observation.

- Future experiments can also study the energy exchanges of the wake meandering modes in the presence of FST with a larger field of view. Although it was shown that wake meandering modes were stronger in the presence of FST, drawing more energy from the mean flow, no significant change was observed in the dominant mean velocity gradient. Experiments with a larger field of view that captures the freestream, the turbine and the wake simultaneously might shed more light into the energy transfer process.

- The evolution of the wake can be further studied by capturing the dispersion of a passive scalar such as a high Schmidt number dye. The dye can be released from certain points such as the end of the nacelle or the rear of the tower at the height of the blade tips. Such experiments can elucidate several interesting phenomena such as the interaction between the low frequency inner wake and the high frequency outer shear layer and the nature of the altered vortex shedding from the tower.

- The current experiments were performed at a Reynolds number (Re) two orders of magnitude lower than the typical Re full-scale wind turbines operate at. A faster wake expansion has been reported at a higher Re and the tip vortices can be generally expected to be stronger as Re is increased. It may be possible that the wake, at least the tip vortices at a low Re and high λ behave similarly to that at high Re and low λ. This needs to be

verified with further experiments at different Res.

- Future studies may consider using a different data-driven modal decomposition technique such as spectral proper orthogonal decomposition (sPOD) to evaluate the modal energy exchanges. Especially in the presence of FST, it could be easier to obtain the low frequency energetic modes using sPOD. Other equation based methods such as local/global linear stability analysis and resolvent analysis can provide deeper insights on the origin of various modes.

Bibliography

A. Abraham and T. Leweke. Experimental investigation of blade tip vortex behavior in the wake of asymmetric rotors. *Experiments in Fluids*, 64(6):109, 2023.

A. Abraham, T. Dasari, and J. Hong. Effect of turbine nacelle and tower on the near wake of a utility-scale wind turbine. *Journal of Wind Engineering and Industrial Aerodynamics*, 193: 103981, 2019.

M. M. Alam, M. Moriya, and H. Sakamoto. Aerodynamic characteristics of two side-by-side circular cylinders and application of wavelet analysis on the switching phenomenon. *Journal of Fluids and Structures*, 18(3-4):325–346, 2003.

S. Aubrun, S. Loyer, P. E. Hancock, and P. Hayden. Wind turbine wake properties: Comparison between a non-rotating simplified wind turbine model and a rotating model. *Journal of Wind Engineering and Industrial Aerodynamics*, 120:1–8, 2013.

P. Baj. *Experimental investigation of wake development and mixing behind a multi-scale array of bars*. PhD thesis, Imperial College London, 2018.

P. Baj and O. R. Buxton. Interscale energy transfer in the merger of wakes of a multiscale array of rectangular cylinders. *Physical Review Fluids*, 2(11):114607, 2017.

P. Baj and O. R. Buxton. Passive scalar dispersion in the near wake of a multi-scale array of rectangular cylinders. *Journal of Fluid Mechanics*, 864:181–220, 2019.

P. Baj, P. J. Bruce, and O. R. Buxton. The triple decomposition of a fluctuating velocity field in a multiscale flow. *Physics of Fluids*, 27(7):075104, 2015.

C. Barbi, D. Favier, C. Maresca, and D. Telionis. Vortex shedding and lock-on of a circular cylinder in oscillatory flow. *Journal of Fluid Mechanics*, 170:527–544, 1986.

E. Barlas, S. Buckingham, and J. van Beeck. Roughness effects on wind-turbine wake dynamics in a boundary-layer wind tunnel. *Boundary-Layer Meteorology*, 158:27–42, 2016.

R. Barthelmie, O. F. Hansen, K. Enevoldsen, J. Højstrup, S. Frandsen, S. Pryor, S. Larsen, M. Motta, and P. Sanderhoff. Ten years of meteorological measurements for offshore wind farms. *J. Sol. Energy Eng.*, 127(2):170–176, 2005.

M. Bastankhah and F. Porté-Agel. A new analytical model for wind-turbine wakes. *Renewable Energy*, 70:116–123, 2014.

P. Bearman and A. Wadcock. The interaction between a pair of circular cylinders normal to a stream. *Journal of Fluid Mechanics*, 61(3):499–511, 1973.

M. Beit-Sadi, J. Krol, and A. Wynn. Data-driven feature identification and sparse representation of turbulent flows. *International Journal of Heat and Fluid Flow*, 88:108766, 2021.

E. Berger, D. Scholz, and M. Schumm. Coherent vortex structures in thewake of a sphere and a circular disk at rest and under forced vibrations. *Journal of Fluids and Structures*, 4(3): 231–257, 1990.

G. Berkooz, P. Holmes, and J. L. Lumley. The proper orthogonal decomposition in the analysis of turbulent flows. *Annual review of fluid mechanics*, 25(1):539–575, 1993.

L. Biferale, S. Musacchio, and F. Toschi. Inverse energy cascade in three-dimensional isotropic turbulence. *Physical review letters*, 108(16):164501, 2012.

C. Bingham, C. Morton, and R. J. Martinuzzi. Influence of control cylinder placement on vortex shedding from a circular cylinder. *Experiments in Fluids*, 59(10):1–22, 2018.

N. Biswas and O. R. Buxton. Effect of tip speed ratio on coherent dynamics in the near wake of a model wind turbine. *Journal of Fluid Mechanics*, 979:A34, 2024a.

N. Biswas and O. R. Buxton. Energy exchanges between coherent modes in the near wake of a wind turbine model at different tip speed ratios. *Journal of Fluid Mechanics*, 996:A8, 2024b.

N. Biswas, M. M. Cicolin, and O. R. H. Buxton. Energy exchanges in the flow past a cylinder with a leeward control rod. *Journal of Fluid Mechanics*, 941:A36, 2022.

M. Bourhis, M. Pereira, and F. Ravelet. Experimental investigation of the effects of the Reynolds number on the performance and near wake of a wind turbine. *Renewable Energy*, 209:63–70, 2023.

K. Brown, D. Houck, D. Maniaci, C. Westergaard, and C. Kelley. Accelerated wind-turbine wake recovery through actuation of the tip-vortex instability. *AIAA Journal*, 60(5):3298–3310, 2022.

L. Browne, R. Antonia, and D. Shah. Turbulent energy dissipation in a wake. *Journal of Fluid Mechanics*, 179:307–326, 1987.

T. Burton, N. Jenkins, D. Sharpe, and E. Bossanyi. *Wind energy handbook*. John Wiley & Sons, 2011.

B. Cantwell and D. Coles. An experimental study of entrainment and transport in the turbulent near wake of a circular cylinder. *Journal of Fluid Mechanics*, 136:321–374, 1983.

F. Carbajo Fuertes, C. D. Markfort, and F. Porté-Agel. Wind turbine wake characterization with nacelle-mounted wind lidars for analytical wake model validation. *Remote Sensing*, 10 (5):668, 2018.

I. Castro. Wake characteristics of two-dimensional perforated plates normal to an air-stream. *Journal of Fluid Mechanics*, 46(3):599–609, 1971.

L. Chamorro, C. Hill, S. Morton, C. Ellis, R. Arndt, and F. Sotiropoulos. On the interaction between a turbulent open channel flow and an axial-flow turbine. *Journal of Fluid Mechanics*, 716:658, 2013.

L. P. Chamorro and F. Porté-Agel. A wind-tunnel investigation of wind-turbine wakes: boundary-layer turbulence effects. *Boundary-layer Meteorology*, 132(1):129–149, 2009.

K. K. Chen, J. H. Tu, and C. W. Rowley. Variants of dynamic mode decomposition: boundary condition, koopman, and fourier analyses. *Journal of nonlinear science*, 22:887–915, 2012.

M. Cicolin, O. Buxton, G. Assi, and P. Bearman. The role of separation on the forces acting on a circular cylinder with a control rod. *Journal of Fluid Mechanics*, 915, 2021.

A. Crespo, J. Hernandez, and S. Frandsen. Survey of modelling methods for wind turbine wakes and wind farms. *Wind Energy: An International Journal for Progress and Applications in Wind Power Conversion Technology*, 2(1):1–24, 1999.

C. Dalton, Y. Xu, and J. Owen. The suppression of lift on a circular cylinder due to vortex shedding at moderate Reynolds numbers. *Journal of fluids and structures*, 15(3-4):617–628, 2001.

G. De Cillis, S. Cherubini, O. Semeraro, S. Leonardi, and P. De Palma. Pod-based analysis of a wind turbine wake under the influence of tower and nacelle. *Wind Energy*, 24(6):609–633, 2021.

M. Debnath, C. Santoni, S. Leonardi, and G. V. Iungo. Towards reduced order modelling for predicting the dynamics of coherent vorticity structures within wind turbine wakes. *Philosophical Transactions of the Royal Society A: Mathematical, Physical and Engineering Sciences*, 375 (2091):20160108, 2017.

I. Delbende, C. Selçuk, and M. Rossi. Nonlinear dynamics of two helical vortices: A dynamical system approach. *Physical Review Fluids*, 6(8):084701, 2021.

C. Desmond, J. Murphy, L. Blonk, and W. Haans. Description of an 8 mw reference wind turbine. In *Journal of Physics: Conference Series*, volume 753, page 092013. IOP Publishing, 2016.

A. Dipankar, T. Sengupta, and S. Talla. Suppression of vortex shedding behind a circular cylinder by another control cylinder at low Reynolds numbers. *Journal of Fluid Mechanics*, 573:171–190, 2007.

D. L. Elliott and J. B. Cadogan. Effects of wind shear and turbulence on wind turbine power curves. Technical report, Pacific Northwest Lab., Richland, WA (USA), 1990.

G. Espana, S. Aubrun, S. Loyer, and P. Devinant. Spatial study of the wake meandering using modelled wind turbines in a wind tunnel. *Wind Energy*, 14(7):923–937, 2011.

M. Felli, R. Camussi, and F. Di Felice. Mechanisms of evolution of the propeller wake in the transition and far fields. *Journal of Fluid Mechanics*, 682:5, 2011.

D. Foti, X. Yang, M. Guala, and F. Sotiropoulos. Wake meandering statistics of a model wind turbine: Insights gained by large eddy simulations. *Physical Review Fluids*, 1(4):044407, 2016.

D. Foti, X. Yang, F. Campagnolo, D. Maniaci, and F. Sotiropoulos. Wake meandering of a model wind turbine operating in two different regimes. *Physical Review Fluids*, 3(5):054607, 2018.

S. Frandsen, R. Barthelmie, S. Pryor, O. Rathmann, S. Larsen, J. Højstrup, and M. Thøgersen. Analytical modelling of wind speed deficit in large offshore wind farms. *Wind Energy: An International Journal for Progress and Applications in Wind Power Conversion Technology*, 9(1-2):39–53, 2006.

S. Gambuzza and B. Ganapathisubramani. The influence of free stream turbulence on the development of a wind turbine wake. *Journal of Fluid Mechanics*, 963:A19, 2023.

R. Gomes-Fernandes, B. Ganapathisubramani, and J. Vassilicos. Particle image velocimetry study of fractal-generated turbulence. *Journal of Fluid Mechanics*, 711:306–336, 2012.

R. Gomes-Fernandes, B. Ganapathisubramani, and J. Vassilicos. The energy cascade in near-field non-homogeneous non-isotropic turbulence. *Journal of Fluid Mechanics*, 771:676–705, 2015.

B. Gupta and R. Loewy. Theoretical analysis of the aerodynamic stability of multiple, interdigitated helical vortices. *AIAA journal*, 12(10):1381–1387, 1974.

V. Gupta and M. Wan. Low-order modelling of wake meandering behind turbines. *Journal of Fluid Mechanics*, 877:534–560, 2019.

P. E. Hancock and F. Pascheke. Wind-tunnel simulation of the wake of a large wind turbine in a stable boundary layer: Part 2, the wake flow. *Boundary-layer Meteorology*, 151(1):23–37, 2014.

C. B. Hasager, L. Rasmussen, A. Peña, L. E. Jensen, and P.-E. Réthoré. Wind farm wake: The horns rev photo case. *Energies*, 6(2):696–716, 2013.

M. Heisel, J. Hong, and M. Guala. The spectral signature of wind turbine wake meandering: A wind tunnel and field-scale study. *Wind Energy*, 21(9):715–731, 2018.

J. Hinze. *Turbulence*. McGraw-Hill classic textbook reissue series. McGraw-Hill, 1975. ISBN 9780070290372.

A. Hodgkin, S. Laizet, and G. Deskos. Numerical investigation of the influence of shear and thermal stratification on the wind turbine tip-vortex stability. *Wind Energy*, 2022.

E. L. Hodgson, M. H. A. Madsen, and S. J. Andersen. Effects of turbulent inflow time scales on wind turbine wake behavior and recovery. *Physics of Fluids*, 35(9), 2023.

K. B. Howard, A. Singh, F. Sotiropoulos, and M. Guala. On the statistics of wind turbine wake meandering: An experimental investigation. *Physics of Fluids*, 27(7):075103, 2015.

P. Huerre and P. A. Monkewitz. Local and global instabilities in spatially developing flows. *Annual review of fluid mechanics*, 22(1):473–537, 1990.

D. Hurst and J. Vassilicos. Scalings and decay of fractal-generated turbulence. *Physics of Fluids*, 19(3), 2007.

A. F. Hussain. Coherent structures and turbulence. *Journal of Fluid Mechanics*, 173:303–356, 1986.

A. K. M. F. Hussain and W. C. Reynolds. The mechanics of an organized wave in turbulent shear flow. *Journal of Fluid Mechanics*, 41(2):241–258, 1970.

G. V. Iungo, F. Viola, S. Camarri, F. Porté-Agel, and F. Gallaire. Linear stability analysis of wind turbine wakes performed on wind tunnel measurements. *Journal of Fluid Mechanics*, 737:499–526, 2013.

S. Ivanell, R. Mikkelsen, J. N. Sørensen, and D. Henningson. Stability analysis of the tip vortices of a wind turbine. *Wind Energy*, 13(8):705–715, 2010.

N. Jensen. A note on wind turbine interaction. *Riso-M-2411, Risoe National Laboratory, Roskilde, Denmark*, page 16, 1983.

B. Jin, S. Symon, and S. J. Illingworth. Energy transfer mechanisms and resolvent analysis in the cylinder wake. *Physical Review Fluids*, 6(2):024702, 2021.

S. Kang, X. Yang, and F. Sotiropoulos. On the onset of wake meandering for an axial flow turbine in a turbulent open channel flow. *Journal of Fluid Mechanics*, 744:376–403, 2014.

K. S. Kankanwadi. *Turbulent/turbulent entrainment: a detailed examination of entrainment, and the behaviour of the outer interface as affected by background turbulence.* PhD thesis, Imperial College London, 2022.

D. K. Kinjangi and D. Foti. Characterization of energy transfer and triadic interactions of coherent structures in turbulent wakes. *Journal of Fluid Mechanics*, 971:A7, 2023.

S. Laizet and J. Vassilicos. Fractal space-scale unfolding mechanism for energy-efficient turbulent mixing. *Physical Review E*, 86(4):046302, 2012.

S. Laizet and J. Vassilicos. Stirring and scalar transfer by grid-generated turbulence in the presence of a mean scalar gradient. *Journal of Fluid Mechanics*, 764:52–75, 2015.

K. M. Lam, P. Wong, and N. W. M. Ko. Interaction of flows behind two circular cylinders of different diameters in side-by-side arrangement. *Experimental thermal and fluid science*, 7(3): 189–201, 1993.

G. C. Larsen, H. A. Madsen, K. Thomsen, and T. J. Larsen. Wake meandering: a pragmatic approach. *Wind Energy: An International Journal for Progress and Applications in Wind Power Conversion Technology*, 11(4):377–395, 2008.

L. Lignarolo, D. Ragni, C. Krishnaswami, Q. Chen, C. S. Ferreira, and G. Van Bussel. Experimental analysis of the wake of a horizontal-axis wind-turbine model. *Renewable Energy*, 70: 31–46, 2014.

L. Lignarolo, D. Ragni, F. Scarano, C. S. Ferreira, and G. Van Bussel. Tip-vortex instability and turbulent mixing in wind-turbine wakes. *Journal of Fluid Mechanics*, 781:467, 2015.

L. Lignarolo, D. Ragni, C. Ferreira, and G. Van Bussel. Experimental comparison of a wind-turbine and of an actuator-disc near wake. *Journal of Renewable and Sustainable Energy*, 8 (2):023301, 2016.

P. Lissaman. Low-Reynolds-number airfoils. *Annual Review of Fluid Mechanics*, 15(1):223–239, 1983.

X. Liu and F. O. Thomas. Turbulent kinetic energy budget measurement of planar wake flow in pressure gradients. *Experiments in Fluids*, 2004.

H. Lu and F. Porté-Agel. Large-eddy simulation of a very large wind farm in a stable atmospheric boundary layer. *Physics of Fluids*, 23(6):065101, 2011.

J. L. Lumley. The structure of inhomogeneous turbulent flows. *Atmospheric turbulence and radio wave propagation*, pages 166–178, 1967.

X. Mao and J. Sørensen. Far-wake meandering induced by atmospheric eddies in flow past a wind turbine. *Journal of Fluid Mechanics*, 846:190–209, 2018.

N. Mazellier and J. Vassilicos. Turbulence without Richardson-Kolmogorov cascade. *Physics of fluids*, 22(7):075101, 2010.

B. J. McKeon and A. S. Sharma. A critical-layer framework for turbulent pipe flow. *Journal of Fluid Mechanics*, 658:336–382, 2010.

J. McMasters and M. Henderson. Low-speed single-element airfoil synthesis. *Technical Soaring*, 6(2):1–21, 1980.

S. McTavish, D. Feszty, and F. Nitzsche. Evaluating Reynolds number effects in small-scale wind turbine experiments. *Journal of Wind Engineering and Industrial Aerodynamics*, 120: 81–90, 2013.

D. Medici. *Experimental studies of wind turbine wakes: power optimisation and meandering.* PhD thesis, KTH, 2005.

D. Medici and H. Alfredsson. Wind turbine near wakes and comparisons to the wake behind a disc. In *43rd AIAA Aerospace Sciences Meeting and Exhibit*, page 595, 2005.

D. Medici and P. Alfredsson. Measurements on a wind turbine wake: 3d effects and bluff body vortex shedding. *Wind Energy: An International Journal for Progress and Applications in Wind Power Conversion Technology*, 9(3):219–236, 2006.

D. Medici and P. H. Alfredsson. Measurements behind model wind turbines: further evidence of wake meandering. *Wind Energy: An International Journal for Progress and Applications in Wind Power Conversion Technology*, 11(2):211–217, 2008.

M. A. Miller, J. Kiefer, C. Westergaard, M. O. Hansen, and M. Hultmark. Horizontal axis wind turbine testing at high Reynolds numbers. *Physical Review Fluids*, 4(11):110504, 2019.

S. Mittal and A. Raghuvanshi. Control of vortex shedding behind circular cylinder for flows at low Reynolds numbers. *International journal for numerical methods in fluids*, 35(4):421–447, 2001.

E. M. Morris, N. Biswas, S. S. Aleyasin, and M. F. Tachie. Particle image velocimetry measurements of turbulent jets issuing from twin elliptic nozzles with various orientations. *Journal of Fluids Engineering*, 143(2):021501, 2021.

A. Nekkanti and O. T. Schmidt. Frequency–time analysis, low-rank reconstruction and denoising of turbulent flows using spod. *Journal of Fluid Mechanics*, 926:A26, 2021.

I. Neunaber, M. Hölling, J. Whale, and J. Peinke. Comparison of the turbulence in the wakes of an actuator disc and a model wind turbine by higher order statistics: A wind tunnel study. *Renewable Energy*, 179:1650–1662, 2021.

A. Niayifar and F. Porté-Agel. Analytical modeling of wind farms: A new approach for power prediction. *Energies*, 9(9):741, 2016.

V. Okulov, I. Naumov, R. Mikkelsen, I. Kabardin, and J. Sørensen. A regular strouhal number for large-scale instability in the far wake of a rotor. *Journal of Fluid Mechanics*, 747:369, 2014.

N. R. Panchapakesan and J. L. Lumley. Turbulence measurements in axisymmetric jets of air and helium. Part 1. Air jet. *Journal of Fluid Mechanics*, 246:197–223, 1993.

V. Parezanović and O. Cadot. Experimental sensitivity analysis of the global properties of a two-dimensional turbulent wake. *Journal of Fluid Mechanics*, 693:115–149, 2012.

V. Parezanović, R. Monchaux, and O. Cadot. Characterization of the turbulent bistable flow regime of a 2 D bluff body wake disturbed by a small control cylinder. *Experiments in Fluids*, 56(1):1–8, 2015.

F. Pierella and L. Sætran. Wind tunnel investigation on the effect of the turbine tower on wind turbines wake symmetry. *Wind Energy*, 20(10):1753–1769, 2017.

F. Porté-Agel, M. Bastankhah, and S. Shamsoddin. Wind-turbine and wind-farm flows: a review. *Boundary-Layer Meteorology*, 174(1):1–59, 2020.

F. A. Portela, G. Papadakis, and J. Vassilicos. The turbulence cascade in the near wake of a square prism. *Journal of Fluid Mechanics*, 825:315–352, 2017.

A. Prasad and C. H. Williamson. Three-dimensional effects in turbulent bluff-body wakes. *Journal of Fluid Mechanics*, 343:235–265, 1997.

H. U. Quaranta, H. Bolnot, and T. Leweke. Long-wave instability of a helical vortex. *Journal of Fluid Mechanics*, 780:687–716, 2015.

H. U. Quaranta, M. Brynjell-Rahkola, T. Leweke, and D. S. Henningson. Local and global pairing instabilities of two interlaced helical vortices. *Journal of Fluid Mechanics*, 863:927–955, 2019.

N. Ramos-García, A. Abraham, T. Leweke, and J. N. Sørensen. Multi-fidelity vortex simulations of rotor flows: Validation against detailed wake measurements. *Computers & Fluids*, 255: 105790, 2023.

W. Reynolds and A. Hussain. The mechanics of an organized wave in turbulent shear flow. Part 3. Theoretical models and comparisons with experiments. *Journal of Fluid Mechanics*, 54(2): 263–288, 1972.

A. Roshko. Experiments on the flow past a circular cylinder at very high Reynolds number. *Journal of fluid mechanics*, 10(3):345–356, 1961.

S. Sarmast, R. Dadfar, R. F. Mikkelsen, P. Schlatter, S. Ivanell, J. N. Sørensen, and D. S. Henningson. Mutual inductance instability of the tip vortices behind a wind turbine. *Journal of Fluid Mechanics*, 755:705–731, 2014.

P. J. Schmid. Dynamic mode decomposition of numerical and experimental data. *Journal of fluid mechanics*, 656:5–28, 2010.

P. J. Schmid. Dynamic mode decomposition and its variants. *Annual Review of Fluid Mechanics*, 54:225–254, 2022.

O. T. Schmidt, A. Towne, G. Rigas, T. Colonius, and G. A. Bres. Spectral analysis of jet turbulence. *Journal of Fluid Mechanics*, 855:953–982, 2018.

A. S. Sharma and B. J. McKeon. On coherent structure in wall turbulence. *Journal of Fluid Mechanics*, 728:196–238, 2013.

M. Sherry, A. Nemes, D. Lo Jacono, H. M. Blackburn, and J. Sheridan. The interaction of helical tip and root vortices in a wind turbine wake. *Physics of Fluids*, 25(11):117102, 2013a.

M. Sherry, J. Sheridan, and D. L. Jacono. Characterisation of a horizontal axis wind turbine's tip and root vortices. *Experiments in fluids*, 54(3):1–19, 2013b.

J. H. Silvestrini and E. Lamballais. Direct numerical simulation of oblique vortex shedding from a cylinder in shear flow. *International Journal of Heat and Fluid Flow*, 25(3):461–470, 2004.

L. Sirovich. Turbulence and the dynamics of coherent structures, parts i, ii and iii. *Quart. Appl. Math.*, pages 561–590, 1987.

F.-L. Song, W.-T. Lu, and C.-H. Kuo. Interactions of lock-on wake behind side-by-side cylinders of unequal diameter at Reynolds number 600. *Experimental thermal and fluid science*, 44: 736–748, 2013.

J. N. Sørensen, R. F. Mikkelsen, D. S. Henningson, S. Ivanell, S. Sarmast, and S. J. Andersen. Simulation of wind turbine wakes using the actuator line technique. *Philosophical Transactions of the Royal Society A: Mathematical, Physical and Engineering Sciences*, 373(2035):20140071, 2015.

R. J. Stevens and C. Meneveau. Flow structure and turbulence in wind farms. *Annual Review of Fluid Mechanics*, 49:311–339, 2017.

P. J. Strykowski and K. R. Sreenivasan. On the formation and suppression of vortex 'shedding' at low Reynolds numbers. *Journal of Fluid Mechanics*, 218:71–107, 1990.

S. Sunada, A. Sakaguchi, and K. Kawachi. Airfoil section characteristics at a low Reynolds number. 1997.

K. Taira, S. L. Brunton, S. T. Dawson, C. W. Rowley, T. Colonius, B. J. McKeon, O. T. Schmidt, S. Gordeyev, V. Theofilis, and L. S. Ukeiley. Modal analysis of fluid flows: An overview. *Aiaa Journal*, 55(12):4013–4041, 2017.

V. Theofilis. Global linear instability. *Annual Review of Fluid Mechanics*, 43(1):319–352, 2011.

W. Thielicke and E. Stamhuis. PIVlab–towards user-friendly, affordable and accurate digital particle image velocimetry in matlab. *Journal of open research software*, 2(1), 2014.

M. Toloui, L. P. Chamorro, and J. Hong. Detection of tip-vortex signatures behind a 2.5 mw wind turbine. *Journal of Wind Engineering and Industrial Aerodynamics*, 143:105–112, 2015.

A. Towne, O. T. Schmidt, and T. Colonius. Spectral proper orthogonal decomposition and its relationship to dynamic mode decomposition and resolvent analysis. *Journal of Fluid Mechanics*, 847:821–867, 2018.

M. Türk and S. Emeis. The dependence of offshore turbulence intensity on wind speed. *Journal of Wind Engineering and Industrial Aerodynamics*, 98(8-9):466–471, 2010.

D. Vahidi and F. Porté-Agel. A new streamwise scaling for wind turbine wake modeling in the atmospheric boundary layer. *Energies*, 15(24):9477, 2022.

L. Vermeer, J. N. Sørensen, and A. Crespo. Wind turbine wake aerodynamics. *Progress in Aerospace Sciences*, 39(6-7):467–510, 2003.

M. K. Vinnes, S. Gambuzza, B. Ganapathisubramani, and R. J. Hearst. The far wake of porous disks and a model wind turbine: Similarities and differences assessed by hot-wire anemometry. *Journal of Renewable and Sustainable Energy*, 14(2):023304, 2022.

P. Welch. The use of fast fourier transform for the estimation of power spectra: a method based on time averaging over short, modified periodograms. *IEEE Transactions on audio and electroacoustics*, 15(2):70–73, 1967.

S. E. Widnall. The stability of a helical vortex filament. *Journal of Fluid Mechanics*, 54(4): 641–663, 1972.

C. H. Williamson. Vortex dynamics in the cylinder wake. *Annual review of fluid mechanics*, 28 (1):477–539, 1996.

J. Winslow, H. Otsuka, B. Govindarajan, and I. Chopra. Basic understanding of airfoil characteristics at low Reynolds numbers (10^4–10^5). *Journal of Aircraft*, 55(3):1050–1061, 2018.

Y.-T. Wu and F. Porté-Agel. Atmospheric turbulence effects on wind-turbine wakes: An les study. *energies*, 5(12):5340–5362, 2012.

A. Wynn, D. Pearson, B. Ganapathisubramani, and P. J. Goulart. Optimal mode decomposition for unsteady flows. *Journal of Fluid Mechanics*, 733:473–503, 2013.

Z. Yang, P. Sarkar, and H. Hu. Visualization of the tip vortices in a wind turbine wake. *Journal of visualization*, 15:39–44, 2012.

I. Yildirim, C. Rindt, and A. Steenhoven. Vortex dynamics in a wire-disturbed cylinder wake. *Physics of Fluids*, 22(9):094101, 2010.

Appendix A

Additional notes on PIV resolution and convergence of the OMD modes

A.1 Spatial resolution of the PIV data used in chapter 5

Prior to performing the coherent energy budget analysis on the simple multiscale flow presented in chapter 5, it was verified if the spatial resolution of the data was enough to resolve the coherent structures produced from the control rod. The size of the interrogation windows in the current experiments was $0.37d$ (where d is the diameter of the control rod). However, the interrogation windows had a 75% overlap along the x and y directions. As a result, the separation between adjacent vectors in the processed data was $\approx 0.09d$. Hence, even very close to the control rod, where the coherent structures can be assumed to be smallest, *i.e.* $\sim O(d)$, there were nearly 11 data points to capture their effect. Nevertheless, in order to verify if the spatial resolution correctly captured the energy content in the control rod's wake, results from two different data sets with different spatial resolutions were compared. Apart from the data utilised in chapter 5, Cicolin et al. (2021) also obtained data in a narrow strip spanning $\approx 0.41D - 0.90D$ in the streamwise direction. The spatial resolution of the strip was $\approx 0.15d$ for each vector, and with a 75% overlap it yields a distance of $0.03d$ between adjacent vectors. This additional data therefore had a resolution higher than the data used in chapter 5. Figure A.1(a) shows the evolution of mean kinetic energy in the vicinity of the control rod's wake at the mid section of the strip,

i.e. $x/D = 0.65$ for $\theta = 90°$ obtained from the two data sets. The results from the two data sets agree remarkably well. Additionally, the multiscale triple decomposition is performed for the new data set to extract the energy content in the control rod's shedding mode (denoted by k_c here). Figure A.1(b) here shows the profile of k_c at the same streamwise location as figure A.1(a) and the agreement between the two data sets is again satisfactory.

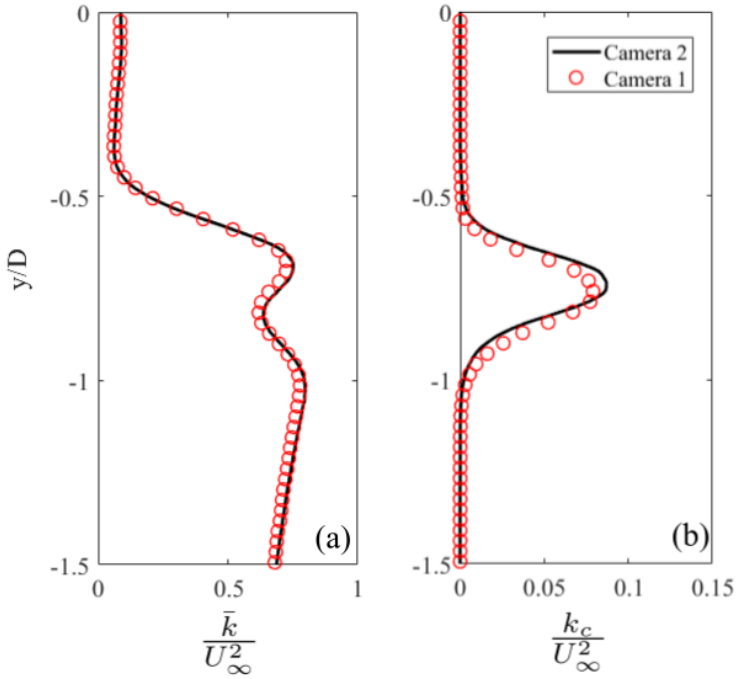


Figure A.1: (a) Mean turbulent kinetic energy and (b) Kinetic energy of the control rod's shedding mode obtained from two data sets at $x/D = 0.65$.

A.2 Convergence and selection of the OMD modes in the wind turbine wake presented in chapter 6

In chapter 6, the rank of the OMD matrices (r) was set to 175. To estimate the possible effects of the choice of r, the decomposition is performed with different rs. OMD is first applied to the data set from experiment 1E for $\lambda = 6$ for different rs. The resultant spectra are shown in figure A.2(a). For $r = 125$, only the modes from $f_r - 3f_r$ are captured. While, for the higher ranks, $4f_r$ is also captured. The dominant wake meandering frequency around $St_D \approx 0.2$ was captured for all the rs as well as frequencies in the range $0.4 \lesssim St_D \lesssim 0.5$ and $0.7 \lesssim St_D \lesssim 0.9$

which are associated with the vortex sheddings from the nacelle and the tower respectively. To evaluate the effect of r on the energy budget analysis, the primary source term for f_r and f_{wm}, *i.e.* the coherent energy production term ($\tilde{P}_l$) is compared for different rs. The streamwise evolution of the spanwise averaged $\tilde{P}_l$ term for the frequencies are shown in figure A.2(b) and A.2(c) for different rs. For f_r, there was no significant variation in $\tilde{P}_l$ with changes in r. A similar observation was noted for all the budget terms for all the tip vortex related modes. The $\tilde{P}_l$ term for f_{wm} was however found to be more sensitive to the selection of r. Especially for $r = 125$, the term looks significantly off from the other two curves in figure A.2(c). This can be expected as the energy budget terms were much noisier for the low-frequency modes. Nevertheless, the energy budget terms did not change significantly when summed over the entire domain, particularly after $r = 175$. Accordingly, the analysis was presented for $r = 175$ only.

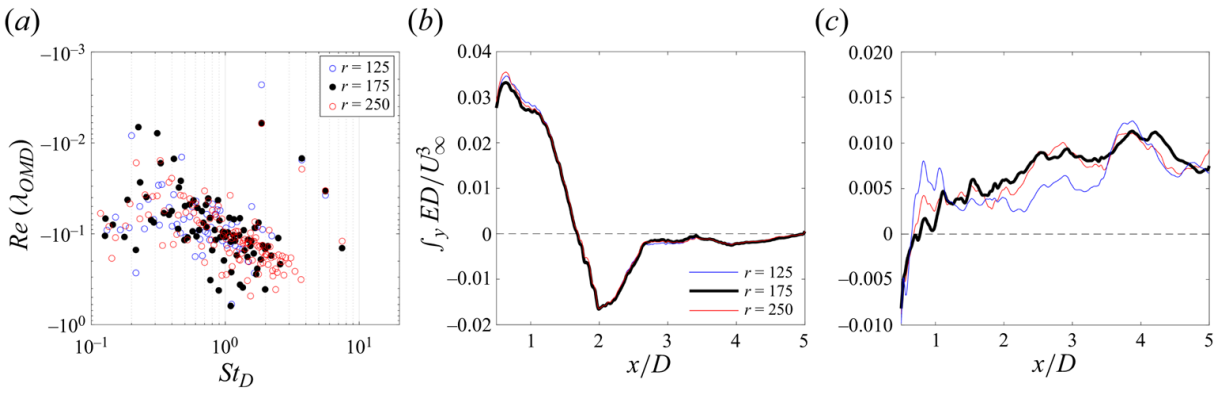


Figure A.2: (a) OMD spectra for different ranks r. (b) and (c) show the streamwise evolution of the spanwise-averaged $\tilde{P}_l$ term for f_r and f_{wm} respectively for different r.

The selection of the OMD modes to form a reduced representation of the flow is non-trivial as there does not exist a strict rule for mode reduction (Beit-Sadi et al., 2021). For the wind turbine wake, the modes were selected based on their growth rates and knowledge of frequencies present in the flow from the prior results in chapter 3. In chapter 3, the dominant low frequency ($St_D < 1$) features were found to be wake meandering ($0.2 \lesssim St_D \lesssim 0.3$), and the sheddings from the nacelle ($0.4 \lesssim St_D \lesssim 0.5$) and the tower ($0.7 \lesssim St_D \lesssim 0.9$). The least damped modes in these frequency ranges were selected and associated with their respective physical features. The selection of the tip-vortex related modes is more definitive due to their discrete temporal nature. Nevertheless, the energy budget analysis was repeated for $\lambda = 6$ for experiment 1E,

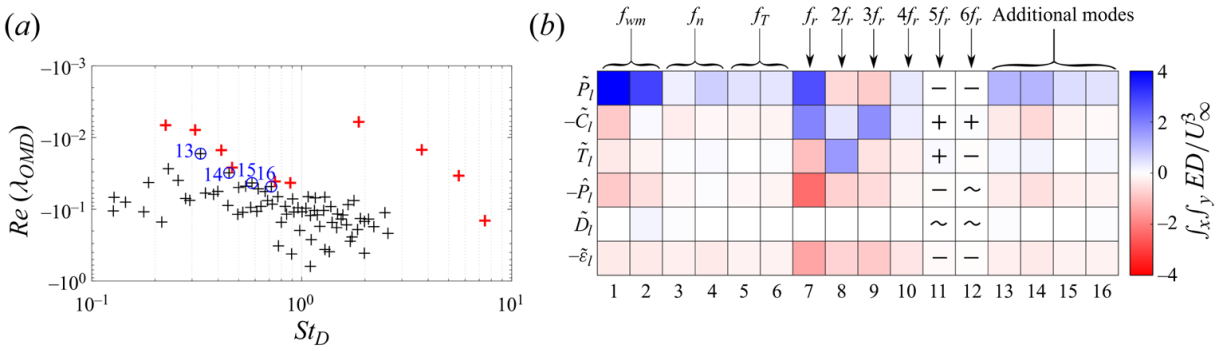


Figure A.3: (a) OMD spectrum for $\lambda = 6$ from experiment 1E. The '$\circ$' symbols show the additional low-frequency modes ($St_D < 1$) retained. (b) shows the energy budget terms of equation 5.5 summed over the domain of investigation for all the modes including the additional low frequency modes.

by including 4 more low-frequency modes which were in the vicinity of the least damped low-frequency modes. These modes are marked by a '$\circ$' symbol (also numbered 13-16) in figure A.3(a) along with the originally selected modes shown by a '$+$' symbol. The integrated energy budget terms of all the modes are shown in figure A.3(b). A comparison with the results in chapter 6 (see figure 6.6(a)) reveals no discernible difference in the energy budget terms of the tip-vortex related modes ($f_r - 6f_r$). The streamwise variation of the spanwise (along y) averaged energy budget terms of the tip vortices also remain unaltered. Mode 13 has a frequency close to the wake meandering frequency range, but shows much weaker energy exchanges (especially in terms of mean flow production, *i.e.* the $\tilde{P}_l$ term which is the primary source term) compared to the originally selected wake meandering modes. Interestingly however, modes 14-16, which are in an intermediate frequency range between the nacelle's (f_n) and tower's shedding frequency (f_T) show energy exchanges with magnitudes comparable to the originally selected f_n and f_T modes (modes 3-6). Comparing with figure 6.6(a) it can be said that exclusion of the modes 13-16 results in a slight increase in the $\tilde{P}_l$ term of the low-frequency modes, especially for f_n. Further, when the modes are excluded, they are considered to be a part of the stochastic velocity component (u''). This results in a slightly stronger stochastic kinetic energy production term ($\hat{P}_l$) for the originally selected modes, mainly for f_{wm} and f_n. Nevertheless, inclusion or exclusion of the modes 13-16 does not alter the main conclusion about the low-frequency modes, *i.e.* they are primary modes driven by the mean flow (through the $\tilde{P}_l$ term) and they do not exhibit any significant nonlinear triadic interaction with the other modes.

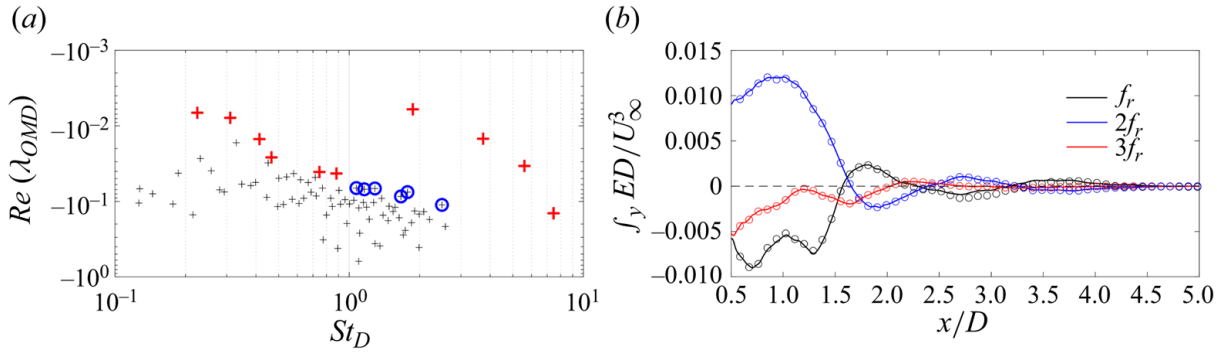


Figure A.4: (a) OMD spectrum for $\lambda = 6$ from experiment 1E. The '$\circ$' symbols show the additional modes retained in the range $1 \lesssim St_D \lesssim 3$. (b) shows the streamwise evolution of the spanwise-averaged net triadic energy production term for $f_r - 3f_r$ with (circles) and without (solid lines) the inclusion of the additional modes.

The OMD spectrum in figure A.3 also shows a number of modes with characteristic frequencies in the range $1 \lesssim St_D \lesssim 3$. The modes could be related to non-linear interactions between the f_r mode and one of the low-frequency modes (the wake meandering mode or the sheddings from the nacelle or the tower). These modes were, however, not selected in the reduced order representation of the flow due to their highly-damped nature. To assess the possible effects of this exclusion in the energy exchange patterns observed, especially in the non-linear triadic energy exchanges, the analysis is repeated by including some of these modes for $\lambda = 6$. The OMD spectrum for $\lambda = 6$ (with $r = 175$) is reproduced in figure A.4(a). The originally selected modes are shown by a '$+$' and the extra modes selected in the range $1 \lesssim St_D \lesssim 3$ are marked by a '$\circ$' sign. In figure A.4(b) the streamwise evolution of the spanwise averaged net triadic energy production (the $\tilde{T}_l^+ - \tilde{T}_l^-$ term in equation 5.5) is shown for f_r, $2f_r$ and $3f_r$ obtained by using fewer modes (shown by solid lines) and by including the additional modes in the range $1 \lesssim St_D \lesssim 3$ (using circles). Inclusion of the additional modes clearly does not alter the triadic energy exchanges in the tip vortex system, indicating negligible non-linear interaction between the tip vortex system and the low-frequency modes, at least within the field of view considered.